

On Entanglement Dynamics in Holographic Theories

Hanzhi Jiang

Lady Margaret Hall



University of Oxford

A thesis presented for the degree of

Doctor of Philosophy

Michaelmas 2025

Acknowledgements

I would like to first thank my advisor, Prof. Ard A. Louis, for accepting me to Oxford, for introducing me to algorithmic information theory, for teaching me to think critically, and for giving me the freedom to explore other fields in the middle of my DPhil.

I am extremely grateful to Prof. Márk Mezei, who kindly agreed to co-supervise me at the beginning of my third year. In my early days, Márk found interesting and reasonably doable projects for me to work on, spent hours answering all my elementary questions and guided me through calculations; later on, he encouraged me to be independent, albeit still provided generous help even to projects that he did not actively involved. I cannot imagine what my DPhil would be like without the supervision of Márk.

I am much obliged to Prof. Vijay Balasubramanian, Prof. Mike Blake, Prof. Richard Davison, Prof. Simon F. Ross, Julio Virrueta, Anthony Thompson, Tom Yildirim and Prof. Kamaludin Dingle for fruitful collaborations. I am grateful to Prof. Andrei Starinets and Prof. Benjamin Withers for being my thesis committee and for providing constructive feedback to this thesis.

I would like to thank all my friends and colleagues at Rudolf Peierls Centre for Theoretical Physics and Mathematical Institute, University of Oxford. I extend my appreciation to Stacey Doyle and Jordan Summers for helping me with all the admin-related issues. I am grateful to my College, Lady Margaret Hall, for financial support. I would also like to acknowledge my college advisor, Prof. Gianluca Gregori, for all the academic advice.

Last but not least, I would like to express my gratitude to my parents for their love and support. This thesis is dedicated to them.

Abstract

Entanglement entropy (EE) is a concept of paramount importance in modern theoretical physics. Nevertheless, calculating EE in generic interacting theories with non-trivial time dependence is notoriously difficult. In this thesis, we address the real-time dynamics of EE in certain strongly-coupled quantum field theories (QFT) using the Anti-de Sitter/Conformal Field Theory (AdS/CFT) correspondence. We first study the time evolution of EE in an exactly solvable model of two-dimensional CFT with an inhomogeneous sine-square deformation (SSD). We argue that the non-trivial time evolutions driven by the SSD Hamiltonian can be regarded as changing the foliations of spacetime. Remarkably, this leads to the presence of new horizons in the dual three-dimensional bulk. We then compute the EE in SSD CFT using holography and found agreement with CFT results in all comparable cases. Afterwards, we proceed to entanglement dynamics in generic chaotic quantum many-body systems. In the limit of large subsystems and late times, entanglement dynamics is believed to be described by an entanglement membrane effective theory. For 2d CFTs, a degenerate tension function reproduces several results regarding the dynamics of the entropy; this stands in contrast to higher dimensions where the tension is non-degenerate. We use holography to show that, in order to correctly capture the reflected entropy in 2d CFT, one needs to add an additional degree of freedom to the membrane description. Furthermore, we show that the conventional non-degenerate membrane tension function emerges upon introducing a relevant deformation to the CFT, dual to a planar Banados-Teitelboim-Zanelli (BTZ) black hole with scalar hair and with an interior Kasner universe. Subsequently, we establish a membrane effective theory for the dynamics of reflected entropy in higher dimensions. Lastly, we apply the membrane theories for reflected entropy to study the time evolution of multiparty entanglement signals. We found that scrambling dynamics generate multiparty entanglement with rich structures.

Table of Contents

1 Introduction **1**

1.1 Entanglement entropy 5

1.1.1 UV and IR properties 7

1.2 Holographic entanglement entropy 9

1.2.1 CFT$_d$ in the vacuum on $\mathbb{R}^{d-1,1}$ 12

1.2.2 Holographic UV properties 16

1.2.3 Multiple regions 17

1.2.4 Thermal CFT$_d$ on $\mathbb{R}^{d-1,1}$ 17

1.2.5 Entanglement plateaux 19

1.3 Time evolution of holographic entanglement entropy 21

1.3.1 CFTs driven by unconventional Hamiltonians 21

1.3.2 Time evolution of entanglement entropy from black hole interior 23

1.3.3 Entanglement membrane from holography 26

1.3.3.1 The entanglement membrane for a half space subregion 28

1.4 Reflected entropy 33

1.5 Signals of multiparty entanglement 35

1.5.1 Review of multiparty entanglement signals 36

2 New horizons for inhomogeneous quenches **42**

2.1 Introduction 42

2.2 A special quantum quench 43

2.2.1 Setup 43

2.2.2 The sine-squared deformed time evolution 45

2.2.3 Boundary triangle 47
2.3 Gravity dual for the special quantum quench 51
2.3.1 Bulk geometry 51
2.3.2 New horizon in AdS_3 54
2.3.3 New horizon on BTZ 56
2.4 Dynamics of entanglement entropy 59
2.4.1 Gravity dual of SSD: ground state 61
2.4.1.1 Holographic computation 61
2.4.1.2 Match with field theory result 62
2.4.2 Gravity dual of SSD: thermal state 64
2.4.2.1 Holographic computations 64
2.4.2.2 Non-equal-time entanglement plateau 65
2.4.2.3 Holographic cooling/heating effect 66
2.4.2.4 Comparison with field theory result on a line . . 68

3 The entanglement membrane in 2d CFT: reflected entropy and RG flow 69
3.1 Entanglement membrane and 2d CFT 70
3.1.1 The entanglement membrane shape for a half space 71
3.1.2 Membranes for saturated strips 75
3.2 Reflected entropy from the entanglement wedge cross section in 2d CFT 78
3.2.1 Setup of the problem 78
3.2.2 Non-equilibrium EWCS 81
3.2.3 Equilibrium EWCS 82
3.3 Reflected entropy in the membrane effective theory 85
3.3.1 Time evolution of entanglement cross-section 86
3.3.2 Membrane theory for reflected entropy 90

3.3.3 Comparison between the generalised and ordinary membrane results for reflected entropy 94
3.4 Entanglement membrane and 2d RG flows 95
3.4.1 Holographic RG flow from BTZ to AdS_3-Kasner 95
3.4.2 Small ϕ perturbation theory 98
3.4.2.1 Expansion near the singularity 101
3.4.2.2 Expansion near the horizon 103

4 Time Evolution of Multiparty Entanglement Signals 107
4.1 Dynamics of R_3 108
4.1.1 A single finite region 109
4.1.2 Two finite regions 111
4.2 Dynamics of I_3 and Q_4 117

5 Conclusion 127

Bibliography 129

Appendix A Appendices to Chapter 2 143
A.1 Review of SSD CFT 143
A.1.1 SSD CFT 143
A.1.1.1 The action of H_1 143
A.1.1.2 Trigonometric forms of the coordinate transformations 146
A.1.1.3 SSD CFT as a CFT on curved spacetime 147
A.1.1.4 H_q with $q > 1$ 148
A.1.2 General Cases 149
A.2 Changing the cutoff in AdS/CFT 150
A.2.1 AdS/CFT with a nonuniform cutoff 150

A.2.2 The Fefferman-Graham expansion with a curved boundary 151
A.3 Asymptotic symmetries of AdS_3 . . . 153
A.4 Geodesic equations . . . 154
A.4.1 Null geodesics . . . 155
A.4.1.1 Pure AdS_3 . . . 155
A.4.1.2 BTZ . . . 157
A.4.2 Spacelike geodesics . . . 159
A.4.2.1 Pure AdS_3 . . . 160
A.4.2.2 BTZ . . . 162
A.5 Time evolution of SSD horizons . . . 165
A.6 Comments on bulk reconstruction . . . 166
A.7 Quenches governed by other $SL(2)$ Virasoro subalgebras . . . 167
A.8 Two-point functions of twist operators . . . 169

Appendix B Appendices to Chapter 3 172

B.1 Detailed analysis of solutions in the generalised membrane theory 172
B.1.1 Displaced half-space . . . 172
B.1.2 Saturated EWCS . . . 174
B.2 Exact solutions of entanglement entropy in BTZ black hole . . . 176
B.2.1 Difference between Schwarzschild and infalling time . . . 178
B.2.2 Map between BTZ and Poincare AdS_3 . . . 178
B.2.3 Spacelike Geodesics in Poincare AdS_3 . . . 182
B.2.4 Displaced half spaces . . . 184
B.2.4.1 In Poincare AdS_3 . . . 184
B.2.4.2 In planar BTZ . . . 186
B.2.5 Static geodesic . . . 189
B.2.5.1 In Poincare AdS_3 . . . 191
B.2.5.2 In planar BTZ . . . 192

B.2.6 Entanglement entropy of displaced half space 193
B.2.6.1 Gravity calculation 193
B.2.6.2 CFT calculation 195
B.3 Exact solutions of EWCS in BTZ black hole 197
B.3.1 Non-equilibrium EWCS 197
B.3.2 Saturated Entanglement Wedge Cross Section 200
B.3.2.1 Length of saturated EWCS 201
B.3.2.2 In Poincare AdS_3 202
B.3.2.3 In planar BTZ 204
B.4 RT surfaces with spherical regions 209
B.5 Scaling behaviour of EWCS in $d > 2$ 210
B.6 Adding ϕ^4-interactions 211

Appendix C Appendices to Chapter 4 **215**
C.1 Generalised entanglement membrane for CFT_2 215
C.1.1 S_R in the case of adjacent intervals 215
C.1.2 Dynamics of R_3 218
C.1.2.1 A single finite interval 218
C.1.2.2 Two finite regions 219
C.1.3 Dynamics of Q_4 220
C.2 Higher partite entanglement signals 222
C.3 Saturation of S_R in finite adjacent intervals 226

1 | Introduction

A characteristic phenomenon in quantum physics is the presence of entanglement. The entanglement in quantum systems can be quantitatively described by an information-theoretic quantity, the entanglement entropy (EE). EE plays a crucial role in understanding the structures of quantum matters. For example, the ground state of interacting quantum many-body systems can be understood in terms of the entanglement structures of their wavefunctions: EE serves as an order parameter describing the phase structures of these systems (Kitaev & Preskill, 2006; Levin & Wen, 2006). The study of EE is also of paramount importance in time-dependent cases. Interacting systems thermalise. For isolated systems, while unitary time evolutions map pure states to pure states, the reduced density matrix of a subregion is expected to be very close to a thermal density matrix (Deutsch, 1991; Srednicki, 1994; Rigol, Dunjko, & Olshanii, 2008), which has EE proportional to the volume of the subregion. Therefore, the thermalisation of quantum many-body systems are fundamentally characterised by their entanglement dynamics. In addition to theoretical interests, thermalisation as probed by entanglement dynamics can be measured experimentally in cold atom systems under a quench (Kaufman et al., 2016), i.e. a sudden change of the Hamiltonian. Observations in their setup are consistent with the aforementioned volume law of EE.[1]

While EE is a profound quantity in modern theoretical physics, the calculation of EE in generic interacting systems is a formidable task, and has been carried out mostly in special systems like two-dimensional conformal field theories (CFTs) (Holzhey, Larsen, & Wilczek, 1994; Calabrese & Cardy, 2004, 2005) and free field theories (Calabrese & Cardy, 2004). In recent years, nevertheless, impor-

[1] To be more precise, the observable in (Kaufman et al., 2016) is the quantum purity, whose natural logarithm is the 2nd Renyi entropy defined in (1.1.4) that is related to EE.

tant progress has been made thanks to the AdS/CFT correspondence (Maldacena, 1998; Gubser, Klebanov, & Polyakov, 1998; Witten, 1998), the idea that certain quantum matter systems are mathematically equivalent to quantum gravity theories in one dimension higher. The strong-weak nature of the AdS/CFT correspondence allows one to map problems in strongly-interacting quantum systems to weakly coupled gravitational theories that are computationally tractable. In particular, the Ryu-Takayanagi (RT) (Ryu & Takayanagi, 2006b, 2006a) and Hubeny-Rangamani-Takayanagi (HRT) (Hubeny, Rangamani, & Takayanagi, 2007) proposals equate EE in field theory to the area of certain co-dimension 2 extremal surfaces (in the former case, minimal surfaces) in the dual gravitational theories.

The goal of this thesis is to employ the AdS/CFT correspondence to explore the time evolution of entanglement entropy in certain strongly interacting quantum many-body systems with holographic gravity duals. The thesis is organised as follows:

To proceed, we will first review the essentials of entanglement entropy in section 1.1, and then survey holographic entanglement entropy in the simpler time-symmetric case in section 1.2. We will turn to our main interest, the time evolution of holographic entanglement entropy, in section 1.3, where we review the basis and point out the open problems that led to the original research in Chapter 2 and 3. Subsequently, in section 1.4 and 1.5, we will review information-theoretic quantities characterising multipartite correlations that can be regarded as generalisations of the RT/HRT proposals.

To gain intuitions for the difficult problem of entanglement dynamics, it is often instructive to look into special toy models with nice theoretical properties. In Chapter 2, we first consider the time evolution of EE in an exactly solvable setup of a two-dimensional CFT driven by Hamiltonians built out of conformal symmetry gen-

erators (Wen & Wu, 2018b): in this case, the quantum dynamics can be understood using two-dimensional geometry. We investigate how the dynamics is reflected in the holographic dual three-dimensional spacetime and find *new horizons*. Our result provides a novel example demonstrating the emergence of horizons when quantum systems are driven by alternative Hamiltonians: a familiar example of this kind is the Rindler horizon in general relativity. We then compute the EE in SSD CFT using holography and found agreement with CFT results in all comparable cases.

In Chapter 3, we move on to exploring entanglement dynamics in generic chaotic many-body systems. We focus on the the limit of late time and large region, i.e. the "hydrodynamic" limit, under which the time evolution of EE has an effective description in terms of a minimal membrane (Jonay, Huse, & Nahum, 2018; Mezei, 2018). For 2d CFTs, a degenerate tension function reproduces several results regarding the dynamics of the EE; this stands in contrast to higher dimensions where the tension is non-degenerate. In Chapter 3, we use holography to propose the *generalised membrane* effective theory for entanglement dynamics in 2d CFT by adding *an additional degree of freedom* to the membrane description. This additional degree of freedom has two important consequences: First, it plays a crucial role in the dynamics of a novel information-theoretic function known as reflected entropy. Second, it is believed to be related to the infinite-dimensional conformal symmetry of 2d CFT, which prevents the emergence of dissipative hydrodynamics. Indeed, as we will also address in Chapter 3, when we break this infinite-dimensional conformal symmetry by introducing a relevant deformation, we can recover the ordinary membrane theory with a non-degenerate tension function. We then briefly comment on the consistency of our holographic studies with dual field-theoretic results on universal hydrodynamics in two-dimensional

QFTs at high temperature (Davison & Delacretaz, 2024).[2] Finally, we also found that the dynamics of reflected entropy in higher dimensions are captured by ordinary membrane theory.

Subsequently, in Chapter 4, we apply the (generalised) membrane theories for reflected entropy to study the real-time dynamics of multiparty entanglement signals (Balasubramanian, Kang, Murdia, & Ross, 2025) in chaotic quantum many-body systems, including holographic gauge theories. We find that the time evolution profile of multipartite entanglement signals depict rich structures. This indicates that scrambling dynamics often produces non-trivial multipartite entanglement. On the other hand, entanglement dynamics in integrable models are described by the quasi-particle picture (Calabrese & Cardy, 2005; Casini, Liu, & Mezei, 2016). Assuming no initial multipartite entanglement,[3] the entanglement dynamics in the quasiparticle picture are bipartite by construction, and involve free-streaming EPR pairs of entangled quasiparticles which can be shared by at most two regions at a time. Compared with the membrane theory result, we can regard generating multiparty entanglement as a common feature of scrambling dynamics. The results in Chapter 4 then unveil an overlooked aspect of scrambling dynamics with potentially abundant novel properties.

Technical details of Chapter 2-4 are presented in the Appendices.

[2] In a subsequent work (Davison & Jiang, 2026), holography was used to verify the universal hydrodynamics in two-dimensional QFTs, through the phenomenon of "pole skipping" (Grozdanov, Schalm, & Scopelliti, 2018; Blake, Lee, & Liu, 2018; Blake, Davison, Grozdanov, & Liu, 2018).

[3] See (Casini et al., 2016) for discussions on the quasiparticle picture with initial multiparty entanglement.

1.1 Entanglement entropy

Suppose we have a quantum system in a pure state $|\psi\rangle$, whose density matrix is $\rho = |\psi\rangle \langle\psi|$. We divide the system into two subregions A and $\overline{A}$, and denote the artificial boundary ∂A separating them as the entangling surface. The Hilbert space of the system equals the tensor product

$$\mathcal{H}_{A\overline{A}} = \mathcal{H}_A \otimes \mathcal{H}_{\overline{A}}. \tag{1.1.1}$$

The reduced density matrix ρ_A of subregion A is defined by the partial trace

$$\rho_A = \mathrm{Tr}_{\overline{A}}\, \rho. \tag{1.1.2}$$

Intuitively, ρ_A captures the degrees of freedom in A while assuming complete ignorance of what happens in $\overline{A}$. If $|\psi\rangle$ is factorized, we would have a pure state in $\mathcal{H}_A$; the presence of quantum entanglement, nevertheless, leads to a density matrix, i.e. a list of probabilities for the occurrence of potential states in $\mathcal{H}_A$, characterising the price we pay for our ignorance.

The entanglement entropy (EE) of the subregion A is given by the von Neumann entropy associated with the reduced density matrix ρ_A of A

$$S(A) = -\,\mathrm{Tr}_A(\rho_A \log \rho_A). \tag{1.1.3}$$

From this definition, it is evident that $S(A) = S(\overline{A})$. If A and $\overline{A}$ are unentangled, $S(A) = 0$; $S(A)$ reaches its maximum when A and $\overline{A}$ are maximally entangled.

To illustrate the definition of entanglement entropy, let us consider an elementary example with A and $\overline{A}$ each being a spin-$\frac{1}{2}$ particle. The Hilbert space of the full

system is then spanned by $|\uparrow\uparrow\rangle$, $|\uparrow\downarrow\rangle$, $|\downarrow\uparrow\rangle$, $|\downarrow\downarrow\rangle$. Suppose the system is in the following pure state $|\psi\rangle = \cos\theta\,|\uparrow\downarrow\rangle + \sin\theta\,|\downarrow\uparrow\rangle$. The reduced density matrix of A is $\rho_A = \cos^2\theta\,|\uparrow\rangle\langle\uparrow| + \sin^2\theta\,|\downarrow\rangle\langle\downarrow|$, and $S(A) = -2\cos^2\theta\log\cos\theta - 2\sin^2\theta\log\sin\theta$. One can easily verify that $S(A)$ takes its maximal value $S(A) = \log 2$ when $\cos^2\theta = \frac{1}{2}$, i.e. when A and $\overline{A}$ are maximally entangled. More generally, if we had q qubits in A and q qubits in $\overline{A}$ that are maximally entangled, $S_A = q\log 2$. Hence, we can intuitively understand S_A as counting the number of bits, and, since q qubits have 2^q states, e^{S_A} as counting the number of entangled states.

In the above elementary example, S_A is computed by the eigenvalues λ_i of ρ_A. More generally, in any finite systems, the Schmidt decomposition allows one to diagonalize the operator ρ_A and find its eigenvalues λ_i. The entanglement entropy is then simply $S_A = -\sum_i \lambda_i \log\lambda_i$.

Instead of finite systems, in physics, we are often interested in entanglement entropy in continuum QFTs. In these cases, we have wavefunctionals $\Psi[\Phi(x)]$ on Cauchy slices, where we define the subregion A, its complement $\overline{A}$, as well as the entangling surface ∂A.[4] Afterwards, one may use (1.1.3) to calculate $S(A)$: tracing out $\overline{A}$ amounts to integrating out all fields in $x \in \overline{A}$. Once we have the reduced density matrix ρ_A, we need to further obtain the operator $\log\rho_A$. This is very subtle, and it is more practical to obtain the entanglement entropy as the appropriate analytic continuation of the nth-Renyi entropy $S^{(n)}(A)$

$$S^{(n)}(A) = \frac{1}{1-n}\log \mathrm{Tr}_A\,\rho_A^n, \qquad S(A) = \lim_{n\to 1} S^{(n)}(A). \tag{1.1.4}$$

The quantity $\mathrm{Tr}_A\,\rho_A^n$ in the definition of Renyi entropy (1.1.4) admits a replica path

[4] Note that for gauge theories, in general $\mathcal{H}_{A\overline{A}} \neq \mathcal{H}_A \otimes \mathcal{H}_{\overline{A}}$. In what follows, we will ignore this subtlety as it won't affect the discussions too badly. See, for example (Lin, 2017; Lin & Radičević, 2020) for discussions regarding this issue in holographic theories that this thesis primarily concerns.

integral derivation; in cases with non-trivial time-dependences, the Schwinger-Keldysh formalism is needed, where the forward-backward evolution allows one to cancel out unknown information of the final state in the time evolution. See e.g. (Rangamani & Takayanagi, 2017) for formalism and (Calabrese & Cardy, 2004) for explicit calculations in two-dimensional conformal field theories.

1.1.1 UV and IR properties

When working in the continuum, we expect UV singularities. In the UV, any finite energy state is the same as the vacuum state. Therefore, to study the UV divergences, we can restrict to $\rho = |0\rangle \langle 0|$. Physically, the UV divergence arises from the short-distance correlations in the UV. The definition of ρ_A entails bi-partitioning the system across the entangling surface ∂A. One then expects the correlations of modes across ∂A to have a leading contribution to EE, and needs to account for these modes within a cutoff ϵ distance away from ∂A. Intuitively, the divergences are proportional to the number of EPR pairs that are shared between the two sides of the entangling surface ∂A. Hence, it should scales as the *area* of this entangling surface. Indeed, in d-dimensional free field theory, it has been proved that the leading UV divergent of EE obeys the area law (Bombelli, Koul, Lee, & Sorkin, 1986; Srednicki, 1993).

$$S_A = \alpha \frac{\text{Area}(\partial A)}{\epsilon^{d-2}} + ..., \tag{1.1.5}$$

where d denotes the spacetime dimensions, and the power $d-2$ of ϵ ensures that S_A is dimensionless, α depends on the field theory in question, and the ellipses include less divergent terms. In general, for a d-dimensional relativistic QFT, the

UV divergence takes the form

$$S_A = \begin{cases} a_{d-2}\left(\frac{L}{\epsilon}\right)^{d-2} + a_{d-4}\left(\frac{L}{\epsilon}\right)^{d-4} + ... + a_1\frac{L}{\epsilon} + (-1)^{\frac{d-1}{2}}\mathcal{S}_A + ... & d \text{ odd}, \\ a_{d-2}\left(\frac{L}{\epsilon}\right)^{d-2} + a_{d-4}\left(\frac{L}{\epsilon}\right)^{d-4} + ... + (-1)^{\frac{d-2}{2}}\mathcal{S}_A \log\frac{L}{\epsilon} + ... & d \text{ even}, \end{cases} \tag{1.1.6}$$

where L characterises the size of the system. Notice that only even powers appear. This is because the UV divergence is related to the extrinsic curvature $K \sim \nabla n$ of the entangling surface ∂A, where n is the unit normal vector. K flips sign if we consider A vs $\overline{A}$. $S_{\text{div}}(A) = S_{\text{div}}(\overline{A})$ then implies that only even powers of K are allowed. The constants a_n are in general theory-dependent. However, $\mathcal{S}_A$ is universal. We note that in $d = 2$ there is only a logarithmic divergence. In this case, the entangling surface ∂A are sets of disconnected points.

The above area law holds generally for QFTs in the ground state. For highly excited or thermal states, however, EE scales differently. To illustrate this behaviour, let us consider a 1-dimensional chain of N spin-$\frac{1}{2}$ particles. We take A to be a spatial region containing k spins ($1 \ll k \ll N$), and $\overline{A}$ to be everything else. The most general state of the system is given by

$$|\Psi\rangle = \sum_{s_i} c_{s_1...s_N} |s_1\rangle ... |s_N\rangle , \qquad s_i \in \{0, 1\}. \tag{1.1.7}$$

A highly excited or thermal state is expected to be random, i.e. for such states $c_{s_1...s_N}$ is drawn from a random distribution. Since $k \ll N$, Page's theorem (Page, 1993) indicates that $\lambda_i \sim \frac{1}{2^k}$. As such, $S(A) \sim -\sum \frac{1}{2^k}\log\frac{1}{2^k} = k\log 2$, where the sum runs over all 2^k eigenvalues. We see that $S(A)$ goes as the number of spins k in A. In other words, for this 1-dimensional system, $S(A) \sim \text{vol}(A)$. Intuitively, this volume scaling can be understood as the cumulative effects of long-range

correlations between generic points contained in A and those outside. Hence, we expect the volume law

$$S_{\mathrm{reg},A} = s_{\mathrm{th}} \,\mathrm{vol}(A) \sim L^{d-1} \tag{1.1.8}$$

to be generic for highly excited or thermal states. The subscript "reg" is due to the following reason: Unlike the above example (1.1.7), which is on a discrete spin chain, for EE in a highly excited or thermal state in a continuous system, there are UV divergent terms (1.1.6) including the leading area law divergence (1.1.5). To distil the IR behaviour of EE, in (1.1.8) we regulate S_A by subtracting these UV divergent terms.[5]

Apart from in specific cases such as two-dimensional conformal field theories (Calabrese & Cardy, 2004, 2005) and free field theory (Calabrese & Cardy, 2004), entanglement entropy is generally difficult to compute using the replica trick mentioned in the previous subsection. In particular, calculating EE in interacting QFTs is a formidable task. Fortunately, the Ryu-Takayanagi(RT) (Ryu & Takayanagi, 2006b, 2006a)/Hubeny-Rangamani-Takayanagi(HRT) (Hubeny et al., 2007) formula allows one to calculate EE in certain strongly-interacting quantum field theories with large degrees of freedom using holography.

1.2 Holographic entanglement entropy

Intuitively, the AdS/CFT correspondence states that certain conformal field theory in d spacetime dimensions (the "boundary") with a large degree of freedom is equivalent to a quantum gravity theory in asymptotically $\mathrm{AdS}_{d+1} \times M$ spacetime

[5] Notice that there is a potential subtlety regarding this regularisation scheme: the UV divergence could be state-dependent (Marolf & Wall, 2016).

(the "bulk"), where the asymptotically AdS$_{d+1}$ metric can be written as

$$ds^2 = g_{rr}dr^2 + g_{\mu\nu}dx^\mu dx^\nu, \tag{1.2.1}$$

with r being the bulk radial coordinate, and the AdS boundary at $r = \infty$. M is some compact manifold. A more precise statement is as follows.

A d-dimensional conformal field theory has a semiclassical dual if there exists a finite set of CFT primary operators O_i, and a bulk effective action $S_{\text{eff}}[\phi_i]$, and ϕ_i are a finite set of bulk fields such that

$$\int \mathcal{D}\phi_i e^{iS_{\text{eff}}[\phi_i]} O_{i_1}(t_1, \vec{x}_1)...O_{i_n}(t_n, \vec{x}_n) \approx \langle O_{i_1}(t_1, \vec{x}_1)...O_{i_n}(t_n, \vec{x}_n)\rangle_{\text{CFT}}, \tag{1.2.2}$$

where

$$\lim_{r\to\infty} r^{\Delta_i}\phi_i(t, r, \vec{x}) = O_i(t, \vec{x}) \tag{1.2.3}$$

and Δ_i are the scaling dimensions of O_i. Equation (1.2.2) establishes a quantitative relation between the bulk fields ϕ_i and boundary operators O_i, and is known as the extrapolate dictionary (Maldacena, 1998; Gubser et al., 1998; Witten, 1998). For example, the boundary stress tensor $T_{\mu\nu}$ is dual to bulk metric $g_{\mu\nu}$; the Noether current J_μ of a continuous global symmetry is dual to a gauge field A_μ in the bulk.

In a conformal field theory with semiclassical gravity dual, the entanglement entropy is holographically computed by the Ryu-Takayanagi(RT) (Ryu & Takayanagi, 2006b, 2006a)/Hubeny-Rangamani-Takayanagi(HRT) (Hubeny et al., 2007) formula. The original RT formula concerns only time-independent cases, which is then generalised by HRT to include non-trivial time dependences. The HRT formula (Hubeny et al., 2007) states that if we consider states in a CFT$_d$ with a holographic dual, the von Neumann entropy of a spatial subregion A lying on some

Cauchy slice is computed by the area of a co-dimension 2 *extremal* surface $\mathcal{E}_A$ in the asymptotically AdS$_{d+1}$ bulk that is *homologous to* A, i.e. anchored on ∂A and smoothly retractable to A on the AdS$_{d+1}$ boundary. Among the family of extremal surfaces that satisfy the homological constraints, we should pick the one with the smallest area,

$$S(A) = \frac{\text{Area}(\mathcal{E}_A)}{4G_N}. \tag{1.2.4}$$

Notice that the condition of the co-dimension 2 surface being extremal is equivalent to the vanishing of the null extrinsic curvatures in the two normal directions to the surface (Hubeny et al., 2007).

If the field theory state in question is static, one can uniquely extend the boundary Cauchy slice to the corresponding constant time slice in the asymptotically AdS$_{d+1}$ bulk.[6] Consequently, the co-dimension 2 extremal surface $\mathcal{E}_A$ degenerates to a *minimal* surface that lies on it. This is because we can decompose the null extrinsic curvature into timelike $K^{(t)}$ and spacelike $K^{(s)}$ components. Under the presence of a time reflection symmetry, $K^{(t)} = 0$ automatically. Solving the latter $K^{(s)} = 0$ is then equivalent to finding minimal surfaces (Rangamani & Takayanagi, 2017). (1.2.4) in this static special case is the original RT formula (Ryu & Takayanagi, 2006b, 2006a)

With the RT/HRT formula, the calculation of $S(A)$ is then *geometrised* to the computation of the area of $\mathcal{E}_A$. The RT formula has been proved in (Lewkowycz & Maldacena, 2013). See (Dong, Lewkowycz, & Rangamani, 2016) for progress on deriving the HRT formula.

Now let us find the area of the HRT surface $\text{Area}(\mathcal{E}_A)$ in (1.2.4). We denote the metric of the asymptotically AdS$_{d+1}$ spacetime as $ds^2 = g_{\mu\nu}dx^\mu dx^\nu$ ($\mu, \nu =$

[6] This is in contrast to the time dependent cases studied above, where Cauchy slices in the bulk are not uniquely specified by Cauchy slices on the boundary.

$1, \ldots, d+1$). We parametrise the co-dimension 2 extremal surface $\mathcal{E}_A$ with coordinate $\vec{\xi}$. The induced metric γ_{ab} ($a, b = 1, \ldots, d-1$) of $\mathcal{E}_A$ is

$$\gamma_{ab} = g_{\mu\nu} \frac{\partial x^\mu}{\partial \xi^a} \frac{\partial x^\nu}{\partial \xi^b}. \tag{1.2.5}$$

The area of $\mathcal{E}_A$ is then simply the determinant of γ_{ab}

$$S = \frac{1}{4G_N} \int d^{d-1}\xi \sqrt{\det(\gamma_{ab})}. \tag{1.2.6}$$

To find the EE, we *extremise* S (1.2.6), i.e. find $\mathcal{E}_A$ such that $\delta S = 0$. In the static case, the extremal surfaces reduces to minimal surfaces and the practice *minimises* S.

1.2.1 CFT$_d$ in the vacuum on $\mathbb{R}^{d-1,1}$

Now, let us consider general d-dimensional CFT in the vacuum state on $\mathbb{R}^{d-1,1}$. Since the state is static, we are instructed to use the RT formula and find minimal surfaces in the dual bulk geometry on a constant time slice (which we can, without loss of generality, take to be $t = 0$). The dual geometry is Poincare AdS$_{d+1}$, whose metric is

$$ds^2 = \frac{1}{z^2}(-dt^2 + dz^2 + d\vec{x}_{d-1}^2), \tag{1.2.7}$$

and the AdS boundary is at $z = 0$. In $d > 2$, there are different possible shapes for the entangling subregions. Here we pick two most symmetric cases: strip and spherical regions. In the strip case, the RT surfaces have non-trivial shapes only along the x_1 direction, and it would be more convenient to adapt Cartesian coordinate for the boundary spatial directions: $d\vec{x}_{d-1}^2 = dx_1^2 + d\vec{x}_{d-2}^2$. We choose $\xi^i = x^i$ ($i = 1, ..., d-1$) to parametrise the co-dimension 2 minimal surface. This

surface can then be specified by the function $z(x_1)$. Using (1.2.5), the induced metric of the minimal surface is

$$ds^2 = \gamma_{ab} d\xi^a d\xi^b = \frac{1}{z^2}\Big(1 + \Big(\frac{\partial z(x_1)}{\partial x_1}\Big)^2\Big) dx_1^2 + \frac{1}{z^2} dx_2^2 + ... + \frac{1}{z^2} dx_{d-1}^2, \quad (1.2.8)$$

and the EE (1.2.6) is hence

$$S_{\text{strip}} = \frac{1}{4G_N} L^{d-2} \int dx_1 \frac{\sqrt{1 + z'(x_1)^2}}{z^{d-1}}, \quad (1.2.9)$$

where L is the IR regulator of the translationally-invariant directions. To calculate the EE, we need to *minimise* the area functional in (1.2.9), i.e. to find $z(x_1)$ such that $\delta S = 0$. This is a problem in the calculus of variation like those in classical mechanics. Generally speaking, the EE (1.2.6) we are minimising can be regarded as an "action", hence $\sqrt{\det(\gamma_{ab})}$ in (1.2.6) plays the role of the "Lagrangian". In the case of (1.2.9), this "Lagrangian" is

$$\mathcal{L}\big(z(x_1), z'(x_1), x_1\big) = \frac{\sqrt{1 + z'(x_1)^2}}{z^{d-1}}, \quad (1.2.10)$$

where the coordinate x_1 parametrising the minimal surface serves as "time", and the function $z(x_1)$ describing the minimal surface acts as the "generalised coordinate". In general, one can find $z(x_1)$ from the Euler-Lagrange equation with "Lagrangian" (1.2.10); in practice, however, it is easier to invoke *conservation laws*. Since the "Lagrangian" (1.2.10) does not contain "time" x_1, the "energy" $\mathcal{H}$ is conserved

$$\mathcal{H} = z'(x_1) \frac{\partial \mathcal{L}}{\partial z'(x_1)} - \mathcal{L} = -\frac{1}{z^{d-1}\sqrt{1 + z'^2}} = -\frac{1}{z_0^{d-1}}, \quad (1.2.11)$$

where we have evaluate the "energy" at the deepest point z_0 the RT surface can reach into the bulk, at which point $z'|_{z_0} = 0$. From (1.2.11), we can solve for $z'(x_1)$

$$z'(x_1) = \frac{\sqrt{z_0^{2(d-1)} - z^{2(d-1)}}}{z^{d-1}}. \tag{1.2.12}$$

To relate z_0 with the size $2a$ of the entangling subregion A, we can integrate (1.2.12) to find the x displacement of the RT surface

$$a = \int dx = \int_0^{z_0} \frac{dz}{z'(x)}, \qquad \Rightarrow \qquad z_0 = a\frac{\Gamma\left(\frac{1}{2(d-1)}\right)}{\sqrt{\pi}\Gamma\left(\frac{d}{2(d-1)}\right)}. \tag{1.2.13}$$

From the differential equation (1.2.12), we can solve $x_1(z)$ in terms of hypergeometric function

$$x_1(z) = \frac{z^d}{z_0^{d-1}d}{}_2F_1\Big(\frac{1}{2}, \frac{d}{2(d-1)}, 1 + \frac{d}{2(d-1)}, \Big(\frac{z}{z_0}\Big)^{2(d-1)}\Big) - \frac{\sqrt{\pi}}{d}\frac{\Gamma\left(\frac{3d-2}{2(d-1)}\right)}{\Gamma\left(\frac{2d-1}{2(d-1)}\right)}, \tag{1.2.14}$$

which then allows us to compute S in (1.2.9)

$$S = \frac{1}{4G_N}\frac{L^{d-2}}{d-2}\Big(\frac{2}{\epsilon^{d-2}} - \Big(\frac{2}{z_0}\Big)^{d-1}\frac{1}{a^{d-2}}\Big). \tag{1.2.15}$$

In evaluating (1.2.9), we have introduced a UV cutoff $z = \epsilon \ll 1$. This is due to the fact that the minimal surfaces extend to the AdS boundary, and have infinite area. Notice that the resulting divergent term scales as $\frac{\text{Area}(\partial A)}{\epsilon^{d-2}}$, as is expected for EE in the ground state in a QFT (1.1.5).

In the special case of $d = 2$, (1.2.15) becomes degenerate. Now, let us calculate the EE in this case separately. In $d = 2$, the co-dimension 2 minimal surface

is a 1-dimensional geodesic. The solution to (1.2.12) is a semi-circle $z(x) = \pm\sqrt{a^2 - (x + C_1)^2}$. We can adopt an alternative parametrisation α, and describe it with two functions

$$x(\alpha) = a\cos\alpha, \qquad\qquad z(\alpha) = a\sin\alpha. \tag{1.2.16}$$

With this parametrisation, the "action" (1.2.9) can be written as

$$S = \frac{1}{4G_N}\int d\alpha \frac{\sqrt{x'(\alpha)^2 + z'(\alpha)}}{z^2} = \frac{c}{6}\cdot 2\int_{\frac{\epsilon}{a}}^{\frac{\pi}{2}} \frac{d\theta}{\sin\theta} = \frac{c}{3}\log\frac{2a}{\epsilon}, \tag{1.2.17}$$

where in getting the second equality, we have also used the Brown-Henneaux central charge (Brown & Henneaux, 1986) $c = \frac{3\ell_{AdS}}{2G_N}$. The divergence behaves as $\log\frac{2a}{\epsilon}$, as is expected from (1.1.6). The holographic calculation (1.2.17) matches with CFT$_2$ results (Holzhey et al., 1994; Calabrese & Cardy, 2004).

We can likewise study the case with spherical entangling subregions. For this case, it would be more convenient to adapt spherical coordinates the boundary spatial coordinate: $d\vec{x}_{d-1}^2 = dr^2 + r^2 d\vec{\theta}_{d-2}^2$. We choose $\xi^i = (r, \theta_{d-2})$ to parametrise the minimal surface, and describe this surface with the function $z(r)$. Using (1.2.5), we have the induced metric

$$ds^2 = \frac{1}{z^2}\Big(1 + \Big(\frac{\partial z(r)}{\partial r}\Big)^2\Big)dr^2 + \frac{r^2}{z^2}d\theta_1^2 + ... + \frac{r^2}{z^2}d\theta_{d-1}^2, \tag{1.2.18}$$

which then leads to the EE

$$S_{\text{sphere}} = \frac{1}{4G_N}\omega_{d-2}\int dr \frac{r^{d-2}}{z^{d-1}}\sqrt{1 + z'(r)^2}, \tag{1.2.19}$$

where $\omega_{d-2} = \frac{2\pi^{\frac{d-1}{2}}}{\Gamma(\frac{d-1}{2})}$ is the area of unit S^{d-2}. Now, the "Lagrangian" $\mathcal{L}\big(z(r), z'(r), r\big) = \frac{r^{d-2}}{z^{d-1}}\sqrt{1 + z'(r)^2}$ does explicitly contain the "time" r, so

there's no "energy" conservation any more. One thus needs to solve the Euler-Lagrange equation directly (Hubeny, 2012)

$$\frac{d}{dr}\frac{\partial\mathcal{L}\big(z(r),z'(r),r\big)}{\partial z'(r)}-\frac{\partial\mathcal{L}\big(z(r),z'(r),r\big)}{\partial z(r)}=0, \tag{1.2.20}$$

$$\Rightarrow z''+(1+z'^2)\Big(\frac{d-2}{r}z'+\frac{d-1}{z}\Big)=0. \tag{1.2.21}$$

One can easily verify that the hemisphere

$$z^2+r^2=R^2 \tag{1.2.22}$$

obeys the differential equation (1.2.21).[7]

The EE is more technical to evaluate. It is shown (Ryu & Takayanagi, 2006a) that like in the strip case, the leading contribution is proportional to the area of the boundary of the entangling subregion A, $\frac{\text{Area}(\partial A)}{\epsilon^{d-2}}$.

1.2.2 Holographic UV properties

We have seen that for both strip and spherical subregions, the EE scales as $\frac{\text{Area}(\partial A)}{\epsilon^{d-2}}$ ($d>2$). This behaviour is in fact general for RT as well as HRT surfaces. This is because the bulk z coordinate corresponds to the energy scale of the dual field theory (Susskind & Witten, 1998), and the UV physics of the field theory is determined by the $z\to 0$ regions of the dual gravitational theories. The $(d+1)$-dimensional bulk metric takes universal form asymptotically. This reflects the fact that in the dual field theories, any finite energy states in the UV are the same as the vacuum. Choosing z as one of the coordinates $\vec{\xi}$ for the RT/HRT surface, the

[7] Obviously, (1.2.22) agrees with (1.2.16) when $d=2$. In this case there's no distinction between strip or spherical entangling subregions.

induced metric of the RT/HRT surface at small z can be written as

$$ds^2 = \frac{1}{z^2}(dz^2 + h_{ab}d\xi^a d\xi^b + ...). \tag{1.2.23}$$

The area of the RT/HRT surface is then given by

$$A = \int_\epsilon^z \frac{dz'}{z'^{d-1}} \int d^{d-2}\xi\sqrt{h} + ... = \frac{\text{Area}(\partial A)}{\epsilon^{d-2}} + ..., \tag{1.2.24}$$

in agreement with field theory considerations (1.1.5).

1.2.3 Multiple regions

We can use the RT surfaces as fundamental building block to evaluate the EE when A is a disjoint interval $A = \cup_i A_i$. While the calculation in field theory is difficult, the holographic computation turns to be simple: we just minimise all possible configurations of RT surfaces homologous to $A = \cup_i A_i$. Taking vacuum AdS_3 as an example, in which case RT surfaces are semi-circle geodesic, we have

$$S_A = \frac{c}{3}\min\Big(\sum_{i,j}\log\frac{|u_i - v_j|}{\epsilon}\Big). \tag{1.2.25}$$

Notice that depending on the subregion sizes, the minimal RT configurations are in general different, see Figure (1.1). This strategy of minimizing over all possible RT surface configurations obeying the homology condition keeps to hold in higher dimensions and for thermal states.

1.2.4 Thermal CFT$_d$ on $\mathbb{R}^{d-1,1}$

Having studied the case of vacuum CFT$_d$ on $\mathbb{R}^{d-1,1}$, we can proceed to studying thermal CFT$_d$ states, which are dual to asymptotically AdS$_{d+1}$ black holes. In

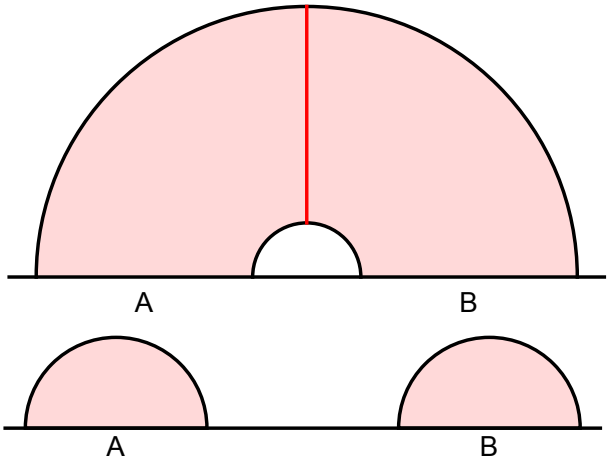

Figure 1.1: A demonstration of different RT surface configurations for $AB = A \cup B$. The bulk regions enclosed by the RT surfaces and the boundary, which are depicted as shaded, are the AB entanglement wedges. In the upper figure, the entanglement wedge cross-section computing the reflected entropy is shown in red.

the simplest neutral case, the dual geometry is planar AdS$_{d+1}$ black holes, whose metric is given by[8]

$$ds^2 = \frac{1}{z^2}\Big(- f(z)dt^2 + \frac{dz^2}{f(z)} + d\vec{x}_{d-1}^2\Big), \quad f(z) = 1 - z^d, \tag{1.2.26}$$

where $d \geq 2$. Following the same steps in section 1.2.1, we adopt Cartesian and spherical coordinates for $d\vec{x}_{d-1}^2$, parametrise the minimal surface with $\xi^i = x^i$ and $\xi^i = (r, \theta_{d-2})$, and describe them with $z(x_1)$ and $z(r)$, respectively. The EE are then given by

$$S_{\text{strip}} = \frac{1}{4G_N} L^{d-2} \int dx_1 \frac{1}{z^{d-1}} \sqrt{1 + \frac{z'(x_1)^2}{f(z)}}, \tag{1.2.27}$$

$$S_{\text{sphere}} = \frac{1}{4G_N} \omega_{d-2} \int dr \frac{r^{d-2}}{z^{d-1}} \sqrt{1 + \frac{z'(r)^2}{f(z)}}. \tag{1.2.28}$$

[8]Notice that unlike the vacuum case (1.2.7), the metric (1.2.26) is no longer in Fefferman-Graham gauge (de Haro, Solodukhin, & Skenderis, 2001), as $g_{zz} = \frac{1}{z^2 f(z)} \neq \frac{1}{z^2}$. See (Hubeny, 2012) for conversion of (1.2.26) to Fefferman-Graham gauge.

When the entangling subregion is large, due to the $\frac{1}{z^2}$ factor in (1.2.26), the RT surfaces consist of large plateau regions where they skim the horizon. In these plateau regions, $z \approx 1$ and $z' \approx 0$. Plugging these into (1.2.27), subtracting the universal UV divergent term $\propto \frac{\text{Area}(\partial A)}{\epsilon^{d-2}}$, we have

$$S_{\text{strip}} = \frac{1}{4G_N} L^{d-2} \cdot \Delta x_1 = \frac{1}{4G_N} \text{vol}(A), \tag{1.2.29}$$

and into (1.2.28) we have

$$S_{\text{sphere}} = \frac{1}{4G_N} \omega_{d-2} \frac{r^{d-1}}{d-1}\Big|_0^R = \frac{1}{4G_N} \frac{\pi^{\frac{d-1}{2}}}{\Gamma(\frac{d+1}{2})} R^{d-1} = \frac{1}{4G_N} \text{vol}(A). \tag{1.2.30}$$

In both cases, the EE is given by the *volume* of the entangling subregion A. This is expected for EE in the thermal state in a QFT (1.1.8).

1.2.5 Entanglement plateaux

So far we have been focusing on planar AdS spacetime. It would also be interesting to study global AdS$_{d+1}$ geometry, dual to CFT$_d$ on $\mathbb{R} \times \mathbb{S}^{d-1}$. When the state of the total system is a thermal density matrix, S_A and S_{A^c} are not equal, as the minimal surfaces M_A and M_{A^c} computing them encircle complementary parts of the black hole horizon (Ryu & Takayanagi, 2006b, 2006a) (see Figure 1.2). Let us study S_A in the $d = 2$ case that is relevant to the discussions in Chapter 2 first. In addition to the connected minimal surface M_A, there exists another disconnected minimal surface $M_{A^c} \cup \mathbb{S}_{\text{hor}}$, where $\mathbb{S}_{\text{hor}}$ is the bifurcation surface of the black hole. See Figure 1.2. When A gets large, $M_{A^c} \cup \mathbb{S}_{\text{hor}}$ has a smaller area than M_A and hence becomes the correct RT surface. In other words, we have

$$S_A = \frac{1}{4G_N} \min\{\mathcal{L}(M_A), \mathcal{L}(M_{A^c}) + \mathcal{L}(\mathbb{S}_{\text{hor}})\}\,, \tag{1.2.31}$$

where $\mathcal{L}(\mathbb{S}_{\text{hor}}) = 2\pi r_+$. This phenomenon is known as *entanglement plateaux* (Hubeny, Maxfield, Rangamani, & Tonni, 2013).

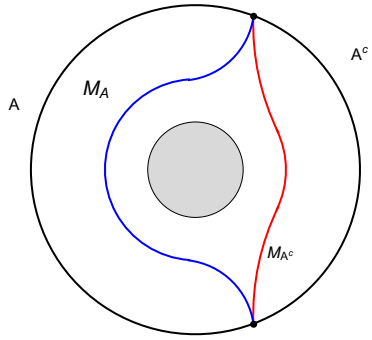

Figure 1.2: A demonstration of the minimal surface for a subregion A and its complementary A^c.

Entanglement plateaux are consistent with the Araki-Lieb inequality (Araki & Lieb, 1970), which upper bounds the difference between S_A and S_{A^c} in a bipartite system with the entropy of the total density matrix S_ρ

$$|\Delta S_A| = |S_A - S_{A^c}| \leq S_{A \cup A^c} = S_\rho. \tag{1.2.32}$$

If we naively take M_A as the RT surface throughout, for large A we would violate (1.2.32), as $|\Delta S_A|$ diverges in the limit of A becoming the entire system (Hubeny et al., 2013). Employing (1.2.31) to minimise between M_A and $M_{A^c} \cup \mathbb{S}_{\text{hor}}$, on the other hand, manifests (1.2.32) for A of all sizes: when $M_{A^c} \cup \mathbb{S}_{\text{hor}}$ becomes the RT surface, the inequality (1.2.32) simply saturates.

Entanglement plateaux also exist in $d > 2$: in these cases, for sufficiently large A there are no connected minimal surfaces M_A at all (Hubeny et al., 2013). This leaves no option but to consider the disconnected $M_{A^c} \cup \mathbb{S}_{\text{hor}}$ as the RT surface for S_A.

1.3 Time evolution of holographic entanglement entropy

So far, we have reviewed the basis of entanglement entropy as well as its holographic calculations at fixed time. Now, we are ready to discuss the major question we would like to address in this thesis, the out-of-equilibrium *dynamics* of EE in interacting many-body systems. This is challenging, as there are no conventional small parameters to expand in and numerical simulations are hampered by the exponentially large Hilbert space that the system explores. There are a handful of special setups, where analytical progress can be made: in random, dual unitary, and stabiliser quantum circuits (Fisher, Khemani, Nahum, & Vijay, 2023); in models of Sachdev-Ye-Kitaev type (Rosenhaus, 2019; Chowdhury, Georges, Parcollet, & Sachdev, 2022); in systems with a holographic gravity dual (Son & Starinets, 2002; Balasubramanian, Bernamonti, de Boer, et al., 2011a; Shenker & Stanford, 2014); and in conformal field theories (CFTs) driven by unconventional Hamiltonians. In this thesis, we will focus on the the latter two cases, both of which describe quantum dynamics in terms of geometry: in terms of gravity in asymptotically AdS spacetimes and in terms of conformal transformations of the complex plane. We will briefly review CFTs driven by unconventional Hamiltonians in section 1.3.1, and entanglement dynamics in holographic CFTs in section 1.3.2.

1.3.1 CFTs driven by unconventional Hamiltonians

In this section, we will review 1+1 dimensional CFTs with inhomogeneous deformations. It provides a framework for analytic studies of entanglement dynamics, which we will address in Chapter 2. 1+1 dimensional CFTs with inhomogeneous deformations have received considerable attention recently (Wen & Wu, 2018b,

2018a; Fan, Gu, Vishwanath, & Wen, 2020; Wen, Fan, Vishwanath, & Gu, 2021; Han & Wen, 2020; Fan, Gu, Vishwanath, & Wen, 2021; Wen, Fan, & Vishwanath, 2022), as they provide exactly solvable models that describe quantum critical systems out of equilibrium. These deformations include the so-called sine square deformation (SSD) (Wen & Wu, 2018b), which is a special case of $SL(2)$ deformations of 2d CFTs. In SSD, one changes the CFT Hamiltonian $H_0 = \int_0^l dx\, T_{00}(x)$ on a circle of circumference l to a new Hamiltonian with a sine-square enveloping function

$$H_1 = 2\int_0^l dx\ \sin^2\left(\frac{\pi x}{l}\right) T_{00}(x). \tag{1.3.1}$$

SSD was first introduced in quantum many-body systems to eliminate boundary effects (Gendiar, Krcmar, & Nishino, 2009; Hikihara & Nishino, 2011; Gendiar, Daniška, Lee, & Nishino, 2011). Later on, 2d CFT with SSD Hamiltonian and its generalisation, the Mobius deformed Hamiltonian were studied in (Katsura, 2012; Ishibashi & Tada, 2015, 2016; Okunishi, 2016; Wen, Ryu, & Ludwig, 2016; Tamura & Katsura, 2017), where it was shown (Ishibashi & Tada, 2015, 2016) that the spectrum of SSD CFT is continuous. In (Wen & Wu, 2018b) explicit expressions for entanglement entropy (EE) after a quantum quench were found. It was also pointed out in (Wen & Wu, 2018b) that SSD CFT can be interpreted as a CFT on curved spacetime.

SSD CFT also serves as the building block for Floquet CFT (Wen & Wu, 2018a; Fan et al., 2020; Wen et al., 2021; Han & Wen, 2020; Fan et al., 2021; Wen et al., 2022). Floquet CFT is constructed by *periodically* driving the CFT with ordinary and SSD Hamiltonians, H_0 and H_1. The physical motivation is to provide an exactly solvable toy model that captures some of the features of the more realisable periodically driven systems including Floquet topological insulators,

Floquet symmetry-protected phases, as well as Floquet time crystals. Floquet CFT describes driven quantum many-body systems at criticality. Floquet CFT was found to have heating and non-heating phases (Wen & Wu, 2018a; Fan et al., 2020), corresponding to different types of $SL(2)$ transformations. In the heating phase, the energy is localised in peaks that also dominate entanglement entropy. If initially prepared in a thermal state, the system outside these peaks cools down and behaves like the vacuum state, leading to the name "Floquet's refrigerators" (Wen et al., 2022). In the non-heating phases, the energy and entanglement show oscillatory behaviour without a fixed period.

In Chapter 2, we study entanglement dynamics in the aforementioned SSD CFT from both field-theoretic and holographic points of view.[9] There are already holographic studies of SSD and Floquet CFTs in the literature. In (MacCormack, Liu, Nozaki, & Ryu, 2019), a $(2+1)$-dimensional bulk metric with SSD boundary is constructed. Holographic dynamics of SSD quench with thermal initial states was investigated in (Goto, Nozaki, Tamaoka, Tan, & Ryu, 2021), and the time evolution of mutual information under this framework was further explored in (Goto, Nozaki, Ryu, Tamaoka, & Tan, 2023). There are also recent works (Bernamonti, Galli, & Ge, 2024; Kudler-Flam, Nozaki, Numasawa, Ryu, & Tan, 2023) exploring holographic aspects of SSD or Mobius quench in boundary conformal field theory, whose gravity dual involves end-of-the-world branes.

1.3.2 Time evolution of entanglement entropy from black hole interior

We would like to understand entanglement dynamics in generic holographic theories, where the time-dependent entanglement entropy is computed by the HRT

[9] The original paper (Jiang & Mezei, 2025) that Chapter 2 is based on also contains holographic as well as field-theoretic studies of Floquet CFTs.

surfaces that enters the black hole interior. We again consider thermal CFT_d states on $\mathbb{R}^{d-1,1}$, dual to asymptotically AdS_{d+1} black hole. It would be convenient to write the metric as[10]

$$ds^2 = -g(\rho)^2 dt^2 + d\rho^2 + h(\rho)^2 dx_{d-1}^2, \tag{1.3.2}$$

where there's a horizon at $\rho = 0$, near which $g(\rho) = \rho + O(\rho^3)$ and $h(\rho) = C + O(\rho^2)$. In the interior $\rho = i\kappa$, and $t_I = t - i\pi/2$ (the Schwarzschild time t becomes complex in the black hole interior (Fidkowski, Hubeny, Kleban, & Shenker, 2004)).

We consider the entanglement entropy of subregion A consisting of half of the space of each of the two copies of the thermofield double. We evolve time forward on both copies of the field theory. Due to the symmetry of the problem, the HRT surface lies on the $x_1 = 0$ plane, and extends along the $x_2, ..., x_{d-1}$ directions. Noticing that the co-dimension 2 extremal surface no longer lies on a constant time slice, we choose to parametrise it with $\xi^i = (t, \vec{x}_{d-2})$. The HRT surface is then described by the function $\rho(t)$ (or $t(\rho)$). Using (1.2.5) and (1.2.6), we find

$$S = \frac{1}{4G_N} L^{d-2} \int dt\, h\big(\rho(t)\big)^{d-2} \sqrt{-g\big(\rho(t)\big)^2 + \dot{\rho}(t)^2}. \tag{1.3.3}$$

To calculate the EE, we need to *extremise* the area functional in (1.3.3). Like in the static RT case, it would be easier to apply conservation laws: we notice that the "Lagrangian" $\mathcal{L}\big(\rho(t), \dot{\rho}(t), t\big) = h\big(\rho(t)\big)^{d-2} \sqrt{-g\big(\rho(t)\big)^2 + \dot{\rho}(t)^2}$ is t-independent.

[10] In the special case of AdS_{d+1}-Schwarzschild (1.2.26), we have (Hartman & Maldacena, 2013)

$$d\rho = \frac{dz}{z\sqrt{1 - z^d}}$$

Hence, the "energy" is conserved

$$\mathcal{H} = \dot{\rho}(t)\frac{\partial \mathcal{L}}{\partial \dot{\rho}(t)} - \mathcal{L} = \frac{g^2 h^{d-2}}{\sqrt{-g^2+\dot{\rho}^2}} = -ig_0 h_0^{d-2}, \tag{1.3.4}$$

where we again evaluate the "energy" at the deepest point $\rho_0 = i\kappa_0$ the HRT surface can reach in the interior, at which point $\dot{\rho}|_{\rho_0} = 0$. From (1.3.4), we can solve for $\dot{\rho}$. This then allows us to find the integral expression describing the HRT surface[11]

$$t(\rho) = \int \frac{d\rho}{\dot{\rho}} = -i\frac{\pi}{2} - \int_{i\kappa_0}^{\rho} \frac{d\rho'}{\sqrt{1-\frac{g^2 h^{2d-4}}{g_0^2 h_0^{2d-4}}}}. \tag{1.3.5}$$

Using $\dot{\rho}$, we can also express the area (1.3.3) integral

$$S = L^{d-2}\int \frac{d\rho}{\dot{\rho}}\, h(\rho)^{d-2}\sqrt{-g(\rho)^2+\dot{\rho}^2}, \tag{1.3.6}$$

$$= 2L^{d-2}\int_{i\kappa_0}^{\infty} d\rho \frac{h^{d-2}}{\sqrt{1-\frac{g_0^2 h_0^{2d-4}}{g^2 h^{2d-4}}}}. \tag{1.3.7}$$

Now let us study the $t(\rho)$ integral (1.3.5), and denote $a(\rho) = -ig(\rho)h(\rho)^{d-2}$ for convenience. We expand the integrand $\frac{1}{g\sqrt{1-\frac{a^2}{a_0^2}}}$ around $\rho = \rho_0$. If a is not extremized at $\rho_0 = i\kappa_0$, i.e. $a'(\rho_0) \neq 0$, we find that the $t(\rho)$ integral (1.3.5) goes as $\sqrt{\rho-\rho_0}$ as $\rho \to \rho_0$ and is hence finite; nevertheless, if $a'(\rho_0) = 0$, the integral instead goes as $\log(\rho-\rho_0)$ as $\rho \to \rho_0$ and diverges. We denote this point where $a(\rho)$ reach its extremum (typically a maximum, as can be explicitly checked in AdS$_{d+1}$-Schwarzschild) as ρ_*. These mean that the boundary time $t_b = t(\rho = \infty)$ remains finite for $\rho_0 < \rho_*$, but becomes large, i.e. $t_b \to \infty$ as $\rho_0 \to \rho_*$. In other words, at late time, the HRT surface gets stuck at the constant ρ slice $\rho = \rho_*$ instead of going deeper into the black hole interior. In addition to this portion at

[11] Notice that the integral has a pole at $\rho = 0$, and the integral should be taken along a ϵ-ball around $\rho = 0$.

$\rho \to \rho_*$, the late-time HRT surface also has a part that exits the horizon and goes to the boundary. For large t_b, this part gives a constant contribution of EE (after regularisations). On the other hand, from (1.3.3), it is evident that the area of the interior part of the HRT surface at $\rho \to \rho_*$ grows linear in t_b: as the HRT surface lies close to ρ_*, we have $\dot{\rho} = 0$, and hence

$$S = \frac{1}{4G_N} L^{d-2} \int dt\ h(\rho_*)^{d-2} \sqrt{-g(\rho_*)^2} = L^{d-2} h(\rho_*)^{d-2} \sqrt{-g(\rho_*)^2} \cdot t_b. \tag{1.3.8}$$

This means that the entanglement entropy also grows *linearly* with time t_b, with the proportional constant v_E specified by the interior geometry of the black hole at $\rho_* = i\kappa_*$.

$$S = \frac{1}{4G_N} L^{d-2} s v_E t_b, \qquad v_E = \frac{\sqrt{-g(\rho_*)^2} h(\rho_*)^{d-2}}{h(0)^{d-1}}. \tag{1.3.9}$$

where $s = \frac{h(0)^{d-1}}{4G_N}$ is the coarse-grained entropy density. The speed v_E at which EE grows linearly is called the *entanglement velocity*. For the planar AdS_{d+1}-Schwarzschild black hole, we have

$$\tan \frac{\kappa_* d}{2} = \sqrt{\frac{d}{d-2}}, \qquad v_E = \frac{\left(\frac{d-2}{d}\right)^{\frac{d-2}{2d}}}{\left(\frac{2(d-1)}{d}\right)^{\frac{d-1}{d}}}. \tag{1.3.10}$$

1.3.3 Entanglement membrane from holography

From the derivation of (1.3.8), (1.2.29) and (1.2.30), it is evident that while the full expressions of EE appear to be somewhat complicated and often have no analytic solutions, major simplifications occur in the limit of late time and large entangling subregions. Under such limits, only certain portions of the full RT/HRT

expressions play roles to leading order. This simplification suggests the existence of an *effective theory* that governs the leading dynamical behaviour of EE in the late time and large region limit. Indeed, in chaotic many-body quantum systems, there is mounting evidence that the dynamics of entanglement and Rényi entropies in the limit of large region sizes and long times can be captured by an effective description in terms of a minimal membrane (Nahum, Ruhman, Vijay, & Haah, 2017; Jonay et al., 2018; Mezei, 2018). This effective description states that the entanglement entropy is computed by the action

$$S = \min_{x(\xi)} \int d^{d-1}\xi \, \sqrt{|\gamma(\xi)|} \, \frac{s_{\text{th}} \, \mathcal{E}(v(\xi))}{\sqrt{1 - v^2(\xi)}} \, . \tag{1.3.11}$$

In the above formula, ξ are the membrane worldvolume coordinates,[12] $x(\xi)$ is its embedding into spacetime, γ is the induced metric on the membrane, s_{th} is the coarse grained entropy density, $v(\xi)$ is local transverse velocity of the membrane, and $\mathcal{E}(v)$ is the membrane tension function that depends the microscopic details of the many-body system. The minimisation is performed over all membrane shapes satisfying boundary conditions determined by the situation of interest. If we wish to study a quench, the membrane connects the time slice of the boundary of the subregion $A(t)$ and the time slice of the initial state; similarly, if we are interested in operator entanglement, the membrane connects the A_{bra} and A_{ket} subregions of the operator, see Fig. 1.3.

The membrane effective description can be derived for random quantum circuits (Nahum et al., 2017; Jonay et al., 2018; Zhou & Nahum, 2019), Floquet circuits (up to a plausible assumption about the convergence of an RG scheme) (Zhou & Nahum, 2020), generalised dual-unitary circuits (Rampp, Rather, & Claeys, 2024), Brownian Hamiltonians (Vardhan & Moudgalya, 2024), holo-

[12] In $d = 1 + 1$, the membrane is a curve in spacetime.

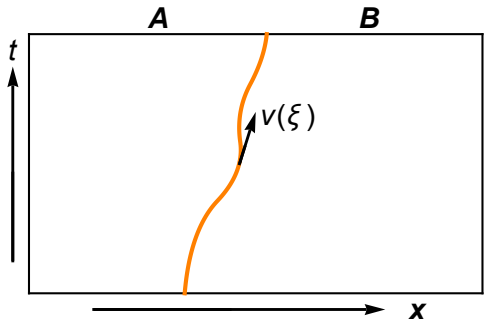

Figure 1.3: Cartoon of a minimal membrane (orange) extending in spacetime in $(1+1)$-dimensions. The top and bottom horizontal lines denote the constant time slices at t and 0, respectively. We are computing the time-dependent EE for a single region A (its complement is denoted as B). The minimal membrane is obtained by minimising the action (1.3.11) over all possible membranes obeying the boundary condition: that it anchors on ∂A at time t. The figure can either represent entropy dynamics in a quench, where $A(t)$ is on the top time slice and the bottom time slice represents the initial state, or the operator entanglement of the time evolution operator $e^{-(\beta/2+it)H}$, where the top region is A_{ket} and the bottom one is A_{bra}.

graphic CFTs (Mezei, 2018; Mezei & Virrueta, 2020), and Brownian SYK chain (Mezei & Rajgadia, 2025). There is also convincing numerical evidence for this description in chaotic spin chains (Jonay et al., 2018). In this thesis, we will focus on the holographic case.

1.3.3.1 The entanglement membrane for a half space subregion

The holographic derivation of the entanglement membrane (Mezei, 2018) starts with the study of HRT (Hubeny et al., 2007) and RT (Ryu & Takayanagi, 2006b, 2006a) surfaces in black brane spacetimes. In the quench setup, at early times we have some non-equilibrium features in the spacetime that get encoded in boundary conditions for the membrane. At later times local thermal equilibrium is reached, which is dual to the black brane. In the operator entanglement setup, we consider an eternal black brane and put the A_{bra} and A_{ket} subregions on the left and right asymptotic boundaries (Hartman & Maldacena, 2013).

Hence, we consider an asymptotically AdS$_{d+1}$ black brane in infalling coordinates:

$$ds^2 = \frac{1}{z^2}\left(-a(z)du^2 - \frac{2}{b(z)}dudz + dx^2 + d\vec{y}_{d-2}^2\right), \tag{1.3.12}$$

where the conformal boundary is at $z = 0$, and the horizon is at $z = 1$; therefore $a(1) = 0$. The AdS$_{d+1}$ asymptotics requires $a(0) = b(0) = 1$. For a neutral black brane $a(z) = 1 - z^d$, $b(z) = 1$.

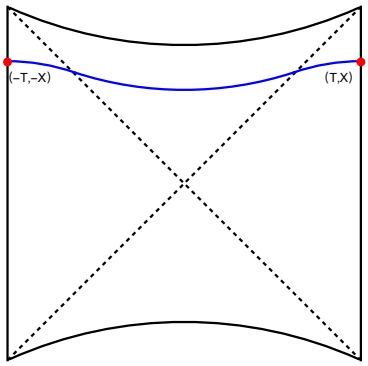

Figure 1.4: Penrose diagram of the HRT surface computing the time-dependent entanglement entropy in planar AdS$_{d+1}$-Schwarzschild ($d > 2$) with entangling subregion taken to be half the space on both side of the thermofield double. The $\pm X$ displacement in the x direction is perpendicular to the plane of the paper.

We would like to determine the two-sided entanglement entropy for half spaces extending in the $\vec{y}$ directions at late-time, see Fig. 1.4. We parametrise the HRT surface as $x(u)$, $z(u)$, and obtain the area functional for the metric (1.3.12):

$$S = s_{\text{th}}\,\text{vol}(\partial A)\int du\frac{\sqrt{Q}}{z^{d-1}}, \qquad Q \equiv \dot{x}^2 - a(z) - \frac{2}{b(z)}\dot{z}, \tag{1.3.13}$$

where $\dot{f} \equiv \frac{df}{du}$.

As is reviewed in section (1.3.2), for $d > 2$ black branes the leading behaviour of entanglement entropy in the late time and large entangling subregion limit is determined by the portion of the HRT surfaces that lie inside the horizon; at late

time, the HRT surfaces get stuck at some special extremal slice $z = z_* > 1$ in the interior instead of moving deeper towards the singularity.[13] Therefore, to extract the leading behaviour of entanglement entropy in the late time and large entangling subregion limit, we can impose the following self-consistent scaling Ansatz (Mezei, 2017, 2018):

$$u \to \Lambda u, \qquad x \to \Lambda x, \qquad z \to z\,, \tag{1.3.14}$$

for $\Lambda \gg 1$. In this scaling the $\dot{z}$ term can be dropped from Q in (1.3.13). Then the z equation of motion becomes algebraic in z

$$v^2 \equiv \dot{x}^2 = a(z) - \frac{z a'(z)}{2(d-1)} \equiv c(z)\,; \tag{1.3.15}$$

e.g. for neutral black branes $c(z) = 1 - \frac{d-2}{2(d-1)}\, z^d$. The function $c(z)$ is monotonically decreasing and positive in the range $1 \leq z \leq z_*$, where z_* is the first zero of $c(z)$. Then z in this range can be solved for in terms of v^2 and we have managed to reduce the problem in dimension (from $d+1$ to d). The resulting reduced action is the membrane theory introduced around (1.3.11):

$$S = s_{\text{th}}\, \text{vol}(\partial A) \int du\, \mathcal{E}(v^2)\,, \qquad \mathcal{E}(v^2) = \sqrt{\frac{-a'(z)}{2(d-1)z^{2d-3}}}\bigg|_{z=c^{-1}(v^2)}\,. \tag{1.3.16}$$

The bulk infalling time u assumes the role of boundary theory time. (Recall that at the AdS boundary infalling and boundary times agree.) As the reduction in dimension amounts to integrating out the bulk radial z degree of freedom using (1.3.16), we can understand the geometric meaning of the membrane as the *projection* of the codimension-2 bulk HRT surface in the scaling limit (1.3.14) to

[13] As we will see in section 3.4, these conclusions also hold for $d = 2$ hairy BTZ black branes (strings).

the AdS boundary along constant infalling time.

We have seen that the RT/HRT surfaces possess universal UV divergences as $z \to 0$ (1.2.24),

$$d > 2 : \ \frac{\text{Area}(\partial A)}{\epsilon^{d-2}} \qquad \text{or} \qquad d = 2 : \ \log \frac{2}{\epsilon} \tag{1.3.17}$$

for some UV cutoff $\epsilon \ll 1$. When projecting the HRT surfaces to the boundary along constant infalling time to obtain the membranes, we subtract these UV divergences of the (H)RT surfaces. In the scaling limit, due to the $1/z^2$ factor in (1.3.12), the remaining parts of the (H)RT surfaces that compute finite entropy are inside or close to the horizon.[14]

The function $\mathcal{E}(v^2)$ obeys a series of properties. To state them, we further introduce the butterfly velocity v_B (Roberts, Stanford, & Susskind, 2015), related to the out-of-time order correlator (OTOC)

$$v_B = \sqrt{-\frac{a'(1)}{2(d-1)}} \, . \tag{1.3.18}$$

$c(z)$ maps v_B to the horizon at $z = 1$. In previous work (Mezei, 2018) the near-horizon region around $z = 1$ was not treated with enough care. In the later part of this thesis, we fix the resulting imprecisions that involve membrane with regions, where $v = v_B$.

In general, $v_E \leq v_B$ due to the constraint from null energy condition (Mezei,

[14] In the original membrane theory from holographic CFTs (Mezei, 2018), the prescription was to cut the HRT surfaces at the horizon and keep only the interior parts, as it is only these parts that grow linearly with time (Hartman & Maldacena, 2013). In a later work (Jiang, Mezei, & Virrueta, 2025), it was discovered that for saturated RT surfaces, as well as certain half-space HRT surfaces with displacement in the x direction, portions of the (H)RT surfaces that are outside but near the horizon can also contribute finite entropy in the scaling limit. As such, here we adopt the latter more general prescription to cut out the UV divergences of the (H)RT surfaces.

2017).[15] We are now ready to state the constraints obeyed by the membrane tension function: it is an even function, monotonically increasing and convex for $0 \leq v < 1$. It diverges as $v \to 1$ and certain important values are (Mezei, 2018):[16]

$$\mathcal{E}(0) = v_E\,, \quad \mathcal{E}'(0) = 0\,, \quad \mathcal{E}(v_B) = v_B\,, \quad \mathcal{E}'(v_B) = 1\,, \quad \mathcal{E}'(v) > 0\,, \quad \mathcal{E}''(v) > 0\,. \tag{1.3.19}$$

In the above discussion, we have focused on strip entangling subregions. Nevertheless, entanglement membranes can be derived from holography with sphere and generic regions, see (Mezei, 2018; Mezei & van der Schee, 2020).

While entanglement membrane is elegant and profound, the theory is still at the developing stage. An issue of the theory is that when the geometry (1.3.12) is the BTZ black brane, $a(z) = 1 - z^2$, $b(z) = 1$, we get $v_E = v_B = \mathcal{E}(v) = 1$. This signals the breakdown of entanglement membrane for two-dimensional CFTs, even though they were some of the first studied examples of entanglement dynamics (Calabrese & Cardy, 2005, 2007) that are generically chaotic for central charge above some threshold value.[17] One could dismiss this issue by attributing it to some peculiarity of the dual 3d gravity. Indeed, the entanglement entropy dynamics in quenches and in the operator entanglement setup obtained using 2d CFT technology is reproduced by the membrane effective description, provided we choose the degenerate membrane tension function $\mathcal{E}(v) = 1$. However, there are two indications that there is a fundamental issue at play: first, the Rényi

[15] This inequality also follows from general quantum many-body considerations that are independent from holography (Mezei & Stanford, 2017).

[16] The behaviour around v_B follows from consistency conditions related to operator spreading (Jonay et al., 2018).

[17] If they only have Virasoro symmetry, the criterion is $c > 1$. If they have extended chiral symmetry characterised by an effective central charge c_{currents} for the chiral sector of the theory, then the criterion is $c > c_{\text{currents}}$ (Asplund, Bernamonti, Galli, & Hartman, 2015a). Below these threshold values the CFTs are integrable and their entanglement dynamics are described by the quasiparticle effective description (Calabrese & Cardy, 2005, 2007).

entropy dynamics in 2d CFT for two intervals or more (Asplund et al., 2015a) is incompatible with the membrane theory (Mezei, 2018). Second, in quantum circuits the entropy dynamics is translated to the dynamics of a domain wall in a lattice spin model. The diffusion constant of the domain wall is proportional to $1/\mathcal{E}''(v)$ (Zhou & Nahum, 2020), which diverges for the degenerate membrane tension; indeed, just like 2d CFTs, dual unitary circuits formally give rise to the degenerate membrane tension $\mathcal{E}(v) = 1$ (Zhou & Nahum, 2020), and in the equivalent lattice model the domain wall delocalises. In Chapter 3, we will address this issue and propose the effective theory underlying entanglement in 2d CFT to be the *generalised membrane theory* that is equipped with an additional degree of freedom on the membrane.

1.4 Reflected entropy

The von Neumann entropy (1.1.3) that we have been focusing on concerns only systems in bipartite pure states, where we divide the system into two subregions A and $\overline{A}$ and study the entanglement between them. However, in physical systems, it is often of interest to study bipartite mixed states or multipartite states. For these cases, the von Neumann entropy appears to be somewhat insufficient to account for the richer entanglement structures. As such, it would be important to study further information-theoretic quantities that capture aspects of mixed or multipartite state correlations. One such quantity is the mutual information

$$I(A:B) = S(A) + S(B) - S(AB), \tag{1.4.1}$$

as for a pure state $|\psi\rangle_{AB}$ we have $S(AB) = 0$ and $S(A) = S(B)$, so $I(A:B) = 2S(A)$. However, the mutual information is just a linear combination of entanglement entropy, and hence cannot be regarded as a new quantity characterising

mixed or multipartite state correlations. In what follows, we will investigate another information-theoretic quantity for mixed or multipartite states known as *reflected entropy* (Dutta & Faulkner, 2019). It has the advantage of having a simple holographic dual that can be regarded as natural generalisations of the RT and HRT surface in static and time-dependent cases, respectively.

For a bipartite system with density matrix ρ_{AB}, the reflected entropy is given by

$$S_R(A:B) = S(\rho_{AA^*}), \quad \rho_{AA^*} = \mathrm{Tr}_{BB^*} \left|\rho_{AB}^{1/2}\right\rangle \left\langle\rho_{AB}^{1/2}\right| , \tag{1.4.2}$$

where $\left|\rho_{AB}^{1/2}\right\rangle \in \mathcal{H}_{ABA^*B^*}$ is the canonical purification of ρ_{AB}, and $S(\rho)$ is the von Neumann entropy (Dutta & Faulkner, 2019). The extended Hilbert space $\mathcal{H}_{ABA^*B^*}$ is constructed out of mirror copies of the original system (Engelhardt & Wall, 2019). In applications A and B are often disjoint regions and are parts of a larger system. Then ρ_{AB} is obtained by reducing the state of this larger system onto the region $A \cup B$.

Given the HRT surfaces $\mathcal{E}_{AB}$ homologous to the entangling region $A \cup B$, the entanglement wedge cross section (EWCS) Σ_{AB} is the minimal area surface among the (potentially multiple) extremal surfaces bisecting the entanglement wedge, defined as the causal development of $\mathcal{E}_{AB} \cup A \cup B$ (Takayanagi & Umemoto, 2018; Akers, Faulkner, Lin, & Rath, 2022).

It is believed that the holographic dual of the reflected entropy is the EWCS (Dutta & Faulkner, 2019):

$$S_R(A:B) = \min_{\Sigma_{AB}} \frac{1}{2G_N} \mathrm{Area}(\Sigma_{AB}) , \tag{1.4.3}$$

where the minimisation is done over all extremal surfaces. See Figure 1.1 for an illustration in vacuum AdS_3.

In the static cases, the HRT surfaces $\mathcal{E}_{AB}$ become RT surfaces lying on a bulk constant time slice, and the EWCS also degenerates to the minimal surface bisecting the entanglement wedge on that slice. The formula (1.4.3) has been proved in this case in (Dutta & Faulkner, 2019).

Due to technical difficulties, reflected entropy has been mostly studied in static cases in the literature. In Chapter 3, we will employ entanglement membrane to propose effective theories for the time evolution of reflected entropy in the late-time, large-region limit. Most noticeably, we will see that the additional degree of freedom in generalised membrane theory for 2d CFT plays a crucial role; consequently, there are *two* effective theories for 2d CFT and generic chaotic systems, respectively. These effective theories for reflected entropy allows one to further investigate the time evolution of multipartite entanglement signals that we will review in the next section.

1.5 Signals of multiparty entanglement

Multipartite states depict a much richer structure than bipartite states. In particular, systems with many degrees of freedom can also display intricate multiparty entanglement patterns. Multiparty entanglement has a intricate structure, and we do not have a good general description of the forms it can take (see the review (Walter, Gross, & Eisert, 2016)). Some information about multiparty entanglement can be obtained by considering entanglement across different bipartitions of a system; for example the triple information constructed from such data provides a signal of four-party entanglement (Cui et al., 2019). Further insight can be obtained from the *reflected entropy* reviewed in the previous subsection. As we review below, the difference between reflected entropy and mutual information provides a signal of three-party entanglement (Akers & Rath, 2020; Hayden, Parrikar, & Sorce, 2021).

By "signal" we mean here a quantity whose non-vanishing confirms the presence of multiparty entanglement. The converse need not be true. If one of the signals we consider vanishes, there may still be some multiparty entanglement; it is just not detected by the signal in question.

Recently, the work (Balasubramanian, Kang, Murdia, & Ross, 2025) initiated a study of multiparty entanglement signals for general numbers of parties. They used these signals to show that states with holographically dual geometries contain significant amounts of multiparty entanglement. Using these methods (Balasubramanian, Kang, Cummings, Murdia, & Ross, 2025) derived an inequality showing that purely Greenberger-Horne-Zeilinger-like (GHZ-like) entanglement between any number of parties is forbidden in holography, consistent with arguments for three-party GHZ-like states in (Hayden et al., 2021).

1.5.1 Review of multiparty entanglement signals

In this section, we review some multiparty entanglement signals. We will focus primarily on signals of three- and four-party entanglement, but we also include a brief discussion of higher-party entanglement signals.

We consider multiparty entanglement in a pure state where the system is divided into n disjoint subsystems. For $n = 2$, we have a state $|\psi\rangle_{AB}$, and bipartite entanglement is measured by the von Neumann entropy $S(A)$ of the reduced density matrix $\rho_A = \mathrm{tr}_B(|\psi\rangle_{AB}\langle\psi|_{AB})$.

For three parties, we can trace the state $|\psi\rangle_{ABC}$ over one party, say C, to obtain the reduced density matrix ρ_{AB}. The mutual information (1.4.1) for this reduced density matrix is sensitive to correlation between A and B, which includes contributions from both bipartite entanglement between A and B and tripartite entanglement involving A, B and C. To isolate the tripartite entanglement we need

to combine this with another source of information on correlation between A and B. The reflected entropy introduced in the previous section is also sensitive to both bipartite entanglement between A and B and tripartite entanglement involving A, B, and C. In the residual information

$$R_3(A:B) = S_R(A:B) - I(A:B), \tag{1.5.1}$$

the contribution from bipartite entanglement *cancels*, so the residual information is a signal of three-party entanglement: if $R_3 \neq 0$, the state $|\psi\rangle_{ABC}$ has tripartite entanglement between A, B, and C (Akers & Rath, 2020). To see this more explicitly, let us suppose that $|\psi\rangle_{ABC}$ is a purely bipartite state:

$$|\psi\rangle_{ABC} = |\psi_1\rangle_{A_1B_1} \otimes |\psi_2\rangle_{A_2C_1} \otimes |\psi_3\rangle_{B_2C_2}\,. \tag{1.5.2}$$

One can easily compute the mutual information

$$I(A:B) = 2S(A_1) = 2S(B_1), \tag{1.5.3}$$

$$I(A:C) = 2S(A_2) = 2S(C_1), \tag{1.5.4}$$

$$I(B:C) = 2S(B_2) = 2S(C_2). \tag{1.5.5}$$

Now, let us compute $S_R(A:B)$ via canonical purification. Making use of the fact that S_R is additive under tensor product, we can write the reduced density matrix

ρ_{AB} as

$$\rho_{AB} = \mathrm{Tr}_C \left|\psi\right\rangle_{ABC} \left\langle\psi\right|_{ABC} \tag{1.5.6}$$

$$= \left|\psi_1\right\rangle_{A_1B_1} \left\langle\psi_1\right|_{A_1B_1} \otimes \mathrm{Tr}_{C_1} \left|\psi_2\right\rangle_{A_2C_1} \left\langle\psi_2\right|_{A_2C_1} \otimes \mathrm{Tr}_{C_2} \left|\psi_3\right\rangle_{B_2C_2} \left\langle\psi_3\right|_{B_2C_2} \tag{1.5.7}$$

$$= \rho_{A_1B_1} \otimes \rho_{A_2} \otimes \rho_{B_2}. \tag{1.5.8}$$

The canonical purification of $\rho_{A_1B_1}$ is simply a product state of two copies of $|\psi_1\rangle$, hence $S_R(\rho_{A_1B_1}) = 2S(A_1) = 2S(B_1) = I(A:B)$. As there are no entanglements between A_2 and B in $|\psi_2\rangle$, we have $S_R(\rho_{A_2}) = 0$; similarly, $S_R(\rho_{B_2}) = 0$. Hence, we have $S_R(\rho_{AB}) = S_R(\rho_{A_1B_1}) = I(A:B)$ for purely bipartite states.

The residual information is provably non-negative (Dutta & Faulkner, 2019), but it can nevertheless vanish on states with tripartite entanglement. For example, it vanishes for the GHZ state.

Note that we chose to trace over C; tracing over B or A instead defines other signals of three-party entanglement, $R_3(A:C)$, $R_3(B:C)$. We will see later that these different signals can have qualitatively different behaviour, giving us independent information about aspects of the three-party entanglement.

For a four party state $|\psi\rangle_{ABCD}$, we can obtain a signal of four-party entanglement by tracing over one of the parties, say D, and considering the triple information

$$I_3(A:B:C) = S_A + S_B + S_C - S_{AB} - S_{AC} - S_{BC} + S_{ABC} \tag{1.5.9}$$

for the resulting reduced density matrix (Balasubramanian, Hayden, Maloney, Marolf, & Ross, 2014). This is permutation invariant among the four parties, which is made manifest by defining a four-party analogue $I_4(A:B:C:D)$ (see (1.5.11) for the general n-party definition), and noting that on pure states

$I_4(A:B:C:D) = 2I_3(A:B:C)$. This is analogous to the relation between the mutual information and the von Neumann entropy for two parties. The triple information is not sign-definite in general, although it is always negative on holographic states (Hayden, Headrick, & Maloney, 2013).

In (Balasubramanian, Kang, Murdia, & Ross, 2025), another signal of four-party entanglement was defined using canonical purification. If we consider the reduced density matrix ρ_{AB} obtained from $|\psi\rangle_{ABCD}$, using the canonical purification as above we can define the reflected entropy $S_R(A:B)$. Alternatively, if we reduce over D we obtain a reduced density matrix ρ_{ABC}, with a canonical purification $\left|\sqrt{\rho}\right\rangle_{ABCA^*B^*C^*}$. Reducing this over CC^* defines another reduced density matrix $\bar{\rho}_{AA^*BB^*}$, with a canonical purification $|\sqrt{\bar{\rho}}\rangle_{AA^*BB^*A_*A_*^*B_*B_*^*}$. Using the von Neumann entropy $S(AA^*A_*A_*^*)$ in this state, we can define the four-party residual entropy

$$Q_4 = S(AA^*A_*A_*^*) - 2S_R(A:B), \tag{1.5.10}$$

which is non-zero only if the state has four-party entanglement. As with the residual information, this is not permutation invariant; we can define different signals by tracing out different subsystems.

In (Balasubramanian, Kang, Murdia, & Ross, 2025), the residual information and triple information were generalised to higher numbers of parties. For even numbers of parties we have the n-information

$$I_n(A_1:\ldots:A_n) = -\sum_{i\leq n}(-1)^n S_i, \tag{1.5.11}$$

where S_i is the permutation-invariant combination of all the entropies on sets of i parties chosen from the n parties.[18] On pure states $I_n = 2I_{n-1}$, where I_{n-1} is

[18]Note that it has been recently shown that of these quantities, only the mutual information is monotonic until the partial trace (Hernández-Cuenca, Hubeny, & Jia, 2024). See also (Ju, Pan, Sun,

evaluated on the reduced density matrix obtained by tracing out any one party. For n odd $I_n = 0$ on pure states, so the n-information is not helpful. For odd n we can define instead the n-residual information, by tracing out one party and taking the difference between I_{n-1} evaluated on the canonical purification and I_{n-1} on the density matrix,

$$R_n(A_1 : \ldots : A_{n-1}; A_n) = \frac{1}{2} I_{n-1}(A_1 A_1^* : \ldots : A_{n-1} A_{n-1}^*) - I_{n-1}(A_1 : \ldots : A_{n-1}). \tag{1.5.12}$$

As with the residual information, this depends on which party we trace out, so there are n independent signals. The n-information and the n-residual information for n even and odd respectively are all signals of n-party entanglement; if they are non-zero the state has n-party entanglement. Beyond the cases discussed above nothing is known about their positivity properties.

The discussion in these works, and in the preceding analysis of (Balasubramanian et al., 2014), was restricted to static or time-symmetric cases, such as vacuum AdS_3 and multiboundary wormholes. In Chapter 4, we will consider time evolution of multiparty entalgmement signals reviewed in section 1.5 in chaotic systems in the late time, large region limit, in which entanglement dynamics is believed to be universally captured by the membrane effective theory.

The evolution of the triple information in time-dependent holographic states dual to asymptotically AdS black holes was previously considered in (Balasubramanian, Bernamonti, Copland, Craps, & Galli, 2011).[19] For the analysis there it was sufficient to use the RT/HRT formulas (Hubeny et al., 2007) for entanglement entropy of intervals in holographic theories because the triple information is constructed from such quantities. To construct the entanglement signals studied in

& Zhao, 2024; Ju, Sun, & Zhao, 2025) for further studies on n-information.

[19] In the precise setup of (Balasubramanian, Bernamonti, Copland, et al., 2011) the membrane theory does not apply because they do not examine a late time, large region limit.

(Balasubramanian, Kang, Murdia, & Ross, 2025) we need to additionally compute reflected entropies. The time evolution of reflected entropy was first studied in 2d CFT in (Kudler-Flam, Kusuki, & Ryu, 2020). More recently, as is detailed in Chapter 3, the membrane theory framework was enriched to enable computation of reflected entropy (Jiang et al., 2025). We will use this method to study the dynamics of the multiparty signals considered in (Balasubramanian, Kang, Murdia, & Ross, 2025) in Chapter 4.

2 | New horizons for inhomogeneous quenches

2.1 Introduction

In this chapter, we study the SSD CFT briefly reviewed in Chapter 1.3.1 from both holographic and field-theoretic point of view.

In Section 2.2 we analyse a special quantum quench from H_0 to the SSD Hamiltonian H_1. In Subsection 2.2.3 we point out that SSD Hamiltonian leads to a different *foliation* of the 2-dimensional spacetime as is shown in Figure 2.1. Furthermore, there is a *triangle*-shaped Killing horizon (2.2.11) with *zero* temperature.

Afterwards in Section 2.3, we investigate holographic aspects of SSD CFT. In Subsection 2.3.1, we show that the gravitational dual of SSD CFT prepared in the ground and thermal states are dual to pure AdS_3 and BTZ black hole (Banados, Henneaux, Teitelboim, & Zanelli, 1993; Banados, Teitelboim, & Zanelli, 1992) with non-trivial *foliations*, respectively. Then Subsection 2.3.2 and 2.3.3 demonstrate the existence of new *horizons* in both pure AdS_3 (2.3.8) and BTZ (2.3.13), which are plotted in Figure 2.3 and 2.4, respectively. In Subsection 2.3.2 we show that the AdS_3 new horizon, which is a Killing horizon, also has *zero* temperature. In Subsection 2.3.3 we also compare our new horizon in BTZ geometry with the BTZ black hole horizon and find that the new horizon is *larger* (see Figure 2.5).

In Subsection A.6, we comment on the reconstructions of bulk operators in the presence of the aforementioned new horizons and conclude that bulk operators remain *reconstructable* even after falling into these horizons (as long as they remain outside the BTZ black hole horizon).

In Section A.7 we generalise the SSD quench results to quenches governed by other $SL(2)$ Virasoro subalgebras.

Finally, Section 2.4 is devoted to the study of holographic entanglement entropy (Ryu & Takayanagi, 2006b, 2006a; Hubeny et al., 2007) in the gravity dual of SSD CFT prepared both in the ground and thermal state. We find that due to the non-trivial foliations of the gravity dual of SSD CFT in the bulk, the holographic entanglement entropy is computed by spacelike geodesics anchoring on the boundary that is, in general, at non-equal times, see e.g. Figure 2.6 for an example. The time evolution of large-radius cutoff surfaces (plotted in Figure 2.2) plays a crucial role. In cases where CFTs are initially prepared in thermal states, we discover that holographic entanglement entropy shows the entanglement plateau phenomenon (Hubeny et al., 2013). We find precise agreements between our holographic results and field-theoretic calculations in all comparable cases and reproduce holographically the cooling and heating effects (Wen et al., 2022; Goto et al., 2021) discovered earlier in the field theory context.

2.2 A special quantum quench

2.2.1 Setup

We consider CFT_2 on a *cylinder* $\mathbb{R} \times S^1$ of circumference $l = 2\pi$ with *periodic* boundary conditions,[1] in either the *ground* state $|0\rangle$ or the *thermal* state $\rho = e^{-\beta H}$ at temperature β^{-1}. We are interested in the *Lorentzian* time evolution of driven CFTs, although it is technically easier to work in *Euclidean* and then analytically

[1]The references (Wen & Wu, 2018b, 2018a; Fan et al., 2020; Wen et al., 2021; Han & Wen, 2020; Fan et al., 2021; Wen et al., 2022) sometimes adopt *open* boundary conditions. We will not use this boundary condition in our work but will point out its appearance when referring to their works.

continue to Lorentzian signature. The coordinate on the Euclidean cylinder is

$$\begin{aligned} w &= \tau + ix, \\ \overline{w} &= \tau - ix. \end{aligned} \tag{2.2.1}$$

Here, we use τ and t to denote imaginary and real time, respectively. The spatial variable x is periodic with periodicity 2π: $x \sim x + 2\pi$. The analytic continuation is given by $\tau \to it$, which makes w and $\overline{w}$ (real) light cone coordinates.

We will mostly work in the *Heisenberg picture*: we take a primary operator O of weights $(h, \overline{h})$ on the $t = 0$ time slice with $w = ix$, $\overline{w} = -ix$ and time evolve it using the operator $e^{-\tau H}$ with H made out of the Virasoro generators. Such a time evolution is *geometric*, the operator moves O to *new* positions $(w_{\text{new}}(\tau, x), \overline{w}_{\text{new}}(\tau, x))$,[2]

$$O^{(H)}(\tau, x) \equiv e^{\tau H} O(ix, -ix) e^{-\tau H} = \Big(\frac{\partial w_{\text{new}}}{\partial w}\Big)^{h} \Big(\frac{\partial \overline{w}_{\text{new}}}{\partial \overline{w}}\Big)^{\overline{h}} O(w_{\text{new}}, \overline{w}_{\text{new}})\,, \tag{2.2.2}$$

whose explicit expression depends on the Hamiltonian H that drives the system. This is a powerful result that applies irrespective of the state of the system or the boundary conditions (provided they preserve H).

For example, if H is the CFT Hamiltonian

$$H_0 = \int_0^{2\pi} dx\, T_{00}(x) = L_0 + \overline{L}_0 - \frac{c}{12}, \tag{2.2.3}$$

with the last term being the Casimir energy, then after (imaginary) time τ, $(w_{\text{new}}, \overline{w}_{\text{new}})$ are simply $(w, \overline{w})$ in (2.2.1).

[2]Here $w = ix$, $\overline{w} = -ix$. In later sections we will use the notations $\frac{\partial w_{\text{new}}}{\partial w}$ and $\frac{\partial w_{\text{new}}}{\partial (ix)}$, $\frac{\partial \overline{w}_{\text{new}}}{\partial \overline{w}}$ and $\frac{\partial \overline{w}_{\text{new}}}{\partial (-ix)}$ interchangeably.

2.2.2 The sine-squared deformed time evolution

The fundamental ingredient of the deformation we would like to study is the sine-squared deformation (SSD) (Wen & Wu, 2018b), which deforms the CFT Hamiltonian (2.2.3) with the enveloping function

$$v_1(x) = 2\sin^2\left(\frac{x}{2}\right). \tag{2.2.4}$$

The resulting deformed Hamiltonian is

$$\begin{aligned} H_1 &= 2\int_0^{2\pi} dx\ \sin^2\left(\frac{x}{2}\right) T_{00}(x) \\ &= L_0 - \frac{L_{-1}+L_1}{2} + \overline{L}_0 - \frac{\overline{L}_{-1}+\overline{L}_1}{2} - \frac{c}{12}. \end{aligned} \tag{2.2.5}$$

Note that the SSD enveloping function $v_1(x)$ is *inhomogeneous* in space, in particular, it vanishes at $x = 0$ (or 2π). From (2.2.5) one observes $[H_0, H_1] \neq 0$, because $[L_0, L_{\pm 1}] = \mp L_{\pm 1}$; however, H_0 and H_1 share the same ground state $|0\rangle$, as $L_n|0\rangle = 0$ for $n \geq -1$.

The use of H_1 as a Hamiltonian is unconventional. However, H_1 can be conformally mapped to a dilation (Okunishi, 2016; Wen & Wu, 2018b; Fan et al., 2020); mapping back to the cylinder, we obtain $(w_{\text{new}}, \overline{w}_{\text{new}})$ given by the following logarithms of Mobius transformations (Wen & Wu, 2018b; Goto et al., 2021) (see Appendix A.1.1 for details)

$$w_{\text{new}} = \log\left[\frac{\left(1+\frac{it}{2}\right)e^{ix} - \frac{it}{2}}{\frac{it}{2}e^{ix} + \left(1-\frac{it}{2}\right)}\right], \tag{2.2.6}$$

$$\overline{w}_{\text{new}} = \log\left[\frac{\left(1+\frac{it}{2}\right)e^{-ix} - \frac{it}{2}}{\frac{it}{2}e^{-ix} + \left(1-\frac{it}{2}\right)}\right], \tag{2.2.7}$$

where we have analytically continued to real-time $\tau \to it$. The logarithm is a

multi-valued function; we fix the appropriate sheet by demanding continuity in t. The terms inside the logarithm are $SL(2)$ transformations of the variables $z = e^{ix}$ and $\overline{z} = e^{-ix}$ on the unit circle.[3] The $SL(2)$ transformation has a *fixed point*, i.e. a point that stays invariant under the $SL(2)$ transformation at $x = 0$ (identified with $x = 2\pi$). In analogy with (2.2.1), we can define (Goto et al., 2021)

$$\begin{aligned} w_{\text{new}} &= i(t_{\text{new}} + x_{\text{new}})\,, \\ \overline{w}_{\text{new}} &= i(t_{\text{new}} - x_{\text{new}})\,. \end{aligned} \tag{2.2.8}$$

t_{new} and x_{new} are *real* functions of t and x.[4] We will see that the $SL(2)$ transformation (2.2.6) and (2.2.7) determines (almost) all the physical phenomena of interest: in the $(w_{\text{new}}, \overline{w}_{\text{new}})$ coordinate, the CFT is in equilibrium, and the time-dependent conformal transformations (2.2.6) and (2.2.7) allow us to deduce non-equilibrium phenomena from known equilibrium physics (Wen & Wu, 2018b; Moosavi, 2021).

There is an alternative way of thinking about the SSD CFT: the driving by the Hamiltonian (2.2.5) is equivalent to the natural time evolution of the CFT on the curved spacetime (Wen & Wu, 2018b; MacCormack et al., 2019; de Boer, Godet, Kastikainen, & Keski-Vakkuri, 2023):

$$ds^2 = -v_1(x)^2 dt^2 + dx^2\,. \tag{2.2.9}$$

For the review of the argument, see Appendix A.1.1.3. Thus we have three

[3] z and $\overline{z}$ are coordinates on the *complex plane*, related to the cylinder via the exponential maps $z = e^w$ and $\overline{z} = e^{\overline{w}}$.

[4] As $SL(2)$ transformations preserve unit circles, w_{new} and $\overline{w}_{\text{new}}$ are completely determined by the argument of the logarithm function and are, therefore, purely imaginary.

equivalent ways of thinking about correlation functions

$$\begin{aligned}\left\langle O^{(H_1)}(\tau,x)\ldots\right\rangle &= \left(\frac{\partial w_{\text{new}}}{\partial(ix)}\right)^{h}\left(\frac{\partial \overline{w}_{\text{new}}}{\partial(-ix))}\right)^{\overline{h}}\ldots\left\langle O(w_{\text{new}},\overline{w}_{\text{new}})\ldots\right\rangle_{ds^2=dw_{\text{new}}d\overline{w}_{\text{new}}} \\ &= \left\langle O(\tau,x)\ldots\right\rangle_{ds'^2=v_1(x)^2d\tau^2+dx^2}\ .\end{aligned} \tag{2.2.10}$$

Quantum quenches with SSD CFT at $t>0$ have been studied for systems prepared in ground (Wen & Wu, 2018b) and thermal (Goto et al., 2021) states.[5] Some of the most interesting phenomena that have been found are as follows: In (Goto et al., 2021) it was found that the CFT possesses two energy peaks that move towards the fixed point $x=0$; the entanglement entropy decreases and approaches the *vacuum* entanglement entropy if the subregion A does not include the fixed point $x=0$ (identified with 2π). In the following, we will provide a geometric perspective on these, predominantly in the context of holography.

2.2.3 Boundary triangle

We have seen in Section 2.2.2 that the non-trivial time evolution of SSD CFTs is completely determined by the coordinate transformations (2.2.6) and (2.2.7). The spacetime coordinates $t_{\text{new}}(t,x)$ and $x_{\text{new}}(t,x)$ then follows from (2.2.8). In Figure 2.1, we plot the constant-t lines and constant-x lines on the $(t_{\text{new}},x_{\text{new}})$ plane.[6]

Figure 2.1 shows that the action of H_1 as Hamiltonian changes the *foliation* of the

[5] Note that in (Wen & Wu, 2018b), *open* boundary conditions has been imposed to set up a quench problem, which makes the ground state of H_0 into an excited state of H_1. In this work, we study the non-trivial time evolution of H_1 with periodic boundary conditions. Although this setup cannot strictly be regarded as a quench if the initial state is the ground state, the expression for w_{new} (2.2.6) and $\overline{w}_{\text{new}}$ (2.2.7) remain the same.

[6] It is more convenient to plot with the trigonometric form of t_{new} (A.1.19) and x_{new} (A.1.20).

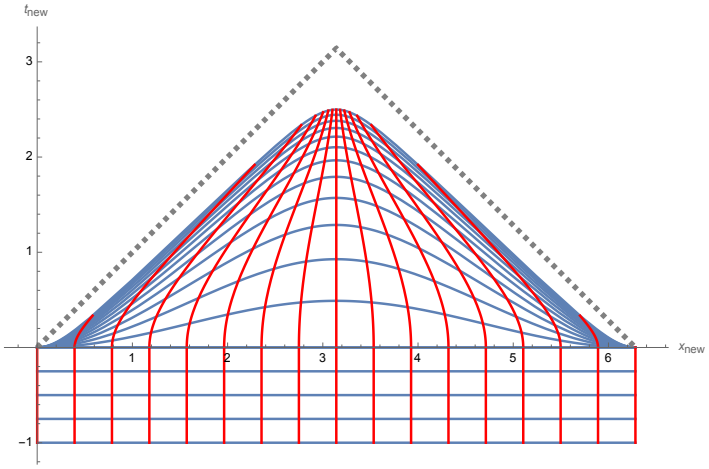

Figure 2.1: Constant t lines (blue) and constant-x lines (red) in the $(t_{\text{new}}, x_{\text{new}})$-plane. At $t < 0$ when the driving Hamiltonian is H_0, constant-t lines and constant-x lines are uniformly distributed horizontal and vertical lines, respectively. At $t > 0$ when the driving Hamiltonian is suddenly switched to H_1, constant-t lines asymptote a triangle-shaped curve (2.2.11), which is plotted as a dashed gray line; constant-x lines converge to the top tip of the triangle, (π, π).

$(t_{\text{new}}, x_{\text{new}})$ spacetime in a non-uniform manner.[7] As time evolves, constant-t lines approach a *triangle*-shaped curve

$$t_{\text{new}} = \begin{cases} x_{\text{new}}, & 0 \leq x_{\text{new}} < \pi \\ 2\pi - x_{\text{new}}, & \pi \leq x_{\text{new}} < 2\pi \end{cases} \tag{2.2.11}$$

instead of moving towards $t_{\text{new}} \to \infty$ homogeneously as is in the H_0 evolution case; constant-x lines converge to the top tip of the triangle, (π, π). Indeed, from the expression of t_{new} (A.1.19) and x_{new} (A.1.20), one can verify that

$$\lim_{t\to\infty} t_{\text{new}} = \pi \qquad\qquad \lim_{t\to\infty} x_{\text{new}} = \pi \tag{2.2.12}$$

regardless of x ($x \neq 0, 2\pi$). As the triangle (2.2.11) separates points that are

[7] This reflects the *inhomogeneous* nature of H_1; in particular, the fixed point $x = 0$ (which maps to $(t_{\text{new}}, x_{\text{new}}) = (0, 0)$) does not time evolve at all.

connected to infinity (outside the triangle) from those that are not (inside the triangle), it can be regarded as a new *horizon* in the $(t_{\rm new}, x_{\rm new})$ plane. Note that the new horizon is ultimately the consequence of the fixed points $x = 0, 2\pi$ on the circle. If there were no such fixed points, the entire constant t line in $(t_{\rm new}, x_{\rm new})$ would evolve as t grows, and there would be no new horizons.

The SSD Hamiltonian (2.2.5) evolves the CFT along a conformal Killing vector field, hence the horizon (2.2.11) is a *Killing* horizon associated with this vector field. From the expression (2.2.5), the conformal Killing vector k_1 corresponds to H_1 can be written as

$$k_1 = -z_{\rm new}\partial_{z_{\rm new}} - \overline{z}_{\rm new}\partial_{\overline{z}_{\rm new}} + \frac{z_{\rm new}^2+1}{2}\partial_{z_{\rm new}} + \frac{\overline{z}_{\rm new}^2+1}{2}\partial_{\overline{z}_{\rm new}} \tag{2.2.13}$$

$$= (\cosh\tau_{\rm new}\ \cos x_{\rm new} - 1)\partial_{\tau_{\rm new}} + \sinh\tau_{\rm new}\ \sin x_{\rm new}\partial_{x_{\rm new}}, \tag{2.2.14}$$

where $z_{\rm new} = e^{\tau_{\rm new}+ix_{\rm new}}$ and $\overline{z}_{\rm new} = e^{\tau_{\rm new}-ix_{\rm new}}$.[8] One can easily check that k_1 obeys the conformal Killing equation

$$\partial_{(\mu}(k_1)_{\nu)} = \delta_{\mu\nu}\partial_\rho(k_1)^\rho\,. \tag{2.2.15}$$

The analytic continuation of the conformal Killing vector (2.2.14) to Lorentzian signature is

$$k_1 = (1 - \cos t_{\rm new}\ \cos x_{\rm new})\partial_{t_{\rm new}} + \sin t_{\rm new}\ \sin x_{\rm new}\partial_{x_{\rm new}}\,, \tag{2.2.16}$$

where we have removed the overall i so that the vector field implements Lorentzian time evolution. The conformal Killing horizon is located where the conformal

[8]The conformal Killing vector (2.2.14) is a time translation along the τ direction in the $(\tau_{\rm new}, x_{\rm new})$ coordinate, as can be seen from (2.2.2). We will only rarely use $\tau_{\rm new}$ as a time coordinate.

Killing vector becomes null, so we compute its norm squared:

$$|k_1|^2 = (\cos t_{\text{new}} - \cos x_{\text{new}})^2 = 0 \qquad \Longrightarrow \qquad t_{\text{new}} = \pm x_{\text{new}} + 2n\pi \ (n \in \mathbb{Z}). \tag{2.2.17}$$

As $t_{\text{new}} \in [0, \pi]$, $t_{\text{new}} = x_{\text{new}}$ or $t_{\text{new}} = -x_{\text{new}} + 2\pi$, which is exactly the expression of the triangle (2.2.11). Since (2.2.17) has a double zero, this is an *extremal* conformal Killing horizon, hence it has zero temperature.[9] The physical reason for this is that H_0 and H_1 share the *same* ground state.[10]

We close this section by comparing the H_1 time evolution to those under CFT modular Hamiltonians in the literature, see the comprehensive recent references (Cardy & Tonni, 2016; de Boer et al., 2022; Das, Ezhuthachan, Porey, & Roy, 2024). The operators $K_{\text{full}} = s_0 L_0 + s_1 L_1 + s_{-1} L_{-1}$ are full/complete modular Hamiltonians associated to an interval A for the vacuum of a 2d CFT on a circle, $K_{\text{full}} = K_A - K_{\bar{A}}$. Just like H_1, K_{full} also annihilates the vacuum. If we consider the reduced density matrix of the interval, it is a thermal state under modular evolution $\rho \propto e^{-K_A}$. In our study, we do not consider subregions and focus on H_1 defined on the entire S^1.

[9] A simple calculation on (2.2.14) (after analytic continuation) confirms this reasoning,

$$T = \frac{1}{2\pi} \sqrt{\nabla_\mu |k_1| \nabla^\mu |k_1|}\Big|_{\text{hor.}} = \sqrt{-\sin^2 t_{\text{new}} + \sin^2 x_{\text{new}}} = 0 \tag{2.2.18}$$

where $|k_1|$ is given by (2.2.17).

[10] This is in contrast to the Unruh effect, where the Minkowski vacuum is an excited state of and Rindler observer and vice versa.

2.3 Gravity dual for the special quantum quench

2.3.1 Bulk geometry

The gravity dual of a generic (global) quench involves the changing of boundary conditions for the gravity fields, corresponding to uniform injection of energy into the bulk from the near boundary region. In the simplest scenario, the spacetime reaches equilibrium by settling to a black hole, the dual of thermalisation in the boundary QFT.

In the special quench we analyse, the Heisenberg evolution on the cylinder can be described by the t-depending coordinate transformation $(t_{\rm new}, x_{\rm new})$ (2.2.8) expressing non-equilibrium physics from equilibrium results. Correspondingly, the matter stress tensor in the bulk remains zero and the spacetime does not change. What changes is the cutoff surface that the field theory lives on. This among other things leads to the change in energy in the boundary theory.

To construct the holographic dual of SSD CFT, we introduce the emergent bulk radial coordinate $r_{\rm new} \in [0, \infty)$. Holographic CFTs in their ground and thermal states are dual to pure AdS_3 and BTZ black holes (Banados et al., 1993, 1992), respectively. As the CFT in $(t_{\rm new}, x_{\rm new})$ are in equilibrium, the dual bulk metrics in the $(t_{\rm new}, r_{\rm new}, x_{\rm new})$ coordinate are given by those of the pure AdS_3 and BTZ black hole metrics,

$$|0\rangle : \qquad ds^2 = -(r_{\rm new}^2 + 1)dt_{\rm new}^2 + \frac{dr_{\rm new}^2}{r_{\rm new}^2 + 1} + r_{\rm new}^2 dx_{\rm new}^2, \tag{2.3.1}$$

$$\rho = e^{-\beta H_0} : \qquad ds^2 = -(r_{\rm new}^2 - r_+^2)dt_{\rm new}^2 + \frac{dr_{\rm new}^2}{r_{\rm new}^2 - r_+^2} + r_{\rm new}^2 dx_{\rm new}^2, \tag{2.3.2}$$

where r_+ is the radius of the BTZ black hole, related to the inverse temperature β via $r_+ = \frac{2\pi}{\beta}$.

Besides the movement of the insertion points of operators, there are explicit factors showing up in formulas (2.2.2) and (2.2.10) multiplying equilibrium correlators. These correspond to taking the holographic cutoff at

$$\epsilon = \frac{1}{\sqrt{\frac{\partial w_{\text{new}}}{\partial w}\frac{\partial \overline{w}_{\text{new}}}{\partial \overline{w}}}\, R_{\text{new}}(t_{\text{new}}, x_{\text{new}})}\,, \tag{2.3.3}$$

resulting in a *nonuniform* cutoff surface in the radial coordinate $R_{\text{new}}(t_{\text{new}}, x_{\text{new}})$. Note that the formula is applicable for $t > 0$, for $t \leq 0$ we have $R_{\text{new}} = 1/\epsilon$. A plot of the cutoff surface (2.3.3) can be found in Figure 2.2. This formula has appeared in the literature before in (Goto et al., 2021) based on different arguments; in Appendix A.2.1 we give a detailed new argument that this nonuniform cutoff produces the appropriate $\left(\frac{\partial w_{\text{new}}}{\partial w}\right)^h$ factors in correlators.

We have seen that in the boundary theory a horizon appears, this in the holographic dual leads to a new horizon in the bulk. As constant t-slices in the bulk are anchored on the constant t-lines on the boundary, this induces a change in the *foliation* of the bulk, see Figure 2.2. (There is a natural extension of H_1 into the bulk in the pure AdS case, but not in BTZ.) As $t \to \infty$, constant-t slices asymptote the bulk null hypersurface anchored on the boundary triangle (2.2.11) instead of moving towards $t_{\text{new}} \to \infty$. As this hypersurface separates bulk points that are connected to the boundary spacetime explored by the CFT from those that are not, it is a new *horizon* in the bulk.

An alternative approach is provided by the CFT in curved spacetime perspective: we set the boundary metric to agree with (2.2.9), and use Fefferman-Graham coordinates (Skenderis & Solodukhin, 2000; de Haro et al., 2001) to build a coordinate system adapted to the boundary spacetime. The uniform cutoff surface in the Fefferman-Graham radial coordinate will coincide with the cutoff surface found from (2.3.3). In 3d pure gravity, the Fefferman-Graham expansion is known

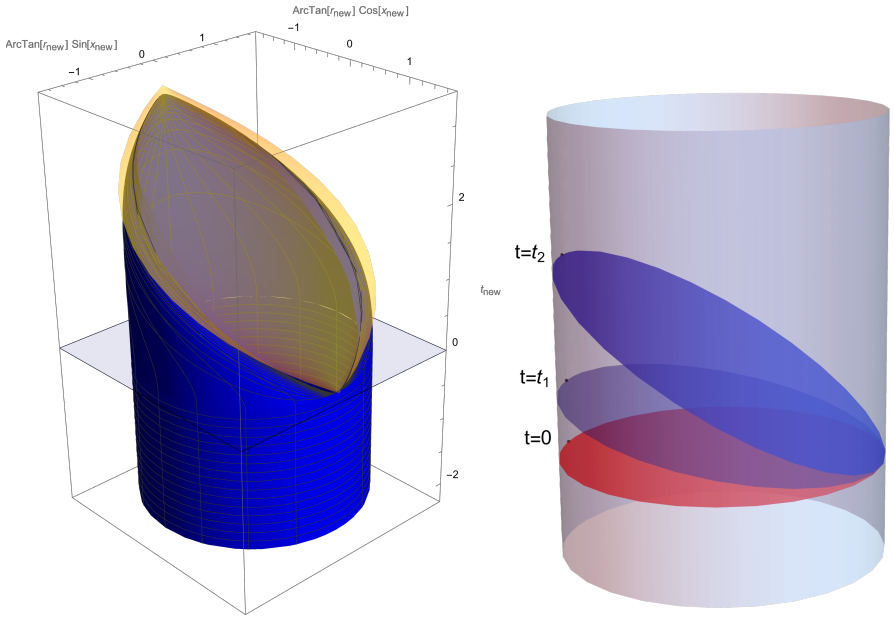

Figure 2.2: Left: Plot of the cutoff surface in $(t_{\text{new}}, r_{\text{new}}, x_{\text{new}})$ spacetime. The light blue surface denotes the $t_{\text{new}} = t = 0$ slice, during which we suddenly switch the Hamiltonian from H_0 to H_1. At $t < 0$ when the driving Hamiltonian is H_0, the uniform cutoff $R_{\text{new}} = \epsilon^{-1}$ is shown in blue. At $t > 0$ the driving Hamiltonian becomes H_1, and the cutoff surface $R_{\text{new}}(t_{\text{new}}, x_{\text{new}})$ is no longer uniform according to (2.3.3). This significant change leads to the presence of a new horizon, which is depicted above in light yellow. This new horizons is also plotted in Figure 2.3 along with its generators. Note that the cutoff surface ends on the horizon (up to finite cutoff corrections). Right: Cartoon of constant t slices in $(t_{\text{new}}, r_{\text{new}}, x_{\text{new}})$ spacetime in global AdS_3.

to terminate. By solving the Einstein equations order by order in r we obtain the metric (Skenderis & Solodukhin, 2000):

$$ds^2 = \frac{dr^2}{r^2} + r^2\big(-v_1(x)^2dt^2 + dx^2\big) + g^{(1)}_{ab}(x^c)\,dx^a dx^b + \frac{g^{(2)}_{ab}(x^c)\,dx^a dx^b}{r^2}\,, \tag{2.3.4}$$

where $g^{(j)}_{ab}(x^c)$ is given in Appendix A.2.2 for the most general solution. There we also give the explicit form of the metric for the case of the vacuum and thermal states. Of course, (2.3.4) is just the reslicing of the AdS_3 (2.3.1) and BTZ (2.3.2) spacetimes. (The reslicing of AdS_3 was written down in (MacCormack et al., 2019) before studying the vacuum physics of the SSD CFT.) One advantage of these coordinates is that now the cutoff is at $R = 1/\epsilon$ instead of the nonuniform cutoff in $r_{\rm new}$ coordinates.

Note that as discussed in Appendix A.1.1.3, the curved spacetime (2.2.9) is obtained by a Weyl transformation from the flat spacetime $ds^2 = dw_{\rm new}d\overline{w}_{\rm new}$. It has been understood from the early days of AdS/CFT (Witten, 1998; Henningson & Skenderis, 1998) that changing the conformal factor of the boundary metric corresponds to choosing a different cutoff prescription.

2.3.2 New horizon in AdS_3

The isometries of AdS_3 form two copies of $SL(2)$ algebras (Brown & Henneaux, 1986). The Killing vectors ζ_i and $\overline{\zeta_i}$ ($i = -1, 0, 1$) of AdS_3 are given in Appendix A.3. From these Killing vectors, we can find a linear combination that asymptotes to the conformal Killing vector k^μ_1 (2.2.14). This provides the natural extension of

the H_1 evolution into the bulk:

$$\begin{aligned} K_1 &= \zeta_0 + \overline{\zeta_0} - \frac{\zeta_1 + \overline{\zeta_1}}{2} - \frac{\zeta_{-1} + \overline{\zeta_{-1}}}{2} \\ &= \Big(1 - \frac{r_{\text{new}}}{\sqrt{r_{\text{new}}^2+1}} \cos t_{\text{new}} \ \cos x_{\text{new}}\Big)\partial_{t_{\text{new}}} - \sqrt{r_{\text{new}}^2+1} \ \sin t_{\text{new}} \ \cos x_{\text{new}} \partial_{r_{\text{new}}} \\ &+ \frac{\sqrt{r_{\text{new}}^2+1}}{r_{\text{new}}} \sin t_{\text{new}} \ \sin x_{\text{new}} \partial_{x_{\text{new}}}. \end{aligned} \tag{2.3.5}$$

In the near-boundary $r_{\text{new}} \to \infty$ limit, the components of K_1^μ (2.3.5) along the boundary indeed goes to the boundary conformal Killing vector k_1^μ (2.2.14),

$$\lim_{r_{\text{new}}\to\infty} K_1^\mu = \big(1 - \cos t_{\text{new}} \ \cos x_{\text{new}}, \sin t_{\text{new}} \ \sin x_{\text{new}}\big) = k_1^\mu. \tag{2.3.6}$$

The Killing horizon is located where a Killing vector becomes null. From (2.3.5), we have for the norm square:

$$|K_1|^2 = \big(\sqrt{r^2+1}\cos t_{\text{new}} - r\cos x_{\text{new}}\big)^2 = 0 \tag{2.3.7}$$

$$\Rightarrow \quad t_{\text{new}}(r_{\text{new}}, x_{\text{new}}) = \arccos\left[\frac{r}{\sqrt{r_{\text{new}}^2+1}} \cos x_{\text{new}}\right]. \tag{2.3.8}$$

(2.3.8) is the new horizon in pure AdS$_3$. Since $|K_1|^2$ has a double zero, this is an extremal Killing horizon with zero associated temperature.[11] Just like on the CFT side, the intuition behind this result is that H_0 and H_1 share the same vacuum state. A plot of the Killing horizon (2.3.8) along with its null generators can be found in Figure 2.3.

[11] A direct calculation shows that this is indeed the case:

$$T = \frac{1}{2\pi}\sqrt{\nabla_\mu |K_1| \nabla^\mu |K_1|}\Big|_{\text{hor.}} = \sqrt{r_{\text{new}}^2+1}\cos t_{\text{new}} - r\cos x_{\text{new}} = 0. \tag{2.3.9}$$

where $|K_1|$ given by (2.3.7).

We can find the horizon (2.3.8) in an alternative manner, which will be a useful method in the following. To find the horizon as a null hypersurface, we need to investigate the null geodesics emanating from a point $(t_{\text{new}}, x_{\text{new}}) = (y, y)$ on the boundary triangle. The congruence of null geodesics that maximise t_{new} in the bulk then generates the null hypersurface. Here, for simplicity, we study only half of the triangle, i.e. $y \in [0, \pi]$; the result of the other half follows from reflection.

We will start with the metric (2.3.1) in the $(t_{\text{new}}, r_{\text{new}}, x_{\text{new}})$ coordinate. The null geodesics anchored on a point $(t_{\text{new}}, x_{\text{new}}) = (y, y)$ on the boundary triangle (see Appendix A.4.1.1 for details) is

$$t_{\text{new}}(r_{\text{new}}, x_{\text{new}}, y) = \arctan \frac{-r_{\text{new}} \cot(x_{\text{new}} - y)}{\sqrt{r_{\text{new}}^2 + \csc^2(x_{\text{new}} - y)}} + y - \frac{\pi}{2}, \tag{2.3.10}$$

where $y \in [0, \pi]$. (2.3.10) increases monotonically with y (see (A.4.17)). Hence, the maximal value of t is at $y = \pi$, which is the top tip of the boundary triangle. After some work detailed in Appendix A.4.1.1, one arrives at

$$t_{\text{new}}(r_{\text{new}}, x_{\text{new}}) = \arccos\left[\frac{r_{\text{new}}}{\sqrt{r_{\text{new}}^2 + 1}} \cos x_{\text{new}}\right], \tag{2.3.11}$$

agreeing with (2.3.8) obtained by the Killing vector method.

2.3.3 New horizon on BTZ

The $SL(2)$ isometry of AdS_3 is broken to $\mathbb{R} \times U(1)$ in BTZ geometry (Keski-Vakkuri, 1999). Hence, the new horizon is no longer a Killing horizon, nor can we associate temperature with it. To find the explicit expression of the horizon, one needs to investigate the null geodesic equation using the second method of the previous section. The null geodesics anchored a point on the boundary triangle

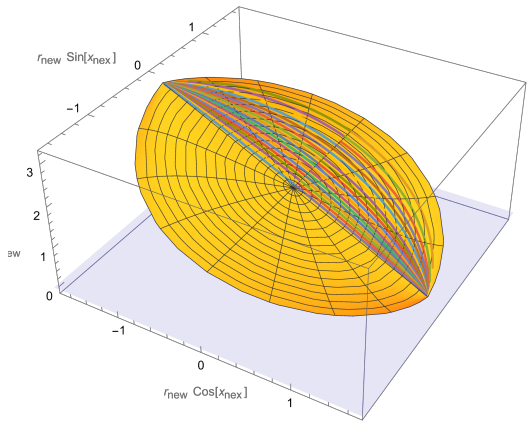

Figure 2.3: A plot of the new Killing horizon (2.3.11) in global AdS_3. The coloured lines are null geodesics emanating from the top tip of the triangle (π, π) that generate the hypersurface (2.3.11); for visualization, we only plotted them on half of the horizon. The light blue surface is the quench surface $t_{\text{new}} = t = 0$.

.

$(t_{\text{new}}, x_{\text{new}}) = (y, y)$ (see Appendix A.4.1.2 for details) is

$$t_{\text{new}}(r_{\text{new}}, x_{\text{new}}, y) = \frac{1}{2r_+} \log \frac{r_{\text{new}}\sqrt{1 + r_+^2 \sinh^2(x_{\text{new}} - y)} - r_+\sqrt{1 + r_{\text{new}}^2 \sinh^2(x_{\text{new}} - y)}}{r_{\text{new}}\sqrt{1 + r_+^2 \sinh^2(x_{\text{new}} - y)} + r_+\sqrt{1 + r_{\text{new}}^2 \sinh^2(x_{\text{new}} - y)}} + y, \tag{2.3.12}$$

where $y \in [0, \pi]$. (2.3.12) increases monotonically with y (see (A.4.30)). Hence, the maximal value of t is at $y = \pi$, which is the top tip of the boundary triangle. After some work detailed in Appendix A.4.1.2, one arrives at

$$t_{\text{new}}(r, x) = \frac{1}{2r_+} \log \frac{r_{\text{new}}\sqrt{1 + r_+^2 \sinh^2(x_{\text{new}} - \pi)} - r_+\sqrt{1 + r_{\text{new}}^2 \sinh^2(x_{\text{new}} - \pi)}}{r_{\text{new}}\sqrt{1 + r_+^2 \sinh^2(x_{\text{new}} - \pi)} + r_+\sqrt{1 + r_{\text{new}}^2 \sinh^2(x_{\text{new}} - \pi)}} + \pi. \tag{2.3.13}$$

A plot of the new horizon (2.3.13) along with its null generators can be found in

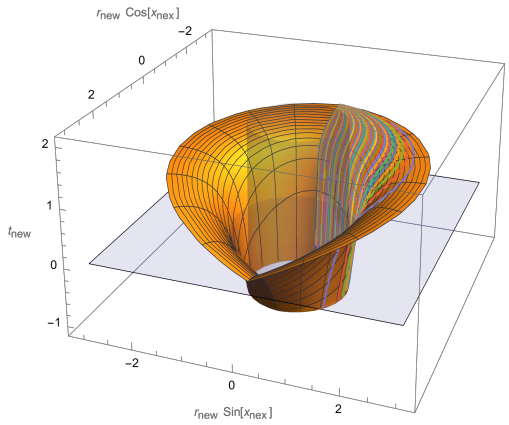

Figure 2.4: Plot of the new horizon (2.3.13) in the BTZ geometry. The coloured lines are null geodesics emanating from the top tip of the triangle (π, π) that generate the hypersurface (2.3.13); for visualization, we only plotted them on half of the horizon. The light blue surface is the quench surface $t_{\text{new}} = t = 0$. The BTZ black hole horizon is set to $r_+ = 1$ and plotted in light gray. The new horizon (2.3.13) is larger than the BTZ black hole horizon.

.

Figure 2.4.

For comparison with ref. (Goto et al., 2021), we use the coordinate system they were working in to plot time slices of both the new horizon (2.3.13) and the BTZ horizon.[12] (See Appendix A.5 for details.) From Figure 2.4 it is clear that the new horizon will be slightly *larger* than the BTZ black hole horizon, and indeed this is what we find in Figure 2.5. Note also that the new horizon (2.3.13) touches the boundary at the fixed point $x = 0$.

The horizon (2.3.13) in Figure 2.5 develops two peaks that move towards the fixed point $x = 0$, as is observed for the BTZ horizon in (Goto et al., 2021). It was also pointed out in (Goto et al., 2021) that the horizon deformation mimics the energy peaks of the boundary stress tensors. We note that the two peaks of the

[12]The Feffermann-Graham coordinates discussed around (2.3.4) and Appendix A.2.2 generically break down before encountering horizons, as was recently discussed in (Abajian, Aprile, Myers, & Vieira, 2024). Hence we cannot use them for addressing this question.

horizons (both the BTZ horizon and the new horizon) originate from the Weyl factor $\frac{\partial w_{\rm new}}{\partial w}\frac{\partial \overline{w}_{\rm new}}{\partial \overline{w}}$ in (A.5.1); in (Goto et al., 2021), the peaks of the boundary stress tensors also originate from these prefactors $\frac{\partial w_{\rm new}}{\partial w}$ and $\frac{\partial \overline{w}_{\rm new}}{\partial \overline{w}}$ in $\langle T(w)\rangle$ and $\langle \overline{T}(\overline{w})\rangle$, respectively. This then explains the qualitative[13] correlations between horizon deformations and energy peaks were first observed in (Goto et al., 2021).

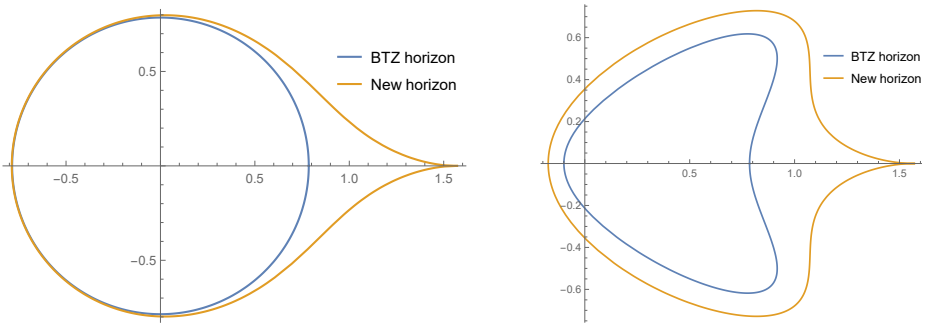

Figure 2.5: Comparison of the new horizon (2.3.13) and the BTZ black hole horizon in the coordinates employed by 2112.14388, at $t = 0$ (left) and $t = 3$ (right), respectively. The blue line denotes the BTZ horizon, whereas the orange line represents the new horizon (2.3.13)

2.4 Dynamics of entanglement entropy

In this section, we study the holographic entanglement entropy of a single interval $A = [x_1, x_2]$ at a constant t-slice. To this end, we again work in the $(t_{\rm new}, x_{\rm new}, r_{\rm new})$ geometry, and then perform a coordinate transformation back to (t, x, r). At time t, the endpoints of $A = [x_1, x_2]$ are obtained from (2.2.6), (2.2.7), (2.2.8),

$$w_{{\rm new},j} = \frac{1}{2i}(t_{{\rm new},j} + x_{{\rm new},j}), \quad \overline{w}_{{\rm new},j} = \frac{1}{2i}(t_{{\rm new},j} - x_{{\rm new},j}), \quad (j = 1, 2). \tag{2.4.1}$$

[13] As the metric (A.5.1) is not in Fefferman-Graham gauge (Skenderis & Solodukhin, 2000; de Haro et al., 2001), it is hard to draw a quantitative connection.

The holographic entanglement entropy of a single interval A is given by the length of the spacelike geodesic anchored on $\partial A = \{(t_{\text{new},1}, x_{\text{new},1}), (t_{\text{new},2}, x_{\text{new},2})\}$ on the boundary (Ryu & Takayanagi, 2006b, 2006a):

$$S_A = \frac{\mathcal{L}}{4G_N} = \frac{c}{6}\mathcal{L}. \tag{2.4.2}$$

where we have used the Brown-Henneaux central charge, $c = 3/2G_N$ (Brown & Henneaux, 1986). Therefore, to calculate the holographic entanglement entropy, one needs to obtain the geodesic length $\mathcal{L}$, using the temporal and angular separation $\Delta t_{\text{new}} = t_{\text{new},2} - t_{\text{new},1}$ and $\Delta x_{\text{new}} = x_{\text{new},2} - x_{\text{new},1}$ as inputs, and then transform back to (t, x, r). Note that in general $\Delta t_{\text{new}} \neq 0$, so our calculation is *not* of equal time ("time" as t_{new}). See Figure 2.6 for a demonstration.

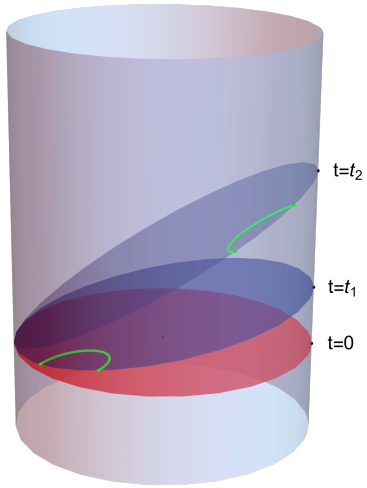

Figure 2.6: A demonstration of non-equal-t_{new} spacelike geodesics, plotted as green curves in the bulk anchoring on the two endpoints of the subregion A on the boundary constant-t lines. These spacelike geodesics compute the holographic entanglement entropy.

The length of the spacelike geodesic anchoring on the boundary is infinite, therefore, we need to regulate it by imposing a *cutoff* at some large radius $r_{\text{new}} = R_{\text{new}}$, and adopt the *regulated* length $\mathcal{L}_{\text{reg}}$. As is discussed in Subsection 2.3.1, the cutoff

surface is non-uniform in the radial direction, with $R_{\text{new}}(t_{\text{new}}, x_{\text{new}})$ given by (2.3.3). See Figure 2.2 for a plot of the cutoff surface.

2.4.1 Gravity dual of SSD: ground state

2.4.1.1 Holographic computation

The metric (2.3.1) leads to two conserved quantities for geodesics, $E = (r_{\text{new}}^2 + 1)\frac{dt_{\text{new}}}{d\lambda}$ and $L = r_{\text{new}}^2 \frac{dx_{\text{new}}}{d\lambda}$, where λ is the affine parameter along the geodesic. In (Hubeny, 2012), it was found that in pure AdS_3, the temporal and angular distances are given in terms of the two conserved quantities by

$$\cos(\Delta t_{\text{new}}) = \frac{L^2 - E^2 + 1}{\sqrt{(L^2 - E^2 + 1)^2 + 4E^2}}, \tag{2.4.3}$$

$$\cos(\Delta x_{\text{new}}) = \frac{L^2 - E^2 - 1}{\sqrt{(L^2 - E^2 - 1)^2 + 4L^2}}. \tag{2.4.4}$$

From which one can solve for E and L. Using these E and L, we compute the regulated length of the spacelike geodesic (Hubeny, 2012) in Appendix A.4.2.1

$$\mathcal{L}_{\text{reg}} = -\log\sqrt{(E^2 - L^2 + 1)^2 + 4L^2} + \log(4R_{\text{new},1}R_{\text{new},2}) \tag{2.4.5}$$

$$= \log\left[4\left|\sinh\left(\frac{1}{2}(w_{\text{new},1} - w_{\text{new},2})\right)\,\sinh\left(\frac{1}{2}(\overline{w}_{\text{new},1} - \overline{w}_{\text{new},2})\right)\right|\right] + \log(R_{\text{new},1}R_{\text{new},2})\,, \tag{2.4.6}$$

where $\log(4R_{\text{new},1}R_{\text{new},2})$ is the universal diverging piece. From (2.3.3), we have for the large-radius cutoff

$$R_{\text{new},i} = \frac{R_i}{\sqrt{\frac{\partial w_{\text{new},i}}{\partial w_i}\frac{\partial \overline{w}_{\text{new},i}}{\partial \overline{w}_i}}}, \tag{2.4.7}$$

where $i = 1, 2$ labels the two large-radius cutoffs near the two endpoints of the geodesic. With (2.4.7), the holographic entanglement entropy is:[14]

$$S_A = \frac{\mathcal{L}_{\text{reg}}}{4G_N} = \frac{c}{6}\log\left[4\frac{\left|\sinh\left(\frac{1}{2}(w_{\text{new},1}-w_{\text{new},2})\right)\ \sinh\left(\frac{1}{2}(\overline{w}_{\text{new},1}-\overline{w}_{\text{new},2})\right)\right|}{\prod_{i=1}^{2}\sqrt{\frac{\partial w_{\text{new},i}}{\partial w_i}\frac{\partial \overline{w}_{\text{new},i}}{\partial \overline{w}_i}}\epsilon_i}\right], \tag{2.4.8}$$

where we have introduced the regularization parameter $\epsilon_i = R_i^{-1}$. One can easily verify that $S_A = S_{A^c}$, which is a property of pure states. An example of the spacelike geodesic computing the holographic entanglement entropy is in Figure 2.6.[15]

2.4.1.2 Match with field theory result

In 1+1 dimensional CFT, the entanglement entropy of a single interval $A = [x_1, x_2]$ can be evaluated from the two-point function of twist operators (Calabrese & Cardy, 2004),

$$S_A = -\lim_{n\to 1}\frac{\partial}{\partial n}\text{Tr}\rho_A^n, \qquad \text{Tr}\rho_A^n \propto \langle \mathcal{T}_n(w_1,\overline{w}_1)\mathcal{T}_{-n}(w_2,\overline{w}_2)\rangle. \tag{2.4.9}$$

[14] Note that as w_{new} is purely imaginary, the terms inside the logarithm are in fact sin functions of t_{new} and x_{new}.

[15] One may wonder what general statements we can make about geodesics computing entropies in these coordinates. Due to the Killing symmetry of AdS_3 discussed in Appendix A.3, a spacelike geodesic whose endpoints are on a constant-t line on the boundary entirely lies on a constant-t slice in the bulk. As the new horizon (2.3.8) is the $t = \infty$ slice and a Killing horizon, any spacelike geodesic is upper bounded by the new horizon. These statements do not continue to hold in the thermal state.

with dimension $h = \overline{h} = \frac{c}{24}(n - \frac{1}{n})$. The time evolution of the two-point function is captured by the $SL(2)$ transformation $(w, \overline{w}) \to (w_{\rm new}, \overline{w}_{\rm new})$:

$$\langle \mathcal{T}_n(w_1, \overline{w}_1)\mathcal{T}_{-n}(w_2, \overline{w}_2)\rangle = \prod_{i=1}^{2} \left(\frac{\partial w_{{\rm new},i}}{\partial w}\right)^h \left(\frac{\partial \overline{w}_{{\rm new},i}}{\partial \overline{w}}\right)^h \langle \mathcal{T}_n(w_{{\rm new},1}, \overline{w}_{{\rm new},1})\mathcal{T}_{-n}(w_{{\rm new},2}, \overline{w}_{{\rm new},2})\rangle. \tag{2.4.10}$$

The two-point function $\langle \mathcal{T}_n(w_{1,\rm new}, \overline{w}_{1,\rm new})\mathcal{T}_{-n}(w_{2,\rm new}, \overline{w}_{2,\rm new})\rangle$ is evaluated following the methods in (Calabrese & Cardy, 2004) but paying close attention to the difference between holomorphic and antiholomorphic parts (see Appendix A.8 for details),

$$\begin{aligned} &\langle \mathcal{T}_n(w_{{\rm new},1}, \overline{w}_{{\rm new},1})\mathcal{T}_{-n}(w_{{\rm new},2}, \overline{w}_{{\rm new},2})\rangle \\ &= \left[4 \sinh\left(\frac{1}{2}(w_{{\rm new},1} - w_{{\rm new},2})\right) \sinh\left(\frac{1}{2}(\overline{w}_{{\rm new},1} - \overline{w}_{{\rm new},2})\right)\right]^{-2h}, \end{aligned} \tag{2.4.11}$$

where

$$w_{\rm new} = \tau_{\rm new} + i x_{\rm new}, \qquad \overline{w}_{\rm new} = \tau_{\rm new} - i x_{\rm new}\,. \tag{2.4.12}$$

Substituting (2.4.11) into (2.4.10) and then into (2.4.9) and performing the analytic continuation $\tau_{\rm new} \to i t_{\rm new}$, the CFT entanglement entropy is then

$$S_A = \frac{c}{6} \log\left[\frac{4\left|\sinh\left(\frac{1}{2}(w_{{\rm new},1} - w_{{\rm new},2})\right) \sinh\left(\frac{1}{2}(\overline{w}_{{\rm new},1} - \overline{w}_{{\rm new},2})\right)\right|}{\prod_{i=1}^{2}\sqrt{\frac{\partial w_{{\rm new},i}}{\partial w_i}\frac{\partial \overline{w}_{{\rm new},i}}{\partial \overline{w}_i}}\epsilon_i}\right], \tag{2.4.13}$$

where we have introduced the UV cutoff ϵ_i. The terms multiplying ϵ_i in the denominator in (2.4.13) come from the Jacobian factors in (2.4.10). The field theory

calculation (2.4.13) precisely matches our earlier holographic result (2.4.8).[16]

2.4.2 Gravity dual of SSD: thermal state

2.4.2.1 Holographic computations

The metric (2.3.2) has two conserved quantities, $E = (r_{\rm new}^2 - r_+^2)\frac{dt_{\rm new}}{d\lambda}$ and $L = r_{\rm new}^2 \frac{dx_{\rm new}}{d\lambda}$, where λ is the affine parameter along the geodesic. We will focus on the region outside the BTZ horizon, $r > r_+$. In Appendix A.4.2.2, we calculated the temporal and angular separation of the two endpoints of the spacelike geodesic

$$\cosh(r_+\Delta t_{\rm new}) = \frac{L^2 - E^2 - r_+^2}{\sqrt{(L^2 - E^2 - r_+^2)^2 - 4r_+^2E^2}}, \tag{2.4.14}$$

$$\cosh(r_+\Delta x_{\rm new}) = \frac{L^2 - E^2 + r_+^2}{\sqrt{(L^2 - E^2 + r_+^2)^2 - 4r_+^2L^2}}, \tag{2.4.15}$$

where $L \geq E + r_+$ so that the spacelike geodesic does not enter the BTZ horizon (see Appendix A.4.2.2 for details).[17] Therefore one can solve for E and L. Using these E and L, we computed the regulated length of the spacelike geodesic in Appendix A.4.2.2.

$$\mathcal{L}_{\rm reg} = -\log\sqrt{(L^2 - E^2 + r_+^2)^2 - 4r_+^2L^2} + \log(4R_{\rm new,1}R_{\rm new,2}) \tag{2.4.16}$$

$$= \log\left[\left(\frac{2}{r_+}\right)^2 \left|\sin\left(r_+\frac{w_{\rm new,1} - w_{\rm new,2}}{2}\right)\,\sin\left(r_+\frac{\overline{w}_{\rm new,1} - \overline{w}_{\rm new,2}}{2}\right)\right|\right] + \log(R_{\rm new,1}R_{\rm new,2}). \tag{2.4.17}$$

For the BTZ black hole, the radius and inverse temperature are related via $r_+ = 2\pi/\beta$. The large-radius cutoff is the same as (2.4.7). The holographic entanglement

[16] Note, however, that the field theory result is valid for *generic* CFTs, while our holographic result is limited to *holographic*, i.e. large c, large gap CFTs only.

[17] Note that if one sets the BTZ black hole radius $r_+^2 = -1$ and hence replaces $\cosh$ with $\cos$ in (2.4.14) and (2.4.15), one recovers (2.4.3) and (2.4.4) in pure AdS_3, respectively.

entropy is:[18]

$$S_A^{(1)} = \frac{\mathcal{L}_{\text{reg}}}{4G_N} = \frac{c}{6}\log\left[\frac{\left(\frac{\beta}{\pi}\right)^2\left|\sin\left(\frac{\pi}{\beta}(w_{\text{new},1}-w_{\text{new},2})\right)\,\sin\left(\frac{\pi}{\beta}(\overline{w}_{\text{new},1}-\overline{w}_{\text{new},2})\right)\right|}{\prod_{i=1}^{2}\sqrt{\frac{\partial w_{\text{new},i}}{\partial w_i}\frac{\partial \overline{w}_{\text{new},i}}{\partial \overline{w}_i}}\epsilon_i}\right]. \tag{2.4.18}$$

Where the meaning of the superscript (1) will be clear in later subsections. $S_A^{(1)}$ and $S_{A^c}^{(1)}$ are not equal, as the state is no longer pure but thermal. An example of the spacelike geodesic computing the holographic entanglement entropy is in the left plot of Figure 2.7.

2.4.2.2 Non-equal-time entanglement plateau

As is reviewed in section 1.2.5, an important phenomenon of holographic entanglement entropy in thermal states with finite spatial regions is the entanglement plateaux. Here, the entanglement plateaux take place in a non-equal-time setup, which is a straightforward generalisation of (Hubeny et al., 2013): in addition to the connected minimal surface (see the red curve in the right plot of Figure 2.7) that computes (2.4.18), there is also a *disconnected* minimal surface, given by the *union* of the minimal surface for A^c (i.e. Δt_{new} stays the same while Δx_{new} becomes the complementary value $2\pi - \Delta x_{\text{new}}$, see the green curve in the right plot of Figure 2.7) and the bifurcation surface of the event horizon.[19] The holographic entanglement entropy is then computed by,

$$S_A = \min\{S_A^{(1)}, S_A^{(2)}\}, \tag{2.4.19}$$

[18] Note that as w_{new} is purely imaginary, the terms inside the logarithm are in fact $\sinh$ functions of t_{new} and x_{new}.

[19] The bifurcation surface is minimal in all static black hole geometries (Hubeny et al., 2013).

where $S_A^{(1)}$ is given by (2.4.18), and

$$S_A^{(2)} = \frac{2\pi^2 c}{3\beta} + \frac{c}{6}\log\left[\left(\frac{\beta}{\pi}\right)\frac{\left|\sinh\left[\frac{\pi}{\beta}((t_{\mathrm{new},1}-t_{\mathrm{new},2})+(2\pi-(x_{\mathrm{new},1}-x_{\mathrm{new},2}))\right]\right|}{\prod_{i=1}^{2}\sqrt{\frac{\partial w_{\mathrm{new},i}}{\partial w_i}\epsilon_i}}\right]$$
$$+\frac{c}{6}\log\left[\left(\frac{\beta}{\pi}\right)\frac{\left|\sinh\left[\frac{\pi}{\beta}((t_{\mathrm{new},1}-t_{\mathrm{new},2})-(2\pi-(x_{\mathrm{new},1}-x_{\mathrm{new},2}))\right]\right|}{\prod_{i=1}^{2}\sqrt{\frac{\partial \overline{w}_{\mathrm{new},i}}{\partial \overline{w}_i}\epsilon_i}}\right]. \tag{2.4.20}$$

The plateau phenomenon in thermal SSD quench was first proposed in (Goto et al., 2021). We remark that while our results are qualitatively similar, our holographic construction is quantitatively different, as the holographic entanglement entropy is computed by spacelike geodesics anchoring on the boundary at non-equal times.

2.4.2.3 Holographic cooling/heating effect

To further understand the time-evolution of holographic entanglement entropy, let us first note that the endpoints of the interval $t_{\mathrm{new},i}$ and $x_{\mathrm{new},i}$ $(i=1,2)$ can flow to the top tip of the triangle (2.2.12) from the same or different side, depending on whether A includes the fixed point $x=0$ or not.

- If A does not include $x=0$, $(t_{\mathrm{new},1}, x_{\mathrm{new},1})$ and $(t_{\mathrm{new},2}, x_{\mathrm{new},2})$ flow to the top tip of the triangle from the *same* side, and $|x_{\mathrm{new},1}-x_{\mathrm{new},2}| \to 0$ in (2.4.18). See the left plot of Figure 2.7. Therefore, $S_A^{(1)}$ is always smaller than $S_A^{(2)}$, so we have $S_A = S_A^{(1)}$ at all $t>0$. At late-time, one can show (Goto et al., 2021) that S_A is given by the *vacuum* entanglement entropy,

$$S_A = S_A^{(1)} \to \frac{c}{3}\log\left[2\left(\sin\frac{1}{2}(x_2-x_1)\right)\right]. \tag{2.4.21}$$

- If A includes $x = 0$, $(t_{\text{new},1}, x_{\text{new},1})$ and $(t_{\text{new},2}, x_{\text{new},2})$ flow to the top tip of the triangle from *different* sides, making $|x_{\text{new},1} - x_{\text{new},2}| \to 2\pi$ in (2.4.18). At some point, therefore, the entanglement entropy switches from $S_A^{(1)}$ to $S_A^{(2)}$. See the right plot of Figure 2.7. At late time, the second and third terms in (2.4.20) become much smaller than the first term,[20] so that S_A is dominated by the *thermal* entanglement entropy,

$$S_A = S_A^{(2)} \to S_\rho = \frac{2\pi^2 c}{3\beta} \,. \tag{2.4.22}$$

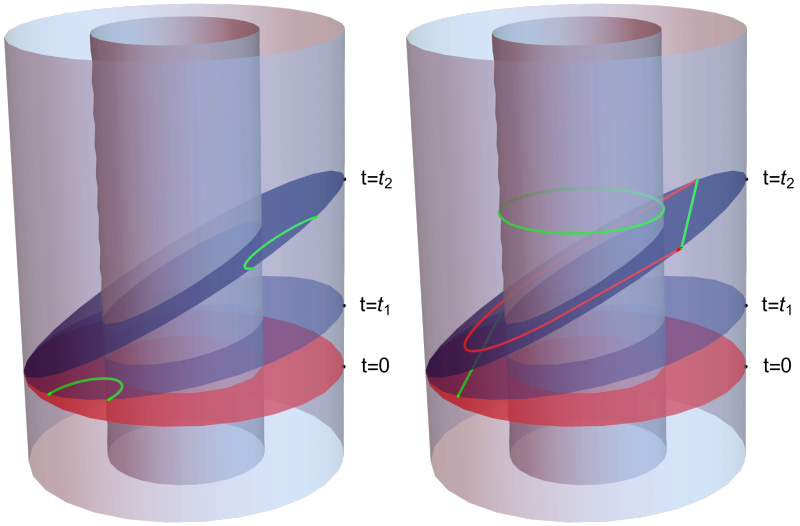

Figure 2.7: Non-equal time spacelike geodesics in BTZ geometry. The two geodesic endpoints flow towards the top tip of the triangle (π, π) as t evolves, from either the same (left) or different (right) side. In the latter case, at late time, the minimal surfaces computing holographic entanglement entropy switches from the red surface homologous to A to the union of the green surface homologous to A^c and the bifurcation surface of the black hole horizon (also coloured in green).

.

We conclude that whether the entanglement entropy cools down to the vacuum value or heats up and eventually reaches thermal value has a simple geometric

[20] For this the time has to compensate the smallness of the cutoff ϵ_i.

interpretation in the bulk, which is whether the spacelike geodesic computing the holographic entanglement entropy winds around the BTZ black hole or not at late time. Again, (2.4.21) and (2.4.22) match the results in (Goto et al., 2021) qualitatively, albeit the setup is quantitatively different.

2.4.2.4 Comparison with field theory result on a line

Computing the entanglement entropy of 1+1 dimensional CFT on a finite interval at finite temperature β is difficult. However, one can compare the holographic result (2.4.18) with that of the thermal state of CFT_2 on a line. This CFT result can be obtained by Wick rotating $w_{\text{new}} \to i w_{\text{new}}$ and rescaling $2\pi \to \beta$ the cylinder that computes (2.4.13) (see Appendix A.8 for details),

$$S_A = \frac{\mathcal{L}_{\text{reg}}}{4G_N} = \frac{c}{6} \log \left[\frac{\left(\frac{\beta}{\pi}\right)^2 \left| \sin\left(\frac{\pi}{\beta}(w_{\text{new},1} - w_{\text{new},2})\right) \sin\left(\frac{\pi}{\beta}(\overline{w}_{\text{new},1} - \overline{w}_{\text{new},2})\right) \right|}{\prod_{i=1}^{2} \sqrt{\frac{\partial w_{\text{new},i}}{\partial w_i} \frac{\partial \overline{w}_{\text{new},i}}{\partial \overline{w}_i}} \epsilon_i} \right] . \tag{2.4.23}$$

This result matches with the holographic result $S_A^{(1)}$ before the switch in the dominant extremal surface (2.4.20). In (Asplund, Bernamonti, Galli, & Hartman, 2015b), it is explained that the coincidence of (2.4.18) and (2.4.23) is due to properties of large-c Virasoro identity blocks arising from a CFT calculation obtaining entanglement entropy from four point functions with two heavy and two light operators of the cyclic orbifold $\text{CFT}^n/\mathbb{Z}_n$. In particular, the identity block in the dominant channel corresponds to the spacelike geodesic computing (2.4.18).

3 | The entanglement membrane in 2d CFT: reflected entropy and RG flow

In this chapter, we present holographic studies of the entanglement dynamics of 2d CFTs and their deformations. We derive a generalised membrane with an additional scalar degree of freedom, that we will represent in figures as a colour, on its worldline as an effective theory of entanglement dynamics in 2d CFT. We show that upon adding a relevant deformation to the CFT, this additional degree of freedom gets "gapped out" and we recover the entanglement membrane with non-degenerate membrane tension. This dichotomy is analogous to how hydrodynamics emerges from holomorphic stress tensor dynamics once a 2d CFT is deformed by a relevant operator (Davison & Delacretaz, 2024). These observations make us speculate that the additional degree of freedom on the generalised membrane worldline is capturing the infinite-dimensional symmetry charge dynamics of 2d CFT.[1]

We also show that the reflected entropy, that is computed holographically by the entanglement wedge cross section (EWCS), is also captured by the generalised membrane in 2d CFT, and that this quantity, in contrast to entanglement entropy, is not captured by the ordinary membrane with degenerate membrane tension. To complete our investigations, we also study the reflected entropy in higher dimensional CFTs, and demonstrate that the ordinary membrane correctly captures them.

[1] An additional evidence in this direction is the aforementioned failure of the ordinary membrane to capture the Rényi entropy for multiple intervals, since Rényi entropy should be more sensitive to the conserved charge dynamics. See evidence in this direction in Refs. (Rakovszky, Pollmann, & von Keyserlingk, 2019; Huang, 2019; Žnidarič, 2020; Rakovszky, Pollmann, & von Keyserlingk, 2020).

3.1 Entanglement membrane and 2d CFT

From the reviews in section 1.3.3, we see that for the $d = 2$ BTZ black hole, we get $c(z) = 1$, which either enforces $\dot{x}^2 = 1$ or signals the breakdown of the scaling Ansatz. Indeed, two-sided geodesics reach e^{Λ} depths inside the BTZ black hole (Hartman & Maldacena, 2013). Then a different scaling can be applied: let us define $z \equiv e^{\xi}$ and scale ξ, u, x linearly with Λ. The resulting action in the $d = 2$ BTZ black hole is

$$\begin{aligned} S &= s_{\text{th}} \int du \sqrt{1 + \frac{\dot{x}^2 - 1 - 2\dot{z}}{z^2}} \\ &= s_{\text{th}} \int du \left[1 + \frac{d(e^{-\xi})}{du} + \frac{1}{2} e^{-2\xi} (\dot{x}^2 - 1 - \dot{\xi}^2) + \dots \right] . \end{aligned} \tag{3.1.1}$$

We note that to leading order the action is simply given by the difference in infalling times u. All curves that obey the scaling assumptions and stretch between the same endpoints have the same leading order action. The shape of the curves is determined by the $e^{-2\xi}$ term (since the $e^{-\xi}$ term is a total derivative). We can think of (3.1.1) as a generalised membrane theory, where besides the membrane shape $x(u)$ there is an extra degree of freedom $\xi(u)$ that lives on the membrane. Of course, we have not done much compared to the HRT prescription: $\xi(u) = \log z(u)$ is the logarithm of the bulk depth, and we expanded for large ξ, u, x.

Since irrespective of the value of ξ or the membrane shape we get the same value for the entropy, one may question the utility of the above exercise: to obtain the entropy we could just as well use the ordinary membrane theory with $\mathcal{E}(v) = 1$. However, we will show how ξ plays an essential role in computing the reflected entropy in 2d CFT. We will also analyse how the membrane theory arises in an RG flow from a 2d CFT, by gapping out the ξ degree of freedom, which then can be integrated out, leaving us with a local theory for $x(u)$, the membrane shape.

3.1.1 The entanglement membrane shape for a half space

The membrane shape is determined from the effective Lagrangian

$$\mathcal{L}_{\text{eff}} = \frac{1}{2}\, e^{-2\xi}(\dot{x}^2 - 1 - \dot{\xi}^2)\,. \tag{3.1.2}$$

derived from (3.1.1). The momentum $p = e^{-2\xi}\,\dot{x}$ is conserved and the ξ equation of motion is

$$\ddot{\xi} = -1 + \dot{\xi}^2 + p^2 e^{4\xi}\,, \tag{3.1.3}$$

which motivates us to introduce $p \equiv e^{-2\xi_p}$. We can understand the gross features of the solutions that stay in the large ξ region for long u as follows: For $\xi < \xi_p$ the $p^2e^{4\xi}$ term is negligible, and the solution is $\xi(u) = u$ with exponentially small corrections. Once this curve reaches the vicinity of ξ_p it transitions to the solution $\xi(u) = \xi_p$ with exponentially small corrections. The transition between the two behaviours is abrupt and can be neglected in the scaling regime. All of these statements can be verified by straightforward numerical solutions of (3.1.3). It turns out that (3.1.3) can also be solved in closed form, see Appendix B.1.1; the exact solution also confirms the above approximations in the large T, large X limit. Finally, since the BTZ black brane is AdS_3 with some identifications, we are studying AdS_3 geodesics in disguise: this perspective is developed in Appendix B.2.4..

In summary we find (when $T > X$)

$$(x(u), \xi(u)) = \begin{cases} (-X, T+u) & -T < u < -X\,, \\ (u, T-X) & -X < u < X\,, \\ (X, T-u) & X < u < T\,, \end{cases} \tag{3.1.4}$$

where we used the result $\xi_p = T - X$ obtained from matching to boundary conditions. See Fig. 3.1 (left) for a plot of (3.1.4). In this and subsequent figures we plot the membrane shape $u(x)$ and visualise the extra degree of freedom ξ on the membrane worldline with a colour interpolating between blue ($\xi = 0$) to orange ($\xi = \xi_p$). In Fig. 3.1 we also plotted $\xi(x)$ with green, which is redundant information. Also in plots we will always take the time and space extents to be $T\Lambda$ and $X\Lambda$ with $T, X = O(1)$ and $\Lambda \to \infty$.

The corresponding operator entanglement entropy is

$$S_{\text{op}} = s_{\text{th}}\, 2T\,, \tag{3.1.5}$$

which simply follows from the extent of the generalised membrane in u, see the discussion below (3.1.1). In mapping the HRT surface to the boundary generalised membrane, we have to decide when to switch from the right to the left infalling time. It does not matter at what exact point we switch, as long as the HRT surface is not at or very close to the horizon, see a detailed analysis in (Mezei, 2017). The right and left time extents of the membrane then add up to $2T$.[2]

[2]A good choice is to switch between the two sides, when the HRT surface reaches the deepest point behind the horizon z_*. If we parametrise the membrane in boundary polar coordinates as $r(u, \Omega)$, then generically the switch will happen at different locations as we move in polar angle, $u_{\text{switch}}(\Omega)$, so the mapping will be dependent on the subsystem through the membrane shape. A simpler choice would be to switch at $u = 0$, but this choice is not time translation invariant, and under large time shifts (corresponding to boosts in the near-horizon region) it leads to the switch happening in the problematic near-horizon region.

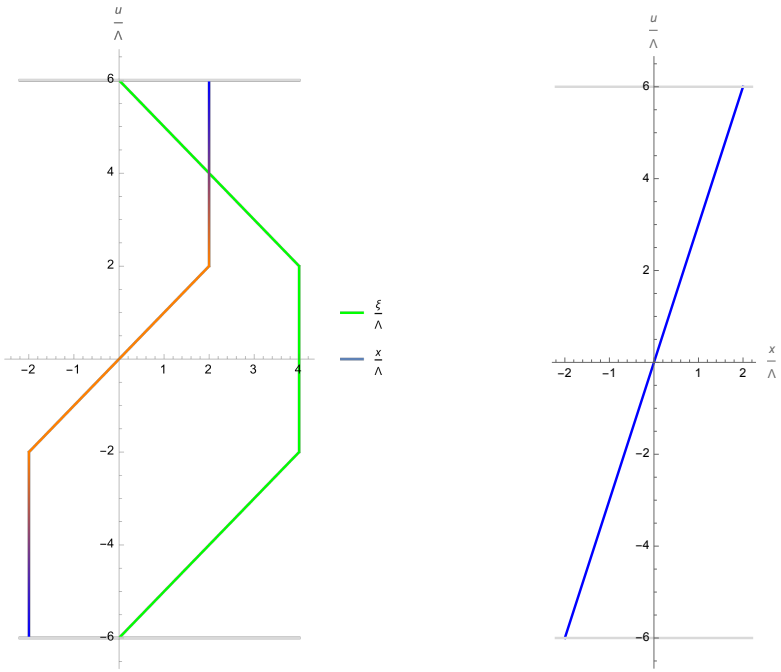

Figure 3.1: *Left*: A plot of $x(u)$ and $\xi(u)$ (green) in (3.1.4) in the scaling, i.e. large Λ limit in generalised membrane theory. The light gray horizontal lines denote $u = \pm T\Lambda$. As for $x(u)$, we use blue $\to$ orange to denote the increase in the bulk depth in ξ. *Right*: A plot of the membrane shape function (3.1.6) in planar AdS$_{d+1}$-Schwarzchild black brane ($d \geq 2$), with $v = \frac{1}{3}$. The membrane is of uniform blue colour as it stays at a constant $z \in O(1)$ at late time.

It is instructive to compare the generalised membrane theory equations of motion (3.1.4) to that in the ordinary membrane theory (Mezei, 2018), where the HRT surface is described solely by the membrane shape function $x(u)$, since the bulk z degree of freedom can be integrated out. For the two-sided entanglement entropy in half spaces offset by $2X$ ($v_B T > X$), the membrane shape is a straight line of slope v (Jonay et al., 2018; Mezei, 2018)

$$x(u) = vu\,, \qquad\qquad v = \frac{X}{T} \in [0, v_B)\,. \tag{3.1.6}$$

The comparison between ordinary (3.1.6) and generalised (3.1.4) membrane theory is illustrated in Fig. 3.1. The corresponding operator entanglement entropy however should not differ between the generalised and ordinary membrane prediction, which is (Jonay et al., 2018; Mezei, 2018)

$$S_{\text{op}} = s_{\text{th}}\, 2T\, \mathcal{E}(v)\,. \tag{3.1.7}$$

For the degenerate membrane tension $\mathcal{E}(v) = 1$ this indeed agrees with (3.1.5).

So far we have focused on the $T > X$ case. When $T < X$, one can show that ξ is small, i.e. the geodesic goes just inside the horizon. As z is no longer large, the effective action (3.1.1) is no longer valid. In the discussion above (3.1.1) we

There is one extra subtlety: there exist HRT surfaces that live entirely or partly (for some region of Ω) in the near-horizon region. Hence they never reach z_* and the above switch procedure is not well-defined for them. These membranes or membrane sections have $v = v_B$, which maps to the near-horizon region $z = 1$. In these cases we use the $u_{\text{switch}} = \text{const}$ switch, with the constant set by continuity in Ω or if the entire membrane has $v = v_B$ we set $u_{\text{switch}} = -T, 0, T$ depending on what looks most natural, see Fig. 3.2. This choice however cuts out some portion of the HRT surface, which we need to account for to correctly compute the entropy. We glue in a horizontal membrane for this portion. This rule is consistent, because $\mathcal{E}(v_B)/v_B = 1$. It is also natural from the circuit perspective, where it corresponds to a horizontal cut of legs (Jonay et al., 2018). See the first membrane in Fig. 3 in (Mezei, 2018) for illustration. Unfortunately, the last membrane on that figure, corresponding to saturation is misleading: we explain below that saturated membranes are more naturally v_B cones.

encountered the possibility that $z = O(1)$ and $\dot{x}^2 = 1$, and this is exactly the HRT surface we need for $T < X$. This conclusion is also supported by the exact BTZ geodesics as shown in Appendix B.2.4. The membrane mapping of this HRT surface is a a bit unnatural, see Fig. 3.2, as we need to include a horizontal membrane section between sections of $v = v_B = 1$ ones. We can add this section at arbitrary positions, and all of these shapes map to the same HRT surface in the bulk. See footnote 2 for an explanation.[3] The corresponding operator entanglement is:

$$S_{\text{op}} = s_{\text{th}}\, 2X\,, \tag{3.1.8}$$

in agreement with earlier results in (Jonay et al., 2018; Mezei, 2018).

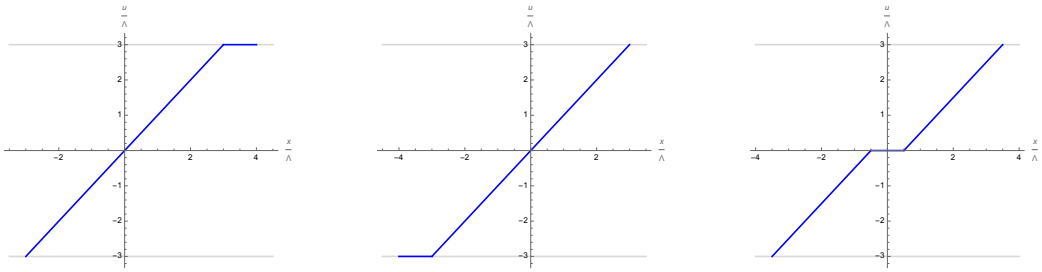

Figure 3.2: Equivalent membranes computing the operator entanglement for $T < X$ in the scaling limit. Here we plotted for $T = 6\Lambda$ and $X = 7\Lambda$. The membranes are in blue, as the corresponding HRT surface is in the near-horizon region.

3.1.2 Membranes for saturated strips

The displaced half space discussion is easily generalised for displaced intervals of width D. In this case there are two candidate HRT surfaces or equivalently

[3] For this setup, it may seem more natural from the bulk point of view to extend the time extent of spacetime from $2T$ to $2X$, and then the membrane would be a straight $v = 1$ line. However, such a choice would lead to a very convoluted membrane mapping for more complicated shapes in higher dimensions. To us, the addition of horizontal membrane segments produces the most intuitive membrane theory.

generalised membranes: the first is the doubling of the HRT surface corresponding to displaced half spaces and it connects the interval endpoints on the two sides, the second is a static RT surface that connects the interval endpoints on the same sides. For early times $T < D$, the first is minimal, and for late times $T > D$ the second becomes dominant, leading to the saturation of operator entanglement entropy. In this section we discuss the static RT surface and its membrane equivalent.

We show the derivation in detail, as the mapping of the near-horizon region to the membrane was not considered with enough care in prior literature. We consider static RT surfaces outside the horizon on a constant Schwarzschild time slice $t = T$.[4] We can choose a coordinate system such that our two boundary endpoints are symmetric at $\left(\pm \frac{D}{2}, T \right)$.[5] The static geodesic on the $t = T$ slice in BTZ is depicted in Fig. 3.3 (see Appendix B.2.5 for the explicit expressions). We observe that the geodesic roughly consists of two parts: a *plateau*,[6] where it lies close to the horizon $z = 1$ and moves transversely; and two regions where it *shoots* from the near-horizon region towards the conformal boundary $z = 0$.

The static curve shown in Fig. 3.3 is on the constant Schwarzschild time slice $t = T$. In (generalised) membrane theory, however, we would like to understand the projection of this RT surface to the boundary along constant infalling time. In $d = 2$, the infalling time u along the static geodesic on the $t = T$ slice is given by

[4]The Schwarzschild time t in the geometry (1.3.12) is defined as

$$t = u + \int_0^z \frac{dz'}{a(z')b(z')}. \tag{3.1.9}$$

[5]To study the static geodesic only, it is easiest to set $T = 0$ as its geometry does not change with time.

[6]Throughout this paper, we use the word “plateau" to refer the portion of the HRT surface that stays at constant z (either inside or outside the horizon) in the scaling limit.

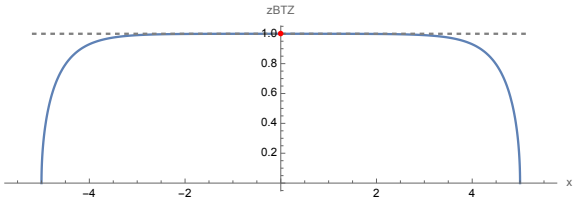

Figure 3.3: Plot of the static spacelike geodesic on the $t = T$ slice. The dashed gray line is the black hole horizon. The geodesic consists of a plateau and two parts that shoot towards the conformal boundary. The red dot denotes the deepest point $\tanh \frac{D}{2}$ the geodesic can reach in the bulk.

(see Appendix B.2.1)

$$\begin{aligned} u(z) &= T - \text{arctanh} z \\ &\to T + \frac{1}{2}\log\frac{1-z}{2}, \quad (z \to 1^-). \end{aligned} \tag{3.1.10}$$

Notice that $u(z) \to -\infty$ as $z \to 1^-$. Therefore, close to the horizon, a small shift in z leads to a large shift in u. This shift then leads to a finite difference between infalling and Schwarzschild time. See Fig. B.7 in Appendix B.2.5 for an illustration of the geodesic in Fig. 3.3 in infalling coordinates.

The explicit projection of the static geodesic shown in Fig. 3.3 to the boundary along constant infalling time is given by (see Appendix B.2.5 for details)

$$u(x) \approx \begin{cases} x + T - \dfrac{D}{2} - \log 2, & x > 0\,, \\ -x + T - \dfrac{D}{2} - \log 2, & x < 0\,, \end{cases} \tag{3.1.11}$$

where we kept the subleading $\log 2$ term to get a more accurate match on Fig. 3.4. We see that the projection is a *cone* with slope ± 1, as is depicted in Fig. 3.4. Notice that the majority of the cone comes from the projection of the plateau part of the geodesic; the parts that shoot exponentially towards the boundary are projected to the two blunt corners. The latter is because when $z \to 0$, arctanh$z$ is small, so $u(z)$

is close to T. Notice also that the tip of the cone is blunt in a region vanishingly small in the scaling limit, and hence is not captured by (3.1.11).

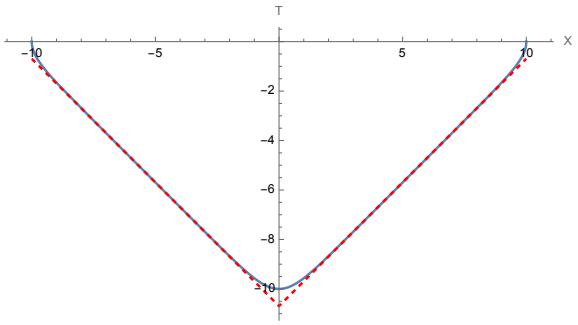

Figure 3.4: Projection of the static RT surface (see (B.2.62) and (B.2.63) for explicit expressions) to the boundary along constant infalling time. In the scaling limit, the projection is a cone of slope ± 1 (3.1.11), which are depicted here as dashed red lines. Notice that its two corners and tip are all blunt.

3.2 Reflected entropy from the entanglement wedge cross section in 2d CFT

The generalised membrane theory and the ordinary membrane theory results with degenerate membrane tension $\mathcal{E}(v) = 1$ predict the same entropy evolution in quenches and for operator entanglement. However, in this and the next section we show that the two give drastically different predictions for reflected entropy: it is the generalised membrane theory computes it correctly for 2d CFTs.

3.2.1 Setup of the problem

In order to study the time evolution of the entanglement wedge cross-section, we consider a bipartite system consisting of the union of two strips: $A \cup B = [0, \ell] \cup [\ell + D, \infty)$. As initial state, we consider $|\psi_0\rangle = e^{-\frac{\beta}{4}H} |B\rangle$, where $|B\rangle$ is a conformal boundary state (Calabrese & Cardy, 2005). The time evolution

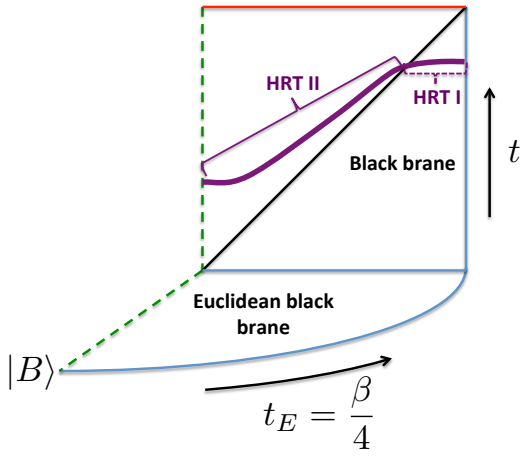

Figure 3.5: The end-of-the-world (EoW) brane quench setup, with initial state $|\psi_0\rangle = e^{-\frac{\beta}{4}H}|B\rangle$, where $|B\rangle$ is a conformal boundary state.

of such a system is described holographically by a one-sided black hole with an end-of-the-world (EoW) brane (Hartman & Maldacena, 2013)[7]. The location of the EoW brane in infalling time is

$$u_{\text{EoW}}(z) = \frac{i\pi}{a'(1)b(1)} - \int_0^z \frac{dz'}{a(z')b(z')}\,. \tag{3.2.1}$$

see Figure 3.5 for an illustration.

The reflected entropy was first studied in this setup in (Kudler-Flam et al., 2020), where three computations were presented: a 2d CFT and the holographic calculation using BTZ geodesics gave agreement, and these were reproduced by a heuristic membrane picture. In what follows, we will reproduce the results of (Kudler-Flam et al., 2020) using the generalised membrane theory, and explain how it is related to their heuristic membrane picture. The main novelty in our treatment is the introduction of a generalised membrane characterising the equilibrium EWCS (section 3.2.3), which describes a spacelike geodesic in BTZ that contains a portion

[7]Another well-known set-up is that of a black hole form from the collapse of null dust, described by the Vaidya geometry. The evolution of the EWCS in this scenario has been studied in (Babaei Velni, Mohammadi Mozaffar, & Vahidinia, 2020, 2023).

that is null in the scaling limit.[8] The computations will build on the results on half-space entanglement discussed in section 3.1.

The case $\ell < D$ is uninteresting for our purposes since its entanglement wedge is always disconnected. Hence we will focus on the $\ell > D$ case. The possible extremal surfaces computing the entanglement entropy are shown in Fig. 3.6. At early times, the entanglement wedge is disconnected, and so the cross section simply vanishes. At time $t = \frac{D}{2}$, there is a transition to a connected entanglement wedge. Our main goal here will be to characterise the dynamics of the EWCS in this scenario.

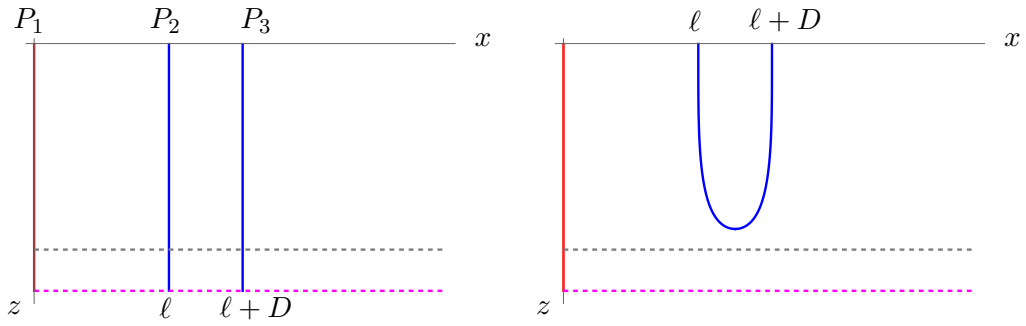

Figure 3.6: HRT and RT surfaces for the interval $[0, \ell] \cup [\ell + D, \infty)$. In the plot, P_1, P_2 and P_3 are on the AdS boundary at some given time t, with x coordinates being 0, ℓ and $\ell + D$, respectively. The black dashed line indicates the horizon, while the magenta line corresponds to the end-of-the-world brane, see Figure 3.5. In the right graph, the non-equilibrium HRT surface and equilibrium RT surface are plotted in red and blue, respectively.

In time-dependent scenarios there are multiple extremal surfaces bisecting the entanglement wedge and, in order to correctly capture the EWCS, one must select the surface with minimal area. For our configuration, the possible surfaces are depicted in Fig. 3.7.

[8] If extended beyond the HRT surface it ends on, it reaches the BTZ singularity (Appendix B.3.2).

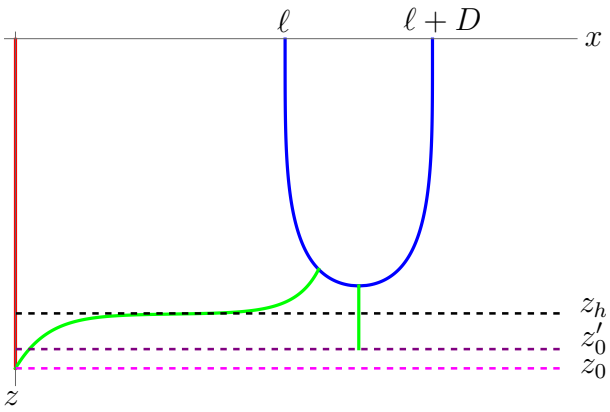

Figure 3.7: Possible non-vanishing entanglement wedge cross sections (green). Since these curves move in time, they may encounter the EoW brane at different z's, which itself is moving according to (3.2.1).

3.2.2 Non-equilibrium EWCS

At $t \geq \frac{D}{2}$, the two HRT surfaces starting from P_2 and P_3 saturate to an RT surface connecting the two points, see Fig. 3.6. The projection of this RT surface is therefore a cone of height $\frac{D}{2}$. The EWCS starts from this RT surface, enters the black hole horizon, and ends on the EoW brane in the interior. The stretch of the spacelike interior time direction (Hartman & Maldacena, 2013) then leads the EWCS to grow in time. The EWCS can also be described by the effective Lagrangian method described in section 3.1.1. The symmetry of the problem indicates the EWCS to be a vertical line starting from the tip of the RT surface, where $u = T - \frac{D}{2}$. Thus, we have $X = 0$ and $T \to T - \frac{D}{2}$ in (3.1.4). The time-dependent EWCS is described by

$$(x(u), \xi(u)) = \left(\ell + \frac{D}{2}, T - \frac{D}{2} - u\right). \tag{3.2.2}$$

See Fig. 3.8. Therefore, the length of the EWCS is $T - \frac{D}{2}$, which starts from 0 at $T = \frac{D}{2}$ and grows linearly in time with slope $v_E = 1$.

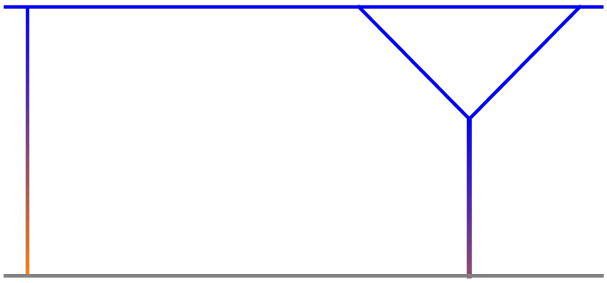

Figure 3.8: Projection of non-equilibrium EWCS in $d = 2$ along constant infalling time in the scaling limit, for $T = 1.2\Lambda$, $\ell = 1.5\Lambda$, and $D = \Lambda$. We use blue $\to$ orange to denote the increase in the bulk depth in ξ, and plot the EWCS as thick to contrast with HRT. The non-equilibrium EWCS starts from the top tip of the projection of the static RT surface, and then enters the interior where its length grows linearly in time. The non-equilibrium EWCS ends perpendicularly on the EoW brane, whose location is given by $u = 0$ for large z. We plotted the EoW brane as gray, since HRT and EWCS can end on it at any depth. From this projection, one can easily read off the length of the EWCS to be $T - \frac{D}{2}$. See Fig. B.9 for the full 3d plot.

3.2.3 Equilibrium EWCS

To describe the entanglement wedge cross section, we introduce a section of a generalised membrane that moves negligibly in u with a bit of hindsight.[9] Correspondingly, its contribution to the entropy is zero in the scaling limit. It is describing a portion of an HRT surface that becomes null in the scaling limit. Nevertheless it is important in piecing together the generalised membrane that computes the EWCS.

Since this generalised membrane moves a large amount in the x, ξ directions but only a little in the u direction, it is easier to describe it by changing variable from u to x. Implementing this change of variables in (3.1.3) and using momentum

[9] See Appendix B.3.2 for the exact solution of this problem.

conservation $\dot{x} = e^{2(\xi-\xi_p)}$, we get:

$$\begin{aligned} \xi'' &= 1 - \xi'^2 - e^{4(\xi_p-\xi)}\,, \\ u' &= e^{-2(\xi-\xi_p)}\,. \end{aligned} \tag{3.2.3}$$

where $f' = \frac{df}{dx}$. This set of equations has the following solution that will be relevant for us:[10]

$$(u(x), \xi(x)) = \begin{cases} (u_p, -x + x_0 + \xi_p), & 0 < x < x_0 \\ (x + u_p - x_0, \xi_p), & x_0 < x \end{cases} \tag{3.2.4}$$

where the constants are chosen for later convenience, see Fig. 3.9. To match the two HRT surfaces or generalised membranes, we require that

$$\xi_p + x_0 = T - u_p\,, \qquad \text{to match the non-equilibrium HRT,} \tag{3.2.5}$$

$$(u_p + x_c - x_0, \xi_p) = (T + \ell - x_c, 0)\,, \quad \text{to match the equilibrium HRT,} \tag{3.2.6}$$

where x_c is the connection point between the EWCS and the equilibrium HRT in Fig. 3.9. In (3.2.5), the non-equilibrium HRT is described by half of (3.1.4) with $X = 0$, hence $x(u) = 0$; in (C.1.4), the equilibrium HRT is given by $x = -u+T+\ell$ and $\xi(u) = 0$ (as it is outside the horizon). Only three out of four parameters get determined:

$$\xi_p = 0\,, \qquad u_p = T + \frac{\ell}{2} - x_c\,, \qquad x_0 = x_c - \frac{\ell}{2}\,. \tag{3.2.7}$$

The EWCS is given by the change of u for these generalised membranes

$$\ell(\text{EWCS}) = x_c - x_0 = \frac{\ell}{2}\,. \tag{3.2.8}$$

[10] Generically, there is another kink at some $x = x_1$, but this additional feature will not be needed. One can think of the solution presented below as the $x_1 \to \infty$ special case of the general solution.

$\ell(\text{EWCS})$ is independent of x_c, so each of the generalised membranes correctly computes the EWCS. This degeneracy does not get resolved even if we solve the approximate equations of motion (3.2.3) exactly, as is done in Appendix B.1.2. Once we back off from the large z approximation, subleading terms fix x_c to be $x_c = \ell + \frac{D}{4}$, see Appendix B.3.2 for details.

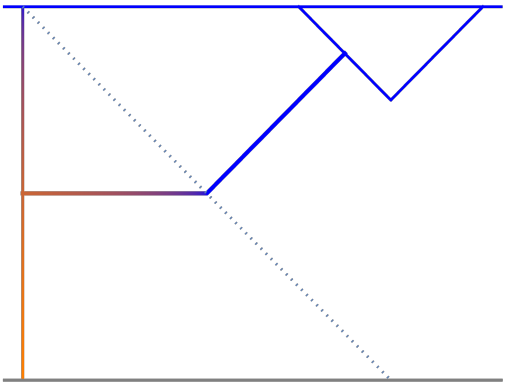

Figure 3.9: Projection of equilibrium EWCS in $d = 2$ along constant infalling time, for $T = 2\Lambda$, $\ell = 1.5\Lambda$, and $D = \Lambda$. We use blue $\to$ orange to denote the increase in the bulk depth in ξ, and plot the EWCS as thick to contrast it with the HRTs. The equilibrium EWCS starts from the mid-point of the projection of static RT surface, enters the horizon, and arrives at a plateau where it moves in x for a distance $\ell/2$. The EWCS then becomes null and shoots deep into the interior, where it meets the HRT surface. Note that at the connection points the colours of the EWCS matches the colours of the HRT surfaces, as required by the boundary conditions. The dotted 45° denotes an alternative projection of the HRT surface along the null generalised membrane, which allows us to match our results with the heuristic picture of 2001.05501. See Fig. B.11 for the full 3d plot.

Our generalised membrane description shown in Fig. 3.9 is different from the heuristic membrane picture of (Kudler-Flam et al., 2020). Recall that in getting Fig. 3.9, we project the bulk HRT surfaces to the boundary along constant infalling time. We can find the connection between our result and that in (Kudler-Flam et al., 2020) by projecting instead along the null generalised membrane in (3.2.4), which amounts to a shift of ξ in the x coordinate compared to projecting along

constant infalling time.[11] Under such a prescription, the horizontal generalised membrane in Fig. 3.9 is projected to a *point*, and the non-equilibrium HRT in the left is projected to the dotted 45° line in Fig. 3.9.[12] The resulting projection then matches with the picture of (Kudler-Flam et al., 2020).[13]

To sum up, in 2d CFT the generalised membrane description of the reflected entropy is given by

$$\frac{S_R}{2} = \begin{cases} 0 & T < \frac{D}{2}\,, \\ T - \frac{D}{2} & \frac{D}{2} < T < \frac{\ell+D}{2}\,, \\ \frac{\ell}{2} & T > \frac{\ell+D}{2}\,. \end{cases} \tag{3.2.9}$$

One can compare (3.2.9) to the exact solution to this problem detailed in Appendix B.3, see Figure 3.10.

3.3 Reflected entropy in the membrane effective theory

In section 3.2 we explored the dynamics of the reflected entropy in the context of $2d$ CFTs. Now, we will show how to describe the corresponding dynamics for the case of $d > 2$. The setup is the same as that in Fig. 3.6, but the equations describing the HRT surfaces and EWCS are different due to the increase in dimensionality. While many of the features explored earlier remain true in higher dimensions, we

[11] Recall that projecting the HRT surfaces to the boundary along constant infalling time is to plot (x, u) on flat spacetime. When projecting along the null generalised membrane, we plot instead $(x + \xi, u)$.

[12] See Fig. B.11 from the exact solution of equilibrium EWCS for a better visualisation.

[13] We find it somewhat unsatisfactory that to make the heuristic picture of (Kudler-Flam et al., 2020) work for the reflected setup $B' \cup A' = (-\infty, -(\ell + D)] \cup [-\ell, 0]$, we would also have to reflect the non-equilibrium membrane, even though it computes the entropy of the complement half-space $(-\infty, 0]$ in a pure state. Relatedly, the mapping from the holographic bulk to the membrane picture would need to be dependent on the EWCS we are interested in computing.

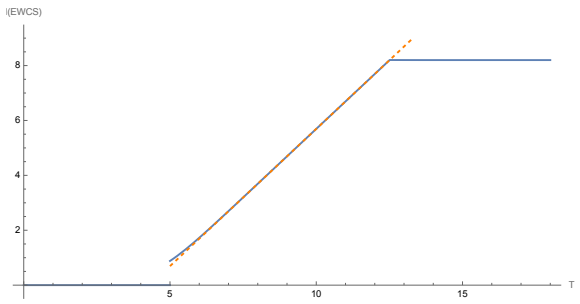

Figure 3.10: Time evolution of EWCS, for $\ell = 15$, and $D = 10$. At early time, the EWCS is 0, as the entanglement wedge is disconnected (Fig. 3.6 left). After $T = \frac{D}{2}$, the RT surface connecting P_2 and P_3 saturates (Fig. 3.6 right), and the EWCS starts to grow linearly with slope 1 in the scaling limit (dashed orange line). Notice that there is a small jump of EWCS length at $T = \frac{D}{2}$; this jump is negligible in the scaling limit. The EWCS then saturates at $\frac{\ell}{2}$ after $T = \frac{\ell+D}{2}$. In the scaling limit, the EWCS dynamics is described by (3.2.9).

also observe some important differences.

While in the preceding sections we only showed computations in the scaling limit that is described by the (generalised) membrane description and relegated finite size computations to appendices, in this section we include finite size numerical computations in the main text, as we believe they may be of methodological interest.

3.3.1 Time evolution of entanglement cross-section

As indicated before, we consider the same configuration as in Fig. 3.6. The evolution of entanglement entropy in this setting was first studied in (Hartman & Maldacena, 2013), and further analysed in (Liu & Suh, 2014b, 2014a; Mezei, 2017; Mezei & Virrueta, 2019).

Following the aforementioned references, we parameterise the equilibrium HRT as $(u_1(z), x_1(z))$. While there is no closed-form solution to the extremisation problem in $d > 2$, we can use reparameterisation invariance and translational symmetry to

express the solutions in terms of integrals as

$$\begin{aligned} u_1(z) &= T - \int_0^z \frac{dz'}{a(z')b(z')}, \\ x_1(z) &= \frac{2\ell + D}{2} + \int_{\tilde{z}}^z \frac{dz'}{b(z')\sqrt{a(z')}} \frac{z'^{d-1}}{\sqrt{\tilde{z}^{2(d-1)} - z'^{2(d-1)}}}\,. \end{aligned} \tag{3.3.1}$$

The parameter $\tilde{z} < 1$ denotes the deepest point reached by the HRT surface in the bulk. This parameter can, in turn, be related to the size of the entangling region by evaluating the integral near the asymptotic boundary, $z = 0$. The boundary time at which the entanglement entropy is evaluated is denoted as T.

The non-equilibrium HRT surface is simply $(u_2(z), 0)$. In this case, reparameterization invariance suffices to solve the extremisation equations as

$$\begin{aligned} u_2(z) &= u_{\text{EoW}}(z_0) - \int_{z_0}^z \frac{dz'}{a(z')b(z')} \left(1 - \frac{\sqrt{-a(z_0)}z'^{d-1}}{\sqrt{z_0^{2(d-1)}a(z') - z'^{2(d-1)}a(z_0)}}\right), \\ x_2(z) &= 0\,, \end{aligned} \tag{3.3.2}$$

where $u_{\text{EoW}}(z)$ is as in eq. (3.2.1) and z_0 denotes the point at which the surface intersects the end-of-the-world brane. In this case, the boundary time T is related to the parameter z_0 by evaluating the integral at $z = 0$.

The EWCS that intersects the end-of-the-world brane corresponds to a portion of the non-equilibrium HRT described above. Concretely, it is parameterised as

$$\begin{aligned} u^{(1)}_{\text{EWCS}}(z) &= u_{\text{EoW}}(z_0') - \int_{z_0'}^z \frac{dz'}{a(z')b(z')} \left(1 - \frac{\sqrt{-a(z_0')}z'^{d-1}}{\sqrt{z_0'^{2(d-1)}a(z') - z'^{2(d-1)}a(z_0')}}\right), \\ x^{(1)}_{\text{EWCS}}(z) &= \frac{2\ell + D}{2}, \end{aligned} \tag{3.3.3}$$

but now the parameter z_0' is determined by the intersection condition

$$u^{(1)}_{\text{EWCS}}(\tilde{z}) = u_1(\tilde{z})\,, \tag{3.3.4}$$

where $\tilde{z}$ is the same parameter as in (3.3.1).

The area of the surface is

$$\mathcal{A}^{(1)}_{\text{EWCS}}(z_0') = \int_{\tilde{z}}^{z_0'} \frac{dz}{z^{d-1}b(z)} \frac{z_0'^{d-1}}{\sqrt{z_0'^{2(d-1)}a(z) - z^{2(d-1)}a(z_0')}}\,. \tag{3.3.5}$$

By solving the intersection condition (3.3.4), and evaluating the integral (3.3.5) at different values of boundary time T, one can obtain the time-dependence of the surface. The result is a monotonic increasing function that is approximately linear for the parameter choices we explored.

The other possible EWCS is a surface connecting the two HRTs, without reaching the EoW brane. Unlike the previous case, this does not correspond to a portion of a known HRT. Fortunately, we can employ the symmetries of the problem to solve the extremisation equations in a similar fashion.

We choose to parameterise this surface as $(u^{(2)}_{\text{EWCS}}(z), x^{(2)}_{\text{EWCS}}(z))$. The area of this surface is given by the functional

$$\mathcal{A} = \int_{z_1}^{z_2} \frac{dz}{z^{d-1}} \sqrt{-a(z)\left(\frac{du}{dz}\right)^2 - \frac{2}{b(z)}\frac{du}{dz} + \left(\frac{dx}{dz}\right)^2}\,. \tag{3.3.6}$$

The equations of motion extremising this expression are both reparameterisation and translation invariant, hence we have a couple of conserved quantities denoted

as (j, e). In terms of these constants, the solution can be written as

$$\begin{aligned} u^{(2)}_{\text{EWCS}}(z) &= u_2(z_2) - \int_{z_2}^{z} \frac{dz'}{a(z')b(z')} \left(1 - \frac{e z'^{d-1}}{\sqrt{H(z')}}\right) , \\ x^{(2)}_{\text{EWCS}}(z) &= -\int_{z_2}^{z} dz' \frac{z'^{d-1}}{b(z')\sqrt{H(z')}} , \\ H(z) &= \left(e^2 - a(z)\right) z^{2(d-1)} + j^2 a(z) , \end{aligned} \tag{3.3.7}$$

where (z_1, z_2) are the values of z at which the surface intersects the corresponding HRT surface. The integration constants were chosen to guarantee intersection with the non-equilibrium surface.

Up to this point, the calculation is not dissimilar to those of usual HRT surfaces. The main difference arises because this new surface does not obey boundary conditions at $z = 0$, instead we demand intersection with the equilibrium surface:

$$\begin{aligned} u^{(2)}_{\text{EWCS}}(z_1) &= u_1(z_1) , \\ x^{(2)}_{\text{EWCS}}(z_1) &= x_1(z_1) . \end{aligned} \tag{3.3.8}$$

The solutions to these conditions provide a family of extremal curves.

For HRT surfaces, we are able to fix the integration constants, $\tilde{z}$ and z_0, by symmetry considerations or by imposing intersection with the end-of-the-world brane. For the new surface associated with the EWCS, we require the intersection with the both HRT surfaces to occur perpendicularly; this guarantees that the surface is not only extremal but also minimal. This perpendicularity condition can be used to determine the integration constants (j, e). We then solve the intersection conditions numerically in order to fix (z_1, z_2).

The area of the surface can be written as

$$\mathcal{A}(z_1, z_2) = \int_{z_1}^{z_2} dz \frac{j}{z^{d-1} b(z) \sqrt{H(z)}}\,, \tag{3.3.9}$$

which we evaluate numerically after solving the intersection conditions.

The first candidate surface for the EWCS directly depends on the position of the EoW brane. The second candidate only depends on the position of the EoW brane through the change in shape of the non-equilibrium HRT $u_2(z)$; it approaches a constant as $T \to \infty$. The total time evolution of the EWCS is depicted in Fig. 3.11. After the linear growth phase, the time dependence becomes negligible for the choice of parameters considered.

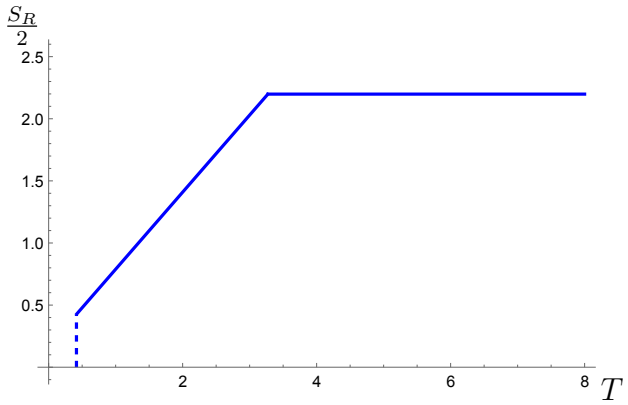

Figure 3.11: Time evolution of EWCS for $D = 1.07$ and $\ell = 1.95$ in $d = 4$.

3.3.2 Membrane theory for reflected entropy

Let us now develop a description for the general behaviour of the reflected entropy as a function of time, assuming the membrane theory for entanglement entropy is valid. We expect the membrane description to be accurate only in the scaling limit. In order to ease the comparison between the exact numerical results and the membrane prediction, we parameterise the size of the finite interval, ℓ, as $\ell = \eta D$,

with $\eta > 1$. We can then take $D \gg 1$.

First, we have to determine the scaling limit of the HRT surfaces. The non-equilibrium HRT does not move in x, hence it corresponds to the $v = 0$ membrane (and most of it sits at $z = z_*$ in the bulk). We have seen in section 3.1.2 that in $d = 2$, the saturated RT surfaces become cones of of slope ± 1 under the membrane mapping. In $d \geq 2$ dimensions this result generalises as follows: we can approximate (3.3.1) by expanding the integrand in z around $\tilde{z} \to 1^-$, giving

$$\begin{aligned} u(z) &= T - \frac{1}{b(1)a'(1)} \log(1-z) + \dots , \\ x(z) &= \frac{2\ell + D}{2} - \frac{\log(1-z)}{b(1)\sqrt{-2(d-1)a'(1)}} , \end{aligned} \tag{3.3.10}$$

and eliminating z we get

$$x(u) = \sqrt{-\frac{a'(1)}{2(d-1)}} u + \text{const} = v_B u + \text{const} , \tag{3.3.11}$$

where we used (1.3.18). Therefore, projections of static RT surfaces to the boundary along constant infalling time are *cones* of slope v_B. These conclusions remain true for arbitrary shapes as can be inferred from the results from (Liu & Mezei, 2014; Mezei & Stanford, 2017; Mezei, 2017). See Appendix B.4 for a calculation with spherical entangling subregions.

We can now propose a membrane description for the reflected entropy for the same configuration above. As observed, at early times the entanglement wedge is disconnected and so its cross section vanishes. This continues until the smaller HRT transitions from linear growth to equilibrium, according to the membrane description of entanglement, this occurs at time $t = \frac{D}{2v_E}$. After this time, the cross section is described by a surface connecting the equilibrium RT surface to the end-of-the-world brane. Such a surface is described by the same type of membrane

as the linear growth of entanglement entropy. Finally, this linear growth continues until the dominant surface is the one connecting the two HRTs. In the scaling limit it is a straight line with slope v_B and its contribution is equal to ℓ. See Fig. 3.12. A check of the consistency of the membrane description with the full HRT surface is that the EWCS connecting the two HRTs (3.3.7) is dominated by the part on the horizon in the large D limit, see Figure 3.7 which is plotted using (3.3.7). A calculation similar to (3.3.11) then shows that the projection of this EWCS to the boundary along constant u is indeed a line of v_B slope.[14]

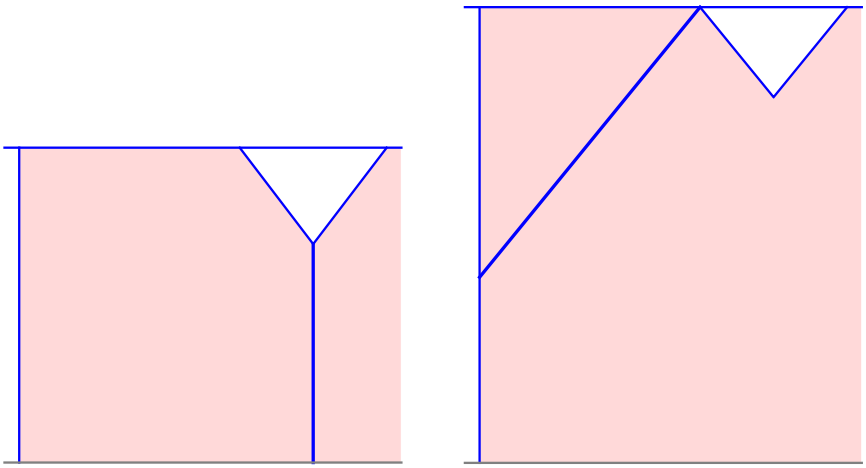

Figure 3.12: Projection of EWCS in $d = 4$ along constant infalling time in the scaling limit, for $\ell = 1.5\Lambda$ and $D = \Lambda$. The entire plots are in blue, as all surfaces are at $z = O(1)$. We plot the EWCS as thick to contrast with HRT. *Left* : Plot at $T = 2\Lambda$. The non-equilibrium EWCS starts from the tip of the static RT surface, and then enters the interior and ends on the EoW brane (plotted in gray, since HRT and EWCS can end on it at any depth). Its length grows linearly in time with slope v_E. *Right* : Plot at $T = 3.1\Lambda$. The equilibrium EWCS skims the horizon from the interior, its projection is therefore a line with slope v_B.

[14]Note that the membrane theory only characterises this surface under the scaling limit and does not encode its local geometry near the connection points to the two HRTs. To investigate these details, one needs to invoke the full equations of motion (3.3.7).

In summary, the membrane description of the reflected entropy is

$$\frac{S_R}{2} = \begin{cases} 0 & T < \frac{D}{2v_E}\,, \\ v_E\left(T - \frac{D}{2v_B}\right) & \frac{D}{2v_E} < T < \frac{\ell}{v_E} + \frac{D}{2v_B}\,, \\ \ell & T > \frac{\ell}{v_E} + \frac{D}{2v_B}\,. \end{cases} \tag{3.3.12}$$

We can compare the membrane theory prediction against the holographic calculation outlined earlier, see Fig. 3.13.

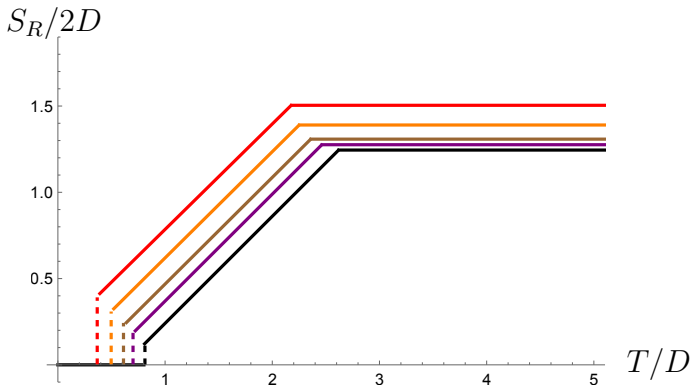

Figure 3.13: Dynamics of entanglement cross section for $D = 1.07$ (red), $D = 1.3$ (orange), $D = 1.95$ (brown), and $D = 3.3$ (purple). This is compared against the membrane prediction (black). As noted in the main text, we emphasise the numerical limitation in solving the intersection problem, which permits us to use only relatively small values of D.

As noted earlier, we expect the membrane theory to be accurate in the limit $D \gg 1$. This seems to be supported by the numerical results depicted in Fig. 3.13, however we are somewhat constrained from a perfect agreement due to numerical limitations. In Appendix B.5, we further explore this point.

3.3.3 Comparison between the generalised and ordinary membrane results for reflected entropy

Let us compare the results for reflected entropy from the generalised (3.2.9) and ordinary membrane results (3.3.12) applicable to 2d and higher-dimensional CFTs (and other generic chaotic systems). There are key differences that we illustrate on Fig. 3.14. On the horizontal axis we put $v_B T/D$ to make them look as similar as possible. The first difference that we notice that the membrane theory result is not continuous, it starts with a jump of size

$$\frac{\Delta S_R}{2D} = \frac{1}{2}\left(1 - \frac{v_E}{v_B}\right) D\,, \qquad \text{at } \frac{v_B T}{D} = \frac{v_B}{2v_E}. \tag{3.3.13}$$

Note however that this difference would vanish if $v_E = v_B$ were to hold, i.e. in the limit of the degenerate membrane tension $\mathcal{E}(v) = 1$. The slope of the two curves are also different, by a factor v_E/v_B, which again would go away for $v_E = v_B$. However, the plateau values of the curves $\ell/2D$ and ℓ/D do not match even for the degenerate membrane tension: *this is the prediction that genuinely distinguishes the two effective theories*.

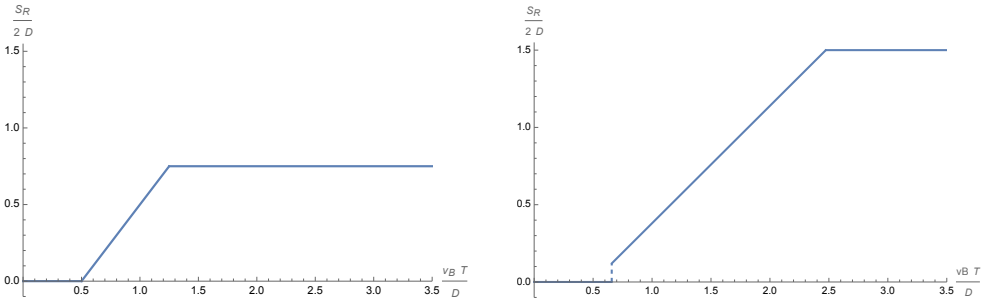

Figure 3.14: Time evolution of reflected entropy in $d = 2$ (left) and $d = 4$ (right) for $\ell/D = 3/2$. We use the same ranges on the horizontal and vertical axes to facilitate the comparison.

3.4 Entanglement membrane and 2d RG flows

In section 3.1, we have explored the generalised entanglement membrane in 2d CFT with a degenerate membrane tension, and compared the resulting equation of motion with that of ordinary membrane theory (Mezei, 2018). In this section, we show that deforming a 2d CFT with a relevant operator leads to a a renormalisation group (RG) flow between the generalised and ordinary membrane theories and the emergence of a non-degenerate membrane tension. In the small deformation limit we maintain full analytic control over this RG interpolation.

3.4.1 Holographic RG flow from BTZ to AdS$_3$-Kasner

We consider a two-sided planar BTZ black hole with a relevant deformation. Such a deformation breaks the infinite-dimensional conformal symmetry of the dual (1+1)-dimensional field theory. The action is given by

$$\mathcal{L} = \frac{1}{2}(R+2) - \frac{1}{2}(g^{ab}\partial_a\phi\partial_b\phi + m^2\phi^2)\,. \tag{3.4.1}$$

Here we choose $m^2 = -\frac{3}{4}$, which is above the Breitenlohner-Freedman bound $m^2_{\text{BF}} = -1$ (Breitenlohner & Freedman, 1982). It is convenient to rewrite the metric (1.3.12) in the following form:

$$ds^2 = \frac{1}{z^2}\Big(- f(z)e^{-\chi(z)}du^2 - 2e^{-\chi(z)/2}dudz + dx^2\Big)\,, \tag{3.4.2}$$

where the horizon is at $z_+ = 1$, hence $f(1) = 0$. Without the relevant deformation, the metric (3.4.2) becomes the planar BTZ metric, where $f(z) = 1 - z^2$ and $\chi(z) = 0$. Unlike BTZ, the metric (3.4.2) does contain a curvature singularity at $z = \infty$. The Einstein-scalar equations of motions can be obtained by varying the

action (3.4.1):[15]

$$\phi'' + \Big(\frac{f'}{f} - \frac{1}{z} - \frac{\chi'}{2}\Big)\phi' + \frac{3}{4}\frac{\phi}{z^2 f} = 0, \tag{3.4.3}$$

$$\chi' - 2\frac{f'}{f} - \frac{3}{4}\frac{\phi^2}{zf} - \frac{4}{zf} + \frac{4}{z} = 0, \tag{3.4.4}$$

$$\chi' - z\phi'^2 = 0. \tag{3.4.5}$$

The scalar field and the geometry behave asymptotically ($z \to 0$) as (Witten, 1998; Gubser et al., 1998; de Haro et al., 2001):

$$\phi = \phi_0 z^{\frac{1}{2}} + \langle O\rangle z^{\frac{3}{2}} + ..., \quad \chi = \frac{\phi_0^2}{4}z + \frac{3}{4}\phi_0\langle O\rangle z^2 + ..., \quad e^{-\chi}f = 1 - \langle T_{tt}\rangle z^2 + ..., \tag{3.4.6}$$

where ϕ_0 serves as the source for the dual boundary operator whose expectation value is $\langle O\rangle$. As $-\frac{d^2}{4} < m^2 < -\frac{d^2}{4} + 1$, both modes are normalizable (Klebanov & Witten, 1999). Here we implement standard quantisation, with the dimension of O given by $\Delta = \frac{d}{2} + \sqrt{\frac{d^2}{4} + m^2} = \frac{3}{2}$. The temperature of the black hole is:

$$T = \frac{|f'_+|e^{-\frac{\chi_+}{2}}}{4\pi}, \tag{3.4.7}$$

where χ_+ and f'_+ are the horizon value of χ and f', respectively.

From the equations of motion (3.4.3)-(3.4.5), one can read off the following near-singularity ($z \to \infty$) behaviours:

$$\phi = \sqrt{2}c\log z + ..., \quad \chi = 2c^2\log z + \chi_\infty + ..., \quad f = -f_\infty z^{2+c^2} + ..., \tag{3.4.8}$$

[15] See (Caceres, Kundu, Patra, & Shashi, 2022) for the Einstein-scalar equations of motions in general $d \geq 2$ dimensions with arbitrary Δ.

where the constant $c = 0$ for BTZ. Let $z^{2+c^2} = \frac{1}{\tau^2}$, the metrics (3.4.2) then takes the Kasner form (Frenkel, Hartnoll, Kruthoff, & Shi, 2020; Kasner, 1921; Belinski & Khalatnikov, 1973) in the interior

$$ds^2 \sim -d\tau^2 + \tau^{2p_t} dt^2 + \tau^{2p_x} dx^2 \,, \qquad \phi \sim -\sqrt{2} p_\phi \log \tau \,, \tag{3.4.9}$$

where the Kasner exponents are given by

$$p_t = \frac{c^2}{2+c^2} \,, \qquad p_x = \frac{2}{2+c^2} \,, \qquad p_\phi = \frac{2c}{2+c^2} \,. \tag{3.4.10}$$

We have $p_t + p_x = 1$, $p_t^2 + p_x^2 + p_\phi^2 = 1$. For the BTZ black hole, $p_t = p_\phi = 0$ and $p_x = 1$. One can think of p_t as measuring the deformation of the geometry away from BTZ and therefore characterising the relevant deformation.

The equations of motion (3.4.3)-(3.4.5) can be solved numerically using the so-called “shooting" method (Hartnoll, Herzog, & Horowitz, 2008a, 2008b). First, expand ϕ, χ and f around the horizon $z_+ = 1$:

$$\phi(z) = \sum_{n=0}^{N} \phi_{(n)} (z-1)^n \,, \quad \chi(z) = \sum_{n=0}^{N} \chi_{(n)} (z-1)^n \,, \quad f(z) = \sum_{n=1}^{N} f_{(n)} (z-1)^n \tag{3.4.11}$$

where N is some positive integer, and we have used $f(1) = 0$. Then, plugging (3.4.11) into the equations of motion (3.4.3)-(3.4.5) allows one to express all the expansion parameters in (3.4.11) in terms of the horizon value of the scalar field $\phi_{(0)} = \phi_+$. One can therefore integrate the field equations numerically in terms of the dimensionless parameter $\frac{\phi_0}{\sqrt{T}}$ from an ϵ-ball centred at the horizon $z = 1$. Here, in addition to integrating to the boundary $z = 0$ (Hartnoll et al., 2008a, 2008b), we also integrate towards the singularity $z = \infty$ (Frenkel et al., 2020). A demonstration of the shooting solution is presented in Fig. 3.15, where we show

the plots of ϕ, χ, and f, as well as the Kasner exponent p_t.[16] Notice that as $\frac{\phi_0}{\sqrt{T}}$ increases from 0 to ∞, p_t first increases and then decreases after reaching its maximal value, indicating that the geometry returns to BTZ in the large ϕ_+ limit. The translation between the metric functions featuring in (1.3.12) and (3.4.2) is $a(z) = f(z)e^{-\chi(z)}$ and $b(z) = e^{\chi(z)/2}$, hence $a(z)$, $b(z)$ move away from their BTZ values under the relevant deformation, and v_E (1.3.10) and v_B (1.3.18) also become non-trivial functions of $\frac{\phi_0}{\sqrt{T}}$, see Fig. 3.16. For the same reason, the membrane tension $\mathcal{E}(v)$ (1.3.16) is no longer degenerate. See Fig. 3.17 for a plot of numerical membrane tensions in AdS_3-Kasner geometry. It is found that as ϕ_+ increases from 0, $\mathcal{E}(v)$ starts to deflect from $\mathcal{E}(v) = 1$ and becomes non-trivial; for large ϕ_+, however, we observe that $\mathcal{E}(v)$ asymptotes to $\mathcal{E}(v) = 1$. This is likely because as $\phi_+ \to \infty$ the Kasner exponent $p_t \to 0$, the BTZ value.

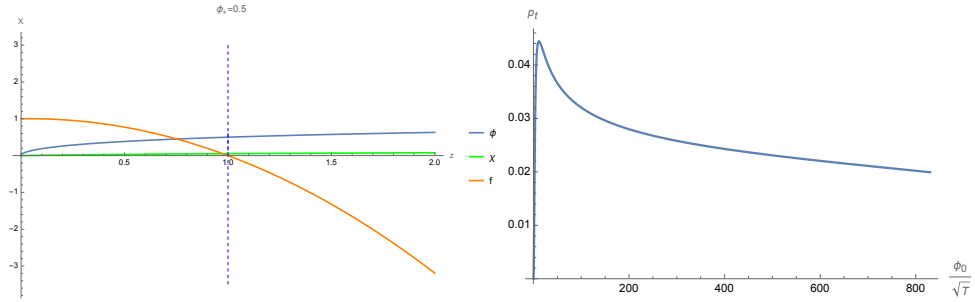

Figure 3.15: A demonstration of the shooting solutions. *Left*: Plot of ϕ (blue), χ (green) and f (orange) when $\phi_+ = 0.5$. The vertical dashed blue line is the black hole horizon $z = 1$. *Right*: Plot of the Kasner exponent p_t with respect to the dimensionless parameter $\frac{\phi_0}{\sqrt{T}}$. Notice that for larger values of $\frac{\phi_0}{\sqrt{T}}$, p_t returns to its BTZ value $p_t = 0$.

3.4.2 Small ϕ perturbation theory

In the previous subsection, we have solved the equations of motion (3.4.3)–(3.4.5) numerically for generic perturbations. For small values of ϕ, however, one can

[16] Notice that $p_t > 0$ in $d = 2$, whereas for $d \geq 3$, $p_t < 0$ (Frenkel et al., 2020).

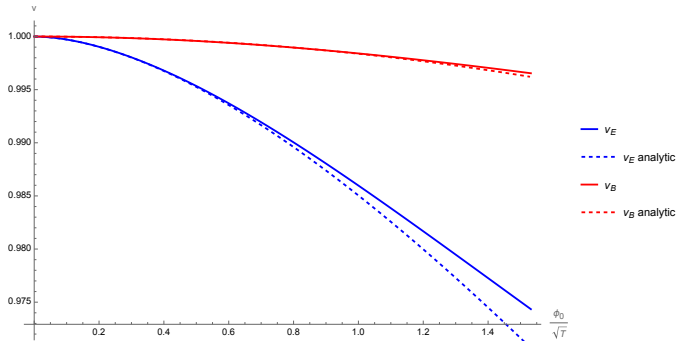

Figure 3.16: Plot of v_E (blue) and v_B (red) with respect to the dimensionless parameter $\frac{\phi_0}{\sqrt{T}}$. The solid lines are numerical solutions, whereas the dashed lines are analytic expansions in the small-ϕ limit. At $\phi_0 = 0$, i.e. when the geometry is planar BTZ black hole, $v_E = v_B = 1$. When $\phi_0 > 0$, we have $v_E < v_B$ due to the constraint from null energy condition. When $\frac{\phi_0}{\sqrt{T}}$ is small, the numerical solutions of both v_E and v_B are well approximated by small-ϕ perturbation theory.

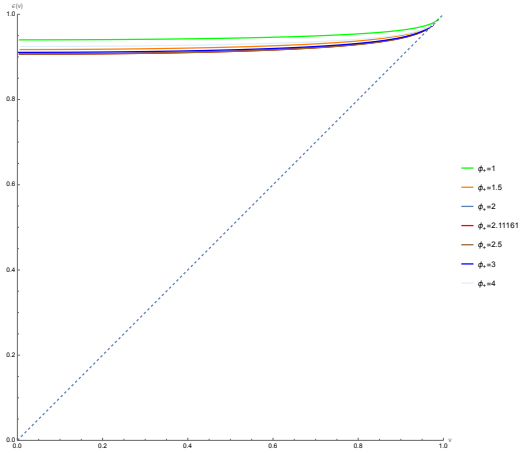

Figure 3.17: Plot of $\mathcal{E}(v)$ in AdS$_3$-Kasner geometry, for $\phi_+ = 1, 1.5, 2, , 2.11, 2.5, 3, 4$. The dashed line is at $45°$. As ϕ_+ gets large, the membrane tension returns to its undeformed degenerate BTZ value $\mathcal{E}(v) = 1$, see Fig. 3.15 (right).

establish a perturbation theory and find analytic solutions order by order. Let us consider the leading order perturbation in ϕ

$$\phi(z) = \lambda\phi_1(z), \tag{3.4.12}$$

where λ is a small constant. From the equations of motion (3.4.5) and the action (3.4.1), both $\chi(z)$ and $f(z)$ are second order in λ,

$$\chi(z) = \lambda^2\chi_1(z), \tag{3.4.13}$$

$$f(z) = 1 - z^2 + \lambda^2 f_1(z). \tag{3.4.14}$$

Plugging (3.4.12)-(3.4.14) into the equations of motions (3.4.3)-(3.4.5), one can obtain $\phi_1(z)$ in closed form, and obtain integral expressions for $\chi_1(z)$ and $f_1(z)$,

$$\phi_1(z) = \frac{2}{\pi}\sqrt{z}K\Big(\frac{1-z}{2}\Big), \tag{3.4.15}$$

$$\chi_1(z) = \int_0^z dz' \frac{\left((z'+1)K\left(\frac{1-z'}{2}\right) - 2z'E\left(\frac{1-z'}{2}\right)\right)^2}{\pi^2\left(z'^2-1\right)^2}, \tag{3.4.16}$$

$$f_1(z) = z^2\int_1^z dz' \frac{-(2z'^2+z'-1)K\left(\frac{1-z'}{2}\right)^2 + 2z'(z'+1)K\left(\frac{1-z'}{2}\right)E\left(\frac{1-z'}{2}\right) - 2z'^2E\left(\frac{1-z'}{2}\right)^2}{\pi^2 z'^2\left(z'^2-1\right)}, \tag{3.4.17}$$

where $K(z)$ and $E(z)$ denote the complete elliptic integral of the first and second kind, respectively. Integrating (3.4.5) from 0 to z in (3.4.16) ensures $\chi(0) = 0$. When ϕ_+ is small, one can check that (3.4.15) matches well with numerical solution. According to (3.4.15), $\phi(1) = \lambda$ at the horizon $z = 1$. From (3.4.15), one learns that $\phi(z)$ behaves near the boundary $z \to 0$ as

$$\phi(z) \to \lambda\frac{\Gamma(1/4)}{\sqrt{2\pi}\,\Gamma(3/4)}z^{\frac{1}{2}} + \lambda\frac{\Gamma(-1/4)}{8\sqrt{2\pi}\,\Gamma(5/4)}z^{\frac{3}{2}} + ..., \tag{3.4.18}$$

and near the singularity $z \to \infty$ as

$$\phi(z) \to \lambda \frac{\sqrt{2}}{\pi} \log z + \dots . \tag{3.4.19}$$

Comparing (3.4.18) to (3.4.6), and (3.4.19) to (3.4.8) then yields a relation among the small perturbation parameter λ, the value of ϕ at the horizon ϕ_+, the falloff ϕ_0, as well as the Kasner parameter c,

$$\lambda = \phi_+ = \pi c = \sqrt{2\pi}\, \frac{\Gamma\left(3/4\right)}{\Gamma\left(1/4\right)} \phi_0 \,. \tag{3.4.20}$$

The integral expressions (3.4.16) and (3.4.17) make it hard to derive a closed form expression for $\mathcal{E}(v)$ (1.3.16) even in perturbation theory. To get more insight into its behaviour, in the next subsection we expand $\mathcal{E}(v)$ around $v = 0$ and $v = v_B$ to leading non-trivial orders in λ. As $v^2 = c(z)$ (1.3.15) is monotonically decreasing in z, these expansions take place around $z = z_*$ and $z = 1$, respectively.

3.4.2.1 Expansion near the singularity

Let us first consider the expansion of $\mathcal{E}(v)$ at $v = 0$ or equivalently $z = z_*$, where $\mathcal{E}(0) = v_E$. Intuitively, z_* is large for small λ, as $z_* = \infty$ in the undeformed BTZ black hole. Therefore, to find the expansion of $\mathcal{E}(v)$ at $v = 0$, one can start by studying the behaviours of χ and f at large z:

$$\chi_1(z) \approx \frac{2}{\pi^2} \log z + \frac{-2 - \pi + 12 \log 2}{2\pi^2} \,, \tag{3.4.21}$$

$$f_1(z) \approx -\frac{z^2}{\pi^2} (\log z + 3 \log 2) \,. \tag{3.4.22}$$

(3.4.21) and (3.4.22) then allow us to find the small λ expansion of $v^2(z)$ (1.3.15) to $O(\lambda^2)$

$$v^2(z) \approx 1 - \frac{1}{2\pi^2}\lambda^2 z^2 \qquad \Rightarrow \qquad z(v^2) = \frac{\sqrt{2}\pi}{\lambda}\sqrt{1-v^2}\,, \tag{3.4.23}$$

which is a monotonically decreasing function in z deviating from $v^2 = 1$ in BTZ. z_* is given by the solution of $v^2(z) = 0$,

$$z_* = \frac{\sqrt{2}\pi}{\lambda}\,. \tag{3.4.24}$$

We see that the relevant deformation (3.4.12) of BTZ pulls z_* from ∞ to a finite value. The entanglement dynamics in AdS_3-Kasner geometry is thus in reminiscent of those in planar AdS_{d+1}-Schwarzschild black branes in $d \geq 3$ dimensions, in the sense that at late time, the HRT surface computing entanglement entropy stays at a finite z_* instead of moving towards $z = \infty$. Unlike $z_* \in O(1)$ in AdS_{d+1}-Schwarzschild, however, z_* in AdS_3-Kasner (3.4.24) is large for small perturbations. When $\lambda \to 0$, $z_* \to \infty$, and the entanglement dynamics returns to that in BTZ. As v_E (1.3.10) is determined by the interior geometry at $z = z_*$, one can then proceed to obtain the small λ expansion of v_E

$$v_E \approx 1 + \frac{1}{2\pi^2}\lambda^2 \log\lambda + \frac{1+\pi-7\log 2-2\log\pi}{8\pi^3}\lambda^2\,. \tag{3.4.25}$$

Notice that the leading non-trivial term in λ is at $O(\lambda^2\log\lambda)$. A plot of (3.4.25) with respect to the dimensionless parameter $\frac{\phi_0}{\sqrt{T}}$ can be found in Fig. 3.16.[17] For small ϕ_0, (3.4.25) matches well with numerical result.

[17] In plotting v_E as a function of the dimensionless quantity $\frac{\phi_0}{\sqrt{T}}$, we also need to include the correction of temperature T (2.3.9) due to the deformation (3.4.12):

$$T \approx \frac{1}{2\pi}\Big(1 + \frac{\lambda^2}{4\pi}\Big). \tag{3.4.26}$$

As we have already seen from the numerical solutions, the membrane tension is no longer degenerate in AdS_3-Kasner geometry. By plugging the above results into (1.3.16), we obtain the small λ expansion of $\mathcal{E}(v)$:

$$\mathcal{E}(v) \approx v_E - \frac{\lambda^2}{4\pi^2} \log(1 - v^2). \tag{3.4.27}$$

This formula was obtained from the large z expansion of the metric functions, and this limits its regime of validity in v. From (3.4.23), we see that unless $1 - v = O(\lambda^2)$, we stay in the large z regime, hence (3.4.27) is widely applicable. Indeed, this formula obeys the constraints $\mathcal{E}(0) = v_E$, $\mathcal{E}'(0) = 1$ $\mathcal{E}'(v) \geq 0$, $\mathcal{E}''(v) \geq 0$ from (1.3.19). A plot of the expansion (3.4.27) can be found in Fig. 3.18. For small λ, (3.4.27) matches well with numerical results.

3.4.2.2 Expansion near the horizon

We expect that the butterfly velocity will move from its 2d CFT value $v_B = 1$ to $v_B = 1 - O(\lambda^2)$. Plugging this into (3.4.27) generates a $O(\lambda^2 \log(\lambda))$ term that threatens the validity of the expansion. Indeed v_B is determined by the geometry at the horizon $z = 1$, as in (1.3.18), whereas (3.4.27) was obtained from a large z expansion. Thus we examine the behaviour of $\mathcal{E}(v)$ near the butterfly velocity more carefully.

It is a straightforward exercise to obtain a series representation in $\delta z \equiv z - 1$ of the different metric components near the horizon. From these using (1.3.18), (1.3.15),

Notice that the $O(\lambda^2)$ correction drops out if we only keep the expansion of v_E to $O(\lambda^2)$. The same applies to v_B.

and (1.3.16) we can form:[18]

$$\begin{aligned}
\frac{v_B-1}{\lambda^2} &= -\frac{3}{32}+\frac{1}{4\pi}<0\,,\\
\frac{v^2-1}{\lambda^2} &= \frac{c(z)-1}{\lambda^2} = \left(-\frac{3}{16}+\frac{1}{2\pi}\right)-\frac{9}{128}\delta z-\frac{99}{2048}\delta z^2+\dots\,,\\
\frac{\mathcal{E}(v)-1}{\lambda^2} &= \frac{\sqrt{\frac{-a'(z)}{2z}}-1}{\lambda^2} = \left(-\frac{3}{32}+\frac{1}{4\pi}\right)-\frac{9}{256}\delta z+\frac{45}{4096}\delta z^2+\dots\,,
\end{aligned} \tag{3.4.29}$$

where we have explicitly computed terms up to $O(\delta z^4)$. By expressing δz as a function of

$$\nu \equiv \frac{v^2-v_B^2}{\lambda^2} \ll 1\,, \tag{3.4.30}$$

we can express $\mathcal{E}(v)$ in a v expansion near the butterfly velocity (with a radius of validity in v very small, $O(\lambda^2)$) as follows:

$$\mathcal{E}(v) = 1+\lambda^2\left(\left(-\frac{3}{32}+\frac{1}{4\pi}\right)+\frac{\nu}{2}+\frac{64\nu^2}{9}+\frac{35840\nu^3}{243}+\frac{7813120\nu^4}{2187}+\dots\right). \tag{3.4.31}$$

This expression satisfies the constraints $\mathcal{E}(v_B)=v_B$, $\mathcal{E}'(v_B)=1$, $\mathcal{E}'(v)\geq 0$, $\mathcal{E}''(v)\geq 0$ from (1.3.19), as required. In Fig. 3.18, we plot the expansion (3.4.31). It is found that (3.4.31) agrees with numerical results when v is close to v_B.

It is instructive to convert our holographic results (3.4.29) to those in conformal

[18] To obtain these expansions we need to evaluate the following definite integral:

$$\chi_1(1) = \int_0^1 dz' \frac{\left((z'+1)K\left(\frac{1-z'}{2}\right)-2z'E\left(\frac{1-z'}{2}\right)\right)^2}{\pi^2\left(z'^2-1\right)^2} = \frac{3}{8}-\frac{1}{2\pi}\,. \tag{3.4.28}$$

perturbation theory (Davison & Delacretaz, 2024)

$$S = S_{\text{CFT}} + \sqrt{c}\,\mu \int d^2x O, \tag{3.4.32}$$

where μ is the relevant coupling that deforms the CFT, and the scalar primary operator O is normalised such that its vacuum two-point function is $|x - x'|^{-2\Delta}$. This normalisation is related to our convention via $\phi_0 = -4\sqrt{3}\pi\mu$.[19] The butterfly velocity in (3.4.29) can then be rewritten in terms of the dimensionless coupling $\frac{\mu}{\sqrt{T}}$ as

$$v_B = 1 - \frac{3\pi(3\pi - 8)\Gamma\left(\frac{3}{4}\right)^2}{2\Gamma\left(\frac{1}{4}\right)^2}\left(\frac{\mu}{\sqrt{T}}\right)^2. \tag{3.4.34}$$

The butterfly velocity (3.4.34), and more generally that with general $\Delta \in (1, 2)$

$$v_B = 1 - \frac{3(2\pi)^{2(\Delta-1)}\Gamma(2-\Delta)\Gamma\left(\frac{\Delta}{2}\right)^2}{\Gamma\left(1-\frac{\Delta}{2}\right)^2\Gamma(\Delta)}\left(\frac{\pi\Delta(\Delta-2)\cot\left(\frac{\pi\Delta}{2}\right)}{4(\Delta-1)} - 1\right)\left(\frac{\mu}{T^{2-\Delta}}\right)^2, \tag{3.4.35}$$

calculated using the same method in obtaining (3.4.29) (Davison & Jiang, 2026), is in exact agreement with the prediction from universal hydrodynamics in two-dimensional QFT at high temperature (Davison & Delacretaz, 2024; Davison & Jiang, 2026). Such a prediction is made through locations of pole skipping points of the stress tensor thermal two-point functions in momentum space. See (Davison & Jiang, 2026) for studies of holographic pole skipping in hairy BTZ black hole backgrounds dual to (3.4.32).

[19] The conversion between holographic and CFT normalisations is (Davison & Delacretaz, 2024)

$$\phi = \frac{2\sqrt{3}}{1-\Delta}\mu z^{2-\Delta} + \dots. \tag{3.4.33}$$

Comparing (3.4.33) with our falloff (3.4.6), we have $\phi_0 = \frac{2\sqrt{3}}{1-\Delta}\mu$.

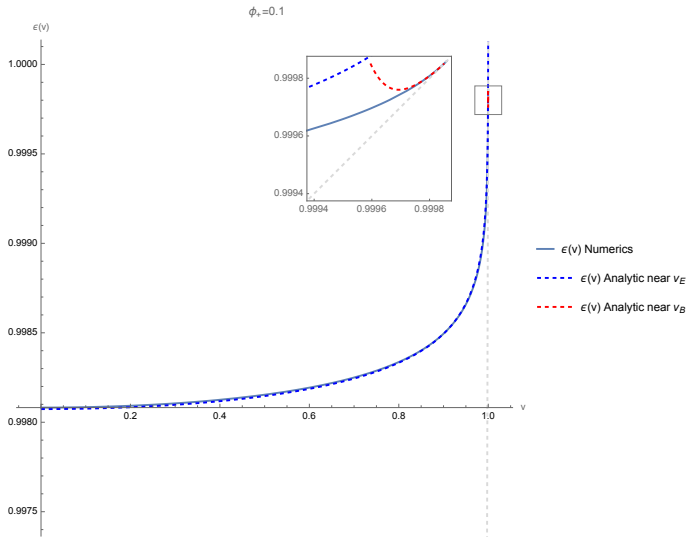

Figure 3.18: Plot of the membrane tension $\mathcal{E}(v)$ when $\phi_+ = 0.1$. For small ϕ_+, $\mathcal{E}(v)$ is close to 1. The solid line is obtained numerically from shooting solutions, whereas the blue and red dashed lines are perturbative expansions around the deepest point z_* (3.4.27) and the horizon $z = 1$ (3.4.31), respectively. The dashed gray line has unit slope, greatly exaggerated here by the scale of the vertical axis. Notice that the near-v_B expansion of $\mathcal{E}(v)$ is valid only in a small interval near $v = v_B$, which is difficult to visualise and hence is plotted in the inset.

4 | Time Evolution of Multiparty Entanglement Signals

In this chapter, we study the real-time ddynamics of multipartite entanglement signals reviewed in section 1.5 using the membrane effective theories for reflected entropy proposed in Chapter 3.

We present the dynamics of three-party and four-party entanglement signals in Secs. 4.1 and 4.2. In Sec. C.2, we consider extensions to more parties. In Sec. C.1 we discuss multiparty entanglement signals in a generalised membrane theory describing two-dimensional conformal field theories.

Overall, we find that scrambling dynamics generally produces multiparty entanglement with rich structure that varies over time. Notably:

- *Different entanglement signals show different dynamical behaviours:* the fact that there are many distinct multiparty entanglement signals is useful, and perhaps necessary, because they likely capture different *kinds* of entanglement patterns.[1] Indeed, we see in our examples that the different signals we consider have qualitatively different dynamical behaviour, capturing different aspects of the dynamics of multiparty entanglement.

- *Discontinuities:* signals based on bipartitions, such as the triple information, are always continuous, but signals based on the reflected entropy can have discontinuities. We will see that there can be dynamical discontinuities in the three-party entanglement in the membrane description. This suggests phase transitions in the entanglement structure of the state.

[1] See (Verstraete, Dehaene, De Moor, & Verschelde, 2002) for a classification of four qubit entanglement patterns.

- *Non-monotonicity:* we consider entanglement between large regions, while the initial state has entanglement at small scales. So our multiparty entanglement signals always vanish in the initial state.[2] Surprisingly, the subsequent evolution is not monotonic: after an initial increase, in some cases the entanglement signal decreases again. We will argue that this behaviour reflects the absence of some kinds of multiparty entanglement in generic holographic states.

- *Saturation of bounds:* the authors of (Balasubramanian, Kang, Murdia, & Ross, 2025) constructed bounds on multiparty entanglement. We will see that in some cases, there are periods where the entanglement captured by the membrane description saturates one of these bounds, indicating that the extensive part of the entanglement of one of the regions is *entirely* multipartite.

4.1 Dynamics of R_3

In this section we use the membrane effective description for the reflected entropy obtained in (Jiang et al., 2025) to calculate the residual information in the simplest cases. We consider an infinite system with a division including one or two finite regions. We discuss here the ordinary membrane theory; the generalised membrane theory which describes the holographic calculations for $d = 2$ has some quantitative differences, and is discussed in Section C.1.

[2] When the state is dual to Vaidya-BTZ spacetime (Balasubramanian, Bernamonti, de Boer, et al., 2011b), the results in (Balasubramanian, Kang, Murdia, & Ross, 2025) indicate that there are non-zero initial multiparty entanglement signals. But these initial signals are negligible compared to entropy in the late time and large region limit (Mezei, 2018).

4.1.1 A single finite region

The simplest case to illustrate the dynamics of R_3 is where we divide the boundary into three regions along x: $A = (-\infty, 0)$, $B = (0, \ell)$, and $C = (\ell, \infty)$.

In this case, $S(A)$ and $S(C)$ grow linearly for all times, while $S(B)$ has linear growth followed by saturation. In this case $S(A) = S(C)$ as they are both vertical surfaces. This gives

$$I(A:B) = S(A) + S(B) - S(C) = S(B) = s_{\text{th}} \begin{cases} 2t & t < \frac{\ell}{2}\,, \\ \ell & t > \frac{\ell}{2}\,, \end{cases} \tag{4.1.1}$$

where we have used the fact that for a pure state, $S(AB) = S(C)$. We also have

$$I(A:C) = S(A) + S(C) - S(B) = s_{\text{th}} \begin{cases} 0 & t < \frac{\ell}{2}\,, \\ 2t - \ell & t > \frac{\ell}{2}\,. \end{cases} \tag{4.1.2}$$

Since A, B are adjoining regions, the AB entanglement wedge cross-section is always non-empty. The cross-section is initially a vertical membrane hanging from the boundary, growing linearly in time. At $t = \ell$, this changes to a diagonal membrane extending across the B region, giving a constant extensive answer for the entanglement wedge cross-section, See Figure 4.1.[3] So we have[4]

[3] In the case of holographic CFTs, the saturated membrane on the right of Figure 4.1 is obtained from an Entanglement Wedge Cross-Section (EWCS) that skims through the planar black brane horizon and then ends on the HRT surface corresponding to the vertical membrane for S(C). This has been checked numerically in certain cases in (Jiang et al., 2025). Notice that the diagonal membrane only captures the scaling behaviour of the EWCS and does not reflect its intersection with the HRT.

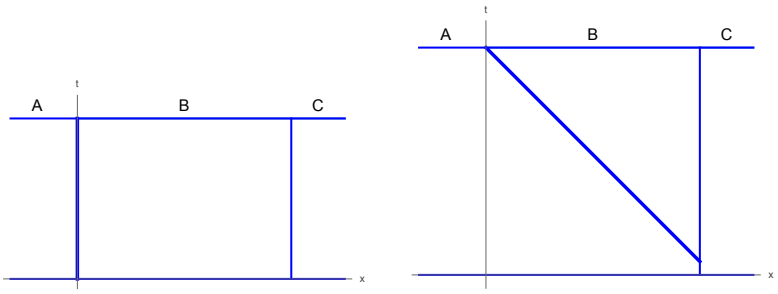

Figure 4.1: Membranes computing $S_R(A:B)$ (thick) in the setup of a single finite region $A = (-\infty, 0)$, $B = (0, \ell)$, and $C = (\ell, \infty)$.

$$S_R(A:B) = s_{\text{th}} \begin{cases} 2t & t < \ell\,, \\ 2\ell & t > \ell\,. \end{cases} \tag{4.1.3}$$

Hence

$$R_3(A:B) = S_R - I = s_{\text{th}} \begin{cases} 0 & t < \frac{\ell}{2}\,, \\ 2t - \ell & \frac{\ell}{2} < t < \ell\,, \\ \ell & t > \ell\,. \end{cases} \tag{4.1.4}$$

This exhibits the same qualitative dynamics as in the semi-infinite case considered in (Jiang et al., 2025); it is initially zero until the initial local entanglement has spread sufficiently to contribute to multiparty entanglement between the three regions, then it grows linearly for a period of time and then saturates.

By contrast, the AC entanglement wedge is initially disconnected, only becoming connected when $S(B)$ saturates. Subsequently, the only possible cross-section is a linearly growing vertical surface, which hangs from the tip of the membrane describing $S(B)$, see Figure 4.2.

[4] In the case of adjacent intervals, S_R is not UV finite (Dutta & Faulkner, 2019; Kudler-Flam et al., 2020). In this case, we can regularize the EWCS the same way as (H)RT, by subtracting UV divergences of the form (1.3.17). These UV divergences cancel in R_3.

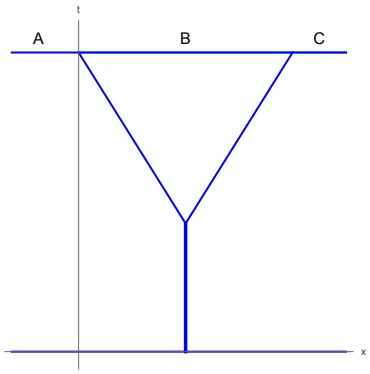

Figure 4.2: Membrane computing $S_R(A:C)$ (thick) in the setup of a single finite region.

This gives

$$S_R(A:C) = s_{\text{th}} \begin{cases} 0 & t < \frac{\ell}{2}\,, \\ 2t - \frac{v_E}{v_B}\ell & t > \frac{\ell}{2}\,. \end{cases} \tag{4.1.5}$$

Note there is a discontinuity in S_R at this transition, and we have an offset in time, as in the case discussed in (Jiang et al., 2025). As a result there is also a discontinuity in the residual information,

$$R_3(A:C) = s_{\text{th}} \begin{cases} 0 & t < \frac{\ell}{2}\,, \\ \ell\left(1 - \frac{v_E}{v_B}\right) & t > \frac{\ell}{2}\,. \end{cases} \tag{4.1.6}$$

This illustrates the general point that different signals can have qualitatively different behaviour, see Figure 4.3.

4.1.2 Two finite regions

Consider now a case where we divide the boundary into four pieces, that is with two finite intervals. To calculate R_3, we first need to combine two of the pieces to form a single region. There are two qualitatively different choices: to combine one of the semi-infinite pieces with a finite piece, or to combine the two semi-infinite pieces.

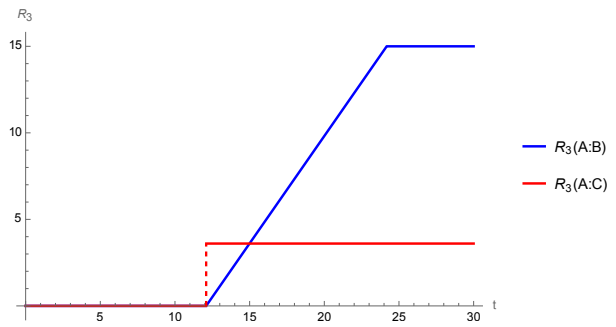

Figure 4.3: Time evolution of $R_3(A:B)$ (4.1.4) (blue) and $R_3(A:C)$ (4.1.6) (red) when $\ell = 15$.

The former is essentially what was considered in (Jiang et al., 2025), so we focus on the latter. That is, we consider dividing the boundary into three regions along x which are now $A = (0, \ell_A)$, $B = (\ell_A, \ell_A + \ell_B)$, and $C = (-\infty, 0) \cup (\ell_A + \ell_B, \infty)$. Let us suppose without loss of generality that $\ell_B < \ell_A$. We will consider both $R_3(A:B)$ and $R_3(A:C)$ ($R_3(B:C)$ is similar to $R_3(A:C)$).

The entropies $S(A)$, $S(B)$ and $S(AB) = S(C)$ exhibit the general linear growth followed by saturation behaviour of finite intervals. We thus have

$$I(A:B) = s_{\text{th}} \begin{cases} 2t & t < \frac{\ell_B}{2}\,, \\ \ell_B & \frac{\ell_B}{2} < t < \frac{\ell_A}{2}\,, \\ \ell_A + \ell_B - 2t & \frac{\ell_A}{2} < t < \frac{\ell_A + \ell_B}{2}\,, \\ 0 & t > \frac{\ell_A + \ell_B}{2}\,. \end{cases} \tag{4.1.7}$$

The AB entanglement wedge is always connected. The cross-section is initially a vertical surface hanging down from the boundary. It transitions to a surface extending across the B region when $t = \ell_B$, see Figure 4.4. When $S(AB)$ saturates at $t = \ell_A + \ell_B$, the cross-section goes back to hanging down from the boundary but just to the v_B cone membrane corresponding to $S(AB)$ (see Figure 4.5). However, this cross-section is no longer described by membrane theory. Intuitively, this is

because it does not grow with t or x in the scaling limit. In Appendix C.3, we show using holography that for this cross-section $S_R = 0$ in the scaling limit (after subtracting the UV divergences as discussed in footnote 4). So

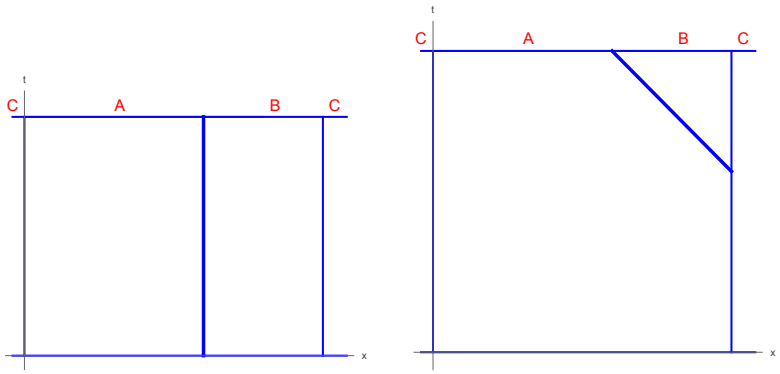

Figure 4.4: Membranes computing $S_R(A:B)$ (thick) in the setup of two finite regions $A = (0, \ell_A)$, $B = (\ell_A, \ell_A + \ell_B)$, and $C = (-\infty, 0) \cup (\ell_A + \ell_B, \infty)$ ($\ell_A > \ell_B$). After the saturation of the $S(AB)$ to a v_B cone, we have $S_R(A:B) = 0$, see Figure 4.5.

$$S_R(A:B) = s_{\text{th}} \begin{cases} 2t & t < \ell_B \,, \\ 2\ell_B & \ell_B < t < \frac{\ell_A + \ell_B}{2} \,, \\ 0 & t > \frac{\ell_A + \ell_B}{2} \,. \end{cases} \tag{4.1.8}$$

The order of transitions in the residual information depends on whether $2\ell_B$ is bigger or smaller than ℓ_A. Suppose for definiteness $\ell_A < 2\ell_B$,[5] which includes the case where the two finite intervals are equal size. Then taking the difference

[5]The other case with $\ell_A > 2\ell_B$ shows the same qualitative behaviour.

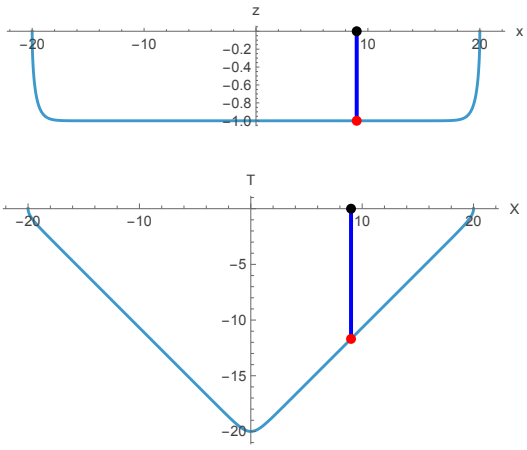

Figure 4.5: *Top*: The minimal cross-section (blue) in finite adjacent intervals after saturation. It is almost radial as it needs to end perpendicularly on the plateau of the RT surface perpendicularly, see Appendix C.3. *Bottom* : Projections of the minimal cross-section (blue) to the AdS boundary along constant infalling time. As discussed in appendix C.3, this vertical surface does not have a membrane description, and we have $S_R = 0$ in this case contrary to what one might expect from the figure.

between (4.1.8) and (4.1.7) we have

$$R_3(A:B) = s_{\text{th}} \begin{cases} 0 & t < \frac{\ell_B}{2}\,, \\ 2t - \ell_B & \frac{\ell_B}{2} < t < \frac{\ell_A}{2}\,, \\ 4t - \ell_A - \ell_B & \frac{\ell_A}{2} < t < \ell_B\,, \\ 2t + \ell_B - \ell_A & \ell_B < t < \frac{\ell_A + \ell_B}{2}\,, \\ 0 & t > \frac{\ell_A + \ell_B}{2}\,. \end{cases} \tag{4.1.9}$$

There is a single discontinuity in the residual information, at the final transition. At the transition point, the residual information reaches its maximum, $R_3(A:B) = 2\ell_B$, saturating a bound from (Balasubramanian, Kang, Murdia, & Ross, 2025), indicating that the extensive part of the entanglement of B is entirely multipartite.

Also, the jump is downward, so the residual information is not monotonically

increasing. The residual information is only a signal of multiparty entanglement, so in general this does not mean that there is no multiparty entanglement in the final equilibrium state. But in holographic cases, in the final equilibrium here the A and B RT surfaces lie close to the AB RT surface (see Figure 4.6), so it is reasonable to believe that the extensive entanglement here *is* purely bipartite, between A and C and B and C.[6]

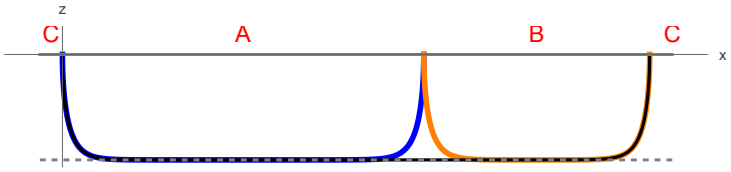

Figure 4.6: In the large subregion limit, RT surfaces have large plateau regions where they skim along the black hole horizon (dashed gray line), so the A RT surface (blue) and B RT surface (orange) lie close to the AB RT surface (black).

Let us also consider $R_3(A:C)$. We have

$$I(A:C) = s_{\text{th}} \begin{cases} 2t & t < \frac{\ell_B}{2}\,, \\ 4t - \ell_B & \frac{\ell_B}{2} < t < \frac{\ell_A}{2}\,, \\ 2t + \ell_A - \ell_B & \frac{\ell_A}{2} < t < \frac{\ell_A + \ell_B}{2}\,, \\ 2\ell_A & t > \frac{\ell_A + \ell_B}{2}\,. \end{cases} \tag{4.1.10}$$

The AC entanglement wedge is always connected between A and C. Initially the cross-section is just the vertical surface at $x = 0$. When B saturates, it acquires an additional component, a vertical surface hanging down from the B membrane, then the two components join up. See Figure 4.7.

[6]The intuition here is that the entanglement can be modelled by a tensor network with locally entangled EPR pairs across the RT surface. This is a good model for the high-temperature thermofield double state, and was also shown to model hot multi-boundary wormholes (Marolf, Maxfield, Peach, & Ross, 2015), which have a similar structure where the RT surfaces for different boundaries lie close to each other along most of their length. When the RT surfaces lie close to each other, the entangled EPR pairs across each surface simply join up to give local bipartite

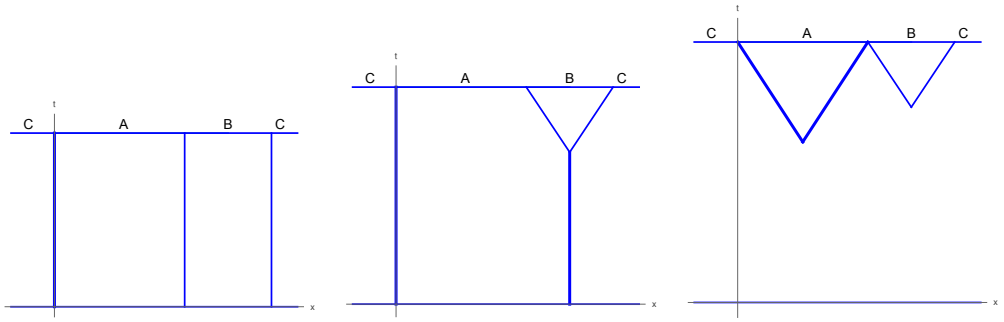

Figure 4.7: Membranes computing $S_R(A:C)$ (thick) in the setup of two finite regions.

Thus

$$S_R(A:C) = s_{\text{th}} \begin{cases} 2t & t < \frac{\ell_B}{2}\,, \\ 4t - \frac{v_E}{v_B}\ell_B & \frac{\ell_B}{2} < t < \frac{\ell_A}{2} + \frac{v_E}{v_B}\frac{\ell_B}{4}\,, \\ 2\ell_A & t > \frac{\ell_A}{2} + \frac{v_E}{v_B}\frac{\ell_B}{4}\,. \end{cases} \tag{4.1.11}$$

This gives

$$R_3(A:C) = s_{\text{th}} \begin{cases} 0 & t < \frac{\ell_B}{2}\,, \\ \ell_B\left(1 - \frac{v_E}{v_B}\right) & \frac{\ell_B}{2} < t < \frac{\ell_A}{2}\,, \\ 2t - \ell_A + \ell_B\left(1 - \frac{v_E}{v_B}\right) & \frac{\ell_A}{2} < t < \frac{\ell_A}{2} + \frac{v_E}{v_B}\frac{\ell_B}{4}\,, \\ \ell_A + \ell_B - 2t & \frac{\ell_A}{2} + \frac{v_E}{v_B}\frac{\ell_B}{4} < t < \frac{\ell_A+\ell_B}{2}\,, \\ 0 & t > \frac{\ell_A+\ell_B}{2}\,. \end{cases} \tag{4.1.12}$$

We see that the two residual information are non-zero in the same region, but their behaviour is otherwise quite different. $R_3(A:C)$ has an initial discontinuity, and then goes smoothly to zero at the end, so we see that R_3 can also decrease smoothly. It is also interesting to notice that $R_3(A:C)$ does not saturate the $2\ell_B$ bound.

entanglement between the two sides.

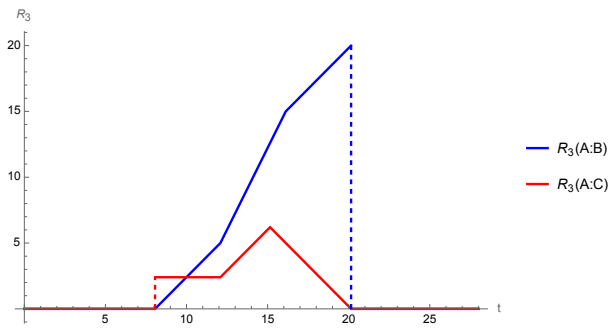

Figure 4.8: Time evolution of $R_3(A:B)$ (blue) and $R_3(A:C)$ (red) when $\ell_A = 15$ and $\ell_B = 10$.

4.2 Dynamics of I_3 and Q_4

We now turn to the dynamics of I_3 and Q_4. We will consider a single example, with regions $A = (0, \ell_A)$, $B = (\ell_A, \ell_A + \ell_B)$, $C = (\ell_A + \ell_B, \ell_A + \ell_B + \ell_C)$ and $D = (-\infty, 0) \cup (\ell_A + \ell_B + \ell_C, \infty)$. For simplicity we restrict to $\ell_A = \ell_C$. The time-dependence of I_3 in this situation at finite time was previously considered in (Balasubramanian, Bernamonti, Copland, et al., 2011). We consider just the late-time, large region behaviour, in the context of the membrane theory. This captures the main qualitative features of the previous discussion. Our main interest here is to compare the behaviour of I_3 and the novel multiparty signal Q_4 introduced in (Balasubramanian, Kang, Murdia, & Ross, 2025). As we will see below, we find non-monotonicity[7] and saturation of bounds for both signals. For I_3 we cannot have discontinuities as it is just a combination of von Neumann entropies, but we do find discontinuities for Q_4.

[7] As already noted for I_3 in (Balasubramanian, Bernamonti, Copland, et al., 2011).

If $\ell_A = \ell_C < \ell_B$, we find

$$I_3(A:B:C) = s_{\text{th}} \begin{cases} 0 & 0 < t < \frac{\ell_B}{2}\,, \\ \ell_B - 2t & \frac{\ell_B}{2} < t < \frac{\ell_A+\ell_B}{2}\,, \\ 2t - 2\ell_A - \ell_B & \frac{\ell_A+\ell_B}{2} < t < \frac{2\ell_A+\ell_B}{2}\,, \\ 0 & t > \frac{2\ell_A+\ell_B}{2}\,. \end{cases} \tag{4.2.1}$$

This gives a simple triangular profile for $-I_3$, initially increasing and then decreasing smoothly to zero.

If $\ell_B < \ell_A = \ell_C < 2\ell_B$, we have a slightly more complex behaviour,

$$I_3(A:B:C) = s_{\text{th}} \begin{cases} 0 & 0 < t < \frac{\ell_A}{2}\,, \\ 2\ell_A - 4t & \frac{\ell_A}{2} < t < \frac{2\ell_A-\ell_B}{2}\,, \\ \ell_B - 2t & \frac{2\ell_A-\ell_B}{2} < t < \frac{\ell_A+\ell_B}{2}\,, \\ 2t - 2\ell_A - \ell_B & \frac{\ell_A+\ell_B}{2} < t < \frac{2\ell_A+\ell_B}{2}\,, \\ 0 & t > \frac{2\ell_A+\ell_B}{2}\,. \end{cases} \tag{4.2.2}$$

The most interesting case is when $\ell_A = \ell_C > 2\ell_B$:

$$I_3(A:B:C) = s_{\text{th}} \begin{cases} 0 & 0 < t < \frac{\ell_A}{2}\,, \\ 2\ell_A - 4t & \frac{\ell_A}{2} < t < \frac{\ell_A+\ell_B}{2}\,, \\ -2\ell_B & \frac{\ell_A+\ell_B}{2} < t < \frac{2\ell_A-\ell_B}{2}\,, \\ 2t - 2\ell_A - \ell_B & \frac{2\ell_A-\ell_B}{2} < t < \frac{2\ell_A+\ell_B}{2}\,, \\ 0 & t > \frac{2\ell_A+\ell_B}{2}\,. \end{cases} \tag{4.2.3}$$

In this case there is a plateau region, where $I_3 = -2\ell_B$. This saturates a bound on

I_3, indicating that the entanglement of B is entirely four-partite. These results are plotted in in figures 4.10, 4.11, 4.12.

Next, we consider the calculation of Q_4 as in (Balasubramanian, Kang, Murdia, & Ross, 2025), tracing over D first and then CC^*. The calculation of $S_R(A:B)$ in (1.5.10) is similar to that in (4.1.3): we regard CD as a single region, and the AB entanglement wedge cross-section is then the same as those in Figure 4.4.[8] To calculate $S_{AA^*A_*A_*^*}$, we consider the AA^*BB^* entanglement wedge cross-section in the canonical purification of ρ_{ABC}. The first purification results in $EW(AA^*BB^*)$ bounded by a membrane κ bisecting the EW of AB (regarded as a single region) and C (Figure 4.9). Notice that κ itself possesses a non-trivial dynamic. After the second purification, $S_{AA^*A_*A_*^*}$ is computed by the minimal membrane bisecting $EW(AA^*BB^*)$ (Figure 4.9).

By comparing the membranes computing $S_{AA^*A_*A_*^*}$ in Figure 4.9 with those calculating $S_R(A:B)$ in Figure 4.4, we see that the EWCS for $S_{AA^*A_*A_*^*}$ and $S_R(A:B)$ at early times are the same.[9] Thus, the contributions cancel and $Q_4 = 0$. This ends when S_{AB} saturates and we get figure 4.5. Then $S_R(A:B) = 0$ in the membrane description, and $Q_4 \neq 0$. This continues until S_{ABC} similarly saturates, after which $S_{AA^*A_*A_*^*}$ also vanishes so we have $Q_4 = 0$ again. So Q_4 follows a unit-pulse-like time evolution profile

$$Q_4 = s_{\text{th}} \begin{cases} 0 & 0 < t < \frac{\ell_A+\ell_B}{2}\,, \\ 4\min\{\ell_A,\ell_B\} & \frac{\ell_A+\ell_B}{2} < t < \frac{\ell_A+\ell_B+\ell_C}{2}\,, \\ 0 & t > \frac{\ell_A+\ell_B+\ell_C}{2}\,. \end{cases} \tag{4.2.4}$$

[8] In Figure 4.4 we considered only the case when $\ell_A > \ell_B$. Here we also allow $\ell_A < \ell_B$ and the AB entanglement wedge cross-section saturates to the smaller value of ℓ_A and ℓ_B.

[9] In the case with $\ell_A > \ell_B$, the EWCS for $S_{AA^*A_*A_*^*}$ in the last panel in figure 4.9 changes, but it has the same area.

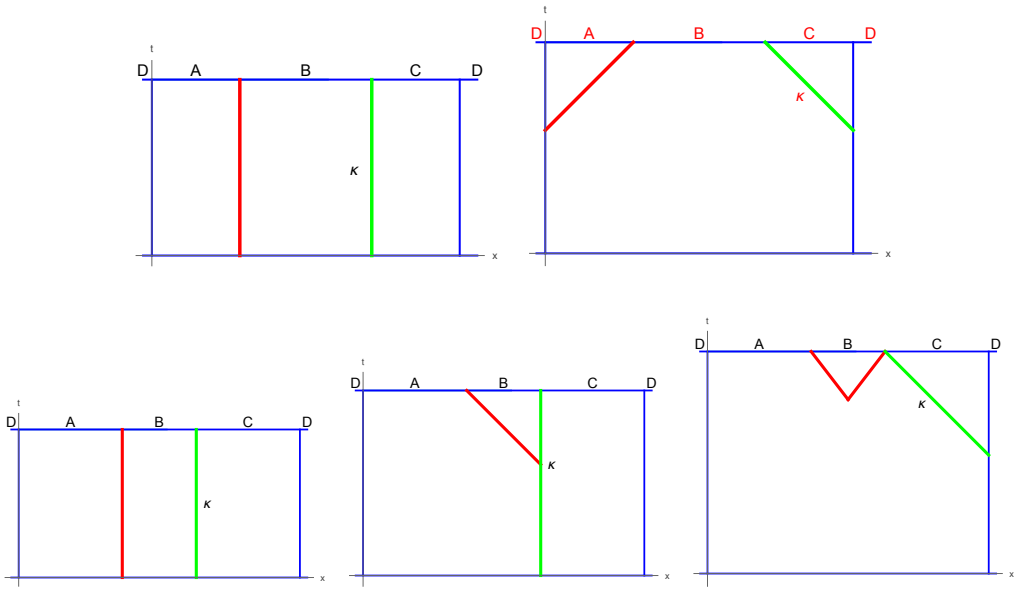

Figure 4.9: Minimal cross-sections computing $S_{AA^*A_*A_*^*}$ (red, thick) in the entanglement membrane description when $\ell_A < \ell_B$ (top row), and $\ell_A > \ell_B$ (bottom row). Notice that in the latter case, although the saturation of κ (green, thick) changes the shape of the membrane computing $S_{AA^*A_*A_*^*}$, it does not change the value of $S_{AA^*A_*A_*^*}$ in the scaling limit. We only plotted membranes before the saturation of the ABC entanglement wedge, after which all the entanglement wedge cross-sections have vanishing area in the membrane description.

where the minimisation in Q_4 between ℓ_A and ℓ_B captures how the saturated cross-section computing $S_{AA^*A_*A_*^*}$ exits the AA^*BB^* entanglement wedge, see Figure 4.9.

We plot the results when $\ell_A = \ell_C$ in Figures 4.10, 4.11, 4.12. We see that the behaviour of I_3 and Q_4 are quite different; I_3 changes smoothly, while Q_4 is piecewise constant, and non-zero only in a subregion of the region where I_3 is varying. The discontinuities in Q_4 suggest phase transitions in the entanglement structure of the state, which are not evident from just considering I_3. In particular, I_3 goes smoothly to zero, but Q_4 shows that multiparty entanglement is *not* smoothly decreasing. It is still large at least up until $t = \frac{1}{2}(\ell_A + \ell_B + \ell_C)$, when it drops suddenly to zero, suggesting a sudden change of entanglement phase.

In Figure 4.12, a bound from (Balasubramanian, Kang, Murdia, & Ross, 2025) is saturated at the plateau for I_3, indicating that the extensive entanglement of B is purely four-party at least in this period. In Q_4, the plateau also saturates a bound, which in this case indicates that the extensive entanglement of either B (if $\ell_B < \ell_A$) or A and C (if $\ell_A = \ell_C < \ell_B$) is purely four-party in that period.

As in the calculation of R_3 in the previous section, the vanishing of Q_4 and I_3 at late times does not necessarily indicate the absence of four-party entanglement, but in the holographic cases, once all the finite regions have saturated the ABC RT surface lies close to the individual A, B, C RT surfaces, suggesting that the extensive part of the entanglement is entirely bipartite entanglement between each of the finite regions and D.

In obtaining (4.2.4), we have traced out D first and then CC^*. We can also consider tracing out C first and the DD^*. This gives an independent signal, which we will denote as $\tilde{Q}_4$. When tracing out C in the first purification, the entanglement wedge of AB (regarded as a single interval) and D is bipartitioned by minimal membranes

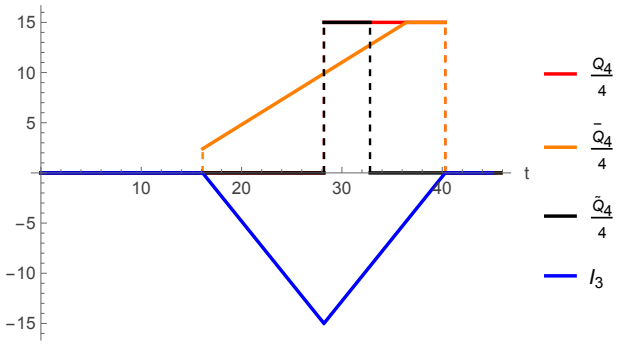

Figure 4.10: Time evolution of $I_3(A:B:C)$ (4.2.1) (blue), Q_4 (4.2.4) (red), $\tilde{Q}_4$ (4.2.5) (black) and $\bar{Q}_4$ (4.2.6) (orange) for $\ell_A = \ell_C < \ell_B$. Here, we plot for $\ell_A = 15$ and $\ell_B = 20$. In this plot, the time at which Q_4 and $\tilde{Q}_4$ start to be non-zero (the first black dashed vertical line) is the same; the time at which Q_4 and $\bar{Q}_4$ drop to 0 (orange dashed vertical line) is the same.

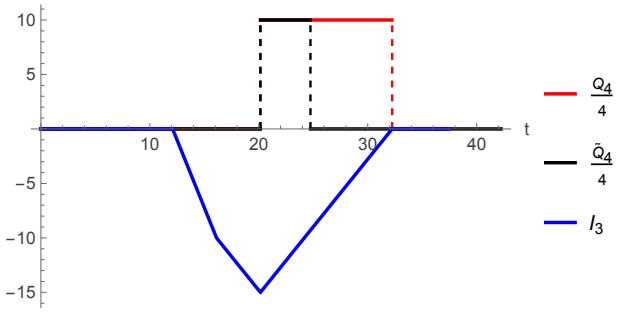

Figure 4.11: Time evolution of $I_3(A:B:C)$ (4.2.1) (blue), Q_4 (4.2.4) (red), and $\tilde{Q}_4$ (4.2.5) (black), for $\ell_B < \ell_A = \ell_C < 2\ell_B$. Here, we plot for $\ell_A = 15$ and $\ell_B = 10$. In this plot, the time at which Q_4 and $\tilde{Q}_4$ start to be non-zero (the first black dashed vertical line) is the same.

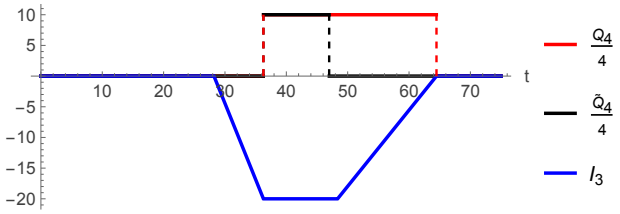

Figure 4.12: Time evolution of $I_3(A:B:C)$ (4.2.1) (blue), Q_4 (4.2.4) (red), and $\tilde{Q}_4$ (4.2.5) (black), for $2\ell_B < \ell_A = \ell_C$. Here, we plot for $\ell_A = 35$ and $\ell_B = 10$.

κ that behave as $S_R(A:C)$ in Figure 4.7. $S_{AA^*A_*A_*^*}$ in the second purification is then computed by the minimal cross-section that bisects the AA^*BB^* entanglement wedge bounded by κ, see Figure 4.13. As such, when fixing $\ell_A = \ell_C$, we have

$$\tilde{Q}_4 = s_{\text{th}} \begin{cases} 0 & 0 < t < \frac{\ell_A+\ell_B}{2}\,, \\ 4\min\{\ell_A,\ell_B\} & \frac{\ell_A+\ell_B}{2} < t < \frac{\ell_A+\ell_B}{2} + \frac{v_E}{4v_B}\ell_A\,, \\ 0 & t > \frac{\ell_A+\ell_B}{2} + \frac{v_E}{4v_B}\ell_A\,. \end{cases} \tag{4.2.5}$$

This is also plotted in figures 4.10, 4.11, 4.12. Note that compared to Q_4, the duration for $\tilde{Q}_4$ to be non-zero is shorter. This illustrates the advantage of having multiple signals, as Q_4 and I_3 capture the existence of 4-party entanglement that $\tilde{Q}_4$ fails to detect after its disappearance.

One can also consider tracing over different regions in the definition of Q_4. For example, we can trace out D and B to obtain another version of Q_4, which we

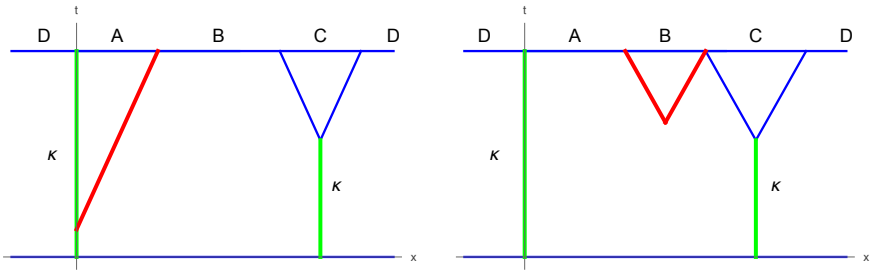

Figure 4.13: Examples of membranes computing $S_{AA^*A_*A_*^*}$ (red, thick) in $\tilde{Q}_4$. Notice that κ (green, thick) behaves as $S_R(A:C)$ by regarding AB as a single interval; $S_{AA^*A_*A_*^*} = 0$ after κ saturates.

denote as $\bar{Q}_4$. When $\ell_A > \ell_B$, the membranes for $S_R(A:C)$ consist of a vertical membrane dangling from the tip of the v_B cone anchored to B at early time as shown in Figure 4.14, followed by a diagonal membrane of slope $|v_B|$ exiting the AC entangling wedge through either of its boundary. When $\ell_A < \ell_B$, we simply have $S_R(A:C) = 0$ at all time, as the AC entanglement wedge is always disconnected.

To calculate $S_{AA^*A_*A_*^*}$, let us first consider the minimal cross-section κ that bisects the entanglement wedge of AC (regarded as one disjoint subregion) and B in the first purification. At early time, κ consists of two vertical membranes. These will later be replaced by a single triangle anchored to B (see Figure 4.14) or two diagonal membranes with slope $\pm v_B$ exiting the ABC entanglement wedge, depending on whether $\ell_B < 2\ell_A$ or $\ell_B > 2\ell_A$. In the latter case, the AA^*CC^* entanglement wedge is always disconnected, and $S_{AA^*A_*A_*^*} = 0$ at all time. As for the former, $S_{AA^*A_*A_*^*}$ is computed by the minimal cross-section bi-partitioning the AA^*CC^* entanglement wedge bounded by κ, which is a vertical membrane dangling from the tip of the v_B cone at early time (as shown in Figure 4.14) and a diagonal membrane of slope $|v_B|$ exiting the AA^*CC^* EW at late time. Notice that these are the *same* membranes as those computing $S_R(A:C)$. Hence, $\bar{Q}_4 \neq 0$ only when $\ell_A < \ell_B < 2\ell_A$: for this choice of ℓ_A and ℓ_B, $S_R(A:C) = 0$ at all times,

but $S_{AA^*A_*A_*^*}$ undergoes a non-trivial dynamic. When $\ell_B > \ell_A$, both $S_R(A:C)$ and $S_{AA^*A_*A_*^*}$ are 0 all the time; when $\ell_A > \ell_B$, both $S_R(A:C)$ and $S_{AA^*A_*A_*^*}$ have non-trivial dynamics, but they are computed by the same membranes at any time, so their contributions cancel. As such, we have that for $\ell_A < \ell_B < 2\ell_A$,

$$\bar{Q}_4 = s_{\text{th}} \begin{cases} 0 & t < \frac{\ell_B}{2}\,, \\ 4\big(t - \frac{v_E}{2v_B}\ell_B\big) & \frac{\ell_B}{2} < t < \ell_A + \frac{v_E}{2v_B}\ell_B\,, \\ 4\ell_A & \ell_A + \frac{v_E}{2v_B}\ell_B < t < \ell_A + \frac{\ell_B}{2}\,, \\ 0 & t > \ell_A + \frac{\ell_B}{2}\,. \end{cases} \tag{4.2.6}$$

This is plotted in Figure 4.10. In the cases in Figures 4.11 and 4.12, $\bar{Q}_4$ is always zero.

Unlike Q_4 or $\tilde{Q}_4$, $\bar{Q}_4$ does not display the dynamics of a unit pulse. Moreover, $\bar{Q}_4$ is non-zero in the whole interval where I_3 is nonvanishing. We also note (see Figure 4.10) that the times at which Q_4, $\tilde{Q}_4$ and $\bar{Q}_4$ saturate the $4\ell_A$ bound are different. We believe that the time at which the extensive part of the entanglement of A is entirely multipartite is when Q_4 stays at its bound $Q_4 = 4\ell_A$, i.e. when $\frac{\ell_A+\ell_B}{2} < t < \frac{\ell_A+\ell_B+\ell_C}{2}$. During this time $\tilde{Q}_4$ and $\bar{Q}_4$ could be 0 or non-maximal, which means that they fail to reflect the fact that the entanglement of A is entirely multipartite. The above different behaviours among Q_4, $\tilde{Q}_4$, and $\bar{Q}_4$ again exemplify the advantage of having multiple signals, as each of them only captures certain aspects of 4-partite entanglement.

There are a number of other versions of Q_4: these can be either positive or negative between $\pm 4\min\{\ell_A, \ell_B\}$, and might saturate these bounds or not, depending on the subregion sizes.

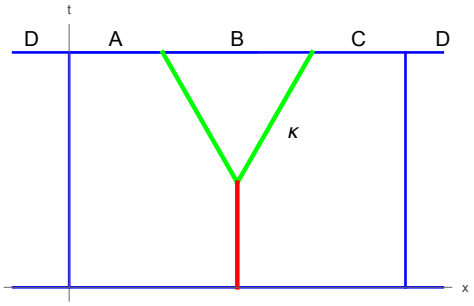

Figure 4.14: An example of the membrane computing $S_R(A:C)$ or $S_{AA^*A_*A_*^*}$ in $\bar{Q}_4$, depicted in red. In the former case, κ along with the two outermost vertical membranes together are the membranes for $S(AC)$.

5 | Conclusion

In this thesis, we studied several aspects of the real-time dynamics of entanglement entropy in various systems that admit holographic gravity duals.

In chapter 2, we studied the gravitational dual of SSD CFT (Wen & Wu, 2018b) prepared in both vacuum and thermal states with periodic boundary conditions. We found that the holographic dual of the non-trivial time evolution of SSD CFT in the ground and thermal states can be understood as pure AdS_3 and BTZ black hole spacetime with novel foliations. Remarkably, this leads to the presence of *new horizons* in both cases. Subsequently, we computed the holographic entanglement entropy in the gravity dual of SSD CFT, found agreement with CFT_2 results in all cases that are comparable, and reproduced the cooling/heating effects holographically.

In chapter 3, we addressed the degeneracy of entanglement membrane (Jonay et al., 2018; Mezei, 2018) in 2d CFT. Using holography, we found that one needs to introduce an additional degree of freedom on the membrane, which we depicted in colour in our figures. Beyond EE, this *generalised membrane theory* also captures the reflected entropy computed holographically by the entanglement wedge cross sections. To study the interpolation between generalised and ordinary membrane theory, we introduced a relevant deformation to the 2d CFT, which is holographically dual to a hairy planar BTZ black hole with an interior Kasner universe (Frenkel et al., 2020). Under such deformation, the conventional non-degenerate membrane tension emerges, which we computed both numerically and from conformal perturbation theory. We also studied reflected entropy in higher dimensional CFTs, and showed that their dynamics in the scaling limit are described by ordinary membrane theory. We found that due to the additional

degree of freedom in generalised membrane theory for 2d CFT, the dynamics of reflected entropy show different behaviours in $d = 2$ and $d \geq 3$.

In chapter 4, we applied the (generalised) membrane theory for reflected entropy introduced in chapter 3 to address the dynamics of multipartite entanglement signals (Balasubramanian, Kang, Murdia, & Ross, 2025) in chaotic systems including but not necessarily restricted to holographic theories. We found that scrambling dynamics generates multiparty entanglement with rich structure including: (a) qualitatively different dynamical behaviours for different signals, likely reflecting different dynamics for different kinds of entanglement patterns, (b) discontinuities possibly indicating dynamical phase transitions in the entanglement structure, (c) transient and non-monotonic multiparty entanglement signals, and (d) periods during which the extensive entanglement of some regions is entirely multipartite.

Bibliography

Abajian, J., Aprile, F., Myers, R. C., & Vieira, P. (2024). Correlation functions of huge operators in AdS_3/CFT_2: domes, doors and book pages. *JHEP*, *03*, 118. doi: 10.1007/JHEP03(2024)118

Akers, C., Faulkner, T., Lin, S., & Rath, P. (2022). The Page curve for reflected entropy. *JHEP*, *06*, 089. doi: 10.1007/JHEP06(2022)089

Akers, C., & Rath, P. (2020). Entanglement Wedge Cross Sections Require Tripartite Entanglement. *JHEP*, *04*, 208. doi: 10.1007/JHEP04(2020)208

Araki, H., & Lieb, E. H. (1970). Entropy inequalities. *Commun. Math. Phys.*, *18*, 160–170. doi: 10.1007/BF01646092

Asplund, C. T., Bernamonti, A., Galli, F., & Hartman, T. (2015a). Entanglement Scrambling in 2d Conformal Field Theory. *JHEP*, *09*, 110. doi: 10.1007/JHEP09(2015)110

Asplund, C. T., Bernamonti, A., Galli, F., & Hartman, T. (2015b). Holographic Entanglement Entropy from 2d CFT: Heavy States and Local Quenches. *JHEP*, *02*, 171. doi: 10.1007/JHEP02(2015)171

Babaei Velni, K., Mohammadi Mozaffar, M. R., & Vahidinia, M. H. (2020). Evolution of entanglement wedge cross section following a global quench. *JHEP*, *08*, 129. doi: 10.1007/JHEP08(2020)129

Babaei Velni, K., Mohammadi Mozaffar, M. R., & Vahidinia, M. H. (2023). Entanglement wedge cross section growth during thermalization. *Phys. Rev. D*, *107*(10), 106014. doi: 10.1103/PhysRevD.107.106014

Balasubramanian, V., Bernamonti, A., Copland, N., Craps, B., & Galli, F. (2011). Thermalization of mutual and tripartite information in strongly coupled two dimensional conformal field theories. *Phys. Rev. D*, *84*, 105017. doi: 10.1103/PhysRevD.84.105017

Balasubramanian, V., Bernamonti, A., de Boer, J., Copland, N., Craps, B., Keski-Vakkuri, E., … Staessens, W. (2011a). Holographic Thermalization. *Phys. Rev. D*, *84*, 026010. doi: 10.1103/PhysRevD.84.026010

Balasubramanian, V., Bernamonti, A., de Boer, J., Copland, N., Craps, B., Keski-Vakkuri, E., … Staessens, W. (2011b). Thermalization of Strongly Coupled Field Theories. *Phys. Rev. Lett.*, *106*, 191601. doi: 10.1103/PhysRevLett.106.191601

Balasubramanian, V., Hayden, P., Maloney, A., Marolf, D., & Ross, S. F. (2014). Multiboundary Wormholes and Holographic Entanglement. *Class. Quant. Grav.*, *31*, 185015. doi: 10.1088/0264-9381/31/18/185015

Balasubramanian, V., Kang, M. J., Cummings, C., Murdia, C., & Ross, S. F. (2025, 9). Purely GHZ-like entanglement is forbidden in holography.

Balasubramanian, V., Kang, M. J., Murdia, C., & Ross, S. F. (2025). Signals of multiparty entanglement and holography. *JHEP*, *06*, 068. doi: 10.1007/JHEP06(2025)068

Banados, M. (1999). Three-dimensional quantum geometry and black holes. *AIP Conf. Proc.*, *484*(1), 147–169. doi: 10.1063/1.59661

Banados, M., Henneaux, M., Teitelboim, C., & Zanelli, J. (1993). Geometry of the (2+1) black hole. *Phys. Rev. D*, *48*, 1506–1525. ([Erratum: Phys.Rev.D 88, 069902 (2013)]) doi: 10.1103/PhysRevD.48.1506

Banados, M., Teitelboim, C., & Zanelli, J. (1992). The Black hole in three-dimensional space-time. *Phys. Rev. Lett.*, *69*, 1849–1851. doi: 10.1103/PhysRevLett.69.1849

Banks, T., Douglas, M. R., Horowitz, G. T., & Martinec, E. J. (1998, 8). AdS dynamics from conformal field theory.

Belinski, V. A., & Khalatnikov, I. M. (1973). Effect of Scalar and Vector Fields on the Nature of the Cosmological Singularity. *Sov. Phys. JETP*, *36*, 591.

Bernamonti, A., Galli, F., & Ge, D. (2024, 2). Boundary-induced transitions in Möbius quenches of holographic BCFT.

Blake, M., Davison, R. A., Grozdanov, S., & Liu, H. (2018). Many-body chaos and energy dynamics in holography. *JHEP*, *10*, 035. doi: 10.1007/JHEP10(2018)035

Blake, M., Lee, H., & Liu, H. (2018). A quantum hydrodynamical description for scrambling and many-body chaos. *JHEP*, *10*, 127. doi: 10.1007/JHEP10(2018)127

Bombelli, L., Koul, R. K., Lee, J., & Sorkin, R. D. (1986). A Quantum Source of Entropy for Black Holes. *Phys. Rev. D*, *34*, 373–383. doi: 10.1103/PhysRevD.34.373

Breitenlohner, P., & Freedman, D. Z. (1982). Stability in Gauged Extended Supergravity. *Annals Phys.*, *144*, 249. doi: 10.1016/0003-4916(82)90116-6

Brown, J. D., & Henneaux, M. (1986). Central Charges in the Canonical Realization of Asymptotic Symmetries: An Example from Three-Dimensional Gravity. *Commun. Math. Phys.*, *104*, 207–226. doi: 10.1007/BF01211590

Caceres, E., Kundu, A., Patra, A. K., & Shashi, S. (2022). Page curves and bath deformations. *SciPost Phys. Core*, *5*, 033. doi: 10.21468/SciPostPhysCore.5.2.033

Calabrese, P., & Cardy, J. (2007). Quantum Quenches in Extended Systems. *J. Stat. Mech.*, *0706*, P06008. doi: 10.1088/1742-5468/2007/06/P06008

Calabrese, P., & Cardy, J. L. (2004). Entanglement entropy and quantum field theory. *J. Stat. Mech.*, *0406*, P06002. doi: 10.1088/1742-5468/2004/06/P06002

Calabrese, P., & Cardy, J. L. (2005). Evolution of entanglement entropy in one-dimensional systems. *J. Stat. Mech.*, *0504*, P04010. doi: 10.1088/1742-5468/2005/04/P04010

Cardy, J., & Tonni, E. (2016). Entanglement hamiltonians in two-dimensional conformal field theory. *J. Stat. Mech.*, *1612*(12), 123103. doi: 10.1088/1742-5468/2016/12/123103

Casini, H., Liu, H., & Mezei, M. (2016). Spread of entanglement and causality. *JHEP*, *07*, 077. doi: 10.1007/JHEP07(2016)077

Chowdhury, D., Georges, A., Parcollet, O., & Sachdev, S. (2022). Sachdev-Ye-Kitaev models and beyond: Window into non-Fermi liquids. *Rev. Mod. Phys.*, *94*(3), 035004. doi: 10.1103/RevModPhys.94.035004

Cui, S. X., Hayden, P., He, T., Headrick, M., Stoica, B., & Walter, M. (2019). Bit Threads and Holographic Monogamy. *Commun. Math. Phys.*, *376*(1), 609–648. doi: 10.1007/s00220-019-03510-8

Das, S., Ezhuthachan, B., Porey, S., & Roy, B. (2024, 6). Notes on heating phase dynamics in Floquet CFTs and Modular quantization.

Davison, R. A., & Delacretaz, L. V. (2024, 9). Universal thermalization dynamics in (1+1)d QFTs.

Davison, R. A., & Jiang, H. (2026). Pole skipping from universal hydrodynamics of (1+1)d QFTs. *JHEP*, *04*, 162. doi: 10.1007/JHEP04(2026)162

de Boer, J., Espíndola, R., Najian, B., Patramanis, D., van der Heijden, J., & Zukowski, C. (2022). Virasoro entanglement Berry phases. *JHEP*, *03*, 179. doi: 10.1007/JHEP03(2022)179

de Boer, J., Godet, V., Kastikainen, J., & Keski-Vakkuri, E. (2023). Quantum information geometry of driven CFTs. *JHEP*, *09*, 087. doi: 10.1007/JHEP09(2023)087

de Haro, S., Solodukhin, S. N., & Skenderis, K. (2001). Holographic reconstruction of space-time and renormalization in the AdS / CFT correspondence. *Commun. Math. Phys.*, *217*, 595–622. doi: 10.1007/s002200100381

Deutsch, J. M. (1991). Quantum statistical mechanics in a closed system. *Phys.*

Rev. A, *43*(4), 2046. doi: 10.1103/PhysRevA.43.2046

Dong, X., Harlow, D., & Wall, A. C. (2016). Reconstruction of Bulk Operators within the Entanglement Wedge in Gauge-Gravity Duality. *Phys. Rev. Lett.*, *117*(2), 021601. doi: 10.1103/PhysRevLett.117.021601

Dong, X., Lewkowycz, A., & Rangamani, M. (2016). Deriving covariant holographic entanglement. *JHEP*, *11*, 028. doi: 10.1007/JHEP11(2016)028

Dutta, S., & Faulkner, T. (2019). A canonical purification for the entanglement wedge cross-section.

Engelhardt, N., & Wall, A. C. (2019). Coarse Graining Holographic Black Holes. *JHEP*, *05*, 160. doi: 10.1007/JHEP05(2019)160

Fan, R., Gu, Y., Vishwanath, A., & Wen, X. (2020). Emergent Spatial Structure and Entanglement Localization in Floquet Conformal Field Theory. *Phys. Rev. X*, *10*(3), 031036. doi: 10.1103/PhysRevX.10.031036

Fan, R., Gu, Y., Vishwanath, A., & Wen, X. (2021). Floquet conformal field theories with generally deformed Hamiltonians. *SciPost Phys.*, *10*(2), 049. doi: 10.21468/SciPostPhys.10.2.049

Fidkowski, L., Hubeny, V., Kleban, M., & Shenker, S. (2004). The Black hole singularity in AdS / CFT. *JHEP*, *02*, 014. doi: 10.1088/1126-6708/2004/02/014

Fisher, M. P. A., Khemani, V., Nahum, A., & Vijay, S. (2023). Random Quantum Circuits. *Ann. Rev. Condensed Matter Phys.*, *14*, 335–379. doi: 10.1146/annurev-conmatphys-031720-030658

Freedman, D. Z., Gubser, S. S., Pilch, K., & Warner, N. P. (1999). Renormalization group flows from holography supersymmetry and a c theorem. *Adv. Theor. Math. Phys.*, *3*, 363–417. doi: 10.4310/ATMP.1999.v3.n2.a7

Frenkel, A., Hartnoll, S. A., Kruthoff, J., & Shi, Z. D. (2020). Holographic flows from CFT to the Kasner universe. *JHEP*, *08*, 003. doi: 10.1007/

JHEP08(2020)003

Gendiar, A., Daniška, M., Lee, Y., & Nishino, T. (2011). Suppression of finite-size effects in one-dimensional correlated systems. *Physical Review A*, *83*(5), 052118.

Gendiar, A., Krcmar, R., & Nishino, T. (2009). Spherical Deformation for One-Dimensional Quantum Systems. *Prog. Theor. Phys.*, *122*(4), 953–967. ([Erratum: Prog.Theor.Phys. 123, 393 (2010)]) doi: 10.1143/PTP.122.953

Girardello, L., Petrini, M., Porrati, M., & Zaffaroni, A. (1998). Novel local CFT and exact results on perturbations of N=4 superYang Mills from AdS dynamics. *JHEP*, *12*, 022. doi: 10.1088/1126-6708/1998/12/022

Girardello, L., Petrini, M., Porrati, M., & Zaffaroni, A. (2000). The Supergravity dual of N=1 superYang-Mills theory. *Nucl. Phys. B*, *569*, 451–469. doi: 10.1016/S0550-3213(99)00764-6

Goto, K., Nozaki, M., Ryu, S., Tamaoka, K., & Tan, M. T. (2023, 2). Scrambling and Recovery of Quantum Information in Inhomogeneous Quenches in Two-dimensional Conformal Field Theories.

Goto, K., Nozaki, M., Tamaoka, K., Tan, M. T., & Ryu, S. (2021, 12). Non-Equilibrating a Black Hole with Inhomogeneous Quantum Quench.

Grozdanov, S., Schalm, K., & Scopelliti, V. (2018). Black hole scrambling from hydrodynamics. *Phys. Rev. Lett.*, *120*(23), 231601. doi: 10.1103/PhysRevLett.120.231601

Gubser, S. S., Klebanov, I. R., & Polyakov, A. M. (1998). Gauge theory correlators from noncritical string theory. *Phys. Lett. B*, *428*, 105–114. doi: 10.1016/S0370-2693(98)00377-3

Hamilton, A., Kabat, D. N., Lifschytz, G., & Lowe, D. A. (2006). Holographic representation of local bulk operators. *Phys. Rev. D*, *74*, 066009. doi: 10.1103/PhysRevD.74.066009

Han, B., & Wen, X. (2020). Classification of SL_2 deformed Floquet conformal field theories. *Phys. Rev. B*, *102*(20), 205125. doi: 10.1103/PhysRevB.102.205125

Hartman, T. (n.d.). Lectures on Quantum Gravity and Black Holes.

Hartman, T., & Maldacena, J. (2013). Time Evolution of Entanglement Entropy from Black Hole Interiors. *JHEP*, *05*, 014. doi: 10.1007/JHEP05(2013)014

Hartnoll, S. A., Herzog, C. P., & Horowitz, G. T. (2008a). Building a Holographic Superconductor. *Phys. Rev. Lett.*, *101*, 031601. doi: 10.1103/PhysRevLett.101.031601

Hartnoll, S. A., Herzog, C. P., & Horowitz, G. T. (2008b). Holographic Superconductors. *JHEP*, *12*, 015. doi: 10.1088/1126-6708/2008/12/015

Hartnoll, S. A., & Neogi, N. (2023). AdS black holes with a bouncing interior. *SciPost Phys.*, *14*(4), 074. doi: 10.21468/SciPostPhys.14.4.074

Hayden, P., Headrick, M., & Maloney, A. (2013). Holographic Mutual Information is Monogamous. *Phys. Rev. D*, *87*(4), 046003. doi: 10.1103/PhysRevD.87.046003

Hayden, P., Parrikar, O., & Sorce, J. (2021). The Markov gap for geometric reflected entropy. *JHEP*, *10*, 047. doi: 10.1007/JHEP10(2021)047

Henningson, M., & Skenderis, K. (1998). The Holographic Weyl anomaly. *JHEP*, *07*, 023. doi: 10.1088/1126-6708/1998/07/023

Hernández-Cuenca, S., Hubeny, V. E., & Jia, H. F. (2024). Holographic entropy inequalities and multipartite entanglement. *JHEP*, *08*, 238. doi: 10.1007/JHEP08(2024)238

Hikihara, T., & Nishino, T. (2011). Connecting distant ends of one-dimensional critical systems by a sine-square deformation. *Phys. Rev. B*, *83*(6), 060414. doi: 10.1103/physrevb.83.060414

Holzhey, C., Larsen, F., & Wilczek, F. (1994). Geometric and renormalized entropy

in conformal field theory. *Nucl. Phys. B*, *424*, 443–467. doi: 10.1016/0550-3213(94)90402-2

Huang, Y. (2019, 2). Dynamics of Rényi entanglement entropy in diffusive qudit systems.
doi: 10.1088/2633-1357/abd1e2

Hubeny, V. E. (2012). Extremal surfaces as bulk probes in AdS/CFT. *JHEP*, *07*, 093. doi: 10.1007/JHEP07(2012)093

Hubeny, V. E., Maxfield, H., Rangamani, M., & Tonni, E. (2013). Holographic entanglement plateaux. *JHEP*, *08*, 092. doi: 10.1007/JHEP08(2013)092

Hubeny, V. E., Rangamani, M., & Takayanagi, T. (2007). A Covariant holographic entanglement entropy proposal. *JHEP*, *07*, 062. doi: 10.1088/1126-6708/2007/07/062

Ishibashi, N., & Tada, T. (2015). Infinite circumference limit of conformal field theory. *J. Phys. A*, *48*(31), 315402. doi: 10.1088/1751-8113/48/31/315402

Ishibashi, N., & Tada, T. (2016). Dipolar quantization and the infinite circumference limit of two-dimensional conformal field theories. *Int. J. Mod. Phys. A*, *31*(32), 1650170. doi: 10.1142/S0217751X16501700

Jafferis, D. L., Lewkowycz, A., Maldacena, J., & Suh, S. J. (2016). Relative entropy equals bulk relative entropy. *JHEP*, *06*, 004. doi: 10.1007/JHEP06(2016)004

Jiang, H., & Mezei, M. (2025). New horizons for inhomogeneous quenches and Floquet CFT. *JHEP*, *04*, 025. doi: 10.1007/JHEP04(2025)025

Jiang, H., Mezei, M., & Virrueta, J. (2025). The entanglement membrane in 2d CFT: reflected entropy, RG flow, and information velocity. *JHEP*, *06*, 114. doi: 10.1007/JHEP06(2025)114

Jonay, C., Huse, D. A., & Nahum, A. (2018, 2). Coarse-grained dynamics of operator and state entanglement.

Ju, X.-X., Pan, W.-B., Sun, Y.-W., & Zhao, Y. (2024, 11). Holographic multipartite entanglement from the upper bound of n-partite information.

Ju, X.-X., Sun, Y.-W., & Zhao, Y. (2025). Upper bound of holographic entanglement entropy combinations. *JHEP*, *09*, 085. doi: 10.1007/JHEP09(2025)085

Kasner, E. (1921). Geometrical theorems on Einstein's cosmological equations. *Am. J. Math.*, *43*, 217–221. doi: 10.2307/2370192

Katsura, H. (2012). Sine-square deformation of solvable spin chains and conformal field theories. *J. Phys. A*, *45*, 115003. doi: 10.1088/1751-8113/45/11/115003

Kaufman, A. M., Tai, M. E., Lukin, A., Rispoli, M., Schittko, R., Preiss, P. M., & Greiner, M. (2016). Quantum thermalization through entanglement in an isolated many-body system. *Science*, *353*(6301), aaf6725. doi: 10.1126/science.aaf6725

Keski-Vakkuri, E. (1999). Bulk and boundary dynamics in BTZ black holes. *Phys. Rev. D*, *59*, 104001. doi: 10.1103/PhysRevD.59.104001

Kitaev, A., & Preskill, J. (2006). Topological entanglement entropy. *Phys. Rev. Lett.*, *96*, 110404. doi: 10.1103/PhysRevLett.96.110404

Klebanov, I. R., & Witten, E. (1999). AdS / CFT correspondence and symmetry breaking. *Nucl. Phys. B*, *556*, 89–114. doi: 10.1016/S0550-3213(99)00387-9

Kudler-Flam, J., Kusuki, Y., & Ryu, S. (2020). Correlation measures and the entanglement wedge cross-section after quantum quenches in two-dimensional conformal field theories. *JHEP*, *04*, 074. doi: 10.1007/JHEP04(2020)074

Kudler-Flam, J., Nozaki, M., Numasawa, T., Ryu, S., & Tan, M. T. (2023, 9). Bridging two quantum quench problems - local joining quantum quench and Möbius quench - and their holographic dual descriptions.

Levin, M., & Wen, X.-G. (2006). Detecting Topological Order in a Ground State Wave Function. *Phys. Rev. Lett.*, *96*, 110405. doi: 10.1103/PhysRevLett.96.110405

Lewkowycz, A., & Maldacena, J. (2013). Generalized gravitational entropy. *JHEP*, *08*, 090. doi: 10.1007/JHEP08(2013)090

Lin, J. (2017, 4). Ryu-Takayanagi Area as an Entanglement Edge Term.

Lin, J., & Radičević, Đ. (2020). Comments on defining entanglement entropy. *Nucl. Phys. B*, *958*, 115118. doi: 10.1016/j.nuclphysb.2020.115118

Liu, H., & Mezei, M. (2014). Probing renormalization group flows using entanglement entropy. *JHEP*, *01*, 098. doi: 10.1007/JHEP01(2014)098

Liu, H., & Suh, S. J. (2014a). Entanglement growth during thermalization in holographic systems. *Phys. Rev. D*, *89*(6), 066012. doi: 10.1103/PhysRevD.89.066012

Liu, H., & Suh, S. J. (2014b). Entanglement Tsunami: Universal Scaling in Holographic Thermalization. *Phys. Rev. Lett.*, *112*, 011601. doi: 10.1103/PhysRevLett.112.011601

MacCormack, I., Liu, A., Nozaki, M., & Ryu, S. (2019). Holographic Duals of Inhomogeneous Systems: The Rainbow Chain and the Sine-Square Deformation Model. *J. Phys. A*, *52*(50), 505401. doi: 10.1088/1751-8121/ab3944

Maldacena, J. M. (1998). The Large N limit of superconformal field theories and supergravity. *Adv. Theor. Math. Phys.*, *2*, 231–252. doi: 10.4310/ATMP.1998.v2.n2.a1

Marolf, D., Maxfield, H., Peach, A., & Ross, S. F. (2015). Hot multiboundary wormholes from bipartite entanglement. *Class. Quant. Grav.*, *32*(21), 215006. doi: 10.1088/0264-9381/32/21/215006

Marolf, D., & Wall, A. C. (2016). State-Dependent Divergences in the Entanglement Entropy. *JHEP*, *10*, 109. doi: 10.1007/JHEP10(2016)109

Mezei, M. (2017). On entanglement spreading from holography. *JHEP*, *05*, 064. doi: 10.1007/JHEP05(2017)064

Mezei, M. (2018). Membrane theory of entanglement dynamics from holography. *Phys. Rev. D*, *98*(10), 106025. doi: 10.1103/PhysRevD.98.106025

Mezei, M., & Rajgadia, H. (2025, 12). Entanglement membrane in the Brownian SYK chain.

Mezei, M., & Stanford, D. (2017). On entanglement spreading in chaotic systems. *JHEP*, *05*, 065. doi: 10.1007/JHEP05(2017)065

Mezei, M., & van der Schee, W. (2020). Black holes often saturate entanglement entropy the fastest. *Phys. Rev. Lett.*, *124*(20), 201601. doi: 10.1103/PhysRevLett.124.201601

Mezei, M., & Virrueta, J. (2019, 9). The Quantum Null Energy Condition and Entanglement Entropy in Quenches.

Mezei, M., & Virrueta, J. (2020). Exploring the Membrane Theory of Entanglement Dynamics. *JHEP*, *02*, 013. doi: 10.1007/JHEP02(2020)013

Moosavi, P. (2021). Inhomogeneous conformal field theory out of equilibrium. In *Annales henri poincaré* (pp. 1–40).

Nahum, A., Ruhman, J., Vijay, S., & Haah, J. (2017). Quantum Entanglement Growth Under Random Unitary Dynamics. *Phys. Rev. X*, *7*(3), 031016. doi: 10.1103/PhysRevX.7.031016

Okunishi, K. (2016). Sine-square deformation and Möbius quantization of 2D conformal field theory. *PTEP*, *2016*(6), 063A02. doi: 10.1093/ptep/ptw060

Page, D. N. (1993). Average entropy of a subsystem. *Phys. Rev. Lett.*, *71*, 1291–1294. doi: 10.1103/PhysRevLett.71.1291

Rakovszky, T., Pollmann, F., & von Keyserlingk, C. W. (2019). Sub-ballistic Growth of Rényi Entropies due to Diffusion. *Phys. Rev. Lett.*, *122*(25), 250602. doi: 10.1103/PhysRevLett.122.250602

Rakovszky, T., Pollmann, F., & von Keyserlingk, C. W. (2020, 10). Comment on "Entanglement growth in diffusive systems".

Rampp, M. A., Rather, S. A., & Claeys, P. W. (2024). Entanglement membrane in exactly solvable lattice models. *Phys. Rev. Res.*, *6*(3), 033271. doi: 10.1103/PhysRevResearch.6.033271

Rangamani, M., & Takayanagi, T. (2017). *Holographic Entanglement Entropy* (Vol. 931). Springer. doi: 10.1007/978-3-319-52573-0

Rigol, M., Dunjko, V., & Olshanii, M. (2008). Thermalization and its mechanism for generic isolated quantum systems. *Nature*, *452*(7189), 854–858. doi: 10.1038/nature06838

Roberts, D. A., Stanford, D., & Susskind, L. (2015). Localized shocks. *JHEP*, *03*, 051. doi: 10.1007/JHEP03(2015)051

Rosenhaus, V. (2019). An introduction to the SYK model. *J. Phys. A*, *52*, 323001. doi: 10.1088/1751-8121/ab2ce1

Ryu, S., & Takayanagi, T. (2006a). Aspects of Holographic Entanglement Entropy. *JHEP*, *08*, 045. doi: 10.1088/1126-6708/2006/08/045

Ryu, S., & Takayanagi, T. (2006b). Holographic derivation of entanglement entropy from AdS/CFT. *Phys. Rev. Lett.*, *96*, 181602. doi: 10.1103/PhysRevLett.96.181602

Shenker, S. H., & Stanford, D. (2014). Black holes and the butterfly effect. *JHEP*, *03*, 067. doi: 10.1007/JHEP03(2014)067

Skenderis, K., & Solodukhin, S. N. (2000). Quantum effective action from the AdS / CFT correspondence. *Phys. Lett. B*, *472*, 316–322. doi: 10.1016/S0370-2693(99)01467-7

Son, D. T., & Starinets, A. O. (2002). Minkowski space correlators in AdS / CFT correspondence: Recipe and applications. *JHEP*, *09*, 042. doi: 10.1088/1126-6708/2002/09/042

Srednicki, M. (1993). Entropy and area. *Phys. Rev. Lett.*, *71*, 666–669. doi: 10.1103/PhysRevLett.71.666

Srednicki, M. (1994, 3). Chaos and Quantum Thermalization. *Phys. Rev. E*, *50*. doi: 10.1103/PhysRevE.50.888

Susskind, L., & Witten, E. (1998, 5). The Holographic bound in anti-de Sitter space.

Takayanagi, T., & Umemoto, K. (2018). Entanglement of purification through holographic duality. *Nature Phys.*, *14*(6), 573–577. doi: 10.1038/s41567-018-0075-2

Tamura, S., & Katsura, H. (2017). Zero-energy states in conformal field theory with sine-square deformation. *PTEP*, *2017*(11), 113A01. doi: 10.1093/ptep/ptx147

Vardhan, S., & Moudgalya, S. (2024, 7). Entanglement dynamics from universal low-lying modes.

Verstraete, F., Dehaene, J., De Moor, B., & Verschelde, H. (2002). Four qubits can be entangled in nine different ways. *Phys. Rev. A*, *65*(5), 052112. doi: 10.1103/PhysRevA.65.052112

Žnidarič, M. (2020). Entanglement growth in diffusive systems. *Commun. Phys.*, *3*(1), 100. doi: 10.1038/s42005-020-0366-7

Walter, M., Gross, D., & Eisert, J. (2016, 12). Multi-partite entanglement.

Wen, X., Fan, R., & Vishwanath, A. (2022, 10). Floquet's Refrigerator: Conformal Cooling in Driven Quantum Critical Systems.

Wen, X., Fan, R., Vishwanath, A., & Gu, Y. (2021). Periodically, quasiperiodically, and randomly driven conformal field theories. *Phys. Rev. Res.*, *3*(2), 023044. doi: 10.1103/PhysRevResearch.3.023044

Wen, X., Ryu, S., & Ludwig, A. W. W. (2016). Evolution operators in conformal field theories and conformal mappings: Entanglement Hamiltonian, the

sine-square deformation, and others. *Phys. Rev. B*, *93*(23), 235119. doi: 10.1103/PhysRevB.93.235119

Wen, X., & Wu, J.-Q. (2018a, 4). Floquet conformal field theory.

Wen, X., & Wu, J.-Q. (2018b). Quantum dynamics in sine-square deformed conformal field theory: Quench from uniform to nonuniform conformal field theory. *Phys. Rev. B*, *97*(18), 184309. doi: 10.1103/PhysRevB.97.184309

Witten, E. (1998). Anti-de Sitter space and holography. *Adv. Theor. Math. Phys.*, *2*, 253–291. doi: 10.4310/ATMP.1998.v2.n2.a2

Witten, E. (2023, 3). Algebras, Regions, and Observers.

Zhou, T., & Nahum, A. (2019). Emergent statistical mechanics of entanglement in random unitary circuits. *Phys. Rev. B*, *99*(17), 174205. doi: 10.1103/PhysRevB.99.174205

Zhou, T., & Nahum, A. (2020). Entanglement Membrane in Chaotic Many-Body Systems. *Phys. Rev. X*, *10*(3), 031066. doi: 10.1103/PhysRevX.10.031066

A | Appendices to Chapter 2

A.1 Review of SSD CFT

In the main text, we introduced the cylinder $\mathbb{R} \times S^1$ with coordinate (2.2.1). To study CFT_2, we map the cylinder to the *complex plane* $\mathbb{C}$ via the exponential map,

$$\begin{cases} z = e^w = e^{\tau + ix}, \\ \overline{z} = e^{\overline{w}} = e^{\tau - ix}. \end{cases} \tag{A.1.1}$$

H_0 is *dilation* on the z-plane. Analytically continuing to real time $\tau \to it$, we have

$$\begin{cases} z = \lambda e^w = e^{i(t+x)}, \\ \overline{z} = \lambda e^{\overline{w}} = e^{i(t-x)}. \end{cases} \tag{A.1.2}$$

where $\lambda = e^\tau$ in Euclidean signature. In Lorentzian signature, z_{new} and $\overline{z}_{\text{new}}$ are on the *unit circle*.

A.1.1 SSD CFT

A.1.1.1 The action of H_1

Under the exponential map (A.1.1), the SSD Hamiltonian (2.2.5) becomes

$$H_1 = 2\int_0^{2\pi} dx\ \sin^2\Big(\frac{x}{2}\Big) T_{00}(x) \tag{A.1.3}$$

$$= \oint \frac{dz}{2\pi i}\Big(-\frac{1}{2} + z - \frac{z^2}{2}\Big) T(z) - (z \to \bar{z}) - \frac{c}{12} \tag{A.1.4}$$

$$= L_0 - \frac{L_{-1} + L_1}{2} + \bar{L}_0 - \frac{\bar{L}_{-1} + \bar{L}_1}{2} - \frac{c}{12}. \tag{A.1.5}$$

While H_0 acts as dilation, the action of H_1 is a more general $SL(2)$ transformation. To see this, we perform a coordinate transformation $(z, \overline{z}) \to (\chi, \overline{\chi})$:

$$\begin{aligned} H_1 &= \oint \frac{dz}{2\pi i} \Big(-\frac{1}{2}(z-1)^2 \Big) T(x) + h.c \\ &= \oint \frac{d\chi}{2\pi i} \frac{dz}{d\chi} \Big(-\frac{1}{2}(z-1)^2 \Big) \Big[\Big(\frac{d\chi}{dz} \Big)^2 T(\chi) + \frac{c}{12} \mathrm{Sch}(\chi, z) \Big] + h.c\,, \end{aligned} \tag{A.1.6}$$

where $\mathrm{Sch}(\chi, z)$ is the Schwarzian. By requiring that H_1 is dilation on the χ-plane (Fan et al., 2020), i.e. that the prefactor of $T(\chi)$ is equal to χ, we obtain a differential equation with the solution:[1]

$$\chi(z) = e^{\frac{z+1}{z-1}}\,, \qquad\qquad \overline{\chi}(\overline{z}) = e^{\frac{\overline{z}+1}{\overline{z}-1}}\,, \tag{A.1.7}$$

Plugging in this map into (A.1.6), we get

$$H_1 = \oint \frac{d\chi}{2\pi i} \Big(\chi T_{00}(\chi) - \frac{c}{24} \frac{1}{\chi} \Big) + h.c\,, \tag{A.1.8}$$

and evaluating the contour integral (together with an identical contribution coming from the anti-holomorphic term) gives the Casimir energy $-c/12$.

To our knowledge, the map (A.1.7) has not appeared in the literature, but we show around (A.1.27) that it can be obtained as a limit of maps known from prior work. Note that the maps contain essential singularities at $z = 1$ and $\overline{z} = 1$, respectively, which means that we need to exclude them in defining (A.1.7). These are the fixed points of the $SL(2)$ transformations (A.1.12) and (A.1.13), so we simply have $z_{\mathrm{new}} = z = 1$ and $\overline{z}_{\mathrm{new}} = \overline{z} = 1$ in these two excluded points. On the χ plane, we

[1] The most general solutions take the form $\chi(z) = c\, e^{\frac{z+1}{z-1}}$ and $\overline{z} = \overline{c}\, e^{\frac{\overline{z}+1}{\overline{z}-1}}$; the constants c and $\overline{c}$ have no effect on the coordinate transformations.

then have the Heisenberg evolution

$$e^{\tau H_1} O(\chi, \bar{\chi}) e^{-\tau H_1} = O(\lambda\chi, \lambda\bar{\chi}), \tag{A.1.9}$$

where $\lambda = e^{\tau}$. Back to the z-plane, the effect of H_1 is to shift the operator O from z to z_{new}, where z_{new} is related to z via (Wen & Wu, 2018b)

$$\chi(z_{\text{new}}) = \lambda\chi(z), \tag{A.1.10}$$

from which one can solve for z_{new}:

$$e^{\frac{z_{\text{new}}+1}{z_{\text{new}}-1}} = e^{\tau} \cdot e^{\frac{z+1}{z-1}}, \tag{A.1.11}$$

$$\Rightarrow z_{\text{new}} = \frac{(1+\frac{\tau}{2})z - \frac{\tau}{2}}{\frac{\tau}{2}z + (1-\frac{\tau}{2})}. \tag{A.1.12}$$

For the anti-holomorphic part, we repeat the above calculation with $z \to \overline{z}$, arriving at

$$\overline{z}_{\text{new}} = \frac{(1+\frac{\tau}{2})\overline{z} - \frac{\tau}{2}}{\frac{\tau}{2}\overline{z} + (1-\frac{\tau}{2})}. \tag{A.1.13}$$

(A.1.12) and (A.1.13) are $SL(2)$ transformations on the complex plane. Transforming back to the cylinder via the inverse of (A.1.1), and performing analytic continuation $\tau = it$ then yields (2.2.6) and (2.2.7) in the main text.

The relation among the cylinder (left), complex plane (middle), and the $SL(2)$

transformed plane (right) are summarised as follows:

$$\begin{array}{ccccc} w, \overline{w} & \xrightarrow[\overline{z}=e^{\overline{w}}]{z=e^{w}} & z, \overline{z} & \xrightarrow[\overline{\chi}=e^{\frac{\overline{z}+1}{\overline{z}-1}}]{\chi=e^{\frac{z+1}{z-1}}} & \chi, \overline{\chi} \\ H_1 \downarrow & & H_1 \downarrow & & H_1 \downarrow \text{Dilations} \\ w_{\text{new}}, \overline{w}_{\text{new}} & \xrightarrow[\overline{z}_{\text{new}}=e^{\overline{w}_{\text{new}}}]{z_{\text{new}}=e^{w_{\text{new}}}} & z_{\text{new}}, \overline{z}_{\text{new}} & \xrightarrow[\lambda\overline{\chi}=e^{\frac{\overline{z}_{\text{new}}+1}{\overline{z}_{\text{new}}-1}}]{\lambda\chi=e^{\frac{z_{\text{new}}+1}{z_{\text{new}}-1}}} & \lambda\chi, \lambda\overline{\chi} \end{array} \tag{A.1.14}$$

A.1.1.2 Trigonometric forms of the coordinate transformations

In Lorentzian signature, $|z_{\text{new}}| = |\overline{z}_{\text{new}}| = 1$ as Mobius transformations preserve the unit circles (A.1.2) z_{new} and $\overline{z}_{\text{new}}$ lives on. For technical conveniences in making Figure 2.1 and 2.2, we follow (Goto et al., 2021) and write z_{new} and $\overline{z}_{\text{new}}$ in trigonometric forms: (A.1.12) and (2.2.6) can be written as

$$z_{\text{new}} = \cos\ 2\varphi + i\ \sin\ 2\varphi, \qquad\qquad w_{\text{new}} = 2i\varphi\,, \tag{A.1.15}$$

where

$$\sin\varphi = \frac{\sin\left(\frac{x}{2}\right)}{\sqrt{1 - t\ \sin x + t^2 \sin^2\left(\frac{x}{2}\right)}}, \quad \cos\varphi = \frac{\cos\left(\frac{x}{2}\right) - t\ \sin\left(\frac{x}{2}\right)}{\sqrt{1 - t\ \sin x + t^2 \sin^2\left(\frac{x}{2}\right)}}\,. \tag{A.1.16}$$

We then have $\varphi \in [\frac{x}{2}, \pi] \in [0, \pi]$ (Goto et al., 2021) as t ranges from $[0, \infty)$. Similarly, (A.1.13) and (2.2.7) can be written as

$$\overline{z}_{\text{new}} = \cos\ 2\overline{\varphi} + i\ \sin\ 2\overline{\varphi}, \qquad\qquad \overline{w}_{\text{new}} = 2i\overline{\varphi}\,, \tag{A.1.17}$$

where

$$\sin\overline{\varphi} = \frac{-\sin\left(\frac{x}{2}\right)}{\sqrt{1+t\ \sin x + t^2\sin^2\left(\frac{x}{2}\right)}}, \quad \cos\overline{\varphi} = \frac{\cos\left(\frac{x}{2}\right)+t\ \sin\left(\frac{x}{2}\right)}{\sqrt{1+t\ \sin x + t^2\sin^2\left(\frac{x}{2}\right)}}\,. \tag{A.1.18}$$

We then have $\overline{\varphi} \in [-\frac{x}{2}, 0] \in [-\pi, 0]$ (Goto et al., 2021) as t ranges from $[0, \infty)$. Note that φ and $\overline{\varphi}$ are in general *not* complex conjugates.

The explicit expressions of $t_{\text{new}}(t,x)$ and $x_{\text{new}}(t,x)$ can be found from (2.2.6), (2.2.7), (2.2.8), (A.1.16) and (A.1.18)

$$t_{\text{new}}(t,x) = \arccos\left[\frac{\cos\left(\frac{x}{2}\right)-t\ \sin\left(\frac{x}{2}\right)}{\sqrt{1-t\ \sin x + t^2\sin^2\left(\frac{x}{2}\right)}}\right] - \arccos\left[\frac{\cos\left(\frac{x}{2}\right)+t\ \sin\left(\frac{x}{2}\right)}{\sqrt{1+t\ \sin x + t^2\sin^2\left(\frac{x}{2}\right)}}\right], \tag{A.1.19}$$

$$x_{\text{new}}(t,x) = \arccos\left[\frac{\cos\left(\frac{x}{2}\right)-t\ \sin\left(\frac{x}{2}\right)}{\sqrt{1-t\ \sin x + t^2\sin^2\left(\frac{x}{2}\right)}}\right] + \arccos\left[\frac{\cos\left(\frac{x}{2}\right)+t\ \sin\left(\frac{x}{2}\right)}{\sqrt{1+t\ \sin x + t^2\sin^2\left(\frac{x}{2}\right)}}\right]. \tag{A.1.20}$$

A.1.1.3 SSD CFT as a CFT on curved spacetime

Under Weyl transformations, primary correlators transform as

$$\langle O(z,\bar{z})\ldots\rangle_{ds'^2=\Omega\bar{\Omega}\,ds^2} = \Omega(z)^{-h}\,\bar{\Omega}(\bar{z})^{-\bar{h}}\ldots\langle O(z,\bar{z})\ldots\rangle_{ds^2}\,. \tag{A.1.21}$$

Now let us choose $\Omega = \left(\frac{\partial w_{\text{new}}}{\partial(ix)}\right)^{-1}$ and similarly for $\bar{\Omega}$. Then the second quantity in (2.2.10) becomes the RHS of the above equation. It only remains to compute metric ds'^2 in τ, x coordinates. To this end, we write:

$$
\begin{aligned}
ds'^2 &= \Omega\bar{\Omega}\, dw_{\rm new} d\overline{w}_{\rm new} \\
&= \Big(\frac{\partial w_{\rm new}}{\partial(ix)}\Big)^{-1}\Big(\frac{\partial \overline{w}_{\rm new}}{\partial(-ix))}\Big)^{-1}\Big(\frac{\partial w_{\rm new}}{\partial\tau}d\tau + \frac{\partial w_{\rm new}}{\partial x}dx\Big)\Big(\frac{\partial \overline{w}_{\rm new}}{\partial\tau}d\tau + \frac{\partial \overline{w}_{\rm new}}{\partial x}dx\Big) \\
&= \Big(\frac{\partial_\tau w_{\rm new}}{\partial_x w_{\rm new}}\, d\tau + dx\Big)\Big(\frac{\partial_\tau \overline{w}_{\rm new}}{\partial_x \overline{w}_{\rm new}}\, d\tau + dx\Big) \\
&= \Big(- iv_1(x)\, d\tau + dx\Big)\Big(iv_1(x)\, d\tau + dx\Big) \\
&= v_1(x)^2 d\tau^2 + dx^2\,,
\end{aligned}
\tag{A.1.22}
$$

which is the curved space metric (2.2.9). Thus the Weyl transformation indeed directly gives the third quantity in (2.2.10).

A.1.1.4 H_q with $q > 1$

As for H_q with $q > 1$, the conformal map $z = e^{qw}$ takes the cylinder to a q-sheet Riemann surface, where H_q takes the same form as H_1

$$
H_q = 2\int_0^{2\pi} dx\, \sin^2\Big(q\cdot\frac{x}{2}\Big)T_{00}(x) \tag{A.1.23}
$$

$$
= q\oint \frac{dz}{2\pi i}\Big(- \frac{1}{2} + z - \frac{z^2}{2}\Big)T(z) - (z\to\bar{z}) - q\frac{c}{12}. \tag{A.1.24}
$$

The calculation then follows the same as above, with $2\pi \to 2\pi/q$. Namely,

$$
z_{\rm new} = \frac{(1+q\frac{\tau}{2})z - q\frac{\tau}{2}}{q\frac{\tau}{2}z + (1-q\frac{\tau}{2})}, \tag{A.1.25}
$$

$$
ds^2 = q^2\frac{e^{2q\tau}}{(1-\cos\ qx)^2}\Big[(1-\cos\ qx)^2 d\tau^2 + dx^2\Big]. \tag{A.1.26}
$$

Note that now z and $\overline{z}$ are coordinates on the q-sheeted Riemann surface and there is a branch cut in the z-plane. The fact that the system is q copies of identical

theories transcribes to the crossing of sheets on the z-plane.

A.1.2 General Cases

(Wen & Wu, 2018b; Goto et al., 2021) also studied quantum quench with the one-parameter generalisation of the SSD Hamiltonian H_1, the Mobius Hamiltonian, The Mobius deformed Hamiltonian H_θ is given by

$$H_\theta = L_0 - \tanh 2\theta \, \frac{L_{-1} + L_1}{2} + \overline{L}_0 - \tanh 2\theta \, \frac{\overline{L}_{-1} + \overline{L}_1}{2} - \frac{c}{12}. \tag{A.1.27}$$

The $\theta \to 0$ and $\theta \to \infty$ limit of H_θ are H_0 and H_1, respectively. This family of Hamiltonians act as dilatations on the ξ plane as $H_\theta^{(\xi)} = \frac{1}{\cosh(2\theta)} \left(L_0^{(\xi)} + \bar{L}_0^{(\xi)} \right) - \frac{c}{12}$ with

$$\xi = -\frac{\cosh\theta \, z - \sinh\theta}{\sinh\theta \, z - \cosh\theta} \, . \tag{A.1.28}$$

By raising this map to the power $\cosh(2\theta)$, we obtain a properly normalised dilatation operator:[2]

$$\chi_\theta = (-\xi)^{\cosh(2\theta)} = \left(\frac{\cosh\theta \, z - \sinh\theta}{\sinh\theta \, z - \cosh\theta} \right)^{\cosh(2\theta)} \, , \tag{A.1.29}$$

which has the the limit

$$\chi = \lim_{\theta \to \infty} \chi_\theta = e^{\frac{z+1}{z-1}} \, . \tag{A.1.30}$$

This agrees with (A.1.7).

The methodology of describing the non-trivial time evolution of inhomogeneous

[2]Through the exponential map we can see that raising the map to some power corresponds to rescaling time on the cylinder.

non-equilibrium CFT as coordinate transformations reviewed in Section 2.2.2 is valid beyond SSD (where only $SL(2)$ deformations are considered) and extends to deformations involving the *full* Virasoro algebras. In these cases, it is shown (Moosavi, 2021) that the projective unitary representation of the universal cover of the orientation-preserving diffeomorphisms of the circle $\widetilde{\mathrm{Diff}}_+(S^1)$ allows one to flatten out the deformation $v(x)$ and map the expectations to ordinary equilibrium CFT under coordinate transformations. Like in the SSD case, these coordinate transformations capture the full information of the time evolution of the deformed CFT. In (de Boer et al., 2023), it is further demonstrated that just as in SSD CFT, these generally deformed CFTs can be understood as CFTs on curved spacetime as well.

A.2 Changing the cutoff in AdS/CFT

A.2.1 AdS/CFT with a nonuniform cutoff

We will show on the example of a scalar field how the extrapolate dictionary (Banks, Douglas, Horowitz, & Martinec, 1998) of AdS/CFT changes under changing the cutoff prescription. In the absence of a source of a scalar field, we have

$$\phi(\rho, y^\mu) = (2\Delta - d)\rho^{-\Delta} O(y^\mu) + (\text{subleading})\,, \tag{A.2.1}$$

where ρ is the bulk radial direction and $O(y^\mu)$ is the boundary CFT primary field. It is clear that if we choose two different bulk radial coordinates related by $r = \Omega(y^\mu) r_{\text{new}}$ then the same bulk physics will give rise to boundary correlators

that differ by some factors

$$\begin{aligned}\langle O(y^\mu)\ldots\rangle_{\text{CFT, flat}} &= \lim_{r_{\text{new}}\to\infty}\frac{r_{\text{new}}^\Delta}{2\Delta-d}\ldots\langle\phi(r_{\text{new}},y^\mu)\ldots\rangle_{\text{AdS}}\\ &= \Omega(y^\mu)^{-\Delta}\ldots\langle O(y^\mu)\ldots\rangle_{\text{wiggly bdy}}\ ,\end{aligned} \tag{A.2.2}$$

where the last object is the boundary correlation function that is computed from the nonuniform cutoff prescription on the gravity side

$$\epsilon = \frac{1}{R} = \frac{1}{\Omega(y^\mu)R_{\text{new}}}\ , \tag{A.2.3}$$

where in our application the choice $\Omega = \sqrt{\frac{\partial w_{\text{new}}}{\partial w}\frac{\partial\overline{w}_{\text{new}}}{\partial\overline{w}}}$ is made. $\langle O(y^\mu)\ldots\rangle_{\text{wiggly bdy}}$ is hence equal to the second object in (2.2.10), as stated in the main text.

It is also equal to the curved space CFT correlation function, as we show on the CFT side from applying a Weyl transformation and on the gravity side by adapting Fefferman-Graham coordinates to the nonuniform cutoff surface.

A.2.2 The Fefferman-Graham expansion with a curved boundary

Let us change the spatial coordinate as

$$x = 2\,\text{arccot}\,X\ , \tag{A.2.4}$$

then the boundary metric (2.2.9) takes the conformally flat form:

$$ds^2_{\text{bdy}} = \frac{4}{(1+X^2)^2}\left(-dt^2+dX^2\right)\ . \tag{A.2.5}$$

The Fefferman-Graham expansion with this boundary metric takes the form:

$$\begin{aligned} ds^2 =& \frac{dr^2}{r^2} - \frac{(4r^2 + X^2 - (1+X^2)^2\, L(t+X))(4r^2 + X^2 - (1+X^2)^2\, R(t-X))}{4r^2(1+X^2)^2}\, dt^2 \\ &+ \frac{(4r^2 - 1 + (1+X^2)^2\, L(t+X))(4r^2 - 1 + (1+X^2)^2\, R(t-X))}{4r^2(1+X^2)^2}\, dX^2 \\ &+ \frac{(8r^2 - 1 + X^2)(L(t+X) - R(t-X))}{4r^2}\, dt\, dX\,, \end{aligned} \tag{A.2.6}$$

where $L(t+X)$ and $R(t-X)$ are arbitrary left and right moving functions corresponding to the holomorphic and anti-holomorphic stress tensor. The geometry (A.2.6) first considered in (Skenderis & Solodukhin, 2000) is the generalisation of the well-known Banados geometries (Banados, 1999) appropriate for a flat boundary, and reduce to them in the limit of small X. We obtained these expressions by solving Einstein's equations in a $1/r$ series expansion, a method reviewed in (Skenderis & Solodukhin, 2000; de Haro et al., 2001). We can easily convert the metric to x coordinates using the relation (A.2.4).

If we set $t = 0$ and convert X back to x, the resulting metric on the $t = 0$ slice should match with the metric on the $t_{\text{new}} = 0$ slice of the empty AdS_3 or BTZ metrics. Converting them to Fefferman-Graham form allows us to read off the functions L and R. For the AdS_3 case, we get that $L = R = 0$. In this case, a redefinition of r reproduces the metric presented in (MacCormack et al., 2019). For BTZ we find:

$$L(y) = R(y) = \frac{1 + r_+^2}{(1+y^2)^2}\,. \tag{A.2.7}$$

A.3 Asymptotic symmetries of AdS_3

In this appendix we present the Killing vectors of global AdS_3 in (Hartman, n.d.):

$$\zeta_{-1} = \frac{1}{2}e^{-i(t+x)}\Big(\frac{r}{\sqrt{r^2+1}}\partial_t + \frac{\sqrt{r^2+1}}{r}\partial_x + i\sqrt{r^2+1}\partial_r\Big), \tag{A.3.1}$$

$$\zeta_0 = \frac{1}{2}(\partial_t + \partial_x), \tag{A.3.2}$$

$$\zeta_1 = \frac{1}{2}e^{i(t+x)}\Big(\frac{r}{\sqrt{r^2+1}}\partial_t + \frac{\sqrt{r^2+1}}{r}\partial_x - i\sqrt{r^2+1}\partial_r\Big), \tag{A.3.3}$$

$$\overline{\zeta_{-1}} = \frac{1}{2}e^{-i(t-x)}\Big(\frac{r}{\sqrt{r^2+1}}\partial_t - \frac{\sqrt{r^2+1}}{r}\partial_x + i\sqrt{r^2+1}\partial_r\Big), \tag{A.3.4}$$

$$\overline{\zeta_0} = \frac{1}{2}(\partial_t - \partial_x), \tag{A.3.5}$$

$$\overline{\zeta_1} = \frac{1}{2}e^{i(t-x)}\Big(\frac{r}{\sqrt{r^2+1}}\partial_t - \frac{\sqrt{r^2+1}}{r}\partial_x - i\sqrt{r^2+1}\partial_r\Big), \tag{A.3.6}$$

where we dropped the "new" scripts for notation simplicity. These vectors are indeed obey the Killing equations

$$\nabla_{(\mu}(\zeta_i)_{\nu)} = 0, \qquad \nabla_{(\mu}(\overline{\zeta_i})_{\nu)} = 0, \qquad (i = 0, \pm 1)\,. \tag{A.3.7}$$

The Killing vectors obey the $SL(2,\mathbb{R})_L \times SL(2,\mathbb{R})_R$ algebra:

$$i\{\zeta_1, \zeta_{-1}\} = 2\zeta_0, \qquad i\{\zeta_1, \zeta_0\} = \zeta_1, \qquad i\{\zeta_{-1}, \zeta_0\} = -\zeta_{-1}, \tag{A.3.8}$$

$$i\{\overline{\zeta_1}, \overline{\zeta_{-1}}\} = 2\overline{\zeta_0}, \qquad i\{\overline{\zeta_1}, \overline{\zeta_0}\} = \overline{\zeta_1}, \qquad i\{\overline{\zeta_{-1}}, \overline{\zeta_0}\} = -\overline{\zeta_{-1}}, \tag{A.3.9}$$

where $\{.\,,.\}$ here denotes the Lie bracket and hence we have extra i's on the LHS compared to when writing commutators.

A.4 Geodesic equations

In this appendix, we study null and spacelike geodesic equations, on pure AdS_3 and BTZ black holes, respectively. Our method is largely based on (Hubeny, 2012). We will be working in geometries in the $(t_{\text{new}}, x_{\text{new}}, r_{\text{new}})$ coordinate throughout this appendix, so we will drop the "new" subscript for notation simplicity.

We consider Lorentzian (2+1)-dimensional metric:

$$ds^2 = -f(r)dt^2 + \frac{dr^2}{f(r)} + r^2 dx^2, \tag{A.4.1}$$

where $\lim_{r\to\infty} f(r) = r^2$ so that the spacetime is asymptotically AdS_3. As the metric is independent of t and x, there are two conserved quantities:

$$E = f(r)\frac{dt}{d\lambda}, \qquad\qquad L = r^2\frac{dx}{d\lambda}, \tag{A.4.2}$$

which correspond to the energy and angular momentum, respectively. The norm of the tangent vector is:

$$\kappa = g_{\mu\nu}\frac{dx^\mu}{d\lambda}\frac{dx^\nu}{d\lambda} = -\frac{1}{f(r)}E^2 + \frac{1}{f(r)}\left(\frac{dr}{d\lambda}\right)^2 + \frac{1}{r^2}L^2, \tag{A.4.3}$$

where $\kappa = +1, 0, -1$ for spacelike, null, and timelike geodesics, respectively. We will focus on null and spacelike geodesics. Equation (A.4.3) can be put into the general form

$$\left(\frac{dr}{d\lambda}\right)^2 + V(r) = 0, \qquad V(r) = -E^2 - \kappa f(r) + L^2\frac{f(r)}{r^2}, \tag{A.4.4}$$

where $V(r)$ can be thought of as an effective potential. Geodesic motion requires $\left(\frac{dr}{d\lambda}\right)^2 \geq 0$. Consequently, the condition for a geodesic to reach the boundary is

$\lim_{r\to\infty} V(r) \leq 0$; for a geodesic emanating from a point on the boundary, the deepest distance, i.e. the smallest r it can reach r_* is given by the largest positive zero of the effective potential $V(r)$ (Hubeny, 2012).

A.4.1 Null geodesics

For null geodesic, we have $\kappa = 0$ in (A.4.4), and the two conserved quantities can be combined to a single parameter $\ell = L/E$ by rescaling the affine parameter λ (Hubeny, 2012). (A.4.4) then becomes

$$\left(\frac{dr}{d\lambda}\right)^2 + \ell^2 \frac{f(r)}{r^2} - 1 = 0\,. \tag{A.4.5}$$

From (A.4.5), it is clear that in order for the null geodesic to reach the boundary, one must have $\ell^2 \leq 1$; $\ell^2 = 1$ corresponds to the case that the null geodesic stays on the boundary (Hubeny, 2012).

A.4.1.1 Pure AdS$_3$

For pure AdS$_3$, we have $f(r) = r^2 + 1$ in (A.4.5), which integrates to

$$r(\lambda) = \sqrt{(1-\ell^2)\,\lambda^2 + \frac{\ell^2}{1-\ell^2}} \qquad \lambda \in \big[0, \infty\big). \tag{A.4.6}$$

The null geodesic reaches the boundary, i.e. $r \to \infty$ when $\lambda \to \infty$.

Substituting (A.4.6) into the two conserved quantities (A.4.2) with $f(r) = r^2 + 1$, one finds

$$E = (r^2+1)\frac{dt}{d\lambda} = \frac{(1-\ell^2)^2\,\lambda^2 + 1}{1-\ell^2}\frac{dt}{d\lambda} = 1, \tag{A.4.7}$$

$$L = r^2 \frac{dx}{d\lambda} = \frac{(1-\ell^2)^2\,\lambda^2 + \ell^2}{1-\ell^2}\frac{dx}{d\lambda} = \ell, \tag{A.4.8}$$

which integrate to

$$t(\lambda) = \arctan[(1-\ell^2)\lambda] + C_t, \tag{A.4.9}$$

$$x(\lambda) = \arctan\Big[\frac{1}{\ell}(1-\ell^2)\lambda\Big] + C_x. \tag{A.4.10}$$

When the null geodesic approaches the boundary

$$\lim_{\lambda\to\infty} t(\lambda) = C_t + \frac{\pi}{2} = y, \qquad \lim_{\lambda\to\infty} x(\lambda) = C_x + \frac{\pi}{2} = y. \tag{A.4.11}$$

The other half of the triangle can be studied by reflection, i.e. by performing a change of variable $x' = 2\pi - x \in [0,\pi]$. The general expressions of null geodesics equations are therefore

$$\begin{cases} r(\lambda) = \sqrt{(1-\ell^2)\,\lambda^2 + \dfrac{\ell^2}{1-\ell^2}}, \\ t(\lambda) = \arctan[(1-\ell^2)\lambda] + y - \dfrac{\pi}{2}, \\ x(\lambda) = \arctan\Big[\dfrac{1}{\ell}(1-\ell^2)\lambda\Big] + y - \dfrac{\pi}{2}. \end{cases} \tag{A.4.12}$$

From the expression of $x(\lambda)$, we can solve for ℓ

$$-\cot(x-y) = \frac{1}{\ell}(1-\ell^2)\lambda, \tag{A.4.13}$$

$$\ell = \frac{r}{\sqrt{1+r^2+\cot^2(x-y)}} \leq 1. \tag{A.4.14}$$

Plugging (A.4.13), (A.4.14) and $r(\lambda)$ into $t(\lambda)$

$$t(r,x,y) = \arctan\Big[\ell\cdot\frac{1}{\ell}(1-\ell^2)\lambda\Big] + y - \frac{\pi}{2} \tag{A.4.15}$$

$$= \arctan\Big[\frac{-r\cot(x-y)}{\sqrt{r^2+\csc^2(x-y)}}\Big] + y - \frac{\pi}{2}, \tag{A.4.16}$$

which is repeated in the main text in (2.3.10). It is easy to see that t increases monotonically with respect to y,

$$\frac{dt}{dy} = 1 - \underbrace{\frac{r}{\sqrt{r^2 + \csc^2(x-y)}}}_{\leq 1} \geq 0. \tag{A.4.17}$$

So t maximises at $y = \pi$

$$t(r, x, y = \pi) = -\arctan\Big[\frac{r\cot x}{\sqrt{r^2 + \csc^2 x}}\Big] + \frac{\pi}{2}. \tag{A.4.18}$$

Further simplifications depend on the range of x:

- For $\cot x > 0$, i.e. $0 < x < \pi/2$, we have

$$t(r, x) = \arctan\Big[\frac{\sqrt{r^2 + \csc^2 x}}{r\cot x}\Big] = \arccos\Big[\frac{r}{\sqrt{r^2+1}}\cos x\Big]. \tag{A.4.19}$$

- For $\cot x < 0$, i.e. $\pi/2 < x < \pi$, we have

$$\begin{aligned} t(r, x) &= -\arctan\Big[\frac{r\cot x}{\sqrt{r^2 + \csc^2 x}}\Big] - \frac{\pi}{2} + \pi = \arctan\Big[\frac{\sqrt{r^2 + \csc^2 x}}{r\cot x}\Big] + \pi \\ &= \arccos\Big[\frac{r}{\sqrt{r^2+1}}\cos x\Big]. \end{aligned} \tag{A.4.20}$$

both of which are (2.3.11) in the main text.

A.4.1.2 BTZ

For BTZ, we have $f(r) = r^2 - r_+^2$ in (A.4.5), which integrates to

$$r(\lambda) = \sqrt{(1-\ell^2)\,\lambda^2 - \frac{\ell^2 r_+^2}{1-\ell^2}}, \qquad \lambda \in \Big[\frac{\ell r_+}{1-\ell^2}, \infty\Big). \tag{A.4.21}$$

The null geodesic reaches the boundary, i.e. $r \to \infty$ when $\lambda \to \infty$.

Substituting (A.4.21) into the two conserved quantities (A.4.2) with $f(r) = r^2 - r_+^2$, we find

$$E = (r^2 - r_+^2)\frac{dt}{d\lambda} = \frac{(1-\ell^2)^2\,\lambda^2 - r_+^2}{1-\ell^2}\frac{dt}{d\lambda} = 1, \tag{A.4.22}$$

$$L = r^2\frac{dx}{d\lambda} = \frac{(1-\ell^2)^2\,\lambda^2 - \ell^2 r_+^2}{1-\ell^2}\frac{dx}{d\lambda} = \ell. \tag{A.4.23}$$

which outside the horizon, $r \geq r_+$ for integrate to:

$$t(\lambda) = \frac{1}{2r_+}\log\frac{(1-\ell^2)\,\lambda - r_+}{(1-\ell^2)\,\lambda + r_+} + C_t \tag{A.4.24}$$

$$x(\lambda) = \frac{1}{2r_+}\log\frac{(1-\ell^2)\,\lambda - \ell r_+}{(1-\ell^2)\,\lambda + \ell r_+} + C_x \tag{A.4.25}$$

When the null geodesic approaches the boundary

$$\lim_{\lambda\to\infty} t(\lambda) = y = C_t, \qquad \lim_{\lambda\to\infty} x(\lambda) = y = C_x. \tag{A.4.26}$$

The general expressions of null geodesics equations outside the horizon are therefore

$$\begin{cases} r(\lambda) = \sqrt{(1-\ell^2)\,\lambda^2 - \dfrac{\ell^2 r_+^2}{1-\ell^2}}, \\ t(\lambda) = \dfrac{1}{2r_+}\log\dfrac{(1-\ell^2)\,\lambda - r_+}{(1-\ell^2)\,\lambda + r_+} + y, \\ x(\lambda) = \dfrac{1}{2r_+}\log\dfrac{(1-\ell^2)\,\lambda - \ell r_+}{(1-\ell^2)\,\lambda + \ell r_+} + y. \end{cases} \tag{A.4.27}$$

From the expression of $x(\lambda)$, we can solve for ℓ

$$\ell = \frac{(-1 + e^{2r_+(x-y)})r}{\sqrt{(-1+e^{2r_+(x-y)})^2 r^2 + 4r_+^2 e^{2r_+(x-y)}}} \leq 1. \tag{A.4.28}$$

Plugging (A.4.28) and $r(\lambda)$ into $t(\lambda)$ gives

$$t(r,x,y)=\frac{1}{2r_+}\log\frac{r\sqrt{1+r_+^2\sinh^2(x-y)}-r_+\sqrt{1+r^2\sinh^2(x-y)}}{r\sqrt{1+r_+^2\sinh^2(x-y)}+r_+\sqrt{1+r^2\sinh^2(x-y)}}+y, \tag{A.4.29}$$

which is (2.3.12) in the main text. It is easy to see that t increases monotonically with respect to y outside the BTZ horizon

$$\frac{dt}{dy}\propto 4r(r^2-r_+^2)\,\sinh(x-y)\geq 0. \tag{A.4.30}$$

So t is maximised at $y=\pi$

$$t(r,x,y=\pi)=\frac{1}{2r_+}\log\frac{r\sqrt{1+r_+^2\sinh^2(x-\pi)}-r_+\sqrt{1+r^2\sinh^2(x-\pi)}}{r\sqrt{1+r_+^2\sinh^2(x-\pi)}+r_+\sqrt{1+r^2\sinh^2(x-\pi)}}+\pi, \tag{A.4.31}$$

which is (2.3.13) in the main text.

A.4.2 Spacelike geodesics

For spacelike geodesic, we have $\kappa=1$ in (A.4.3)

$$\left(\frac{dr}{d\lambda}\right)^2+V(r)=0,\qquad V(r)=-f(r)-E^2+L^2\frac{f(r)}{r^2}=0. \tag{A.4.32}$$

To compute the holographic entanglement entropy, one needs to compute the length of the spacelike geodesic obeying the appropriate homology constraints. In our case, the spacelike geodesic equation is for non-equal time. The length of the spacelike geodesic is given in terms of the temporal and angular separation of the two points on the boundary on which our geodesic anchors.

The length of the spacelike geodesic is given by

$$\mathcal{L} = 2\int_{r_*}^{\infty} d\lambda, \tag{A.4.33}$$

with the factor of two coming from symmetry. But this is of course infinite; to get a finite result, we impose the large-radius cutoffs R_1, R_2 at the two geodesic endpoints as in (Hubeny, 2012). Note that from (A.4.4), one can change integration variable $d\lambda = \frac{dr}{\sqrt{-V(r)}}$, which is appropriate since $V(r) < 0$ in $r \in (r_*, \infty)$. Thus, we have

$$\mathcal{L}_{\text{reg}} = \Big(\int_{r_*}^{R_1} + \int_{r_*}^{R_2}\Big)\frac{dr}{\sqrt{-V(r)}}, \tag{A.4.34}$$

and the universal diverging piece is simply $\log 4R_1R_2$, since $V(r) \propto -r^2$ for spacelike geodesics as r gets large in (A.4.32).

The temporal and angular separation are then given by (Hubeny, 2012)

$$\Delta t = 2\int_{t_*}^{\infty} dt = 2\int_{\lambda_*}^{\infty}\frac{dt}{d\lambda}d\lambda = 2\int_{\lambda_*}^{\infty}\frac{E}{f(r)}d\lambda = 2\int_{r_*}^{\infty}\frac{E}{f(r)\sqrt{-V(r)}}dr, \tag{A.4.35}$$

$$\Delta x = 2\int_{x_*}^{\infty} dx = 2\int_{\lambda_*}^{\infty}\frac{dx}{d\lambda}d\lambda = 2\int_{\lambda_*}^{\infty}\frac{L}{r^2}d\lambda = 2\int_{r_*}^{\infty}\frac{L}{r^2\sqrt{-V(r)}}dr, \tag{A.4.36}$$

where the conserved quantities (A.4.2) have been substituted in.

A.4.2.1 Pure AdS$_3$

For pure AdS$_3$, we have $f(r) = r^2 + 1$ in (A.4.32). The relevant quantities needed in our calculation have been worked out in (Hubeny, 2012). The minimal radius

the spacelike geodesic can reach is

$$r_* = \sqrt{\frac{1}{2}\Big[-(E^2 - L^2 + 1) + \sqrt{(E^2 - L^2 + 1)^2 + 4L^2}\Big]}. \tag{A.4.37}$$

The regulated length of the spacelike geodesic is

$$\mathcal{L}_{\text{reg}} = \Big(\int_{r_*}^{R_1} + \int_{r_*}^{R_2}\Big)\frac{dr}{\sqrt{-V(r)}} = -\log\sqrt{(E^2 - L^2 + 1)^2 + 4L^2} + \log(4R_1R_2), \tag{A.4.38}$$

where we added the universal diverging term $\log(4R_1R_2)$ that (Hubeny, 2012) subtracted off, as it will play a role in our analysis later on. The temporal and angular distance between the two geodesic endpoints on the boundary are

$$\Delta t = 2\int_{r_*}^{\infty}\frac{E}{f(r)\sqrt{-V(r)}}dr = \frac{\pi}{2} + \arcsin\Big[\frac{E^2 - L^2 - 1}{\sqrt{(E^2 - L^2 - 1)^2 + 4E^2}}\Big], \tag{A.4.39}$$

$$\Delta x = 2\int_{r_*}^{\infty}\frac{L}{r^2\sqrt{-V(r)}}dr = \frac{\pi}{2} + \arcsin\Big[\frac{E^2 - L^2 + 1}{\sqrt{(E^2 - L^2 + 1)^2 + 4L^2}}\Big], \tag{A.4.40}$$

which are (2.4.3) and (2.4.4) in the main text. Note that $(E^2 - L^2 - 1)^2 + 4E^2 = (E^2 - L^2 + 1)^2 + 4L^2$.

From (2.4.3) and (2.4.4), we can solve for E and L:

$$E = \frac{\sin\Delta t}{\cos\Delta t - \cos\Delta x}, \qquad L = \frac{\sin\Delta x}{\cos\Delta t - \cos\Delta x}. \tag{A.4.41}$$

Plugging (A.4.41) into (A.4.38), we have,

$$\mathcal{L}_{\text{reg}} = \log\left[\frac{1}{2}\left|\cos\Delta t - \cos\Delta x\right|\right] + \log(4R_1R_2), \tag{A.4.42}$$

$$= \log\left[4\left|\sinh\left(\frac{w_1 - w_2}{2}\right)\sinh\left(\frac{\overline{w}_1 - \overline{w}_2}{2}\right)\right|\right] + \log(R_1R_2), \tag{A.4.43}$$

where we have used (2.4.1) in getting from the second to the third line. Restoring the "new" subscript then gives (2.4.6) in the main text.

A.4.2.2 BTZ

For BTZ, we have $f(r) = r^2 - r_+^2$ in (A.4.32). Let us consider the cases in which the spacelike geodesic never enters the black hole. In such a case, $V(r) \geq 0$ for some $r > r_+$ (Hubeny, 2012). To see what this indicates more concretely, we first note that $V(r)$ peaks at $r = \sqrt{Lr_+}$:

$$\frac{dV(r)}{dr} = -2r + \frac{2L^2r_+^2}{r^3}, \qquad \frac{dV(r)}{dr} = 0 \Rightarrow r = \sqrt{Lr_+}, \tag{A.4.44}$$

where one needs $\sqrt{Lr_+} \geq r_+$, i.e. $L \geq r_+$. The condition for the maximal value of $V(r)$, that is $V(\sqrt{Lr_+})$, to be non-negative is

$$V(\sqrt{Lr_+}) = -E^2 + (L - r_+)^2 \geq 0 \qquad \Rightarrow \qquad L \geq E + r_+, \tag{A.4.45}$$

which is more stringent than $L \geq r_+$. Henceforth, the criterion for the spacelike geodesic not entering the BTZ horizon is $L \geq E + r_+$. The limiting case $L = r_+$ when $E = 0$ corresponds to the known case that the spacelike geodesic gets trapped in a circular orbit at the horizon, which is studied in (Hubeny, 2012). At the minimal radius the spacelike geodesic can reach, $dr/d\lambda = 0$, so the minimal

radius is given by the larger positive zero of $V(r)$

$$0 = r^2 - r_+^2 + E^2 - L^2\frac{r^2 - r_+^2}{r^2}, \tag{A.4.46}$$

$$\Rightarrow r_* = \sqrt{\frac{1}{2}\Big[L^2 - E^2 + r_+^2 + \sqrt{(L^2 - E^2 + r_+^2)^2 - 4r_+^2L^2}\Big]}. \tag{A.4.47}$$

One can verify that for $L = E + r_+$, $r_* = \sqrt{r_+(r_+ + E)} > r_+$; increasing L results in increasing r_*. Hence $r_* > r_+$ for $L \geq E + r_+$. By setting $r_+^2 = -1$ in (A.4.47), we recover (A.4.37) in pure AdS_3.

The regulated geodesic length is then given by integrating (A.4.34)

$$\mathcal{L}_{\text{reg}} = \Big(\int_{r_*}^{R_1} + \int_{r_*}^{R_2}\Big)\frac{dr}{\sqrt{-V(r)}} = -\log\sqrt{(L^2 - E^2 + r_+^2)^2 - 4r_+^2L^2} + \log 4R_1R_2, \tag{A.4.48}$$

Note that by setting the BTZ black hole radius $r_+^2 = -1$ in (A.4.48), we recover (A.4.38) in pure AdS_3. The temporal and angular distance between the two geodesic endpoints on the boundary are given by integrating (A.4.35) and (A.4.36),

respectively

$$\Delta t = 2\int_{r_*}^{\infty} \frac{E}{f(r)\sqrt{-V(r)}}dr \tag{A.4.49}$$

$$= \frac{1}{r_+}\log\Big[\frac{\sqrt{(L^2-E^2+r_+^2)^2-4r_+^2E^2}}{(L-E-r_+)(L+E+r_+)}\Big] \tag{A.4.50}$$

$$= \frac{1}{r_+}\text{arccosh}\Big[\frac{L^2-E^2-r_+^2}{\sqrt{(L^2-E^2-r_+^2)^2-4r_+^2E^2}}\Big], \tag{A.4.51}$$

$$\Delta x = 2\int_{r_*}^{\infty} \frac{L}{r^2\sqrt{-V(r)}}dr \tag{A.4.52}$$

$$= \frac{1}{r_+}\log\Big[\frac{\sqrt{(E^2-L^2-r_+^2)^2-4r_+^2L^2}}{(L+E-r_+)(L-E-r_+)}\Big]$$

$$= \frac{1}{r_+}\text{arccosh}\Big[\frac{L^2-E^2+r_+^2}{\sqrt{(L^2-E^2+r_+^2)^2-4r_+^2L^2}}\Big], \tag{A.4.53}$$

which are (2.4.14) and (2.4.15) in the main text. Note that $(L^2-E^2+r_+^2)^2-4r_+^2L^2 = (L^2-E^2-r_+^2)^2-4r_+^2E^2$. One can verify that when $E=0$, (A.4.53) becomes

$$\Delta x = \frac{1}{r_+}\text{arccosh}\Big(\frac{L^2+r_+^2}{L^2-r_+^2}\Big) = \frac{2}{r_+}\text{arctanh}\Big(\frac{r_+}{L}\Big), \tag{A.4.54}$$

which matches with a known result in section 2.3 of (Hubeny, 2012).

From (2.4.14) and (2.4.15), one can solve for E and L

$$E = r_+\frac{\sinh(r_+\Delta t)}{\cosh(r_+\Delta t)-\cosh(r_+\Delta x)}, \quad L = r_+\frac{\sinh(r_+\Delta x)}{\cosh(r_+\Delta t)-\cosh(r_+\Delta x)}. \tag{A.4.55}$$

Plugging (A.4.55) into (A.4.48), we have,

$$\mathcal{L}_{\text{reg}} = \log\left[\left(\frac{2}{r_+}\right)^2 \frac{1}{2}\left|\cosh(r_+\Delta t) - \cosh(r_+\Delta x)\right|\right] + \log(R_1 R_2) \tag{A.4.56}$$

$$= \log\left[\left(\frac{2}{r_+}\right)^2 \left|\sin\left(r_+\frac{w_1 - w_2}{2}\right)\,\sin\left(r_+\frac{\overline{w}_1 - \overline{w}_2}{2}\right)\right|\right] + \log(R_1 R_2), \tag{A.4.57}$$

where we have used (2.4.1) in getting from the second to the third line. This then gives (2.4.17) in the main text with the "new" subscript restored.

A.5 Time evolution of SSD horizons

In this appendix, we show how the coordinates in Figure 2.5 are established. In (Goto et al., 2021), a redefinition of the radial coordinate

$$r' = \sqrt{\frac{\partial w_{\text{new}}}{\partial w}\frac{\partial \overline{w}_{\text{new}}}{\partial \overline{w}}}\, r_{\text{new}} = \frac{1}{\sqrt{4t^2 \sin^4\frac{x}{2} + \left(1 - t^2\sin^2\frac{x}{2}\right)^2}}\, r_{\text{new}}, \tag{A.5.1}$$

was introduced, and the BTZ black hole horizon was plotted on constant t slices in the (t, x, r') coordinate. In order to compare with their result, we adopt the same (t, x, r') coordinate when plotting Figure 2.5. Notice that unlike (A.2.6), the metric in the (t, x, r') coordinate is not in the Fefferman-Graham gauge (Skenderis & Solodukhin, 2000; de Haro et al., 2001), as r' is t and x dependent, leading to non-zero $dr'dt$ and $dr'dx$ terms in the metric. Therefore quantitative comparisons with the boundary stress tensor are in general hard to achieve.

A.6 Comments on bulk reconstruction

Horizons make information inaccessible. The presence of the horizons (2.3.11) and (2.3.13) in Figure 2.3 and 2.4 makes us wonder if an information puzzle can arise in our setup: e.g. a bulk excitation prepared on the $t = 0$ would fall behind the horizon and become inaccessible leading to tension with unitary time evolution. Equivalently, one asks how to reconstruct local bulk operators (dressed to make them diffeomorphism invariant) inside or outside the new horizons, respectively.

For bulk fields *inside* the causal wedge, i.e. in the bulk region enclosed by the null hypersurfaces in Figure 2.3 or 2.4 and the quench surface at $t = 0$, we can recover the information using HKLL-like reconstructions (Banks et al., 1998; Hamilton, Kabat, Lifschytz, & Lowe, 2006; Witten, 2023). In our case, the $t_{\text{new}} > 0$ part of this subregion is the triangle. (The $t_{\text{new}} < 0$ part is a time strip of width $\pi/2$ for pure AdS and infinite for BTZ.) The reconstruction formula is given by

$$\phi(X) = \int_{\text{triangle+strip}} dx\, K(X|x)O(x), \tag{A.6.1}$$

where $X = (t_{\text{new}}, r_{\text{new}}, x_{\text{new}})$ and $x = (t_{\text{new}}, x_{\text{new}})$ stand for the coordinates on the bulk and boundary, respectively. $K(X|x)$ is a smearing function adapted to the subregion.

For bulk operators *outside* the causal wedge, i.e. behind the horizon (2.3.11) and (2.3.13), the aforementioned HKLL-like reconstruction does not apply anymore. However, information falling through the horizon (2.3.11) or (2.3.13) (but not through the BTZ black hole horizon in the case with (2.3.13)) remains reconstructable, by considering *modular* reconstruction (Jafferis, Lewkowycz, Maldacena, & Suh, 2016; Dong, Harlow, & Wall, 2016). In our case, the modular

Hamiltonian is simply H_0 up to a coefficient $\frac{\beta}{2\pi}$,[3] so the modular evolution is just H_0 time evolution with the modular parameter given by $t_{\text{new}} = t$.[4] We would like to then consider the *modular flow* of local operators O on the boundary, $O(x,t) = U^{-1}(t)O(x,0)U(t)$, where $U(t) = e^{-i\beta H_0 t/2\pi}$. Modular reconstruction then states that *modular flows equal bulk modular flows* (Jafferis et al., 2016). This conclusion allows us to recover the information of all bulk operators within the *entanglement wedges*, which in our case is the entire spacetime for the ground state case and all the spacetime regions outside the BTZ black hole horizon for the thermal state case. In each case, the entanglement wedge is larger than the casual wedge and, importantly, includes the spacetime region that is behind the horizon (2.3.11) or (2.3.13) (but outside the BTZ horizon in the thermal state case).

A.7 Quenches governed by other $SL(2)$ Virasoro subalgebras

It is straightforward to generalise the SSD story, by replacing $L_{\pm 1}$ in the expression of H_1 in (2.2.5) with $L_{\pm q}$ with $q > 1$. This corresponds to the envelope function (Fan et al., 2020)

$$v_q(x) = 2\sin^2\left(q \cdot \frac{x}{2}\right), \tag{A.7.1}$$

[3] In the vacuum since the density matrix is a projector, the modular Hamiltonian is not well defined, so we need to regulate the vacuum with a small temperature.

[4] Note that when the Hamiltonian is H_0, we have $t_{\text{new}} = t$; t_{new} and t are different only when the driving Hamiltonian is H_1.

and the resulting deformed Hamiltonian H_q is given by

$$H_q = 2\int_0^{2\pi} dx\ \sin^2\Big(q\cdot\frac{x}{2}\Big)\,T_{00}(x) \tag{A.7.2}$$

$$= L_0 - \frac{L_{-q}+L_q}{2} + \overline{L}_0 - \frac{\overline{L}_{-q}+\overline{L_q}}{2} - q\cdot\frac{c}{12}. \tag{A.7.3}$$

In order for $\{L_0, L_q, L_{-q}\}$ to form the same algebra as $\{L_0, L_1, L_{-1}\}$, we have to *shift* the Virasoro generators $\{L_0, L_q, L_{-q}\}$,[5]

$$\mathcal{L}_0 = \frac{1}{q}\big(L_0 - \frac{c}{12}q(q^2-1)\big), \qquad\qquad \mathcal{L}_{\pm q} = \frac{1}{q}L_{\pm q}. \tag{A.7.4}$$

Note that such shifts also define a new vacuum $|0\rangle_q$ for each H_q. H_q is now given by

$$H_q = q\Big(\mathcal{L}_0 - \frac{\mathcal{L}_{-q}+\mathcal{L}_q}{2} + \overline{\mathcal{L}}_0 - \frac{\overline{\mathcal{L}}_{-q}+\overline{\mathcal{L}}_q}{2} - \frac{c}{12}\Big), \tag{A.7.5}$$

which follows the same algebraic commutation rules as that of H_1. The relevant coordinate transformations then take the same form as (2.2.6) and (2.2.7), with the circumference 2π replaced by $2\pi/q$. The system can then be regarded as q copies of identical theories driven by H_1, each with a shrunk length scale $2\pi/q$ living in a subregion on the cylinder (see Appendix A.1.1.4 for more details). Hence the constant t lines approach a q-fold triangle, i.e. q triangles, each living in a subregion $\big[(p-1)\frac{2\pi}{q}, p\frac{2\pi}{q}\big]$ $(p = 1, 2, ..., q)$. The boundary conformal Killing vector is

$$k_q^\mu = \Big(\cosh(q\tau_{\rm new})\ \cos(qx_{\rm new}) - 1, \sinh(q\tau_{\rm new})\ \sin(qx_{\rm new})\Big). \tag{A.7.6}$$

[5]There are subtleties regarding the difference between L_q $(q > 1)$ and the global conformal charges $\{L_0, L_1, L_{-1}\}$, as the former generate transformations that are not globally well defined and are associated to conformal Killing vectors with poles. But these poles appear at 0 or ∞ on the complex z-plane or equivalently $\pm\infty$ on the cylinder, where we will not perform calculations. Therefore, our calculation is unaffected by this subtlety.

The boundary conformal Killing horizon is then the aforementioned q-fold triangle.

Generalisation of the new horizon with H_q $(q > 1)$ as Hamiltonian is straightforward. From equation (A.7.6), the boundary horizons when H_q drives are q-triangles each in a subregion; according to the same maximisation procedure of null geodesics in (2.3.10) and (2.3.12), the new horizon then consists of q-copies of (2.3.11) or (2.3.13) when the CFT is in the ground and thermal state, respectively, each anchoring on one of the q triangles on the boundary. An example for $q = 2$ in the thermal state is plotted in Figure A.1. Note that the bulk horizons for H_q $(q > 1)$ in the ground state are no longer Killing horizons. (The naive generalisations of (2.3.5) to $q > 1$ do not obey the Killing equation (A.7.7). This is as anticipated as the bulk does not have an $SL(2)$ isometry for each q.)

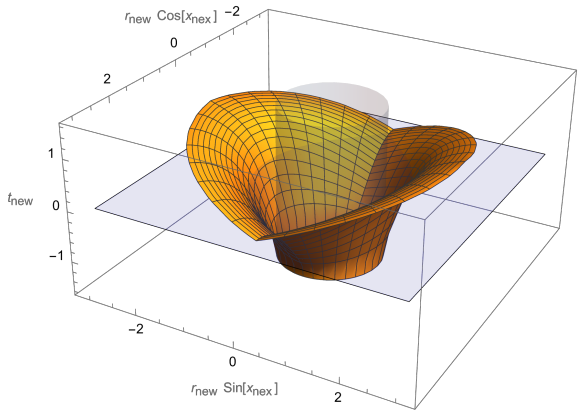

Figure A.1: A plot of the new horizon in BTZ geometry with H_2 as driving Hamiltonian. The light blue surface is the quench surface $t_{\text{new}} = t = 0$. The BTZ black hole horizon is set to $r_+ = 1$ and plotted in light gray. The new horizon is larger than the BTZ black hole horizon.

A.8 Two-point functions of twist operators

In this appendix, we first evaluate the two-point function $\langle \mathcal{T}_n(w_{1,\text{new}}, \overline{w}_{1,\text{new}}) \mathcal{T}_{-n}(w_{2,\text{new}}, \overline{w}_{2,\text{new}}) \rangle$ for a CFT$_2$ on a compact space of length 2π, and then evaluate the thermal two-

point function $\langle \mathcal{T}_n(w_{1,\text{new}}, \overline{w}_{1,\text{new}})\mathcal{T}_{-n}(w_{2,\text{new}}, \overline{w}_{2,\text{new}})\rangle_\beta$ for a CFT_2 at temperature $T = \beta^{-1}$ on a non-compact space. Throughout this appendix, we will be working exclusively in z_{new} and w_{new} coordinate, so we drop the "new" subscript for notation simplicity. Our method is largely based on (Calabrese & Cardy, 2004). Note, however, that we are working in the coordinates

$$w = \tau + ix, \qquad \overline{w} = \tau - ix, \tag{A.8.1}$$

on the Euclidean cylinder as is mentioned in the main text. This results in a different behaviour of the holomorphic and anti-holomorphic parts of the two-point function, in contrast to (Calabrese & Cardy, 2004). We can use the conformal transformation (A.1.1) that maps the Euclidean cylinder to the complex plane, where the two-point function of twist operator is simply

$$\langle \mathcal{T}_n(z_1, \overline{z}_1)\mathcal{T}_{-n}(z_2, \overline{z}_2)\rangle = \frac{1}{(z_1 - z_2)^{2h}} \cdot \frac{1}{(\overline{z}_1 - \overline{z}_2)^{2h}}. \tag{A.8.2}$$

For the holomorphic part, under a conformal transformation $z \to w$,

$$\langle \mathcal{T}_n(z_1)\mathcal{T}_{-n}(z_2)\rangle = \frac{1}{(z_1 - z_2)^{2h}} = \left(\frac{\partial w_1}{\partial z_1}\right)^h \left(\frac{\partial w_2}{\partial z_2}\right)^h \langle \mathcal{T}_n(w_1)\mathcal{T}_{-n}(w_2)\rangle \tag{A.8.3}$$

Substituting (A.1.1), $\langle \mathcal{T}_n(w_1)\mathcal{T}_{-n}(w_2)\rangle$ on the Euclidean cylinder is then

$$\langle \mathcal{T}_n(w_1)\mathcal{T}_{-n}(w_2)\rangle = \left[2\sinh\left(\frac{1}{2}(w_1 - w_2)\right)\right]^{-2h} = \left[2\sinh\left(\frac{1}{2}((\tau_1 - \tau_2) + i(x_1 - x_2))\right)\right]^{-2h}. \tag{A.8.4}$$

The anti-holomorphic part is simply given by $w_i \to \overline{w}_i$,

$$\langle \mathcal{T}_n(\overline{w}_1)\mathcal{T}_{-n}(\overline{w}_2)\rangle = \left[2\sinh\left(\frac{1}{2}(\overline{w}_1 - \overline{w}_2)\right)\right]^{-2h} = \left[2\sinh\left(\frac{1}{2}((\tau_1 - \tau_2) - i(x_1 - x_2))\right)\right]^{-2h}. \tag{A.8.5}$$

Note that (A.8.4) and (A.8.5) are not equal due to (A.8.1) in our setup. The two-point function $\langle \mathcal{T}_n(w_{1,\text{new}}, \overline{w}_{1,\text{new}}) \mathcal{T}_{-n}(w_{2,\text{new}}, \overline{w}_{2,\text{new}}) \rangle$ is then given by the product of (A.8.4) and (A.8.5) and restoring the "new" subscript, which is (2.4.11) in the main text.

To calculate the thermal two-point function, $\langle \mathcal{T}_n(w_{1,\text{new}}, \overline{w}_{1,\text{new}}) \mathcal{T}_{-n}(w_{2,\text{new}}, \overline{w}_{2,\text{new}}) \rangle_\beta$ on non-compact space, we simply perform a Wick rotation of the exponential map, and rescale the circumference of the cylinder from 2π to β (Calabrese & Cardy, 2004),

$$z = e^{\frac{2\pi}{\beta} i w}, \qquad \overline{z} = e^{\frac{2\pi}{\beta} i \overline{w}}, \tag{A.8.6}$$

this amounts to $w \to iw$ and $2\pi \to \beta$ in (A.8.4) and (A.8.5),

$$\langle \mathcal{T}_n(w_1) \mathcal{T}_{-n}(w_2) \rangle_\beta = \left[\frac{\beta}{\pi} \sin\left(\frac{\pi}{\beta}(w_1 - w_2) \right) \right]^{-2h} = \left[\frac{\beta}{\pi} \sinh\left(\frac{\pi}{\beta}((\tau_1 - \tau_2) + i(x_1 - x_2)) \right) \right]^{-2h}, \tag{A.8.7}$$

$$\langle \mathcal{T}_n(\overline{w}_1) \mathcal{T}_{-n}(\overline{w}_2) \rangle_\beta = \left[\frac{\beta}{\pi} \sin\left(\frac{\pi}{\beta}(\overline{w}_1 - \overline{w}_2) \right) \right]^{-2h} = \left[\frac{\beta}{\pi} \sinh\left(\frac{\pi}{\beta}((\tau_1 - \tau_2) - i(x_1 - x_2)) \right) \right]^{-2h}. \tag{A.8.8}$$

The thermal two-point function $\langle \mathcal{T}_n(w_{1,\text{new}}, \overline{w}_{1,\text{new}}) \mathcal{T}_{-n}(w_{2,\text{new}}, \overline{w}_{2,\text{new}}) \rangle_\beta$ is then given by the product of the two, and restoring the "new" subscript.

B | Appendices to Chapter 3

B.1 Detailed analysis of solutions in the generalised membrane theory

B.1.1 Displaced half-space

In this appendix, we solve the equations of motion arising from the effective action $\mathcal{L}_{\text{eff}}$ (3.1.2) exactly. Our solution is still an approximation to the full solution presented in Appendix B.2.4, since the effective action $\mathcal{L}_{\text{eff}}$ (3.1.2) is derived under the scaling limit (3.1.1).

As (3.1.2) does not contain u or x, it has two conserved quantities, the energy E and momentum p,

$$E = \dot{\xi}\frac{\partial \mathcal{L}}{\partial \dot{\xi}} + \dot{x}\frac{\partial \mathcal{L}}{\partial \dot{x}} - \mathcal{L} = \frac{1}{2}e^{-2\xi}\left(1 + \dot{x}^2 - \dot{\xi}^2\right), \tag{B.1.1}$$

$$p = \frac{\partial \mathcal{L}}{\partial \dot{x}} = e^{-2\xi}\dot{x}. \tag{B.1.2}$$

The generalised velocity $\dot{\xi}$ vanishes at the furthest point ξ_0 the geodesic can reach in the interior, $\dot{\xi}|_{\xi=\xi_0} = 0$. Therefore, we can evaluate E (B.1.1) at ξ_0, which then allows us to solve for $\dot{\xi}$

$$e^{-2\xi}\left(1 + p^2 e^{4\xi} - \dot{\xi}^2\right) = e^{-2\xi_0}\left(1 + p^2 e^{4\xi_0}\right), \tag{B.1.3}$$

$$\Rightarrow \dot{\xi}^2 = (e^{2\xi_0} - e^{2\xi})(e^{-2\xi_0} - p^2 e^{2\xi}), \tag{B.1.4}$$

where we have plugged in (B.1.2). We see that by making use of conserved quantity E (B.1.1), we reduced the problem from a second order ODE (3.1.3) to a first order

ODE (B.1.4). Solving (B.1.4), we find

$$\xi(u) = \log\left(\frac{e^{\xi_0}\text{sech}u}{\sqrt{1-e^{4\xi_0}p^2\tanh^2 u}}\right). \tag{B.1.5}$$

Then, plug (B.1.5) into (B.1.2) and integrate, we can further obtain $x(u)$

$$x(u) = \text{arctanh}(pe^{2\xi_0}\tanh u). \tag{B.1.6}$$

From (B.1.6), we can find the total displacement $2X$ in terms of p and z_0 by taking $|u|$ large, resulting in

$$X = \text{arctanh}(Pe^{2\xi_0}) \qquad \Rightarrow \qquad p = e^{-2\xi_0}\tanh X. \tag{B.1.7}$$

(B.1.7) indicates that $p \to e^{-2\xi_0}$ for large X. Plugging (B.1.7) into (B.1.5), we have

$$\xi(u) = \log\left(\frac{e^{\xi_0}\text{sech}u}{\sqrt{1-\tanh^2 X\tanh^2 u}}\right). \tag{B.1.8}$$

This allows us to solve for ξ_0 in terms of T and X from (B.1.8)

$$\xi_0 = \log\left(\sqrt{\frac{\cosh 2T+\cosh 2X}{\cosh 2X+1}}\right), \tag{B.1.9}$$

which matches (B.2.44) obtained from the BTZ-AdS$_3$ mapping method. Plug (B.1.9) and (B.1.7) into (B.1.5) and (B.1.6) we can express the geodesic as a parametric curve parameterised by the infalling time u

$$\xi(u) = \frac{1}{2}\log\left(\frac{\cosh 2T+\cosh 2X}{\cosh 2u+\cosh 2X}\right), \tag{B.1.10}$$

$$x(u) = \text{arctanh}\,(\tanh X\tanh u). \tag{B.1.11}$$

A plot of (B.1.10) and (B.1.11) can be found in Fig. B.1. In the large T, large X ($T > X$) limit, one can check that $\xi(u)$ (B.1.10) and $x(u)$ (B.1.11) match (3.1.4).

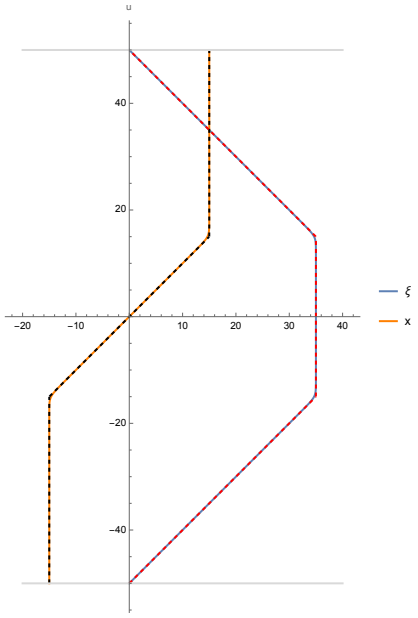

Figure B.1: Plot of $\xi(u)$ (blue) (B.1.10) and $x(u)$ (orange) (B.1.11) when $T = 50$ and $X = 15$. The scaling approximation of $\xi(u)$ and $x(u)$ (3.1.4) are plotted as dashed in red and black, respectively.

B.1.2 Saturated EWCS

With the change of variable from u to x in (3.2.3), E (B.1.1) becomes

$$E = \frac{1}{2} e^{-2\xi} \left(1 - e^{4(\xi - \xi_p)} \left(\xi'^2 - 1\right)\right), \tag{B.1.12}$$

where we have plugged in u' (3.2.3). Again, the conserved E allows us to reduce the problem from a second-order ODE (3.2.3) to a first-order ODE (B.1.12). Solving (B.1.12) we find

$$\xi(x) = \frac{1}{2} \log \left(\frac{e^{4\xi_p} \left(1 - E^2 e^{4\xi_p}\right) e^{-2x} - e^{2x} + 2E e^{4\xi_p}}{2} \right). \tag{B.1.13}$$

Notice that $\xi(-x)$ is also a solution to (B.1.12). This allows us to flip the sign of u' (3.2.3).[1] Plugging (B.1.13) into (3.2.3) and integrating, we have

$$u(x) = u_p + \ell_p - \operatorname{arctanh}(Ee^{2\xi_p} - e^{2(x-\xi_p)}), \tag{B.1.14}$$

where for later convenience we write the integration constant as $u_p + \ell_p$. It can be easily observed from (B.1.14) that as $x \to -\infty$, $u(x)$ asymptotes a constant value. Denoting this value as u_p, we can solve for E

$$E = e^{-2\xi_p} \tanh \ell_p. \tag{B.1.15}$$

Notice the similarity between (B.1.15) and (B.1.7). Plugging (B.1.15) into (B.1.13), one finds

$$\xi(x) = \frac{1}{2}\log\frac{1}{2}\Big(- e^{2x} + e^{-2(x-2\xi_p)}\operatorname{sech}^2\ell_p + 2e^{2\xi_p}\tanh\ell_p\Big), \tag{B.1.16}$$

which, in the large ℓ_p limit, simplifies to

$$\xi(x) = \begin{cases} -x - \ell_p + 2\xi_p + \dfrac{1}{2}\log 2, & x \in (-\infty, -\ell_p + \xi_p + \dfrac{1}{2}\log 2], \\ \xi_p, & x \in [-\ell_p + \xi_p + \dfrac{1}{2}\log 2, \xi_p + \dfrac{1}{2}\log 2). \end{cases} \tag{B.1.17}$$

When $x \in [-\ell_p + \xi_p + \frac{1}{2}\log 2, \xi_p + \frac{1}{2}\log 2)$, the geodesic is on a *plateau* $\xi = \xi_p$. ℓ_p is therefore identified as the (horizontal) *length* of this plateau. When $x \in (-\infty, -\ell_p + \xi_p + \frac{1}{2}\log 2]$, the geodesic shoots into the deep interior exponentially in x. Plugging (B.1.15) into (B.1.14), one finds

$$u(x) = u_p + \ell_p + \operatorname{arctanh}(\tanh\ell_p - e^{2(x-\xi_p)}), \tag{B.1.18}$$

[1] It turned out that the effective theory allows both $\pm$ signs. To match with the exact solution, however, we choose $-$ sign here.

which, in the large ℓ_p limit, simplifies to

$$u(x) = \begin{cases} u_p, & x \in (-\infty, -\ell_p + \xi_p + \frac{1}{2}\log 2], \\ x + u_p + \ell_p - \xi_p - \frac{1}{2}\log 2, & x \in [-\ell_p + \xi_p + \frac{1}{2}\log 2, \xi_p + \frac{1}{2}\log 2). \end{cases} \tag{B.1.19}$$

Notice that when $(-\infty, -\ell_p + \xi_p + \frac{1}{2}\log 2]$, the geodesic is on the $u = u_p$ slice.

In general, one can shift $x \to x - x_c$ in (B.1.16) and (B.1.18). In the scaling limit, the shifted (B.1.16) and (B.1.18) match the approximate solution (3.2.4) in the main text with $x_0 = x_c - \ell_p + \xi_p$. Therefore, one cannot fix all four parameters $(u_p, \ell_p, \xi_p, x_c)$ even solving the approximate equations of motion (3.2.3) exactly.

In the exact solution in Appendix B.3.2, we have $\xi_p = \frac{1}{2}\log 2$ (B.3.37) which is negligible, and $\ell_p = \frac{\ell}{2}$ (B.3.22), $u_p = T - \frac{1}{2}(\ell + \frac{D}{2})$ (B.3.25). Adapting to the coordinate system in Fig. B.10 via a shift $x_c = \ell - \frac{D}{4}$, one finds that (B.1.19) becomes

$$u(x) = x + T - \ell - \frac{D}{2}. \tag{B.1.20}$$

which matches the exact solution (B.3.38) in the scaling limit. Notice that the effective theory in this section is technically much simpler than the exact solution in subsection B.3.2. A plot of (B.1.16)-(B.1.19) with shift $x_c = \ell - \frac{D}{4}$ can be found in Fig. B.2.

B.2 Exact solutions of entanglement entropy in BTZ black hole

In the main text as well as Appendix B.1, we have solved the equation of motions for various geodesics in planar BTZ black hole *approximately* in the scaling limit.

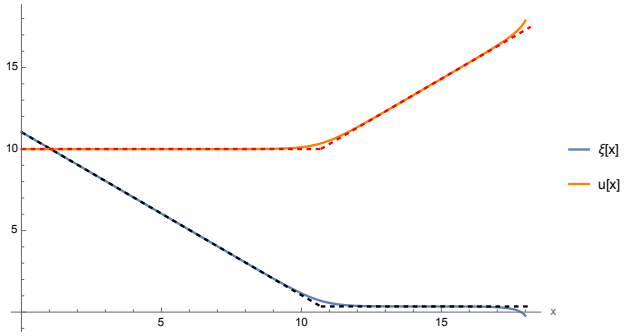

Figure B.2: Plot of $\xi(x)$ (B.1.17) and $u(x)$ (B.1.19) in (3.2.4) when $u_p = 10$, $\ell_p = 7.5$, $x_c = 17.5$ and $\xi_p = \log\sqrt{2}$ which is negligible in the scaling limit. The exact (B.1.16) and scaling approximation (3.2.4) of $\xi(x)$ are plotted in blue and dashed black, respectively; the exact (B.1.18) and scaling approximation (3.2.4) of $u(x)$ are plotted in orange and dashed red, respectively. The scaling approximations (B.1.17) and (B.1.19) match (3.2.4).

These geodesic are in fact solvable *exactly*, by virtue of the map between planar BTZ black hole and Poincare AdS_3 (Hartman & Maldacena, 2013). We will see that all approximate solutions found earlier match with exact results detailed below.

The planar BTZ black brane metric is given by

$$ds^2 = \frac{1}{z^2}\Big(-f(z)dt^2 + \frac{dz^2}{f(z)} + dx^2\Big), \tag{B.2.1}$$

where $f(z) = 1-z^2$ for planar BTZ, and the BTZ horizon is at $z = 1$. Unlike in the main text or Appendix B.1, for technical reasons we will work in Schwarzschild time t in this appendix. The subtlety one needs to bear in mind is that in the interior, t becomes complex (Fidkowski et al., 2004). We will use $\tilde{t} = t + \frac{i\pi}{2}$ to denote the real part of the Schwarzschild time in the interior. As we will see in subsection B.2.1, the differences between Schwarzschild time t and infalling time u turn out to be immaterial in the region $z \gg 1$ that we are mostly interested in.

B.2.1 Difference between Schwarzschild and infalling time

The infalling time u is given by

$$du = dt - \frac{dz}{f(z)}, \tag{B.2.2}$$

where $f(z) = 1 - z^2$. Outside the horizon $z < 1$, one can simply integrate (B.2.2) to obtain (3.1.10). In the interior $z > 1$, notice that (B.2.2) contains a simple pole at the horizon $z = 1$. The resulting residue cancels the imaginary part of the interior Schwarzschild time t, and we have

$$u = \tilde{t} - \text{arccoth}z \approx \tilde{t} - \frac{1}{z} \to \tilde{t} \tag{B.2.3}$$

for large z. Therefore, in the deep interior $z \gg 1$, adopting Schwarzschild time u or infalling time t yields asymptotically the same result.

B.2.2 Map between BTZ and Poincare AdS$_3$

BTZ black hole is a quotient of AdS$_3$ (Banados et al., 1992, 1993). We can therefore unwrap the BTZ angle and obtain Poincare AdS$_3$ as in (Hartman & Maldacena, 2013). In AdS$_3$ there is only one boundary, and the two boundaries on each side of the BTZ black hole become the two Rindler wedges in Poincare AdS$_3$ (See Fig. B.3) (Hartman & Maldacena, 2013). Notice that these two Rindler wedges do not cover the full Poincare AdS$_3$ boundary; the complementary regions are known as the two Milne patches. We would like to obtain from (B.2.1) the Poincare AdS$_3$ metric

$$ds^2 = \frac{1}{Z^2}(-dx_0^2 + dx_1^2 + dZ^2). \tag{B.2.4}$$

It is helpful to discuss the exterior and interior regions of the BTZ black brane metric (B.2.1). To this end, we follow (Hartman & Maldacena, 2013) and massage the BTZ radial coordinate z via a coordinate transformation

$$z = \mathrm{sech}\rho, \tag{B.2.5}$$

where $\rho > 0$ so that $z \in [0, 1]$. The *exterior* part of the BTZ metric (B.2.1) thus becomes

$$ds^2 = -\sinh^2\rho dt^2 + d\rho^2 + \cosh^2\rho dx^2. \tag{B.2.6}$$

The BTZ horizon is now at $\rho = 0$. The coordinate time t in (B.2.6) diverges at the horizon $\rho = 0$. The BTZ interior coordinate can be obtained via an analytic continuation on ρ and adding an imaginary part in t (Hartman & Maldacena, 2013)

$$\rho = i\alpha \;\Rightarrow\; z = \sec\alpha \in [1, +\infty), \qquad \tilde{t} = t + \frac{i\pi}{2}. \tag{B.2.7}$$

The *interior* part of the BTZ metric (B.2.1) is then given by

$$ds^2 = \sin^2\alpha d\tilde{t}^2 - d\alpha^2 + \cos^2\alpha dx^2. \tag{B.2.8}$$

The interior time $\tilde{t}$ in (B.2.8) diverges at the horizon $\alpha = 0$. Notice that in the interior, α is timelike, and $\tilde{t}$ is spacelike.

Using the embedding coordinate in (Hartman & Maldacena, 2013), the coordinate

transformation between BTZ exterior and Poincare AdS_3 are found to be

$$Z = e^x \mathrm{sech}\rho, \tag{B.2.9}$$

$$x_0 = e^x \mathrm{sinh}t\ \tanh\rho, \tag{B.2.10}$$

$$x_1 = e^x \mathrm{cosh}t\ \tanh\rho. \tag{B.2.11}$$

For the convenient of the readers, we also list the inverse of (B.2.9)-(B.2.11)

$$\rho(\lambda) = \mathrm{arcsinh}\frac{\sqrt{x_1(\lambda)^2 - x_0(\lambda)^2}}{Z(\lambda)}, \tag{B.2.12}$$

$$t(\lambda) = \mathrm{arcsinh}\frac{x_0(\lambda)}{\sqrt{x_1(\lambda)^2 - x_0(\lambda)^2}}, \tag{B.2.13}$$

$$x(\lambda) = \frac{1}{2}\log\left(Z(\lambda)^2 - x_0(\lambda)^2 + x_1(\lambda)^2\right). \tag{B.2.14}$$

The coordinate transformation between BTZ interior and Poincare AdS_3 are

$$Z = e^x \mathrm{sec}\alpha, \tag{B.2.15}$$

$$x_0 = e^x \mathrm{cosh}\tilde{t}\ \tan\alpha, \tag{B.2.16}$$

$$x_1 = e^x \mathrm{sinh}\tilde{t}\ \tan\alpha, \tag{B.2.17}$$

the inverses of (B.2.15)-(B.2.17)

$$\alpha(\lambda) = \mathrm{arcsin}\frac{\sqrt{x_0(\lambda)^2 - x_1(\lambda)^2}}{Z(\lambda)}, \tag{B.2.18}$$

$$\tilde{t}(\lambda) = \mathrm{arcsinh}\frac{x_1(\lambda)}{\sqrt{x_0(\lambda)^2 - x_1(\lambda)^2}}, \tag{B.2.19}$$

$$x(\lambda) = \frac{1}{2}\log\left(Z(\lambda)^2 - x_0(\lambda)^2 + x_1(\lambda)^2\right). \tag{B.2.20}$$

Notice that the expression of $x(\lambda)$ is the same in the exterior and interior.

Under the above coordinate transformations, the BTZ black hole horizon $\rho = \alpha = 0$

is mapped to $|x_0| = |x_1|$; the exterior region is mapped to $x_0^2 - x_1^2 \leq 0$; the BTZ black hole interior is mapped to the region $0 \leq x_0^2 - x_1^2 \leq Z^2$ enclosed by the two planes $|x_0| = |x_1|$ and the hyperboloid $Z^2 = x_0^2 - x_1^2$. Notice that $z \to \infty$ in BTZ (B.2.1) is mapped to the hyperboloid $Z^2 = x_0^2 - x_1^2$ in Poincare AdS_3 (B.2.4). See Fig. B.3 for a demonstration.

The above BTZ→AdS $_3$ mapping allows us to map the problem of interest in BTZ to that in AdS_3, where geodesic equations avoid the complexity due to the presence of horizons. In the next subsection, we will find the most general geodesic equations in Poincare AdS_3.

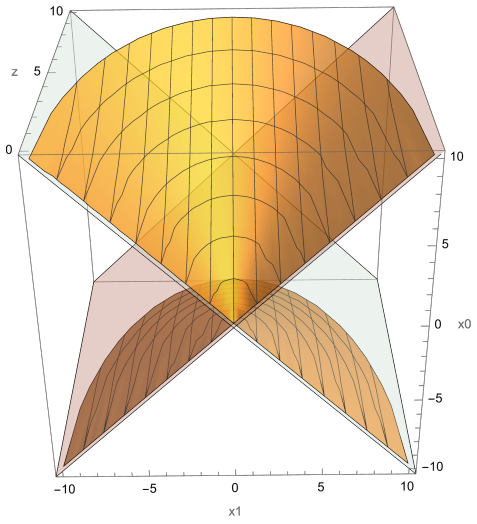

Figure B.3: Map from BTZ black hole to Poincare AdS_3. The two boundaries on each side of the BTZ black hole becomes the two Rindler wedges in Poincare AdS_3. The BTZ black hole horizon is mapped to $|x_0| = |x_1|$, which are plotted in light blue. The exterior and interior regions are mapped to $x_0^2 - x_1^2 \leq 0$ and $0 \leq x_0^2 - x_1^2 \leq Z^2$, respectively. In the interior, the hyperboloid $Z^2 = x_0^2 - x_1^2$ corresponds to $z \to \infty$ in BTZ.

B.2.3 Spacelike Geodesics in Poincare AdS_3

The Poincare AdS_3 metric (B.2.4) indicates that there are two conserved quantities, the Energy and Momentum of the geodesic

$$E = \frac{1}{Z^2}\frac{dx_0}{d\lambda}, \qquad P = \frac{1}{Z^2}\frac{dx_1}{d\lambda}, \tag{B.2.21}$$

where λ is the affine parameter along the geodesic. For spacelike geodesics, the norm of the tangent vector is 1, so we have

$$-\frac{1}{Z^2}\Big(\frac{dx_0}{d\lambda}\Big)^2 + \frac{1}{Z^2}\Big(\frac{dZ}{d\lambda}\Big)^2 + \frac{1}{Z^2}\Big(\frac{dx_1}{d\lambda}\Big)^2 = 1. \tag{B.2.22}$$

Plug (B.2.21) into (B.2.22) then yields the differential equation

$$\Big(\frac{dZ}{d\lambda}\Big)^2 = Z^2\big(1 + (E^2 - P^2)Z^2\big). \tag{B.2.23}$$

We are interested in spacelike geodesics that reach some deepest points Z_0, where $\frac{dZ}{d\lambda} = 0$. If $E^2 - P^2 > 0$, then $\frac{dZ}{d\lambda} \neq 0$ for $\forall\ Z$; if instead $E^2 - P^2 < 0$, then

$$Z_0 = \frac{1}{\sqrt{P^2 - E^2}}, \qquad Z \in [0, Z_0]. \tag{B.2.24}$$

And we can solve the equation (B.2.23)

$$\lambda(Z) = \pm \mathrm{arctanh}\sqrt{1 - (P^2 - E^2)Z^2}. \tag{B.2.25}$$

At the AdS_3 boundary $Z = 1$, $\lambda = \pm\infty$. We choose conventions such that $\lambda = +\infty$ and $\lambda = -\infty$ are at the right and left Rindler wedge boundary points,

respectively. At the furthest point Z_0, $\lambda = 0$. Inverting (B.2.25) then gives

$$Z(\lambda) = \frac{1}{\sqrt{P^2 - E^2}} \text{sech}\lambda. \tag{B.2.26}$$

Plug (B.2.26) into (B.2.21) and integrate, we have

$$x_0(\lambda) = \frac{E}{P^2 - E^2} \tanh\lambda + C_0, \tag{B.2.27}$$

$$x_1(\lambda) = \frac{P}{P^2 - E^2} \tanh\lambda + C_1, \tag{B.2.28}$$

where C_0 and C_1 are integration constants that can be determined by the geodesic endpoints on the AdS_3 boundary.

The separations in x_0 and x_1 determine E and P via

$$\Delta x_0 = 2\int_0^\infty \frac{dx_0}{d\lambda} d\lambda = 2E \int_0^\infty Z^2 d\lambda = 2E \int_0^{Z_0} \frac{Z dZ}{\sqrt{1 - (P^2 - E^2)Z^2}} = \frac{2E}{P^2 - E^2}, \tag{B.2.29}$$

$$\Delta x_1 = 2\int_0^\infty \frac{dx_1}{d\lambda} d\lambda = 2P \int_0^\infty Z^2 d\lambda = 2P \int_0^{Z_0} \frac{Z dZ}{\sqrt{1 - (P^2 - E^2)Z^2}} = \frac{2P}{P^2 - E^2}. \tag{B.2.30}$$

Where in both equations, in the first step the 2 comes from $\lambda \to -\lambda$ symmetry, in the second step we plugged in (B.2.21), and in the third step we change the integration variable from λ to Z using (B.2.23). From (B.2.29) and (B.2.30), one can then solve for E and P in terms of Δx_0 and Δx_1

$$E = \frac{2\Delta x_0}{\Delta x_1^2 - \Delta x_0^2}, \qquad P = \frac{2\Delta x_1}{\Delta x_1^2 - \Delta x_0^2}. \tag{B.2.31}$$

The two points P_1 and P_2 where the geodesic is anchored on the boundary therefore determine the value of E and P.

B.2.4 Displaced half spaces

In this subsection, we find the exact solution to the displaced half space geodesic considered in subsection 3.1.1 and Appendix B.1.1.

B.2.4.1 In Poincare AdS$_3$

We have a spacelike geodesic anchoring on the two boundary points in AdS$_3$

$$P_1 = (e^X \text{sinh}T,\ e^X \text{cosh}T), \qquad P_2 = (e^{-X} \text{sinh}T,\ -e^{-X} \text{cosh}T), \tag{B.2.32}$$

therefore,

$$\Delta x_0 = 2 \sinh X \sinh T, \qquad \Delta x_1 = 2 \cosh X \cosh T. \tag{B.2.33}$$

The explicit values of E and P can be determined by plugging (B.2.33) into (B.2.31). Further substituting these E and P into (B.2.26), (B.2.27) and (B.2.28), fixes $Z(\lambda)$ and leaves $x_0(\lambda)$ and $x_1(\lambda)$ with C_0 and C_1 unknown. C_0 and C_1 can be evaluated by noting that the geodesic is anchored on the point P_1 on the AdS$_3$ boundary,

$$x_0(+\infty) = \text{sinh}T, \qquad x_1(+\infty) = \text{cosh}T. \tag{B.2.34}$$

Put everything together, we have the following parametric curves

$$Z(\lambda) = \sqrt{\frac{\cosh 2T + \cosh 2X}{2}}\ \text{sech}\lambda, \tag{B.2.35}$$

$$x_0(\lambda) = \sinh T(\sinh X \tanh \lambda + \cosh X), \tag{B.2.36}$$

$$x_1(\lambda) = \cosh T(\cosh X \tanh \lambda + \sinh X), \tag{B.2.37}$$

where λ is the affine parameter along the geodesic. At $\lambda = 0$, the geodesic reaches its deepest point Z_0; at P_1 and P_2, $\lambda = \pm\infty$, respectively. When the geodesic is at the horizon, $x_0 = \pm x_1$, one finds $\lambda_{\text{hor}} = \pm T - X$. Therefore, the interior range of the geodesic correspond to $\lambda \in (-T - X, T - X)$, and the exterior range $\lambda \in (-\infty, -T - X) \cup (T - X, +\infty)$. A plot of the parametric curve (B.2.35), (B.2.36), (B.2.37) in Poincare AdS_3 can be found in Fig. B.4.

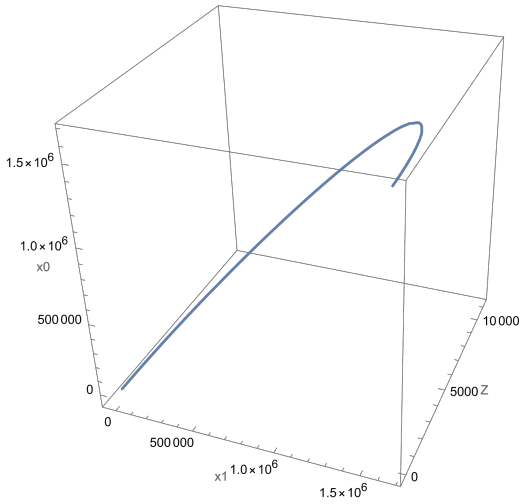

Figure B.4: Spacelike geodesic in Poincare AdS_3, with coordinates (Z, x_0, x_1). Here we plot for $T = 10$ and $X = 5$.

When $X = 0$, the above parametric curve (B.2.35), (B.2.36) and (B.2.37) becomes

$$Z(\lambda) = \cosh T \, \text{sech}\lambda, \quad x_0(\lambda) = \sinh T, \quad x_1(\lambda) = \cosh T \, \tanh \lambda, \quad \text{(B.2.38)}$$

which is the semi-circle

$$Z^2 + x_1^2 = \cosh^2 T, \qquad x_0 = \sinh T \qquad \text{(B.2.39)}$$

studied in (Hartman & Maldacena, 2013). The furthest point this semi-circle can reach in Poincare AdS_3 is $Z_0 = \cosh T$.

B.2.4.2 In planar BTZ

By applying the inverse coordinate transformation (B.2.18)-(B.2.20), one can map the spacelike geodesic (B.2.35), (B.2.36) and (B.2.37) into the BTZ interior [2]

$$z(\lambda) = \sqrt{\frac{\cosh 2T + \cosh 2X}{\cosh(2(\lambda + X)) + \cosh 2X}}, \tag{B.2.41}$$

$$\tilde{t}(\lambda) = \operatorname{arcsinh}\left(\frac{\sqrt{2}\cosh T \sinh(\lambda + X)}{\sqrt{\cosh 2T - \cosh(2(\lambda + X))}}\right), \tag{B.2.42}$$

$$x(\lambda) = \frac{1}{2}\log(\text{sech}\lambda \cosh(\lambda + 2X)). \tag{B.2.43}$$

Notice that λ is still the affine parameter in Poincare AdS_3, although the geodesic is mapped to BTZ. $z(\lambda)$ (B.2.41) peaks at $\lambda = -X$,

$$z_0 = z(-X) = \sqrt{\frac{\cosh 2T + \cosh 2X}{1 + \cosh 2X}} \approx e^{T-X}, \tag{B.2.44}$$

where $\tilde{t} = 0$. Like in the radial $X = 0$ case, z_0 grows exponentially with T for large T. When $X = 0$, (B.2.44) becomes $z_0 = \cosh T$, which is the same as Z_0 in AdS_3. From (B.2.43) one have $x(+\infty) = X$ and $x(-\infty) = -X$. Notice that $x(\lambda)$ does not depend on T.

The complicated parametric curves (B.2.41), (B.2.42) and (B.2.43) in the interior regions $-T - X < \lambda < T - X$ simplify greatly in the large T, large X ($T > X$)

[2] (B.2.41) is obtained from

$$\alpha(\lambda) = \arcsin\left(\sqrt{\frac{\cosh 2T - \cosh(2(\lambda + X))}{\cosh 2T + \cosh 2X}}\right) \tag{B.2.40}$$

using (B.2.7).

limit. one can show that $\tilde{t}$ is *linear* in λ,

$$\tilde{t}(\lambda) = \lambda + X, \tag{B.2.45}$$

and $z(\lambda)$ behaves as

$$z(\lambda) = \begin{cases} e^{T-X-\lambda}, & \lambda \in (0, T-X), \\ e^{T-X}, & \lambda \in (-2X, 0), \\ e^{T+X+\lambda}, & \lambda \in (-T-X, -2X), \end{cases} \tag{B.2.46}$$

which is at a *constant* value $z_0 = e^{T-X}$ for λ between $(-2X, 0)$. This value is the *maximum* value of $z(\lambda)$, i.e. the deepest point z_0 (B.2.44) the geodesic can reach in the BTZ interior. Moreover, $x(\lambda)$ is *piecewise linear* in λ

$$x(\lambda) = \begin{cases} X, & \lambda \in (0, T-X), \\ \lambda + X, & \lambda \in (-2X, 0), \\ -X, & \lambda \in (-T-X, -2X), \end{cases} \tag{B.2.47}$$

In other words, almost all the displacements in the x direction occurred in the region $\lambda \in [-2X, 0]$ linearly with λ, whereas in the complementary region of λ (which includes all the exterior) there are nearly no displacements.

From (B.2.46) and (B.2.47), it can be observed that when $\lambda \in (-2X, 0)$, $z(\lambda)$ stays at z_0 while $x(\lambda)$ varies linearly; in the complementary interior region $\lambda \in (-T-X, -2X) \cup (0, T-X)$, $z(\lambda)$ varies non-trivially while $x(\lambda)$ stays at constant values. Combining with the fact that $\tilde{t}(\lambda) = \lambda + X$ is linear in λ for all interior values $\lambda \in (-T-X, T-X)$, one can eliminate λ and write down the expression $z(\tilde{t})$ and $x(\tilde{t})$ in the scaling limit. Noticing that for large z there is asymptotically no difference between Schwarzschild and infalling time (B.2.3), and making the

change of variable $z = e^{\xi}$, one arrives at (3.1.4) in the main text.

By applying the inverse coordinate transformation (B.2.12)-(B.2.14), one can map the spacelike geodesic (B.2.35), (B.2.36) and (B.2.37) into the BTZ exterior [3]

$$z(\lambda) = \sqrt{\frac{\cosh 2T + \cosh 2X}{\cosh(2(\lambda + X)) + \cosh 2X}}, \tag{B.2.49}$$

$$t(\lambda) = \operatorname{arcsinh}\left(\frac{\sqrt{2}\sinh T \cosh(\lambda + X)}{\sqrt{\cosh(2(\lambda + X)) - \cosh 2T}}\right), \tag{B.2.50}$$

$$x(\lambda) = \frac{1}{2}\log(\operatorname{sech}\lambda \cosh(\lambda + 2X)). \tag{B.2.51}$$

Notice that the expression of $z(\lambda)$ (B.2.49) and $x(\lambda)$ (B.2.51) are the same as those in the BTZ black hole interior (B.2.41) and (B.2.43), respectively. It is just that the range of λ are different.

Under the scaling limit, the parametric curves (B.2.49), (B.2.50) and (B.2.51) in the exterior regions $\lambda \in (-\infty, -T - X) \cup (T - X, +\infty)$ also simplify greatly.

$$t(\lambda) = \begin{cases} T, & \lambda \in (T - X, +\infty), \\ -T, & \lambda \in (-\infty, -T - X), \end{cases} \tag{B.2.52}$$

where we have used the fact that for geodesics in the thermal double, i.e. when $\lambda \in (-\infty, -T - X)$, $\operatorname{Im} t = -i\pi$ (Klebanov & Witten, 1999); we can therefore let $t \to t + i\pi$ in the thermal double, like introducing $\tilde{t} = t + \frac{i\pi}{2}$ (B.2.7) in the interior. (B.2.52) indicates that in the exterior regions, the HRT surface is on a *constant-t slice* $t = T$ ($t = -T$ in the thermal double) apart from the near-horizon

[3] (B.2.49) is obtained from

$$\rho = \operatorname{arccosh}\left(\sqrt{\frac{\cosh(2(\lambda + X)) + \cosh 2X}{\cosh 2T + \cosh 2X}}\right) \tag{B.2.48}$$

using (B.2.5).

divergence. For $z(\lambda)$ and $x(\lambda)$, we have

$$z(\lambda) = \begin{cases} e^{T-X-\lambda}, & \lambda \in (T-X, +\infty), \\ e^{T+X+\lambda}, & \lambda \in (-\infty, -T-X), \end{cases} \tag{B.2.53}$$

$$x(\lambda) = \begin{cases} X, & \lambda \in (T-X, +\infty), \\ -X, & \lambda \in (-\infty, -T-X), \end{cases} \tag{B.2.54}$$

which are the same as $z(\lambda)$ (B.2.46) and $x(\lambda)$ (B.2.47) when $\lambda \in (0, T-X)$ and $\lambda \in (-T-X, -2X)$ in the interior, respectively.

When $T < X$. The expressions of $z(\lambda)$, $\tilde{t}(\lambda)$, $t(\lambda)$ and $x(\lambda)$ are the same as (B.2.41), (B.2.42), (B.2.50), and (B.2.43), respectively, but the scaling of $z(\lambda)$ is different.

$$z(\lambda) = \begin{cases} e^{-\lambda}, & \lambda \in (0, \infty), \\ 1, & \lambda \in (-2X, 0), \\ e^{T+X+\lambda}, & \lambda \in (-\infty, -2X), \end{cases} \tag{B.2.55}$$

(B.2.55) then indicates that z reaches just to the horizon instead of going deeper into the interior. The geodesic moves transversely in x when at the plateau $z = 1$.

Plots of the parametric curves (B.2.41)-(B.2.43), (B.2.49)-(B.2.51) and (B.2.55) can be found in Fig. B.5 and B.6.

B.2.5 Static geodesic

To study the static geodesic only, it suffices to work on the $t = 0$ slice in BTZ; we will, however, work on the $t = T$ slice for the need of subsection B.3.2.

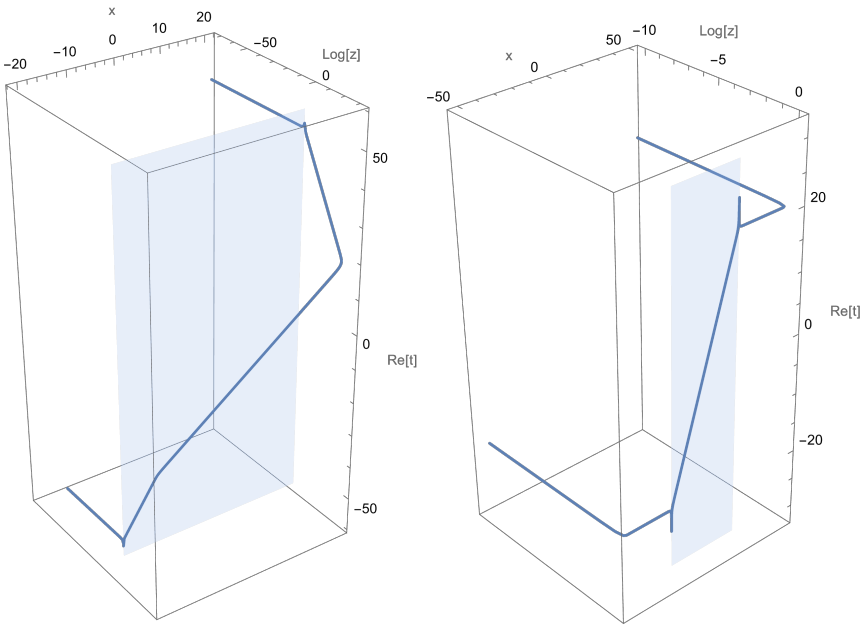

Figure B.5: Spacelike geodesic in BTZ in the coordinates $(\log z, \tilde{t}, x)$. Here we plot for $T = 50$ and $X = 20$ in the left figure and $T = 20$ and $X = 50$ in the right figure. The light blue surface is the black hole horizon.

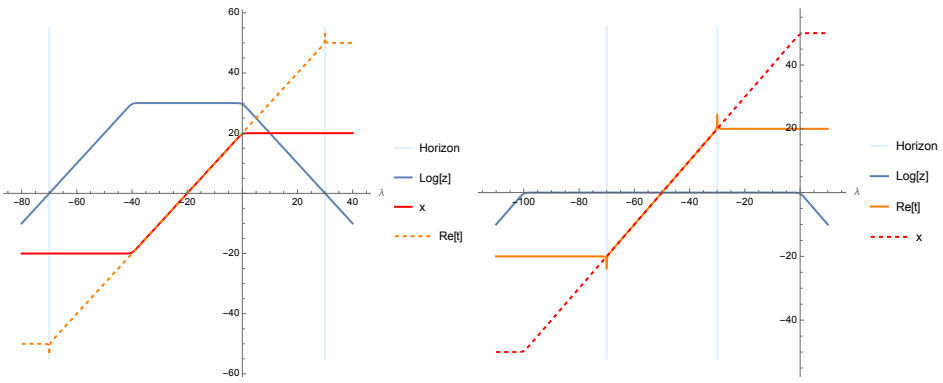

Figure B.6: *Left*: Plot of $\log z(\lambda)$ (blue), $\tilde{t}(\lambda)$ or $t(\lambda)$ (dashed orange) and $x(\lambda)$ (red) when $T = 50$ and $X = 20$. *Right*: Plot of $\log z(\lambda)$ (blue), $\tilde{t}(\lambda)$ or $t(\lambda)$ (orange) and $x(\lambda)$ (dashed red) when $T = 20$ and $X = 50$. The light blue lines are the black hole horizons.

B.2.5.1 In Poincare AdS$_3$

To find the expression of the spacelike geodesic with endpoints P_2 and P_3, with

$$P_2 = \Big(-\frac{D}{2}, T \Big), \qquad P_3 = \Big(\frac{D}{2}, T \Big), \tag{B.2.56}$$

as a parametric curve in BTZ, we again map it to Poincare AdS$_3$ using the transformations in Appendix B.2.2. The general expression of the spacelike geodesic in AdS$_3$ is the parametric curve (B.2.26)-(B.2.28), but the boundary conditions are now given instead by P_2 and P_3 (B.2.56) mapped to Poincare AdS$_3$

$$P_2 = (e^{-\frac{D}{2}} \sinh T,\ e^{-\frac{D}{2}} \cosh T), \quad P_3 = (e^{\frac{D}{2}} \sinh T,\ e^{\frac{D}{2}} \cosh T), \tag{B.2.57}$$

which yields

$$\Delta x_0 = 2 \sinh \frac{D}{2} \sinh T, \qquad \Delta x_1 = 2 \sinh \frac{D}{2} \cosh T. \tag{B.2.58}$$

Plugging (B.2.58) into (B.2.31), and using the boundary condition (B.2.57), one finds

$$Z(\lambda) = \sinh \frac{D}{2}\, \mathrm{sech}\lambda, \tag{B.2.59}$$

$$x_0(\lambda) = \sinh T \Big(\sinh \frac{D}{2} \tanh \lambda + \cosh \frac{D}{2} \Big), \tag{B.2.60}$$

$$x_1(\lambda) = \cosh T \Big(\sinh \frac{D}{2} \tanh \lambda + \cosh \frac{D}{2} \Big). \tag{B.2.61}$$

Notice that $x_0(\lambda) < x_1(\lambda)$ due to $\sinh T < \cosh T$, indicating that the geodesic is always in the exterior region.

B.2.5.2 In planar BTZ

Mapping the geodesic (B.2.59)-(B.2.61) to BTZ using (B.2.12)-(B.2.14), one finds

$$z(\lambda) = \frac{\sinh \frac{D}{2}}{\sqrt{\cosh\lambda \cosh(D+\lambda)}}, \tag{B.2.62}$$

$$x(\lambda) = \frac{1}{2}\log(\text{sech}\lambda \cosh(D+\lambda)), \tag{B.2.63}$$

and $t = T$. In (B.2.62) and (B.2.63) $\lambda \in (-\infty, +\infty)$. $z(\lambda)$ (B.2.62) peaks at $\lambda = -\frac{D}{2}$: $z(-\frac{D}{2}) = \tanh\frac{D}{2}$. As D gets large, $z(-\frac{D}{2}) \to 1$. Notice that $x(\lambda)$ takes the same form as (B.2.43) and (B.2.51) with $2X \to D$. A plot of the full expression (B.2.62)-(B.2.63) can be found in Fig. 3.3.

As is explained in the main text, there is a finite difference between Schwarzschild and infalling time in the plateau regions due to (3.1.10). For example, at the deepest point the RT surfaces reach, we have $u(-\frac{D}{2}) = T - \frac{D}{2}$. The plot of the static RT surface (B.2.62)-(B.2.63) in infalling coordinate can be found in Fig. B.7.

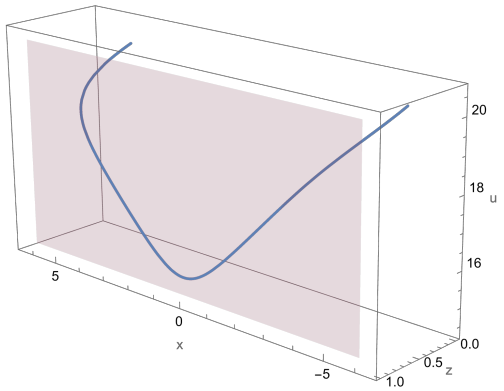

Figure B.7: A 3d plot of the static geodesic given by (B.2.62)-(B.2.63) and shown in Fig. 3.3 in the (u, z, x) coordinate, , for $T = 20$ and $D = 10$. The light blue surface denotes the black hole horizon $z = 1$. The plateau part of the geodesic lies close to the $z = 1$ plane.

In the scaling limit,

$$z(\lambda) = \begin{cases} e^{-\lambda}, & \lambda \in (0, +\infty), \\ 1 - \frac{1}{2}(e^{2\lambda} + e^{-2(\lambda+D)}) \approx 1, & \lambda \in (-D, 0), \\ e^{\lambda+D}, & \lambda \in (-\infty, -D). \end{cases} \tag{B.2.64}$$

One can then obtain (3.1.11) by plugging (B.2.64) into (3.1.10), and using (B.2.47) with $2X \to D$ to eliminate λ.

According to the BTZ-AdS$_3$ map (B.2.9)-(B.2.11), a shift of $\ell + \frac{D}{2}$ in x corresponds to a boost of $e^{\ell+\frac{D}{2}}$ to (B.2.59)-(B.2.61), which are (B.3.10)-(B.3.12) in subsection B.3.2 of the main text.

B.2.6 Entanglement entropy of displaced half space

In this appendix, we calculate the entanglement entropy computed by the displaced half space geodesic solution found in Appendix B.2.4, using both holographic and CFT approaches. We will see that results from these two methods match each other.

B.2.6.1 Gravity calculation

The entanglement entropy is computed by the regulated length A_{12} of the spacelike geodesic connecting P_1 and P_2.

$$A_{12} = \int_{\lambda_2}^{\lambda_1} d\lambda = \lambda_1 - \lambda_2, \tag{B.2.65}$$

where λ_i $(i = 1, 2)$ are the value of λ corresponding to the near boundary cutoffs, $Z(\lambda_1)$ and $Z(\lambda_2)$. $\lambda_1 \to +\infty$ and $\lambda_2 \to -\infty$. In BTZ, the cutoff is at some large radius $\rho = \rho_{\max}$. Following (Hartman & Maldacena, 2013) we introduce the notion

$\epsilon = e^{-\rho_{\max}}$. When mapped to Poincare AdS_3 using (B.2.9), the near-boundary cutoffs $\rho = \rho_{\max}$ on the two sides are mapped to

$$Z(\lambda_1) = e^{x(\lambda_1)}\,\mathrm{sech}\rho_{\max} = 2\epsilon e^{X}, \qquad Z(\lambda_2) = e^{x(\lambda_2)}\,\mathrm{sech}\rho_{\max} = 2\epsilon e^{-X}, \tag{B.2.66}$$

where we have used $x(+\infty) = X$ and $x(-\infty) = -X$ from (B.2.51). Therefore, from (B.2.35), one finds

$$\lambda_1 = -X + \log\Big(\frac{1}{\sqrt{2}\epsilon}\sqrt{\cosh 2T + \cosh 2X}\Big), \tag{B.2.67}$$

$$-\lambda_2 = X + \log\Big(\frac{1}{\sqrt{2}\epsilon}\sqrt{\cosh 2T + \cosh 2X}\Big), \tag{B.2.68}$$

and the regulated geodesic length A_{12} is given by

$$A_{12} = \lambda_1 - \lambda_2 = \log\Big(\frac{1}{2\epsilon^2}(\cosh 2T + \cosh 2X)\Big). \tag{B.2.69}$$

The entanglement entropy is thus

$$S(T) = \frac{1}{4G_N}A_{12} = \frac{c}{6}\log\Big(\frac{1}{2\epsilon^2}(\cosh 2T + \cosh 2X)\Big). \tag{B.2.70}$$

where we have used the Brown-Henneaux central charge (Brown & Henneaux, 1986). Notice that when $X = 0$, $S(T) = \frac{c}{3}\log\big(\frac{\cosh T}{\epsilon}\big)$, which matches the result in (Hartman & Maldacena, 2013). In the scaling limit,

$$S(T) - S_{\text{div}} = \begin{cases} \dfrac{c}{3}T, & T > X, \\ \dfrac{c}{3}X, & T < X, \end{cases} \tag{B.2.71}$$

where $S_{\text{div}} = \frac{c}{3}\log\frac{1}{\epsilon}$. (B.2.71) matches the operator entanglement entropy (3.1.5) ($T > X$) and (3.1.8) ($T < X$) in the main text. For small T,

$$S(T) \approx \frac{c}{3}\log\cosh X + \frac{c}{3(\cosh 2X + 1)}T^2 + S_{\text{div}}, \tag{B.2.72}$$

indicating that the entanglement entropy grows quadratically with T, with a coefficient that depends on X. At $T = 0$, one finds

$$S(T) \approx \frac{c}{3}X + S_{\text{div}} \tag{B.2.73}$$

for large X.

B.2.6.2 CFT calculation

The CFT entanglement entropy is computed by the two-point function of twist operators (Calabrese & Cardy, 2004)

$$\langle \Phi_+(z_1, \overline{z}_1)\Phi_-(z_2, \overline{z}_2)\rangle \tag{B.2.74}$$

with dimension $\Delta_n = \frac{c}{12}\left(n - \frac{1}{n}\right)$. The twist operators are inserted at

$$z_1 = \overline{z}_1 = X, \qquad z_2 = 2T - X + \frac{i\beta}{2}, \qquad \overline{z}_2 = -2T - X - \frac{i\beta}{2}, \tag{B.2.75}$$

see Fig. B.8 for illustrations. Mapping to the complex plane, $w = e^{\frac{2\pi z}{\beta}}$, $\overline{w} = e^{\frac{2\pi\overline{z}}{\beta}}$,

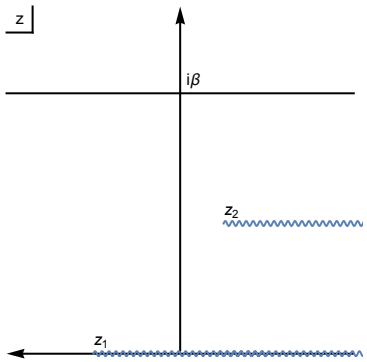

Figure B.8: Insertion of twist operators at z_1 and z_2 on the Euclidean cylinder.

one finds the holomorphic and anti-holomorphic part of (B.2.74) are given by

$$\begin{aligned}\langle\Phi_+(z_1)\Phi_-(z_2)\rangle &= \Big(\frac{\partial z_1}{\partial w_1}\Big)^{-\frac{\Delta_n}{2}}\Big(\frac{\partial z_2}{\partial w_2}\Big)^{-\frac{\Delta_n}{2}}\frac{1}{|w_1-w_2|}\\ &= \Big(\frac{\beta}{4\pi}\cosh\Big(\frac{2\pi}{\beta}(T-X)\Big)\Big)^{-\Delta_n}, \qquad \text{(B.2.76)}\\ \langle\overline{\Phi}_+(\overline{z}_1)\overline{\Phi}_-(\overline{z}_2)\rangle &= \Big(\frac{\partial \overline{z}_1}{\partial \overline{w}_1}\Big)^{-\frac{\Delta_n}{2}}\Big(\frac{\partial \overline{z}_2}{\partial \overline{w}_2}\Big)^{-\frac{\Delta_n}{2}}\frac{1}{|\overline{w}_1-\overline{w}_2|}\\ &= \Big(\frac{\beta}{4\pi}\cosh\Big(\frac{2\pi}{\beta}(T+X)\Big)\Big)^{-\Delta_n}. \qquad \text{(B.2.77)}\end{aligned}$$

Taking the product of (B.2.76) and (B.2.77), setting $\beta = 2\pi$ and introducing the cutoff, one finds

$$\langle\Phi_+(z_1,\overline{z}_1)\Phi_-(z_2,\overline{z}_2)\rangle = \Big(\frac{1}{2\epsilon^2}\big(\cosh 2T+\cosh 2X\big)\Big)^{-\Delta_n}. \qquad \text{(B.2.78)}$$

The entanglement entropy is then obtained by $S(t) = -\partial_n I_n|_{n=1}$, which is precisely (B.2.70).

B.3 Exact solutions of EWCS in BTZ black hole

In this Appendix, we find exact solutions to the dynamics of entanglement wedge cross sections in $d = 2$, adopting the setup in section 3.2 in the main text.

B.3.1 Non-equilibrium EWCS

The time depending EWCS starts from the static RT surface P_2P_3 and ends on the end of the world brane. By symmetry, it starts from the mid-point $(t, x) = (T, \tanh \frac{D}{2})$ of P_2P_3. As all spacelike geodesics in AdS_3 reach the conformal boundary (Hubeny, 2012), we can imagine the EWCS as the part of a spacelike geodesic between $\left(T, \tanh \frac{D}{2}\right)$ and the EoW brane. Let us suppose that this fictitious geodesic starts from the $t = T'$ line on the boundary. As P_1 does not play any roles in this part of calculation, we can choose a coordinate such that this fictitious geodesic is at $x = 0$. The exterior part of this fictitious geodesic is then given by (B.2.49) and (B.2.51) with $X = 0$

$$z(\lambda) = \cosh T' \mathrm{sech} \lambda, \tag{B.3.1}$$

$$\sinh t(\lambda) = \frac{\sinh T'}{\sqrt{1 - \cosh^2 T' \mathrm{sech}^2 \lambda}}. \tag{B.3.2}$$

As the fictitious geodesic passes the mid-point/furthest point of the static geodesic $\left(T, \tanh \frac{D}{2}\right)$, we have 2 equations

$$\tanh \frac{D}{2} = \cosh T' \mathrm{sech} \lambda, \tag{B.3.3}$$

$$\sinh T = \frac{\sinh T'}{\sqrt{1 - \cosh^2 T' \mathrm{sech}^2 \lambda}}, \tag{B.3.4}$$

which allows us to solve for T' and λ in terms of T and D. Plugging (B.3.3) into (B.3.4), we have

$$T' = \text{arcsinh}\Big(\sinh T \text{sech}\frac{D}{2}\Big) \tag{B.3.5}$$

$$\approx T - \frac{D}{2} + \log 2, \tag{B.3.6}$$

where in getting (B.3.6), we have taken the large T, large D limit. This means that the fictitious geodesic emanates from the $t = T - \frac{D}{2} + \log 2$ line on the conformal boundary. Plugging (B.3.5) back into (B.3.3), we can solve for λ. The EWCS intersects the EoW brane at the point of time reflection symmetry $\tilde{t} = 0$. According to (B.2.42) with $X = 0$, this is at $\lambda = 0$. Therefore, the length of EWCS is simply given by λ

$$\ell(\text{EWCS}) = \text{arccosh}\left(\coth\frac{D}{2}\sqrt{\frac{\cosh D + \cosh 2T}{\cosh D + 1}}\right), \tag{B.3.7}$$

$$\approx T - \frac{D}{2} + \log 2, \tag{B.3.8}$$

which grows linearly with T with slope $v_E = 1$, see Fig. 3.10. Notice that the EWCS starts to be non-zero at $t = \text{arccosh}\sinh\frac{D}{2} \approx \frac{D}{2}$. Therefore, apart from the small $\text{arccosh}\sqrt{2}$ factor that is negligible in the scaling limit, the EWCS growth is actually *continuous* in time. This is because the fictitious geodesic starts on the $t = T - \frac{D}{2}$ line (B.3.6) instead of $t = T$ line on the boundary. See Fig. B.9 for a plot of the non-equilibrium EWCS.

As a consistency check, taking the $D \to 0$ limit of (B.3.7), one finds

$$\ell(\text{EWCS}) \approx \log\Big(\frac{4}{D}\cosh T\Big), \tag{B.3.9}$$

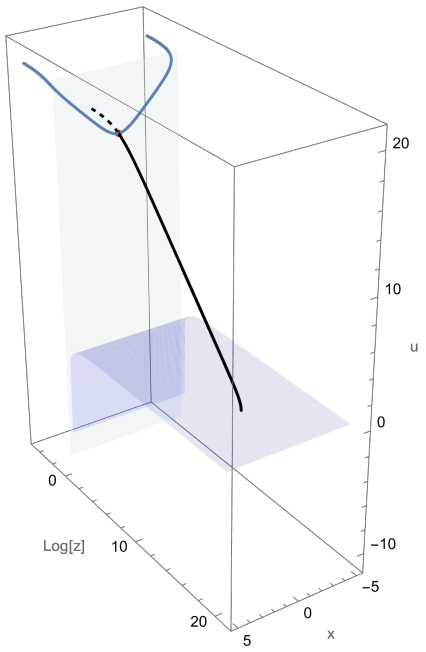

Figure B.9: Plot of non-equilibrium EWCS in $d = 2$ with BTZ coordinates $(u, \log(z), x)$, for $T = 20$ and $D = 10$. The static RT surface (blue) stays close to the horizon $z = 1$ (vertical light green surface) before shooting exponentially towards the boundary $z = 0$ (didn't plot). The saturated EWCS (black) starts from the static RT surface at the midpoint (red dot) of the latter, and then enters the interior where its length grows linearly according to (B.3.8). The non-equilibrium EWCS ends perpendicularly on the EoW brane (light blue surface), whose location is given by $\tilde{t} = 0$ or equivalently $u = -\mathrm{arccoth} z \to 0$ for large z. Notice that if one continues the EWCS to the boundary (black dashed line), it anchors on the $T - \frac{D}{2}$ line, instead of the T line that the static RT surface ends. This $-\frac{D}{2}$ difference ensures that the EWCS growth is continuous in time in the scaling limit.

which reduces to the length of the spacelike geodesic computing the time-depending holographic entanglement entropy (Hartman & Maldacena, 2013). Here, the small D can be interpreted as proportional to the UV cutoff ϵ.

B.3.2 Saturated Entanglement Wedge Cross Section

The saturated EWCS starts from the point A on the static geodesic P_2P_3 and ends on the point B on the radial geodesic ending on the EoW brane. Again, it is most straightforward to map this calculation to Poincare AdS_3. Notice that the static geodesic P_2P_3 is just the parametric curve (B.2.62)-(B.2.63) with a *shift* of $\ell+\frac{D}{2}$ in the x coordinate (B.2.63); in AdS_3, this shift of $\ell+\frac{D}{2}$ in x corresponds to a *boost* of $e^{\ell+\frac{D}{2}}$ to $\big(Z(\lambda), x_0(\lambda), x_1(\lambda)\big)$, see (B.2.9)-(B.2.11). Therefore, in Poincare AdS_3, the coordinates of A on the static geodesic P_2P_3 are given by (see Appendix B.2.5)

$$Z(\lambda) = e^{\ell+\frac{D}{2}} \sinh\frac{D}{2}\,\text{sech}\lambda, \tag{B.3.10}$$

$$x_0(\lambda) = e^{\ell+\frac{D}{2}} \sinh T\,\text{sech}\lambda\cosh\Big(\lambda+\frac{D}{2}\Big), \tag{B.3.11}$$

$$x_1(\lambda) = e^{\ell+\frac{D}{2}} \cosh T\,\text{sech}\lambda\cosh\Big(\lambda+\frac{D}{2}\Big). \tag{B.3.12}$$

As B is on a radial geodesic starts from the boundary point P_1 and ends on the EoW brane, its coordinates are simply given by (B.2.38)

$$Z(\mu) = \cosh T\,\text{sech}\mu, \tag{B.3.13}$$

$$x_0(\mu) = \sinh T, \tag{B.3.14}$$

$$x_1(\mu) = \cosh T\tanh\mu, \tag{B.3.15}$$

where μ is the affine parameter along the geodesic emanating from P_1 and ends on the EoW brane.

B.3.2.1 Length of saturated EWCS

Now, we would like to calculate the geodesic distance between A and B, and find its minimum with respect to the two variables $\lambda \in (-\infty, +\infty)$ and $\mu \in [0, +\infty)$.[4] In $2d$, one can find the geodesic distance between two arbitrary points using the geodesic distance formula in Poincare AdS_3 below, without knowing the explicit expressions of the geodesic connecting them

$$\cosh d(A,B) = T_1^A T_1^B + T_2^A T_2^B - X_1^A X_1^B - X_2^A X_2^B, \tag{B.3.16}$$

where the embedding coordinates are given by

$$T_1 = \frac{1 + (Z^2 - x_0^2 + x_1^2)}{2Z}, \tag{B.3.17}$$

$$T_2 = \frac{x_0}{Z}, \tag{B.3.18}$$

$$X_1 = \frac{x_1}{Z}, \tag{B.3.19}$$

$$X_2 = \frac{1 - (Z^2 - x_0^2 + x_1^2)}{2Z}. \tag{B.3.20}$$

Plugging in the coordinates of A (B.3.10)-(B.3.12) and B (B.3.13)-(B.3.15) into the geodesic distance formula (B.3.16), one can find the geodesic distance $d(A, B)$. The explicit expression appears to be lengthy and uninspiring, so we will only present results in the scaling limit,

$$T \to \Lambda \mathfrak{T}, \qquad \ell \to \Lambda \mathfrak{l}, \qquad d \to \Lambda \mathfrak{D}, \qquad \lambda \to \Lambda s, \qquad \mu \to \Lambda m, \tag{B.3.21}$$

where Λ is taken to be large. The EWCS length in the scaling limit (B.3.21) is

$$d(A,B) \approx \frac{\ell}{2} + \log 2, \tag{B.3.22}$$

[4] This is because the radial geodesic $P_1 B$ ends on the EoW brane, where $\mu = 0$

which takes place at

$$\lambda_A \approx -\frac{3}{4}D, \qquad \mu_B \approx T - \frac{1}{2}\Big(\ell + \frac{D}{2}\Big), \tag{B.3.23}$$

here $\approx$ means up to exponentially small corrections. Henceforth, the "equilibrium" EWCS is not truly in equilibrium, instead it asymptotes the extremal value (B.3.22) exponentially slow. From (B.3.23), one finds that

$$z(\lambda_A) \approx \frac{1}{\sqrt{1+e^{-\frac{D}{2}}}}, \quad u(\lambda_A) \approx T - \frac{D}{4} - \log 2, \quad x(\lambda_A) \approx \ell + \frac{D}{4}, \tag{B.3.24}$$

indicating that A is approximately at the *middle* point of the v_B cone upon projection; and[5]

$$z(\mu_B) \approx e^{\frac{1}{2}\left(\ell+\frac{D}{2}\right)} \gg 1, \quad u(\mu_B) \approx T - \frac{1}{2}\Big(\ell + \frac{D}{2}\Big), \quad x(\mu_B) = 0, \tag{B.3.25}$$

implying that B reaches deep into the interior. Notice that the location of $z(B)$ does not time evolve with T to leading order. This is made possible by B traveling towards the horizon since the geodesic goes deeper into the interior as time evolves, as can be seen from (B.3.23).[6] A plot of the location of A and B upon projections can be found in Fig. B.10.

B.3.2.2 In Poincare AdS$_3$

Having computed $l(EWCS)$ (B.3.22) and the coordinates of A and B (B.3.23), we would like to now obtain the expression of the EWCS. Again, we imagine

[5]Notice that as $z(\mu_B) \gg 1$, the difference between Schwarzschild and infalling time at B is negligible, i.e. $u(\mu_B) \approx \tilde{t}(\mu_B)$. One then have $\tilde{t}(\mu_B) \approx \mu_B$ combining (B.3.24) and (B.3.25), consistent with (B.2.45) in the radial, i.e. $X = 0$ case.

[6]Notice that at where the geodesic meets the EoW brane, $\tilde{t} = 0$ and therefore $\mu = 0$ according to (B.2.45) with $X = 0$. Therefore, μ_B measures the distance between B and the EoW brane along the geodesic.

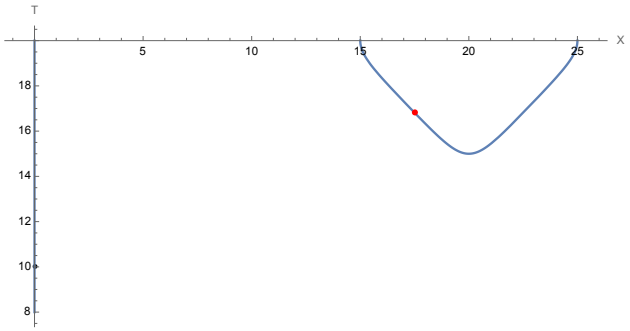

Figure B.10: Locations of A (red) and B (black) upon projections to the boundary along constant infalling time, for $T = 20$, $\ell = 15$ and $D = 10$.

the EWCS as the part of a fictitious spacelike geodesic between A and B. The general expression of a spacelike geodesic in AdS_3 is given as a parametric curve by (B.2.26)-(B.2.28). Imposing the constraints that it passes point A (B.3.24) and B (B.3.25), we have

$$Z(A) = \frac{1}{\sqrt{\mathfrak{P}^2 - \mathfrak{E}^2}} \text{sech}\nu_A, \tag{B.3.26}$$

$$x_0(A) = \frac{\mathfrak{E}}{\mathfrak{P}^2 - \mathfrak{E}^2} \tanh\nu_A + \mathfrak{C}_0, \tag{B.3.27}$$

$$x_1(A) = \frac{\mathfrak{P}}{\mathfrak{P}^2 - \mathfrak{E}^2} \tanh\nu_A + \mathfrak{C}_1, \tag{B.3.28}$$

$$Z(B) = \frac{1}{\sqrt{\mathfrak{P}^2 - \mathfrak{E}^2}} \text{sech}\nu_B, \tag{B.3.29}$$

$$x_0(B) = \frac{\mathfrak{E}}{\mathfrak{P}^2 - \mathfrak{E}^2} \tanh\nu_B + \mathfrak{C}_0, \tag{B.3.30}$$

$$x_1(B) = \frac{\mathfrak{P}}{\mathfrak{P}^2 - \mathfrak{E}^2} \tanh\nu_B + \mathfrak{C}_1, \tag{B.3.31}$$

where ν is the affine parameter along the fictitious geodesic. Now, there are 6 variables $\mathfrak{E}$, $\mathfrak{P}$, $\mathfrak{C}_0$, $\mathfrak{C}_1$, ν_A, and ν_B, as well as 6 constraints (B.3.24) and (B.3.25). To solve for these variables, we can proceed by first finding $\tanh\nu_A$ and $\tanh\nu_B$ from the Z equations above.[7] Substituting them into the x_0 and x_1 equations, and

[7] It turned out that the physical range of parameters corresponds to $\nu_B < \nu_A < 0$.

taking their differences $x_0(\nu_A) - x_0(\nu_B)$ and $x_1(\nu_A) - x_1(\nu_B)$, leaving us with two equations of $\mathfrak{E}$ and $\mathfrak{P}$. We can then solve for all 6 variables. The full expressions are too lengthy to be included in the paper, so we will only discuss their scaling limits (B.3.21) and show plots of this fictitious geodesic.

An interesting feature of this fictitious geodesic is that it hits the hyperboloid $Z^2 = x_0^2 - x_1^2$ corresponding to the BTZ orbifold singularity $z = \infty$ (see Fig. B.3), and then ends on the Milne patch! Of course, only the portion of the geodesic below the hyperboloid is physical when mapped to BTZ. In BTZ, the fictitious geodesic emanates from a point on the conformal boundary, passes A and B, and eventually hits the BTZ singularity.

In the scaling limit (B.3.21), we found

$$\ell(\text{EWCS}) = \nu_A - \nu_B \approx \frac{\ell}{2} + \log 2, \tag{B.3.32}$$

where ν is the affine parameter along the fictitious geodesic. This agrees with (B.3.22).

B.3.2.3 In planar BTZ

When mapped to BTZ, we found that the saturated EWCS shows interesting behaviour as depicted in Fig. B.11: it consists of a plateau in the interior plus an almost null part that shoots exponentially towards the interior on a constant $\tilde{t}$ slice.

The plateau corresponds to $\nu \in (\nu_B, \nu_A]$, excluding a very small region near

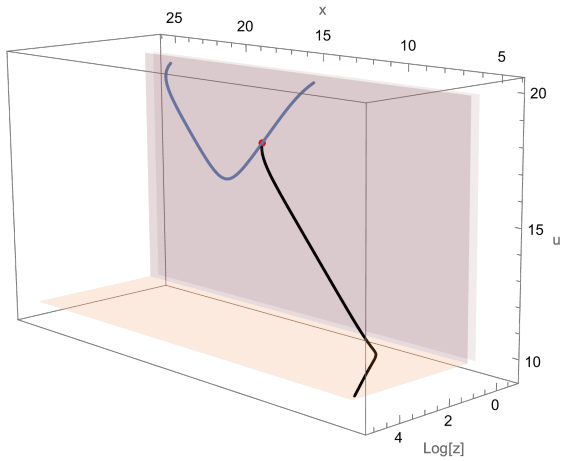

Figure B.11: Plot of saturated EWCS in $d = 2$ with BTZ coordinates $(u, \log(z), x)$, for $T = 20$, $\ell = 15$, and $d = 10$. The static RT surface (blue) stays close to $z = 1$ (vertical light green surface in the back) before shooting exponentially towards the boundary $z = 0$ (didn't plot). The saturated EWCS (black) starts from the static RT surface at point A (red dot), then enters the horizon and stays at $z = \sqrt{2}$ (vertical light blue surface in the front) before becoming almost null and shooting exponentially towards the BTZ singularity $z = \infty$ at constant interior Schwarzschild time $\tilde{t} = T - \left(\ell + \frac{D}{2}\right)$ (horizontal light red surface). Notice that at large z the difference between Schwarzschild and infalling time is negligible.

$\nu \to \nu_B^+$. In this regime we found

$$z(\nu) \approx \sqrt{2}, \tag{B.3.33}$$

$$\tilde{t}(\nu) \approx \nu + T - \frac{D}{4} + \frac{1}{2}\log 2, \tag{B.3.34}$$

$$x(\nu) \approx \nu + \ell + \frac{D}{4} + \frac{1}{2}\log 2, \tag{B.3.35}$$

and therefore

$$u(\nu) \approx \tilde{t}(\nu) - \mathrm{arccoth} z(\nu) = \tilde{t}(\nu) - \mathrm{arccoth}\sqrt{2} \tag{B.3.36}$$

according to (B.2.3), see Fig. B.12. Putting them together yields two equations

$$z \approx \sqrt{2}, \tag{B.3.37}$$

$$u(x) \approx x + T - \ell - \frac{D}{2} - \mathrm{arccoth}\sqrt{2} \tag{B.3.38}$$

describing saturated EWCS. As the range of ν for the plateau region is almost the entire $[\nu_B, \nu_A]$, the EWCS in this region has length

$$\ell(\text{Plateau}) \approx \nu_A - \nu_B \approx \frac{\ell}{2} + \log 2 \approx \ell(\text{EWCS}). \tag{B.3.39}$$

In other words, nearly *all* the length of EWCS (B.3.22) comes from this plateau region.

The EWCS then transforms smoothly into a almost-*null* part that lies on the *constant* $\tilde{t} \approx T - \frac{1}{2}\left(\ell + \frac{D}{2}\right)$ *slice* while shooting exponentially towards the BTZ singularity. In fact, the EWCS is a portion of a spacelike geodesic that *will* hit the BTZ singularity $z = \infty$! To understand the relation between z and x for the

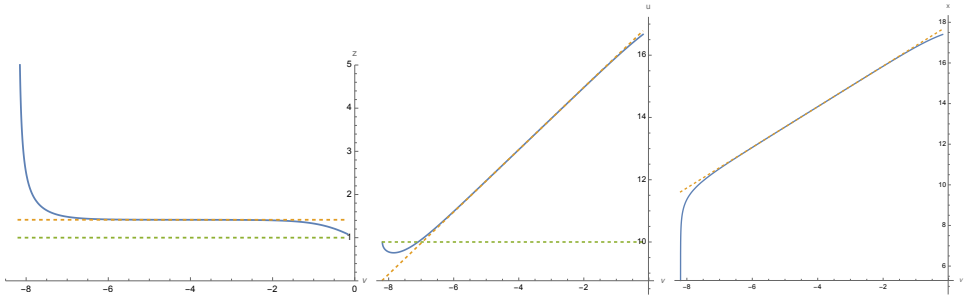

Figure B.12: Plot of $z(\nu)$ (left), $u(\nu)$ (middle) and $x(\nu)$ (right) as well as their scaling limits (dashed), for $T = 20$, $\ell = 15$, and $D = 10$. In the plot of $z(\nu)$, the two dashed lines represent the horizon $z = 1$ and $z = \sqrt{2}$, respectively. In the plot of $u(\nu)$, the 45° and horizontal dashed lines stand for (B.3.36) and the constant interior time slice $\tilde{t} = T - \left(\ell + \frac{D}{2}\right)$ the null geodesic is on, respectively; the small lump near the horizontal dashed line is due to the difference between Schwarzschild and infalling time (B.2.2) when z is not yet large. In the plot of $x(\nu)$, the dashed line is (B.3.35).

almost-null geodesic, we demand the metric (B.2.8) to be null on a constant-$\tilde{t}$ slice,

$$0 = -d\alpha^2 + \cos^2\alpha dx^2 \qquad \Rightarrow \; z = \cosh x \propto e^{|x|}, \tag{B.3.40}$$

where we have used (B.2.7). The *exponential* relation between z and $|x|$ (see Fig. B.13) is consistent with the coordinates of A and B, and the width of the plateau: we have $x(A) \approx \ell + \frac{D}{4}$ according to (B.3.24), and the plateau width is $\Delta x \approx \frac{\ell}{2}$. Therefore, at where the plateau ends and where the exponential growth of z with respect to x starts, we have $x \approx \frac{1}{2}\left(\ell + \frac{D}{2}\right)$. Thus, when the EWCS arrives at B, where $x = 0$, one expects $z(B) \propto e^{\frac{1}{2}\left(\ell + \frac{D}{2}\right)}$ according to (B.3.40). This is indeed the case as in (B.3.25).[8]

The projection of the saturated EWCS along constant infalling time can be found in Fig. B.14. Notice that $u(x)$ agrees with Fig. B.2 obtained from solving the approximate equations of motions in the scaling limit.

[8]Here we work in the scaling limit (B.3.21) and neglect small contributions such as factors of $\log 2$.

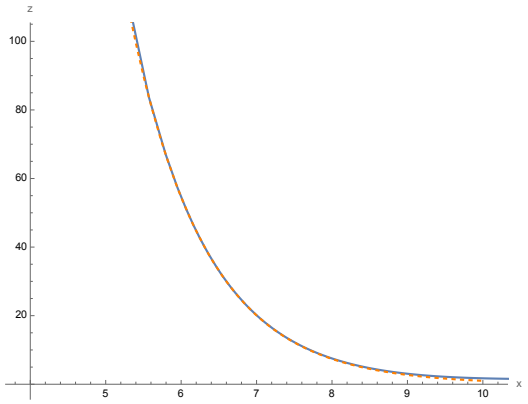

Figure B.13: Exponential relation between z and $|x|$ in the "null" part of EWCS, for $T = 20$, $\ell = 15$, and $D = 10$. The dashed orange line represents $z \propto e^{-x}$.

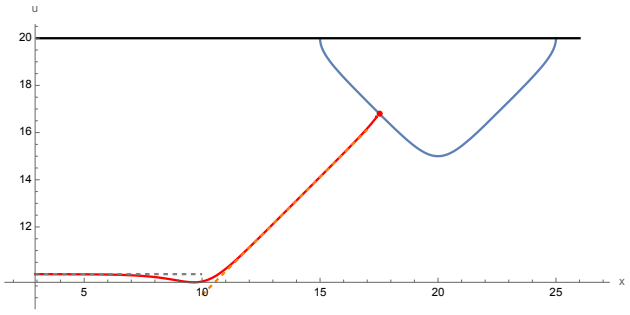

Figure B.14: Projection of saturated EWCS (red) in $d = 2$ along constant infalling time, for $T = 20$, $\ell = 15$, and $D = 10$. The blue triangle is the projection of the static RT surface anchoring on P_2 and P_3 on the boundary. The dashed orange line is the plateau (B.3.38), which is responsible for almost all the length of the EWCS (B.3.22). The horizontal part of the projection is almost null on the $\tilde{t} = T - \frac{\ell}{2}\left(\ell + \frac{D}{2}\right)$ slice (dashed grey). The lump near the transition point is due to the difference between Schwarschild and infalling time (B.2.2) when z is not yet large.

B.4 RT surfaces with spherical regions

Recall that the static RT surface on the $t = T$ slice with a spherical entangling subregion has an area functional given by (1.2.28); in the large entangling subregion limit, this RT surface contains a plateau and two shooting pieces towards the boundary (Hubeny, 2012; Mezei, 2017). As such, we can introduce a near-horizon coordinate $s(r)$ (Mezei, 2017)

$$z(r) = 1 - \epsilon s(r)^2, \tag{B.4.1}$$

where $\epsilon \ll 1$ denotes the closest distance the HRT surface is to the horizon. From (1.2.28), one can obtain the Euler-Lagrange equation $s(r)$. Expanding for small ϵ, and using $a(1) = 0$, one finds the following second-order near-horizon wave equation (Mezei, 2017)

$$s''(r) + \frac{d-2}{r} s'(r) - M^2 s(r) = 0, \quad M^2 = -\frac{d-1}{2} a'(1) b(1)^2 > 0, \tag{B.4.2}$$

whose solution is given by modified Bessel function (Liu & Mezei, 2014)

$$s(r) = C \frac{I_{\frac{d-3}{2}}(Mr)}{r^{\frac{d-3}{2}}} \sim e^{Mr}. \tag{B.4.3}$$

At large r, the solutions (B.4.3) grows exponentially. From (B.4.3), one can write

$$z = 1 - e^{2M(r-r_0)}. \tag{B.4.4}$$

When $0 < r \ll r_0$, $z \to 1^-$, the RT surface is a plateau skimming the horizon; when $r \to r_0^-$, z quickly decays to 0, indicating that the RT surface shoots toward

the conformal boundary. From (B.4.4) we have

$$r - r_0 \sim \frac{\log(1-z)}{b(1)\sqrt{-2(d-1)a'(1)}}. \tag{B.4.5}$$

Combining with (3.3.10) when $z \to 1^-$, we have

$$r \sim \sqrt{\frac{a'(1)}{2(d-1)}} u = v_B u, \tag{B.4.6}$$

where we again used (1.3.18) for v_B. (B.4.6) indicates that like in the strip case (3.3.11), the projection of the RT surface in the large region limit along constant infalling time is a v_B cone.

We remark that the above calculations work for strip entangling subregions as well: the second-order near-horizon wave equation from (1.2.27) is simply $(\frac{d^2}{dx^2} - M^2)s(x)^2 = 0$, with general solution $s(x) = c_1 e^{Mx} + c_2 e^{-Mx}$. $e^{\pm x}$ can be regarded as the $d > 2$ analogue of $e^{\pm\lambda}$ in (B.2.64).

B.5 Scaling behaviour of EWCS in $d > 2$

In this appendix we compare the direct numerical evaluation of the reflected entropy and the corresponding membrane prediction. As described in the main text, these two results should agree in the scaling limit $D \to \infty$. However, we are constrained in our capacity to evaluate the EWCS within this limit. This problem arises from the numerical solution of the intersection equations between the EWCS and the HRT surfaces. Even for the relatively small values of D we do have access to, we can see that the membrane theory is a surprisingly accurate description, able to capture all the main features of the reflected entropy.

To further test the validity of the membrane prediction, we can take a closer look at

some of these key features. First, we can consider the time at which the reflected entropy begins to grow linearly and the size of the gap between the linear growth and the initial vanishing value.

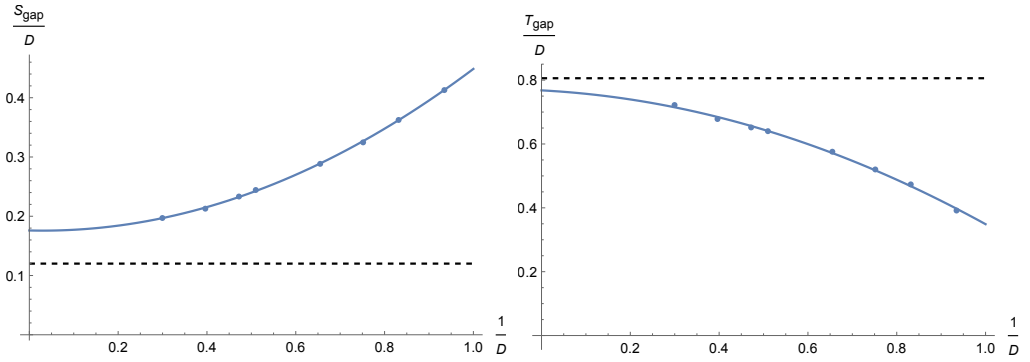

Figure B.15: Comparisson of the time of transition between vanishing EWCS and its regime of linear growth, as well as the size of the discontinuity, as functions of $1/D$. The membrane prediction is depicted in black.

While the discrepancy is somewhat worrying, we can provide an argument for this being simply a numerical issue. The transition between the vanishing and linearly growing regime is dictated not by the EWCS per se, but by the dynamics of entanglement entropy; namely, whether the entanglement wedge is connected or disconnected. This has been shown to be properly captured by the membrane prediction to a high degree of accuracy.

Another point we can compare is the transition between linear growth and the plateau. Once again we see a favorable trend in our evaluation, although precise numerical agreement remains elusive.

B.6 Adding ϕ^4-interactions

An interesting extension of the story in section 3.4.2 is to study an RG flow that interpolates between a UV and an IR CFT. We expect that $\mathcal{E}(v)$ would be

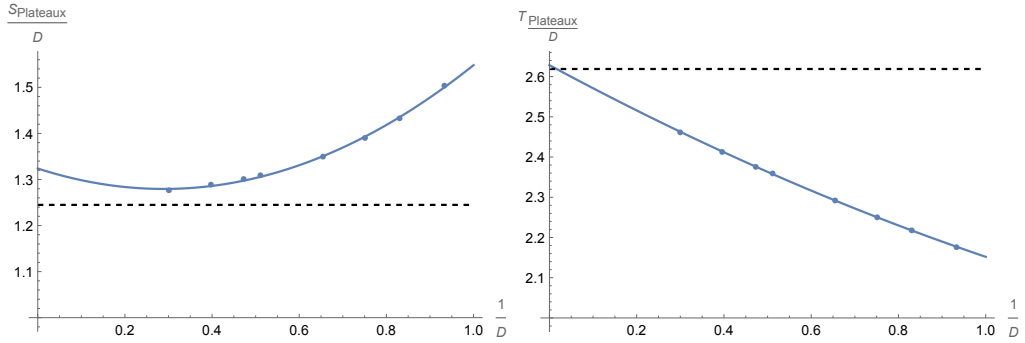

degenerate both in the UV and IR, but nontrivial in between. We could use the effective temperature of the state or operator whose entanglement dynamics we are studying as the RG scale. We can holographically model such an RG flow by adding a $\frac{\mu}{4!}\phi^4$ interaction to the bulk scalar fields in (3.4.1):

$$\mathcal{L} = \frac{1}{2}(R+2) - \frac{1}{2}(g^{ab}\partial_a\phi\partial_b\phi + m^2\phi^2 + \frac{\mu}{12}\phi^4). \tag{B.6.1}$$

The potential term in (B.6.1), now containing both the mass term and the ϕ^4 interaction, takes the form $V(\phi) = -\frac{3}{8}\phi^2 + \frac{\mu}{24}\phi^4$. At zero temperature we would get a domain wall scalar profile that interpolates between $\phi = 0$ at the boundary and the bottom of the potential $\phi_* = \frac{3}{\sqrt{2\mu}}$, representing the IR fixed point (Freedman, Gubser, Pilch, & Warner, 1999; Girardello, Petrini, Porrati, & Zaffaroni, 1998, 2000).

The Einstein-scalar equations of motion in the presence of the ϕ^4 interaction are

$$\phi'' + \left(\frac{f'}{f} - \frac{1}{z} - \frac{\chi'}{2}\right)\phi' + \frac{3}{4}\frac{\phi}{z^2 f} - \frac{\mu}{6}\frac{\phi^3}{z^2 f} = 0\,, \tag{B.6.2}$$

$$\chi' - 2\frac{f'}{f} - \frac{3}{4}\frac{\phi^2}{zf} - \frac{4}{zf} + \frac{4}{z} + \frac{\mu}{12}\frac{\phi^4}{zf} = 0\,, \tag{B.6.3}$$

$$\chi' - z\phi'^2 = 0\,. \tag{B.6.4}$$

From (B.6.2)–(B.6.4), we can obtain the shooting solution for ϕ^4-interacting bulk

scalars. A curious feature of these is that the scalar rolls through the minimum of the potential ϕ_* in the black brane interior and exhibits the same near-singularity behaviour in the presence of ϕ^4 interactions as in their absence. We can understand this as follows: The terms in (B.6.2)–(B.6.4) that originate from $V(\phi)$ are

$$\frac{3}{4}\frac{\phi}{z^2 f}\,, \qquad \frac{\mu}{6}\frac{\phi^3}{z^2 f}\,, \qquad \frac{3}{4}\frac{\phi^2}{zf}\,, \qquad \frac{\mu}{12}\frac{\phi^4}{zf}\,, \tag{B.6.5}$$

which upon substituting the asymptotic behaviour (3.4.8), all go to 0 in the large z limit. This is because ϕ and hence any polynomial of it only diverges *logarithmically*, and the Kasner behaviour (3.4.8) originates from the *kinetic* terms in the action (3.4.1) or (B.6.1). To change (3.4.8) near the singularity, one needs to introduce interactions that are (super-)exponential in ϕ (Hartnoll & Neogi, 2023). This may make us doubt if the IR CFT leaves any imprint on entanglement dynamics that is determined by the interior.

Nevertheless, by tuning ϕ_+, the horizon value of the scalar field, we can explore the RG flow, since for $\phi_+ \to \phi_*$, i.e. approaching the IR CFT, can tune the Kasner exponent close to the BTZ value appropriate for the IR CFT. Our findings are fully consistent with RG intuition and we summarise them on two plots in Fig. B.16. Both show $\mathcal{E}(v)$ scaled differently. On the left we multiplied $\mathcal{E}(v)$ by the dimensionless entropy density factor s_{th}/T that plays the role of the number of degrees of freedom. Recall that it is the combination $s_{\text{th}}\mathcal{E}(v)$ that shows up in the membrane action (1.3.11). This combination indeed gives a monotonically decreasing function under RG flow, which is a satisfactory result on physical grounds. On the right we have also rescaled the horizontal axis by the same factor s_{th}/T to demonstrate that $\mathcal{E}(v)$ still is tangent to the $45°$ line all along the RG flow. We note that we have found similar behaviour in the free scalar case as $\phi_+ \to \infty$, but of course there was no IR CFT there.

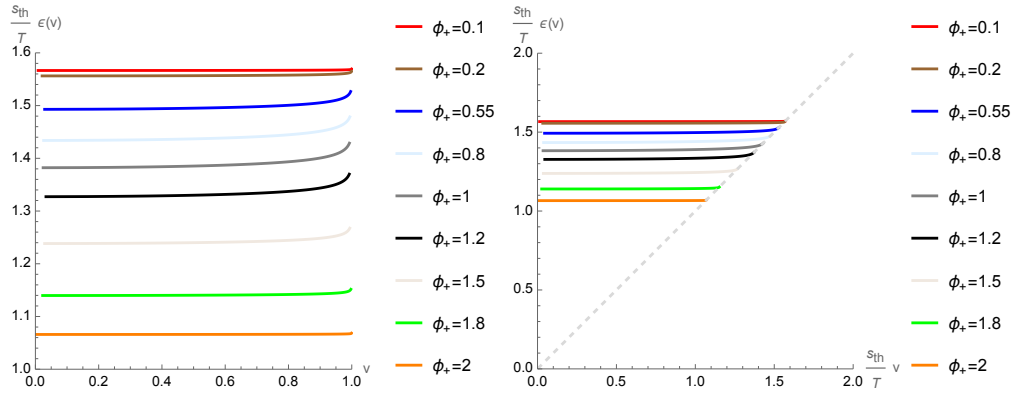

Figure B.16: Plots of the membrane tension $\mathcal{E}(v)$ for a ϕ^4-interacting bulk scalar with $\mu = 1$ for the choices $\phi_+ = 0.1, 0.2, 0.55, 0.8, 1, 1.2, 1.5, 1.8$ and 2. Note that the minimum of the potential that represents the IR fixed point is at $\phi_* = 2.12$.

C | Appendices to Chapter 4

C.1 Generalised entanglement membrane for CFT$_2$

So far, we have been studying multiparty entanglement signals in the membrane effective theory. For the special case of 2d CFT, however, that membrane theory becomes degenerate (Mezei, 2018), and the proper effective theory for entanglement dynamics is the generalised membrane theory introduced in Section 3.2.

C.1.1 S_R in the case of adjacent intervals

The generalised membrane theory for reflected entropy (Jiang et al., 2025) was developed for the case depicted in Figure 3.8 and 3.9 , where an interval of $O(\Lambda)$ size was inserted between A and B. To make our multipartite entanglement signal calculations comparable with the ordinary membrane results in Sections 4.1 and 4.2, we need to develop an effective description for adjacent A and B. We assume that as in the disjoint interval case studied in (Jiang et al., 2025) and reviewed above, the generalised membrane contains a horizontal component that does not contribute to the reflected entropy in the scaling limit. In (Jiang et al., 2025), the equations of motion for these generalised membranes parametrised by $(v(x), \xi(x))$[1] in the scaling limit were found to be

$$\begin{aligned} \xi'' &= 1 - \xi'^2 - e^{4(\xi_p - \xi)} \,, \\ v' &= e^{-2(\xi - \xi_p)} \,. \end{aligned} \tag{C.1.1}$$

[1] A change of variable from v to x has been made to describe the horizontal portion of the generalised membrane.

where $f' = \frac{df}{dx}$. The equations (C.1.1) have the following approximate solutions in the scaling limit

$$(v(x), \xi(x)) = \begin{cases} (v_p, -x + x_0 + \xi_p), & 0 < x < x_0, \\ (x + v_p - x_0, \xi_p), & x_0 < x, \end{cases} \tag{C.1.2}$$

where v_p, ξ_p, and x_0 are constants, with x_0 labeling the location of the membrane's turning point. Like in ordinary membrane theory (Jonay et al., 2018; Mezei, 2018), $v(x)$ describes the shape of the generalised membrane. To visualise the additional degree of freedom $\xi(x)$, we label it as colour on the generalised membrane as in (Jiang et al., 2025). There are two boundary conditions for the EWCS: that $x = \ell_A$ at time t, and that it ends on the vertical membrane at $x = 0$ perpendicularly. Notice that in imposing the boundary conditions for the EWCS in generalised membrane theory, we need to match not only the shape of the membrane v, but also the colour on the membrane ξ. Written explicitly, the two boundary conditions are

$$x_0 + \xi_p = t - v_p \qquad \text{to match the vertical membrane HRT,} \tag{C.1.3}$$

$$(\ell_A + v_p - x_0, \xi_p) = (t, 0) \qquad \text{to match the connection point on the } t \text{ slice,} \tag{C.1.4}$$

where the vertical membrane in (C.1.3) is described by (Jiang et al., 2025)

$$(x(v), \xi(v)) = (0, t - v). \tag{C.1.5}$$

One can then solve for the 3 constants

$$\xi_p = 0, \qquad v_p = t - \frac{\ell_A}{2}, \qquad x_0 = \frac{\ell_A}{2}. \tag{C.1.6}$$

The length of the EWCS is thus

$$\ell(\text{EWCS}) = x_A - x_0 = \frac{\ell}{2}\,. \tag{C.1.7}$$

See Figure C.1 for the plot of this generalised membrane. Notice that the saturation value is half as big compared to that in ordinary membrane theory as shown in Figure 4.1 right.

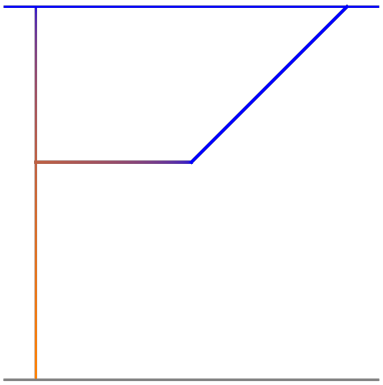

Figure C.1: The generalised membranes computing saturated S_R (thick) in 2d CFT in the case of adjacent intervals. As in 2411.16542, we use colour to denote the additional degree of freedom ξ on the membrane: the change from blue to orange denotes the increase in ξ.

As such, the time evolution of $S_R(A:B)$ is given by[2]

$$\frac{S_R(A:B)}{2} = s_{\text{th}} \begin{cases} t & t < \frac{\ell_A}{2}\,, \\ \frac{\ell_A}{2} & t > \frac{\ell_A}{2}\,. \end{cases} \tag{C.1.8}$$

As we will see shortly, the difference in the saturation of S_R between the ordinary and generalised membrane theories, (4.1.3) vs (C.1.8), leads to strikingly different behaviours of multipartite entanglement signals in 2d CFT and generic chaotic

[2]As in the $d > 2$ case, when considering adjacent intervals S_R is not UV finite (Kudler-Flam et al., 2020), and we subtract the logarithmic UV divergences.

systems. This indicates that the infinite-dimensional conformal symmetry might have substantial effects on multiparty entanglement, a possibility that would be very interesting to investigate in the future.

C.1.2 Dynamics of R_3

We use the generalised membrane theory for reflected entropy (C.1.8) to study the dynamics of residual information in the setups considered in Section 4.1. Quantities based solely on von Neumann entropy can be obtained from those in ordinary membrane theory in section 4.1.1 by simply setting $v_E = v_B = 1$.[3]

C.1.2.1 A single finite interval

We consider the setup of a single finite interval, $A = (-\infty, 0)$, $B = (0, \ell)$, and $C = (\ell, \infty)$, as is studied in section 4.1.1. $I(A : B)$ and $I(A : C)$ can be simply obtained from (4.1.1) and (4.1.2) by setting $v_E = v_B = 1$. Taking the difference between $S_R(A : B)$ (C.1.8) and $I(A : B)$, we find that

$$R_3(A : B) = 0 \ \text{ for } \ t \in [0, +\infty), \tag{C.1.9}$$

which is different from the ordinary membrane result (4.1.4) when setting $v_E = v_B = 1$ due to the difference in saturation of S_R in generalised membrane theory.

$S_R(A : C)$ is computed by the same vertical membrane (with an additional degree of freedom) as is shown in Figure 4.2, which never saturates. As such, $S_R(A : C)$ is given by (4.1.5) with $v_E = v_B = 1$. Taking the difference with $I(A : C)$, we

[3]We note that while setting $v_E = v_B = 1$ in ordinary membrane theory gives the correct generalised membrane theory results, the membranes computing entanglement entropy in generalised membrane theory have 2 degrees of freedom (Jiang et al., 2025). However, the extra degree of freedom will not play any role in determining the value of entanglement entropy if we are not studying the saturation of S_R.

have

$$R_3(A:C) = 0 \ \text{ for } \ t \in [0, +\infty). \tag{C.1.10}$$

Notice that we have $R_3(A:C) = 0$ when setting $v_E = v_B = 1$ in (4.1.6).

As R_3 is only a signal of tripartite entanglement instead of a measure, $R_3(A:B) = R_3(A:C) = 0$ in this setup does not necessarily indicate that there is only bipartite entanglement at any time.

C.1.2.2 Two finite regions

We consider the setup of two finite regions, $A = (0, \ell_A)$, $B = (\ell_A, \ell_A + \ell_B)$, and $C = (-\infty, 0) \cup (\ell_A + \ell_B, \infty)$, as studied in Section 4.1.2. Again, $I(A:B)$ and $I(A:C)$ can be simply obtained from (4.1.7) and (4.1.10) by setting $v_E = v_B = 1$. Since we focus on the $\ell_B < \ell_A$ case, using (C.1.8), $S_R(A:B)$ is given by

$$\frac{S_R(A:B)}{2} = s_{\text{th}} \begin{cases} t & t < \frac{\ell_B}{2}\,, \\ \frac{\ell_B}{2} & \frac{\ell_B}{2} < t < \frac{\ell_A+\ell_B}{2}\,, \\ 0 & t > \frac{\ell_A+\ell_B}{2}\,. \end{cases} \tag{C.1.11}$$

Notice that when AB saturates, $S_R(A:B)$ abruptly drops to 0. The corresponding cross-section is shown in Figure 4.5. Just as in the ordinary membrane theory case (4.1.8), this cross-section is no longer described by generalised membrane theory anymore, as it does not grow with t or x in the scaling limit. See Appendix C.3 for details. The dynamics of S_R in the case of two finite regions were also studied in (Kudler-Flam et al., 2020) from 2d CFT and holographic points of view. Our calculations from the generalised membrane effective theory agree with their results.

Taking the difference with $I(A:B)$ we find that

$$R_3(A:B) = s_{\text{th}} \begin{cases} 0 & t < \frac{\ell_A}{2}\,, \\ 2t - \ell_A & \frac{\ell_A}{2} < t < \frac{\ell_A+\ell_B}{2}\,, \\ 0 & t > \frac{\ell_A+\ell_B}{2}\,. \end{cases} \tag{C.1.12}$$

Notice that $\max\{R_3(A:B)\} = \ell_B$, which is *half* the bound for $R_3(A:B)$ (Balasubramanian, Kang, Murdia, & Ross, 2025). As a comparison, in the same setup in ordinary membrane theory, $R_3(A:B)$ (4.1.9) does saturate the $2\ell_B$ bound.

$S_R(A:C)$ is computed by the same vertical membrane as is shown in Figure 4.7 (again, with an additional degree of freedom). Hence, we can set $v_E = v_B = 1$ in (4.1.11) to obtain $S_R(A:C)$ in generalised membrane theory. Taking the difference with $I(A:C)$, we arrive at

$$R_3(A:C) = s_{\text{th}} \begin{cases} 0 & t < \frac{\ell_A}{2}\,, \\ 2t - \ell_A & \frac{\ell_A}{2} < t < \frac{\ell_A}{2} + \frac{\ell_B}{4}\,, \\ \ell_A + \ell_B - 2t & \frac{\ell_A}{2} + \frac{\ell_B}{4} < t < \frac{\ell_A+\ell_B}{2}\,, \\ 0 & t > \frac{\ell_A+\ell_B}{2}\,. \end{cases} \tag{C.1.13}$$

which is (4.1.12) with $v_E = v_B = 1$. We find that the initial plateau due to the saturation of B in (4.1.12) disappears in (C.1.13). The maximal value of $R_3(A:C)$ is $\max\{R_3(A:C)\} = \frac{\ell_B}{2}$, which reaches half the $R_3(A:C)$ bound.

C.1.3 Dynamics of Q_4

We use the generalised membrane theory for reflected entropy (C.1.8) to study the dynamics of Q_4 in the setup considered in Section 4.2: $A = (0, \ell_A)$, $B = (\ell_A, \ell_A + \ell_B)$, $C = (\ell_A + \ell_B, \ell_A + \ell_B + \ell_C)$ and $D = (-\infty, 0) \cup (\ell_A + \ell_B + \ell_C, \infty)$.

Again, we assume $\ell_A = \ell_C$ for simplicity.

The $\ell_A < \ell_B$ case is similar to that considered in section 4.2 except for the difference in saturation: the saturated EWCS ends on the vertical membrane on the left, but the saturation value is half as big as that in (4.2.4). Therefore, we have

$$Q_4 = s_{\text{th}} \begin{cases} 0 & 0 < t < \frac{\ell_A+\ell_B}{2}\,, \\ 2\ell_A & \frac{\ell_A+\ell_B}{2} < t < \frac{\ell_A+\ell_B+\ell_C}{2}\,, \\ 0 & t > \frac{\ell_A+\ell_B+\ell_C}{2}\,. \end{cases} \tag{C.1.14}$$

Compared to the corresponding ordinary membrane theory result (4.2.4), we see that $\max\{Q_4\} = 2\ell_A$ reaches half the $2\ell_A$ bound.

The $\ell_A > \ell_B$ case is more interesting: since the saturated EWCS now ends on κ, and the saturation value is half as big compared to the ordinary membrane result, the saturation of κ does change the value of $S_{AA^*A_*A_*^*}$ by doubling its value, see Figure C.2. This is in contrast to the ordinary membrane theory case shown in Figure 4.9, where the saturation of κ does not change the value of $S_{AA^*A_*A_*^*}$.

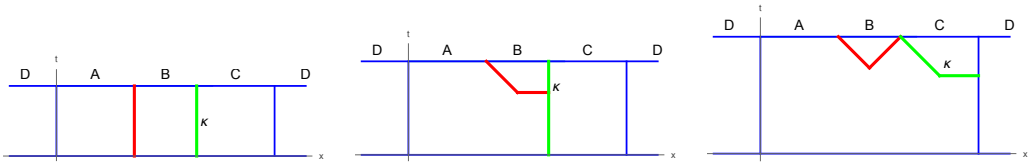

Figure C.2: Minimal cross-sections computing $S_{AA^*A_*A_*^*}$ (red, thick) in Q_4 in the generalised membrane theory for CFT$_2$ when $\ell_A > \ell_B$. Notice that the saturation of κ (green, thick) changes the shape as well as the value of the membrane computing $S_{AA^*A_*A_*^*}$. Here, we do not plot the additional degree of freedom ξ as a colour on the membrane as in Figure C.1, instead we follow the same colour conventions for Q_4 in the ordinary membrane cases in e.g. Figure 4.9.

We thus have

$$Q_4 = s_{\text{th}} \begin{cases} 0 & 0 < t < \frac{\ell_A+\ell_B}{2}\,, \\ 2\ell_B & \frac{\ell_A+\ell_B}{2} < t < \ell_A\,, \\ 4\ell_B & \ell_A < t < \frac{\ell_A+\ell_B+\ell_C}{2}\,, \\ 0 & t > \frac{\ell_A+\ell_B+\ell_C}{2}\,. \end{cases} \tag{C.1.15}$$

Notice that unlike the $\ell_A < \ell_B$ case, now $\max\{Q_4\} = 4\ell_B$ does saturate the $4\ell_B$ bound. This indicates that the extensive part of the entanglement of B is entirely multipartite.

C.2 Higher partite entanglement signals

We can extend the above calculations to higher numbers of parties. The extension is conceptually straightforward, and does not seem to lead to qualitatively new features, but the calculations become more complicated due to the increasing number of regions.

Consider for example the five-party entanglement signal R_5. Suppose we examine a system with subregions $A = (0, \ell)$, $B = (\ell, 2\ell)$, $C = (2\ell, 3\ell)$, $D = (3\ell, 4\ell)$, $E = (-\infty, 0) \cup (4\ell, +\infty)$, and trace over E. We have

$$R_5(A:B:C:D) = \frac{1}{2} I_4(AA^* : BB^* : CC^* : DD^*) - I_4(A:B:C:D), \tag{C.2.1}$$

where

$$\begin{aligned}\frac{1}{2}I_4(AA^*:BB^*:CC^*:DD^*) =& I_3(AA^*:BB^*:CC^*)\\ =& S(AA^*)+S(BB^*)+S(CC^*)+S(DD^*)\\ &-(S(AA^*BB^*)+S(AA^*CC^*)+S(BB^*CC^*)),\end{aligned} \tag{C.2.2}$$

and

$$\begin{aligned}I_4(A:B:C:D) =& S(A)+S(B)+S(C)+S(D)\\ &-(S(AB)+S(AC)+S(AD)+S(BC)+S(BD)+S(CD))\\ &+S(ABC)+S(ABD)+S(ACD)+S(BCD)-S(ABCD).\end{aligned} \tag{C.2.3}$$

We have $S(A)=S(B)=S(C)=S(D)=S_1$, $S(AB)=S(BC)=S(CD)=S_2$, $S(AC)=S(AD)=S(BD)=2S_1$, $S(ABC)=S(BCD)=S_3$, $S(ABD)=S(ACD)=S_2+S_1$, and $S(ABCD)=S_4$, where we use S_n to denote the entanglement entropy of an interval of length $n\ell$. This gives

$$I_4(A:B:C:D)=2S_3-S_2-S_4=s_{\text{th}}\begin{cases}0 & t<\ell,\\ 2t-2\ell & \ell<t<\frac{3\ell}{2},\\ 4\ell-2t & \frac{3\ell}{2}<2\ell,\\ 0 & t>2\ell.\end{cases} \tag{C.2.4}$$

The $ABCD$ entanglement wedge is always connected. Before the transition at $t=2\ell$, it is bounded by two vertical surfaces (Figure C.3). The purification-based quantities $S(XX^*)$ in (C.2.2) are computed by the minimal cross-sections that bisect the entanglement wedge of X and $ABCD/X$ (see Figure C.3 for

examples). As such, we have $S(AA^*) = S(DD^*) = S_2$, $S(BB^*) = S(CC^*) = 2S_1$, $S(AA^*BB^*) = S_4$, $S(AA^*CC^*) = S_2 + 2S_1$, and $S(BB^*CC^*) = 2S_2$. After the transition, the entanglement wedge only extends down to the horizon, and all the canonical purification quantities are given by vertical surfaces which extend down to the horizon (Figure 4.5), so $I_4(AA^* : BB^* : CC^* : DD^*) = 0$ for $t > 2\ell$. Thus

$$\frac{1}{2} I_4(AA^* : BB^* : CC^* : DD^*) = s_{\text{th}} \begin{cases} 0 & t < \frac{\ell}{2}, \\ 2\ell - 4t & \frac{\ell}{2} < t < \ell, \\ -2t & \ell < 2\ell, \\ 0 & t > 2\ell. \end{cases} \tag{C.2.5}$$

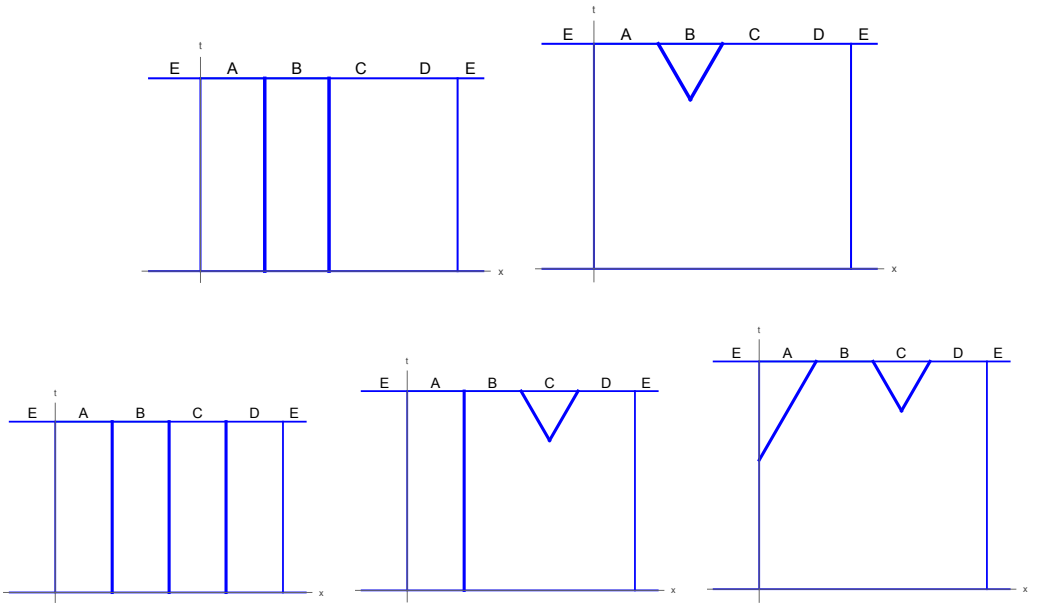

Figure C.3: Membranes computing $S(BB^*)$ (top row) and $S(AA^*CC^*)$ (bottom row) in $R_5(A : B : C : D)$. We only plotted membranes before the saturation of the $ABCD$ EW, after which all the entanglement wedge cross-sections have vanishing area in the membrane description.

This finally gives

$$R_5(A:B:C:D) = s_{\text{th}} \begin{cases} 0 & 0 < t < \frac{\ell}{2}\,, \\ 2\ell - 4t & \frac{\ell}{2} < t < \frac{3\ell}{2}\,, \\ -4\ell & \frac{3\ell}{2} < t < 2\ell\,, \\ 0 & t > 2\ell\,. \end{cases} \tag{C.2.6}$$

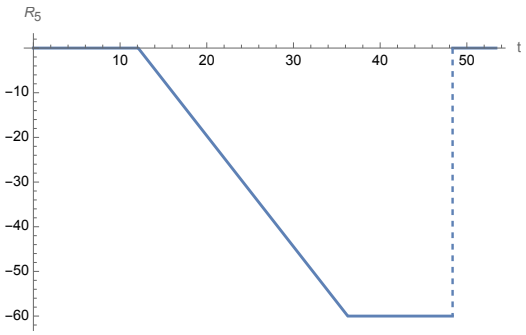

Figure C.4: Time evolution of $R_5(A:B:C:D)$ (C.2.6). Here, we plot for $\ell = 15$.

This gives qualitatively similar behaviour to $R_3(A:B)$ in Section 4.1.2. Notice that $R_5 \leq 0$. In the vacuum AdS_3 case studied in (Balasubramanian, Kang, Murdia, & Ross, 2025), R_5 is mostly negative, but with regions of the moduli where R_5 can be positive. It would be interesting to investigate the sign patterns of R_5 for more generic subsystem sizes here.

We can generalise the R_5 calculation to R_n for arbitrary odd n ($n \geq 3$). Likewise, for arbitrary even n ($n \geq 4$), we can generalise the $I_3 = \frac{1}{2}I_4$ calculation in Section 4.2 to compute the n-partite entanglement signal $I_{n-1} = \frac{1}{2}I_n$. As I_n are functions of von Neumann entropy, their time evolution will be continuous.

C.3 Saturation of S_R in finite adjacent intervals

In this Appendix, we use holography to verify that the saturated S_R in the case of finite adjacent intervals as shown in Figure 4.5 in the main text is indeed a vertical "membrane" that has vanishing extensive entropy in the scaling limit.

We calculate saturated S_R in holographic CFTs by examining the entanglement wedge cross-sections in the dual gravitational theories, where the planar AdS$_{d+1}$-Schwarzschild black brane metric is given by

$$ds^2 = \frac{1}{z^2}\Big(- f(z)dt^2 + \frac{dz^2}{f(z)} + dx^2 + d\vec{y}_{d-2}^2\Big), \quad f(z) = 1 - z^d. \tag{C.3.1}$$

The Schwarzschild time t in (C.3.1) is related to the infalling time v in (1.3.12) via

$$v(z) = t - \int_0^z \frac{dz'}{f(z')} = t - \frac{1}{d} B\left(z^d; \frac{1}{d}, 0\right), \quad z \in [0, 1), \tag{C.3.2}$$

where $B\left(z; a, b\right)$ is the incomplete Euler Beta function. The saturated EWCS lies on a constant Schwarzschild time slice.

We are interested in the bulk RT surface homologous to a boundary subregion AB of size $X = \ell_A + \ell_B$, see Figure 4.5 (top). Like in section 4.1.2, we consider the case $\ell_A > \ell_B$, with the boundary point K between A and B located at $x = k > 0$. We scale ℓ_A, ℓ_B and k to be large.

For simplicity, let us first consider the $d = 2$ special case.[4] In (Jiang et al., 2025), it was shown that the static spacelike geodesic homologous to a finite boundary

[4]Notice that for saturated S_R, all the extremal surfaces involved are outside the black hole horizon. Hence, in this case the additional degree of freedom ξ in generalised membrane theory is always of $O(1)$ value and can be scaled away. The results are thus the $v_E = v_B = 1$ special case of planar AdS$_{d+1}$-Schwarzschild black holes.

subregion is given by the parametric curve $\big(z(\lambda), x(\lambda)\big)$

$$\begin{aligned} z(\lambda) &= \frac{\sinh\frac{X}{2}}{\sqrt{\cosh\lambda\cosh(X+\lambda)}}, \\ x(\lambda) &= \frac{1}{2}\log(\text{sech}\lambda\cosh(X+\lambda)), \end{aligned} \tag{C.3.3}$$

where $\lambda \in (-\infty, +\infty)$. To find the minimal cross-section bisecting the AB entanglement wedge, we minimise the geodesic distance between K [5] and an arbitrary point G on the parametric curve (C.3.3). The geodesic distance formula in planar BTZ black brane is (Mezei, 2017; Shenker & Stanford, 2014)

$$\cosh d(K,G) = T_1^K T_1^G + T_2^K T_2^G - X_1^K X_1^G - X_2^K X_2^G, \tag{C.3.4}$$

where the embedding coordinates are given by

$$\begin{aligned} T_1 &= \frac{\sqrt{1-z^2}}{z}\sinh t, \quad T_2 = \frac{1}{z}\cosh t, \\ X_1 &= \frac{\sqrt{1-z^2}}{z}\cosh t, \quad X_2 = \frac{1}{z}\sinh x. \end{aligned} \tag{C.3.5}$$

The explicit expression for the geodesic distance between K and G is long and uninspiring. In the large region limit, we find that the minimal geodesic distance, after dropping the UV divergent $\log\frac{2}{\epsilon}$ term, is

$$d_{\text{reg}} = 0 \quad \text{at} \quad \lambda_* = -\frac{X}{2} + k. \tag{C.3.6}$$

At λ_*, one finds

$$x(\lambda_*) = k. \tag{C.3.7}$$

[5] To regularize the UV divergence, we consider the point K at $z = \epsilon \ll 1$ in the asymptotic region.

In other words, the minimal geodesic between K and G is the *radial* one in the scaling limit. This result makes sense intuitively, as the geodesic (C.3.3) contains a plateau region where it skims the horizon almost transversely along the x direction, and the EWCS needs to end on it perpendicularly.

Now, let us consider saturated S_R in the adjacent interval case in $d > 2$ with strip entangling subregions. In the large region limit, the intersection point z_0 between the EWCS and the RT surface is close to the horizon, $z_0 = 1 - \delta$ ($\delta \ll 1$). Following the intuition above, the EWCS is also almost radial in the scaling limit when $d > 2$. Thus, it would be convenient to parametrise the RT surface by $x(z)$ (instead of $z(x)$). The area functional is given by

$$A = \int dz d^{d-2}\vec{y}\, \frac{1}{z^{d-1}} \sqrt{\frac{1}{f(z)} + x'(z)^2}. \tag{C.3.8}$$

Noting that $x(z) = k$ and $x'(z) = 0$ for the saturated EWCS, the area functional becomes

$$A = \int_\epsilon^{z_0} dz \frac{1}{z^{d-1}} \frac{1}{\sqrt{1-z^d}} = \frac{1}{d} B\left(z^d; \frac{2}{d} - 1, \frac{1}{2}\right)\Big|_\epsilon^{z_0} \tag{C.3.9}$$

$$= \frac{\sqrt{\pi}\Gamma\left(\frac{2}{d} - 1\right)}{d\Gamma\left(\frac{2}{d} - \frac{1}{2}\right)} - \frac{2}{\sqrt{d}}\sqrt{\delta} + \frac{1}{d-2}\frac{1}{\epsilon^{d-2}}, \tag{C.3.10}$$

where we have eliminated the $\int d^{d-2}\vec{y} = \mathrm{Area}(\partial A)$ infinite factor as in the main text after (1.3.16). Restoring this factor, we find that the last term diverges as $\frac{1}{d-2}\frac{\mathrm{Area}(\partial A)}{\epsilon^{d-2}}$, which is the same as the UV divergence of RT surfaces (Rangamani & Takayanagi, 2017).[6] Dropping this UV divergent $\frac{\mathrm{Area}(\partial A)}{\epsilon^{d-2}}$ term, we have

$$A_{\mathrm{reg}} \sim \#\sqrt{\delta} + O(1) \to 0 \tag{C.3.11}$$

[6]This result makes sense, as both the RT surface and the saturated EWCS end on the boundary perpendicularly, and are hence asymptotically the same.

in the scaling limit. Notice that when $d = 2$, the area/length in (C.3.9) instead integrates to

$$A = -\tanh^{-1}\left(\sqrt{1-z^2}\right)\Big|_{\epsilon}^{z_0} = -\sqrt{2}\sqrt{\delta} + \log\frac{2}{\epsilon}, \tag{C.3.12}$$

which agrees with our $d = 2$ analysis above.

To sum up, we find that in $d \geq 2$ in the large region limit, the regularized area of the saturated EWCS is 0. As these EWCS as shown in Figure 4.5 (top) are radial and reach close to the horizon, their projections to the boundary along constant infalling time are vertical lines dangling from K, see Figure 4.5 (bottom). This is due to the near-horizon logarithmic divergence of infalling time v (C.3.2) (Jiang et al., 2025). Nevertheless, these cross-sections are no longer described by membrane theory for holographic CFT (Mezei, 2018; Jiang et al., 2025). This is because to derive the membrane tension (1.3.11) from the area of the HRT surface in the scaling limit, one needs to integrate out the radial bulk z degree of freedom. However, from e.g. (C.3.9) above, it is clear that for the almost-radial cross-section shown in Figure 4.5, the radial bulk z degree of freedom *cannot* be integrated out. The reason why this cross-section fails to be captured by membrane theory in other chaotic systems than holographic CFTs is technically less clear. Intuitively, one can understand the reason as cross-sections of this kind do not grow with t or x in the scaling limit. Hence, these vertical "membranes" should not be confused with the vertical membranes with tension $\mathcal{E}(0) = v_E$ (Mezei, 2018) obtained from projections of the HRT surfaces in the black hole interior (Hartman & Maldacena, 2013; Liu & Suh, 2014b, 2014a). The latter reaches the $t = 0$ slice in membrane theory, computing entanglement entropy $S = s_{\text{th}} v_E t$ that grows linearly with time.